High-resolution broadband rotational spectroscopy and electrical discharge experiments of astrochemically relevant molecules.

DISSERTATION

zur Erlangung des Doktorgrades
an der Fakultät für Mathematik, Informatik und Naturwissenschaften
Fachbereich Chemie
der Universität Hamburg

Angefertigt am Max-Planck-Institut für
Struktur und Dynamik der Materie
und
am Deutschen Elektronen-Synchrotron,
ein Forschungszentrum der Helmholtz-Gemeinschaft

Benjamin E. Arenas

aus Inverness, Schottland, Vereinigtes Königreich

Hamburg, Deutschland
2020

Gutachter der Dissertation:

Prof. Dr. Melanie Schnell

Prof. Dr. Holger Lange

Gutachter der Disputation:

Prof. Dr. Horst Weller

Prof. Dr. rer. nat. Dr. Sc. Christian Betzel

Prof. Dr. Melanie Schnell

Vorsitzender des Prüfungsausschusses:

Prof. Dr. Chris Meier

Datum der Disputation:

27.11.2020

Freigabe der Dissertation zur Veröffentlichung:

02.12.2020

List of Publications

1. B. E. Arenas, S. Gruet, A. L. Steber, B. M. Giuliano, M. Schnell *Chirped-pulse Fourier transform millimeter-wave spectroscopy of ten vibrationally excited states of i-propyl cyanide: Exploring the far-infrared region*, Physical Chemistry Chemical Physics **19**, 1751-1756 (2017). [Front Cover]

2. B. E. Arenas, S. Gruet, A. L. Steber, M. Schnell *A global study of the conformers of 1,2-propanediol and new vibrationally excited states*, Journal of Molecular Spectroscopy **337**, 9-16 (2017). [Front Cover]

3. B. M. Giuliano, L. Bizzocchi, A. Pietropolli Charmet, B. E. Arenas, A. L. Steber, M. Schnell, P. Caselli, B. J. Harris, B. H. Pate, J.-C. Guillemin, A. Belloche *Rotational spectroscopy of imidazole: Improved rest frequencies for astrophysical searches*, Astronomy and Astrophysics **628**, A53 (2019).

4. M. Fatima, C. Pérez, B. E. Arenas, M. Schnell, A. L. Steber *Benchmarking a new segmented K-band chirped-pulse microwave spectrometer and its application to the conformationally rich amino alcohol isoleucinol* Physical Chemistry Chemical Physics **22**, 17042-17051 (2020). [Front Cover]

5. P. Stahl, B. E. Arenas, S. R. Domingos, G. W. Fuchs, M. Schnell, T. F. Giesen *Laboratory blueprints for interstellar searches of aromatic chiral molecules: Rotational signatures of styrene oxide* Physical Chemistry Chemical Physics **22**, 21474-21487 (2020).

6. B. E. Arenas, M. Fatima, C. Pérez, S. Fischer, A. L. Steber, M. Schnell *Facilitating interstellar searches for simple amino alcohols with accurate rest frequencies into the millimeter-wave regime: Alaninol, valinol, and leucinol* **Under Review**.

7. B. E. Arenas, G. Batra, A. L. Steber, L. Bizzocchi, B. M. Giuliano, P. Caselli, B. J. Harris, B. H. Pate, A. Pietropolli Charmet, M. Schnell *Rotational spectroscopy of imidazole: Three vibrationally excited states and a molecular structure based on an extended frequency range* **In Preparation**.

8. P. Stahl, B. E. Arenas, O. Zingsheim, M. Schnell, L. Margulès, G. W. Fuchs, T. F. Giesen *Deciphering the rotational spectrum of the first excited torsional state of propylene oxide* **In Preparation**.

Abstract

"Somewhere, something incredible is waiting to be known."

Carl Sagan (1934-1996)

Since the discovery of molecules in the interstellar medium in the 1960s, the quest to fully characterise the chemical inventory of interstellar space has resulted in the detection of over 200 distinct molecules. This has been achieved through the combined efforts of laboratory spectroscopy and observational astronomy. Advances in the field of radio astronomy, in particular with the increased sensitivity, widened frequency bandwidth of operation, and higher angular resolution of facilities such as the Atacama Large Millimeter/submillimeter Array, is producing a high throughput of data of unprecedented quality. In order to analyse this data, and, in turn, to address questions surrounding molecular complexity and chemical evolution in space, there needs to be concurrent progress in the field of high-resolution laboratory spectroscopy.

Rotational spectroscopy is a uniquely suited technique for providing data that enables searches for molecules in the interstellar medium. The experimentally recorded transition frequencies, or the line frequencies predicted from the rotational constants derived from spectral analysis, are used to identify molecular species in observational spectra. Rotational spectroscopy is a high-resolution, highly sensitive technique from which structural data about the probed molecules can be obtained. In fact, the fingerprint nature of the technique facilitates the unambiguous conformer- and isotopologue-specific laboratory assignment and interstellar observation of studied molecules. The spectrometers used throughout this work are the Hamburg COMPACT Spectrometer (2-18 GHz), the 18-26 GHz Spectrometer, and a W-band Spectrometer (75-110 GHz) from BrightSpec, Inc. The operating ranges overlap with a number of observational facilities, putting the data presented here at the forefront of experimental astrochemistry and radio astronomy.

The necessary laboratory data to perform observational searches for a number of nitrogen- and oxygen-containing astrochemically relevant molecules is delivered

in this thesis. The pure rotational spectra of the vibronic ground state of *iso*-propyl cyanide, the six lowest energy conformers of 1,2-propanediol, two, four, three, and seven ground state conformers of alaninol, valinol, leucinol, and isoleucinol, respectively, and the ground state of imidazole were assigned. The resulting line lists and rotational constants are the most precise descriptions of these molecules available to date, and they can be used for comparison to observational spectra. Further to this, because of the assignment of isotopologues in natural abundance, extensive structural information is obtained for the molecules studied. The room-temperature experiments performed on the W-band spectrometer allowed for the assignment of low-lying vibrationally excited states, which, if detected in the interstellar medium, can act as probes of the region's physical conditions.

The laboratory data has been used to search for some of the studied species towards the giant molecular cloud Sagittarius B2. Searches for the vibrational states of *iso*-propyl cyanide in the *Re-exploring Molecular Complexity with ALMA* line survey of Sagittarius B2(N2b) revealed the presence of the four lowest energy states ν_{30}, ν_{29}, ν_{17}, and ν_{16}. The detected line profiles could be accurately described using local thermodynamic conditions at 150 K. Imidazole was searched for in the *Exploring Molecular Complexity with ALMA* observational data set towards Sagittarius B2(N), and the ring structure was not detected towards the region. A search towards the Taurus Molecular Cloud, where the aromatic molecule benzonitrile was previously detected, is suggested.

Further, an electrical discharge nozzle was implemented and optimised on the W-band spectrometer. Performing electrical discharge experiments will not only permit the characterisation of reactive species and new molecules, but also allow for the consideration of formation pathways and mechanisms to these molecules from the precursors used. The discharge of acetaldehyde was shown to produce the formyl radical, ketene, propyne, acrolein, and acetone. Mapping the distributions of these species in molecular clouds, something which is possible thanks to the high spatial resolution of observational data sets, can ascertain whether these laboratory determined reaction pathways are relevant for interstellar chemistry. Experimental modifications to promote the detection of products that incorporate functional groups from multiple precursors is also discussed.

The data presented in this thesis will enable searches for the studied molecules in the interstellar medium, and in the case of the amino alcohols, this could establish a new class of interstellar molecule. Detections of these molecules will increase the knowledge of the complexity of interstellar space. The simultaneous mapping of the spatial distributions of molecules and their potential precursors, which can be guided by the results of electrical discharge experiments, will contribute to the understanding of the chemistry occurring in these extraterrestrial environments.

Zusammenfassung

"Irgendwo wartet etwas
Unglaubliches darauf, bekannt
zu werden."

Carl Sagan (1934-1996)

Seit der Entdeckung der ersten Moleküle im interstellaren Raum in den 1960er Jahren hat das Bestreben, das chemische Inventar des interstellaren Raums vollständig zu charakterisieren, zum Nachweis von über 200 verschiedenen Molekülen geführt. Dies wurde durch die kombinierten Anstrengungen von Laborspektroskopie und Teleskopbeobachtungen erreicht. Fortschritte auf dem Gebiet der Radioastronomie, insbesondere mit der erhöhten Empfindlichkeit, der erweiterten Frequenzbandbreite und der höheren Winkelauflösung von Einrichtungen wie dem Atacama Large Millimeter/Submillimeter Array, führen zu einem hohen Datendurchsatz von beispielloser Qualität. Um diese Daten zu analysieren und damit Fragen der molekularen Komplexität und der chemischen Entwicklung im Weltraum zu beantworten, sind gleichzeitig Fortschritte auf dem Gebiet der hochauflösenden Laborspektroskopie erforderlich.

Die Rotationsspektroskopie eignet sich hervorragend zur Bereitstellung von Daten, die die Suche nach Molekülen im interstellaren Raum ermöglichen. Die experimentell gewonnenen Übergangsfrequenzen oder die Linienfrequenzen, die aus den experimentell bestimmten Rotationskonstanten vorhergesagt werden, werden zur Identifizierung von Molekülspezies in Spektren aus radioastronomischen Beobachtungen verwendet. Die Rotationsspektroskopie ist eine hochauflösende, hochempfindliche Technik, mit der auch Strukturdaten über die untersuchten Moleküle gewonnen werden können. Tatsächlich erleichtert diese fingerabdruckartige Technologie die eindeutige konformeren- und isotopologenspezifische Identifikation im Labor und nachfolgend die interstellare Beobachtung der untersuchten Moleküle. Die in dieser Arbeit verwendeten Spektrometer sind das Hamburger COMPACT-Spektrometer (2-18 GHz), das 18-26 GHz-Spektrometer und ein W-Band-Spektrometer (75-110 GHz) von BrightSpec, Inc. Die abgedeckten Frequenzbereiche der Spektrometer

überlappen mit einer Reihe von Radioteleskopen, so dass die hier vorgestellten Daten für eine Weiterentwicklung der Astrochemie und Radioastronomie von großer Relevanz sind.

In dieser Arbeit werden die erforderlichen Labordaten für eine erfolgreiche Suche nach einer Reihe von stickstoff- und sauerstoffhaltigen, astrochemisch relevanten Molekülen geliefert. Es wurden die reinen Rotationsspektren des vibronischen Grundzustandes von *iso*-Propylcyanid, die sechs niederenergetischen Konformere von 1,2-Propandiol, zwei, vier, drei und sieben Grundzustandskonformere von Alaninol, Valinol, Leucinol bzw. Isoleucinol und der Grundzustand von Imidazol zugeordnet. Die daraus resultierenden Linienlisten und Rotationskonstanten sind die präzisesten Beschreibungen dieser Moleküle, die bisher verfügbar sind, und sie können zum Vergleich mit radioastronomischen Spektren verwendet werden. Darüber hinaus erhält man durch die Zuordnung von Isotopologen in natürlicher Häufigkeit umfangreiche Strukturinformationen für die untersuchten Moleküle. Die mit dem W-Band-Spektrometer durchgeführten Raumtemperaturexperimente erlaubten die Zuordnung tiefliegender schwingungsangeregter Zustände, die, wenn sie im interstellaren Raum detektiert werden, als Sonden für die physikalischen Bedingungen der Region dienen können.

Die Labordaten wurden zur Suche nach einigen der untersuchten Moleküle in Richtung der riesigen Molekülwolke Sagittarius B2 verwendet. Die Suche nach den Schwingungszuständen von *iso*-Propylcyanid in der *"Re-exploring Molecular Complexity with ALMA"*-Suche von Sagittarius B2(N2b) ergab das Vorhandensein der vier niedrigsten Schwingungszustände ν_{30}, ν_{29}, ν_{17} und ν_{16}. Die entdeckten Linienprofile konnten mit Hilfe der lokalen thermodynamischen Bedingungen bei 150 K genau beschrieben werden. Nach Imidazol wurde im *"Exploring Molecular Complexity with ALMA"*-Beobachtungsdatensatz in Richtung Sagittarius B2(N) gesucht, allerdings konnte diese Ringstruktur bisher nicht nachgewiesen werden. Eine Suche in Richtung der Taurus-Molekülwolke, wo zuvor das aromatische Molekül Benzonitril nachgewiesen wurde, wird vorgeschlagen.

Weiterhin wurde eine elektrische Entladungsdüse implementiert und am W-Band-Spektrometer optimiert. Die Durchführung elektrischer Entladungsexperimente wird nicht nur die Charakterisierung reaktiver Spezies und neuer Moleküle, sondern auch die Analyse von Bildungswegen und -mechanismen dieser Moleküle aus den verwendeten Vorläufermolekülen ermöglichen. Es konnte gezeigt werden, dass bei der Entladung von Acetaldehyd das Formylradikal, Keten, Propin, Acrolein und Aceton entstehen. Durch die Kartierung der Verteilungen dieser Spezies in Molekülwolken, die dank der hohen räumlichen Auflösung der Beobachtungsdatensätze heutzutage möglich ist, kann im Prinzip festgestellt werden, ob diese im Labor ermittelten Reaktionswege für die interstellare Chemie relevant sind. Experimentelle Modifikationen für einen verbesserten Nachweis von Produkten, die funktionelle

Gruppen aus mehreren Vorläufermolekülen enthalten, werden ebenfalls diskutiert.

Die in dieser Arbeit vorgestellten Daten ermöglichen die Suche nach den untersuchten Molekülen im interstellaren Raum und könnten im Falle der Aminoalkohole eine neue Klasse interstellarer Moleküle etablieren. Der Nachweis dieser Moleküle wird das Wissen über die Komplexität des interstellaren Raums erweitern. Die gleichzeitige Kartierung der räumlichen Verteilung der Moleküle und ihrer potentiellen Vorläufer, die sich an den Ergebnissen von Experimenten mit elektrischen Entladungen orientieren kann, wird zum Verständnis der in diesen extraterrestrischen Umgebungen auftretenden Chemie beitragen.

Contents

Chapter 1

Introduction

1.1 Astrochemistry

astrochemistry *noun* the study of the abundance, interactions, and reactivity of atoms, molecules, ions, and radicals in extraterrestrial environments and their influence on the structure, dynamics, and evolution of astronomical objects

In the 1960s, radio astronomy facilitated the interstellar detections of the hydroxyl radical, $^{\bullet}$OH, ammonia, NH_3, water, H_2O, and formaldehyde, H_2CO [1–4]. Since then, organic molecules have continued to be detected with increasing complexity within the interstellar medium (ISM). They range considerably - from simple organic molecules such as methanol, CH_3OH [5], to larger unsaturated carbon chains such as cyanotriacetylene, HC_7N [6], to molecular C_{60} [7]. These species make up the chemical inventory of the ISM, which has grown significantly over time, with over 200 molecules having been detected to date [8]. Up-to-date lists can be found at the Cologne Database for Molecular Spectroscopy* and the Astrochymist website†. The continued search for new complex organic molecules (COMs), where the community-accepted definition of a COM is a carbon-bearing molecule with six or more atoms [9], is driven by the desire to characterise the chemical complexity of the ISM and to understand the chemical reactions that result in their formation, ultimately with the hope that fundamental questions in astronomy and astrochemistry, such as the extent to which biologically relevant molecules are present in space, will be answered.

The ISM plays a particularly important role in the life cycle of stars, as it is in this region that star systems form. Therefore, the materials already present in the ISM can dictate the composition of the systems that follow. Figure 1.1 shows the

*cdms.astro.uni-koeln.de/cdms/portal

†www.astrochymist.org/astrochymist_ism

general life stages of a star, or stellar, system. A short description follows here for reference [10], where the numbers describe the stages labelled in Figure 1.1 [11].

- DIFFUSE CLOUD: An interstellar cloud (1) of gas and dust of very low density. The density, characterised by the total density of hydrogen nuclei, n_H, is $<$100 cm^{-3}. Typical temperatures in diffuse atomic clouds range from 30-100 K.

- DENSE CLOUD: The increase in mass of a diffuse interstellar cloud facilitates self-gravitation; the system contracts. This leads to the formation of a protostellar system (2). The size and density (n_H $>10^4$ cm^{-3}) of the cloud is such that regions can become shielded from the interstellar radiation field, and complex molecule formation can occur. Temperatures in dense molecular clouds can vary greatly and can reach the order of 10^2 K. Dense clouds can also be characterised by f^n_{CO}, which is the total fraction of carbon in the form of carbon monoxide. This value is typically 0.9 in these regions.

- ACCRETION DISK: A protostellar system contracts further. This forms a central protostar surrounded by a rotating disk of gas and dust (3). Complex molecule formation can also occur here. Material accretion causes the formation of planets and comets in the outer disk.

- STELLAR SYSTEM: Thermonuclear reactions in the star are ignited by further increases in the temperature and density. Planets, comets, and interplanetary materials orbit around the star (4).

- MASS LOSS: Nuclear fuel depletion leads to the star's instability. It begins to lose mass, a process that can also be accompanied by the formation of molecular species. The lost mass is ejected into the ISM, where it forms the basis of new low-density diffuse interstellar clouds.

The physical structures in the ISM that are of particular interest to the work in this thesis are molecular clouds. Interstellar clouds are accumulations of gas, plasma, and dust in the ISM, and molecular clouds are interstellar clouds within which the formation of molecules is possible. Molecules can form and survive because the density and size of the molecular cloud shields the bulk of the gas from the interstellar radiation field. Two such examples that are often studied are the giant molecular cloud Sagittarius B2 (Sgr B2) and the diffuse nebula called the Orion Nebula. Sgr B2 is well-studied because it contains a number of dense and chemically diverse regions known as molecular cores. Within the Orion Nebula, the most characterised region is the active star-forming region called the Kleinmann-Low Nebula (Orion KL).

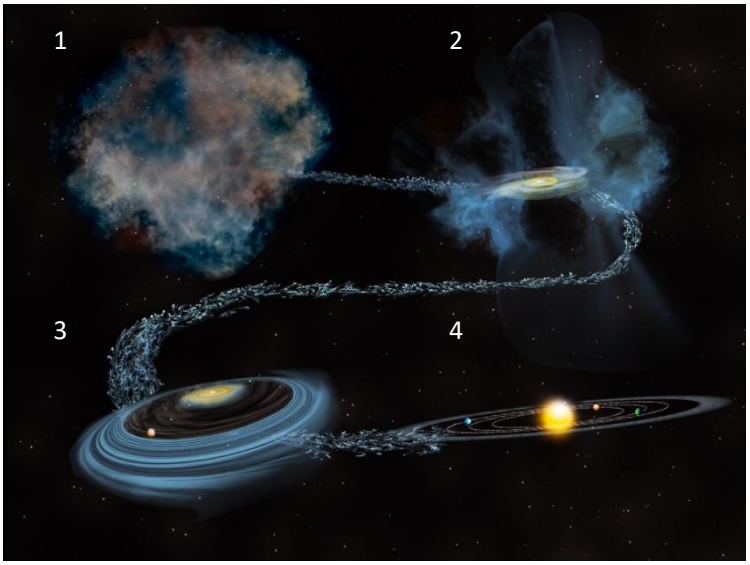

Figure 1.1: The life stages of a star system. The stages labelled are: (1) the interstellar cloud; (2) the collapse of the molecular cloud into an accretion disk by self-gravitation; (3) the formation of planets around the central protostar; (4) the stellar system. See the main text for the descriptions of each of the stages. *Figure adapated from Bill Saxton, National Radio Astronomy Observatory.*

The composition of interstellar clouds can be revealed through a variety of observational techniques. The use of infra-red (IR) astronomy or radio astronomy can be used to characterise diffuse and dense molecular clouds, such as the previously mentioned Sgr B2 and Orion KL [10]. IR astronomy is affected substantially by the Earth's atmosphere. The radiation reaching Earth from space is absorbed by molecules in the atmosphere, in particular water vapour, which results in the need for IR facilities to be elevated such that they are above as much of the atmosphere as is possible. For example, the Stratospheric Observatory for Infrared Astronomy, SOFIA, is a telescope facility carried on an aircraft that can reach altitudes above 99 % of the Earth's IR-blocking atmosphere [12]. Molecules in the atmosphere also emit IR radiation; the recorded IR spectra from ground-based observatories can also be affected by this. Radio astronomy, where radio frequencies range from 30 Hz to 300 GHz, can be used for ground-based observations that, in specific regions, are not affected by the atmosphere in the same way. Since the early 1960s, a number of radio astronomical facilities have been developed and used to detect molecules in molecular clouds. These include the Robert C. Byrd Green Bank Telescope (GBT), the Karl G. Jansky Very Large Array (VLA), the Effelsberg 100m Radio Telescope,

and the Atacama Large Millimeter/Submillimeter Array (ALMA), which are all examples of facilities whose resolutions and sensitivities are among the gold standard. Arguably the most exciting development in radio astronomy over the past decade has been the commission and implementation of ALMA. This facility, located in the Chilean desert, is made up of over 60 single-dish radio telescopes that work together as a telescope array [13]. ALMA has already been used to extensively study the two interstellar structures mentioned above: for Sgr B2, see Refs. [14–18], and for Orion KL, see Refs. [19–21], among many others. The continual upgrading of these radio telescopes, indeed not all of ALMA's operational bands are fully operational at the time of writing, as well as the commissioning of new facilities is creating an ever-growing need for laboratory data to aid in the analysis of observational data.

Laboratory data is required for the disentanglement of the new observations being performed at facilities such as ALMA. Unprecedented sensitivity of the observational facilities is producing data that can only be fully characterised with the aid of high-resolution laboratory studies. The high throughput of observational data is creating an immediate need for laboratory analysis of astrochemically relevant molecules. It is now the case that the standard format of observational data sets is a spatially resolved image of a region of the ISM, where each pixel of the image contains an individual broadband survey of the region the pixel covers [22]. Further, ALMA's broadband operating regimes and high spatial resolution, which was first showcased in the unbiased Protostellar Interferometric Line Survey (PILS) in Ref. [23], allows for the observation of transitions from many molecules in one observation campaign with spatial resolution orders of magnitude higher than previous data sets. This can facilitate the detection of increasingly complex molecules, and as the complexity of molecules being detected increases, so too does the need for the laboratory data of related species.

Pure rotational spectroscopy is a rotationally resolved laboratory technique that provides data leading to the unambiguous identification and quantification of molecular structures in the ISM. In particular, rotational spectroscopy provides line lists and rotational constants for molecules of interest. Astronomers can utilise this data for comparisons to their observational data sets for targeted searches for and detections of the molecule in particular regions of the ISM. The rotational spectrum of a molecule, unlike the data from the aforementioned IR astronomy, is a molecular fingerprint - the spectra are structure and conformer specific, allowing for specific molecules and specific conformers of molecules to be detected. Further to this, the rotational transitions detected can be used to determine the density and temperature of the molecular species in interstellar space [24].

As well as 'standard' molecular species, the emission detected in observational data can be attributed to low-lying vibrationally excited states and isotopologue species [25]. Indeed, as noted in Ref. [26], isotopologues and vibrationally excited

states are believed to be the source of many unidentified lines. The percentage of unidentified lines can be as much as 70% in very deep observations at ALMA Bands 3 (84-116 GHz) and 6 (211-275 GHz) [27]. Further, the 2018 NASA Laboratory Astrophysics Workshop identified "spectral studies producing rotational line lists, especially focusing on vibrational states, [and] isotopologues" as one of the highest-priority recommendations [28]. Vibrationally excited states play an important role in warmer regions of the ISM, such as the molecular clouds previously mentioned - they can act as temperature probes of the surrounding environment [29] and can be involved in chemical reactions [30]. Laboratory isotopologue data can be used to search for isotopologues in the ISM. The rotational spectrum of a singly substituted isotopologue is slightly shifted when compared to the spectrum of the parent species, which is caused by the small change in mass distribution. Detections of isotopologues can shed light on the formation pathways of molecules. For example, the authors of Ref. [31] showed that the $^{12}C/^{13}C$ ratios in CCH and CCS differed from the elemental ratio. They concluded that the ratio was dependent on if the carbon source was the carbon ion or carbon monoxide, CO. Knowledge of isotopic fractionation can also allow for processes involved in the early stages of star formation to be understood. This is particularly true for the examples of the hydrogen/deuterium (H/D) and the $^{12}C/^{13}C$ ratios [32]. Vibrationally excited states and isotopologue species can also be considered as 'weeds' [33] or a hindrance to identifying new COMs in observational data sets. Their elimination from astronomical spectra is an additional result of investigations into these species. Therefore, both vibrational states and isotopologues are important to characterise, so that their interstellar abundances and roles in astrochemical reactions can be determined.

This thesis delivers the necessary rotational constants and line lists to enable searches for the studied molecules in the ISM. What is particularly important is the overlap of the data from the W-band spectrometer, which operates in the 75-110 GHz region, and ALMA Band 3 (84-116 GHz; 2.6-3.6 mm). The assigned laboratory rest frequencies can be directly compared to observational data sets, thus giving confidence in detections, particularly when many features in these confusion-limited broadband astronomical surveys suffer from high line density or line blending. In addition, the centrifugal distortion constants determined from the millimeter-wave (mmw) studies allow for lines in higher frequency regimes to be accurately predicted, meaning the laboratory work can be applied to observational data sets at higher frequencies. The room-temperature experiments provide access to vibrationally excited states; searches for them in the ISM can follow the assignment of their pure rotational spectra. The sensitivity of the instruments, as outlined in Section 1.2 and Chapter 3, allows the laboratory characterisation of isotopologues in natural abundance, providing the ability to determine gas-phase structures of the molecules as well as providing the necessary data for interstellar searches. Finally, the discharge

set-up presented will generate new molecular species, including transient molecules, which can be characterised in the laboratory. This will aid in the quest to discover new molecular classes, such as families of doubly functional molecules which are relatively under-represented in the chemical inventory of the ISM. It will also provide experimental evidence for potential pathways and mechanisms to these molecules in interstellar space.

1.2 Rotational Spectroscopy

Rotational spectroscopy is a technique that is used to study gas-phase molecules which possess an electric dipole moment. Indeed, these two criteria are the only requirements a sample needs in order to have a measureable rotational spectrum. As well as the previously mentioned line lists and rotational constants, analysis of the rotational spectrum also yields molecular structure information. This is because the rotation of the molecule is linked to its moments of inertia. Further, a number of methods exist, which are explored in more depth in Section 2.8, to determine the gas-phase structure of molecules by pinpointing the atomic coordinates. The experiments and analysis can be expanded into the investigation of weakly bound complexes. The prevalence of weakly bound complexes in a supersonic expansion is high - three- or more-body collisions occur, during which the complexes are formed and the excess energy is removed by carrier gas atoms, and the lifetimes of the complexes are extended due to few collisions in the expansion (see Section 3.4). The specificity of rotational spectroscopy allows for the structures of these complexes to be determined. From both the structures that are observed experimentally and from the use of theoretical chemistry [34], the forces that are involved in the formation and maintenance of these complexes in the gas phase can be revealed.

In short, a Fourier transform rotational spectroscopy experiment involves the interaction of electromagnetic radiation, from the microwave, mmw, or the sub-mmw regions, with gas-phase molecules. The interaction between the molecule and radiation that is resonant or near-resonant with a molecular transition induces a macroscopic dipole moment in the gaseous sample, the decay of which is recorded in the form of a free induction decay (FID), which is a coherent molecular emission. Fourier transformation of the FID transforms the time domain data into a frequency domain spectrum. Analysis of the spectrum, which involves the iterative assignment of rotational quantum numbers to the experimental transitions and which is described more fully in Chapter 2, yields a set of rotational constants that describe the molecular system.

The first molecular spectrum recorded in the microwave region was concerned with the inversion of ammonia, NH_3, and this was reported in 1934 [35]. Microwave spectroscopy progressed in leaps and bounds over the following years, and this was

aided by the development of radar for use in World War Two and the advancements in pulsed techniques for nuclear magnetic resonance (NMR) spectroscopy. This culminated, in the late 1970s and early 1980s, with the establishment of a technique that would become one of the pillars of rotational spectroscopy. Balle and Flygare reported the design of a Fourier transform microwave (FTMW) spectrometer that coupled a Fabry-Pérot cavity with a pulsed microwave source and utilised a supersonic expansion as a sample introduction method [36, 37]. The Fabry-Pérot cavity was equipped with tunable mirrors whose positions could be automatically altered, and the excitation radiation was tuned to be resonant with the distance between these mirrors. The broadband search capabilities (in steps of approximately 1 MHz) of the rotational spectrometer could be more easily achieved than previously, and with high sensitivity and narrow linewidths. The supersonic expansion facilitated the study of rotationally and vibrationally cold molecules (see Section 3.4) and weakly bound complexes.

In the 1990s, the Balle-Flygare experimental set-up was improved upon by Grabow *et al.*, who introduced a coaxial arrangement of the molecular beam and the microwave field [38]. This arrangement greatly improved the resolution and sensitivity compared to previous set-ups. In the early 2000s, the design of a chirped-pulse FTMW (CP-FTMW) spectrometer was reported by Brooks Pate and co-workers [39]. This design removed the tunable mirror cavity set-up from the Balle-Flygare design, and it was replaced with broadband horn antennae that have the ability to broadcast chirped pulses covering a large frequency range. These chirped pulses are excitation pulses which span up to tens of GHz in the frequency domain. The excitation pulse is called a chirped pulse because the pulse is a linear sweep of frequency in time. This allows for all of the transitions of the molecular system resonant with a frequency covered by the chirped pulse to be polarised, which speeds up data acquisition considerably.

An extension to this work, which was reported in Ref. [40], was concerned with dividing the chirped pulse into smaller segments. By exploiting the flexibility of arbitrary waveform generators (AWGs) and the development of active multiplier chains (AMCs), which can be used to increase the frequency and bandwidth of the output of AWGs, the CP-FTMW spectroscopy method was extended to the millimeter and sub-millimeter wave regimes. The segmented technique allows for the implementation of high frequency experiments without the need to invest in high-cost AWGs and high-bandwidth digitisers [40]. Lower cost AWGs can be used, as low-frequency excitation pulses can be generated and later frequency up-converted, and low-bandwidth digitisers can be used as the high-frequency molecular emission can be frequency-down-converted before being digitised and Fourier transformed. The segmented approach also circumvents the issue presented by the limited commercial availability of high bandwidth oscilloscopes that would be used in place of the

digitisers. Segmented CP-FTMW spectroscopy and segmented mmw spectroscopy is used, respectively, in the 18-26 GHz spectrometer and the W-band spectrometer introduced in Chapter 3.

There are numerous methods that were developed with the aim of diversifying the types of molecular samples studied with rotational spectroscopy. For example, the use of heatable nozzles for sample introduction, first pioneered to study transient molecules formed via pyrolysis [41, 42], has found wide-spread application in bringing high melting point liquids and solids into the gas phase for probing with rotational spectroscopy. The rotational spectra of inorganic metal species and solid biomolecular samples have been accessed with the use of laser ablation [43, 44].

One method that has found particular application in astronomy and astrochemistry is electrical discharge, which was first reported in the nozzle design in Ref. [45]. This has led to the production and characterisation of transient species, and much work has been carried out, in particular, on extended unsaturated carbon chains (see, for example, Ref. [46–50]). Many of these have subsequently been detected in the ISM. Recently, the combination of acetonitrile, CH_3CN, and hydrogen sulfide, H_2S, in a pulsed discharge CP-FTMW spectroscopy experiment led to the production, characterisation, and interstellar detection of ethanimine, CH_3CHNH [51]. Extensions of these experiments will allow for new molecular species to be created in the laboratory, including reactive intermediates, which can then be searched for in the ISM. This will increase the degree to which the chemical inventory of the ISM is characterised, especially as more complex molecules are detected. For example, propylene oxide [52] and benzonitrile [53], a chiral and an aromatic molecule, respectively, were detected in the ISM in the past few years. The results of discharge experiments can also extend the knowledge of the chemistry occurring in these regions by providing experimental evidence for potential reaction pathways and mechanisms.

1.3 Thesis Outline

In the context of providing laboratory data for the purposes of supporting astronomical searches with radio telescopes, this thesis concentrates on broadband rotational spectroscopic studies of a number of astrochemically relevant molecules. The chemical formulae of the molecules studied can be found in Table 1.1.

In Chapter 2, the theoretical background to rotational spectroscopy is set out, including the application of the results of spectroscopic analysis to astrochemistry and molecular structure determination. Chapter 3 details the three spectrometers used throughout the experimental work. Further, the two distinct experimental conditions for recording rotational spectra with these spectrometers - the supersonic expansion and the room-temperature flow cell - and the information that can be

Table 1.1: The names and chemical formulae of the nitrogen- and oxygen-containing molecules studied in this thesis.

Name	Formula	Chapter
acetonitrile	CH_3CN	3, 8
iso-propyl cyanide	$(CH_3)_2CCN$	4
1,2-propanediol	$CH_2(OH)CH(OH)CH_3$	5
alaninol	$CH_3CH(NH_2)CH_2OH$	6
valinol	$(CH_3)_2CHCH(NH_2)CH_2OH$	6
leucinol	$(CH_3)_2CHCH_2CH(NH_2)CH_2OH$	6
isoleucinol	$CH_3CH_2CH(CH_3)CH(NH_2)CH_2OH$	6
imidazole	c-$C_3N_2H_4$	7
acetaldehyde	CH_3CHO	8

gleaned from each method are compared. Because it is the spectrometer common to all projects in this thesis, there is a particular focus on a commercial W-band spectrometer, which operates in the region 75 - 110 GHz. The W-band spectrometer also underwent specific developments for electrical discharge experiments, and the implementation and optimisation of an electrical discharge nozzle on this instrument is also explored in Chapter 3.

Chapter 4 focuses on the vibrationally excited states of *iso*-propyl cyanide, which was the first branched molecule detected in the ISM. The chapter also includes a summary of an initial search for these vibrationally excited states in Sgr B2(N2b) in the Re-exploring Molecular Complexity with ALMA (ReMoCA) survey. Chapter 5 concentrates on the rotational spectroscopic analysis of the conformers of 1,2-propanediol. The chapter includes extensive comparison to and enrichment of literature data with data recorded in the W-band spectrometer. A number of energetically low-lying vibrationally excited states of 1,2-propanediol are also considered. The rotational spectra of the amino alcohols alaninol, valinol, leucinol, and isoleucinol across the 2-110 GHz frequency region are analysed in Chapter 6. This analysis resulted in rotational constants and line lists for astronomical searches being ascertained, as well as the determination of the experimental gas-phase structures. A structural comparison between the group of four amino alcohols and their respective amino acid analogues completes this chapter. Chapter 7 discusses an extended study of imidazole, including the assignment of the rotational spectra of the vibronic ground state, vibrationally excited states, isotopologues in natural abun-

dance, and an astronomical search with the Exploring Molecular Complexity with ALMA (EMoCA) survey. Chapter 8 details the study of the rotational spectrum of acetaldehyde undergoing electrical discharge as characterised in the W-band spectrometer. The chapter considers the chemistry occurring in the discharge plasma, discusses the application of the method to multi-component mixtures, and explores the astrochemical relevance of such studies.

This portfolio of work demonstrates the wealth of data available from laboratory rotational spectroscopy. It also emphasises the importance of the data in helping to answer fundamental questions in astronomy and astrochemistry, such as the degree of chemical complexity in molecular clouds and the elucidation of pathways towards complex organic molecules in interstellar space.

Chapter 2

Theoretical Aspects of Rotational Spectroscopy

Molecular spectroscopy is broadly defined as the study of the interaction between molecules and electromagnetic radiation [54]. This interaction induces transitions between the electronic, vibrational, and/or rotational quantum energy levels of the molecule, which is shown in Figure 2.1. Rotational spectroscopy, or molecular rotational resonance (MRR) spectroscopy, is concerned with the interaction of microwave or millimeter-wave radiation, predominantly defined as electromagnetic radiation with a wavelength between 1 and 1,000 mm. In this range, transitions occur between the molecule's rotational quantum energy levels [55].

The energy levels of a molecule are quantised, and the total energy of a molecule can be calculated using the time-independent Schrödinger equation:

$$\hat{H}\psi = E\psi. \tag{2.1}$$

The Born-Oppenheimer approximation can be used to separate the properties of a nucleus and its electrons. The total Hamiltonian, $\hat{H}$, can be represented as a sum of the translational, rotational, vibrational, and electronic component parts, which can be treated independently within the Born-Oppenheimer approximation [56]:

$$\hat{H}_{tot} = \hat{H}_{trans} + \hat{H}_{rot} + \hat{H}_{vib} + \hat{H}_{elec}. \tag{2.2}$$

The corresponding total molecular energy, E_{tot}, and wavefunction, ψ_{tot}, terms are written as:

$$E_{tot} = E_{trans} + E_{rot} + E_{vib} + E_{elec}, \tag{2.3}$$

$$\psi_{tot} = \psi_{trans}\psi_{rot}\psi_{vib}\psi_{elec}. \tag{2.4}$$

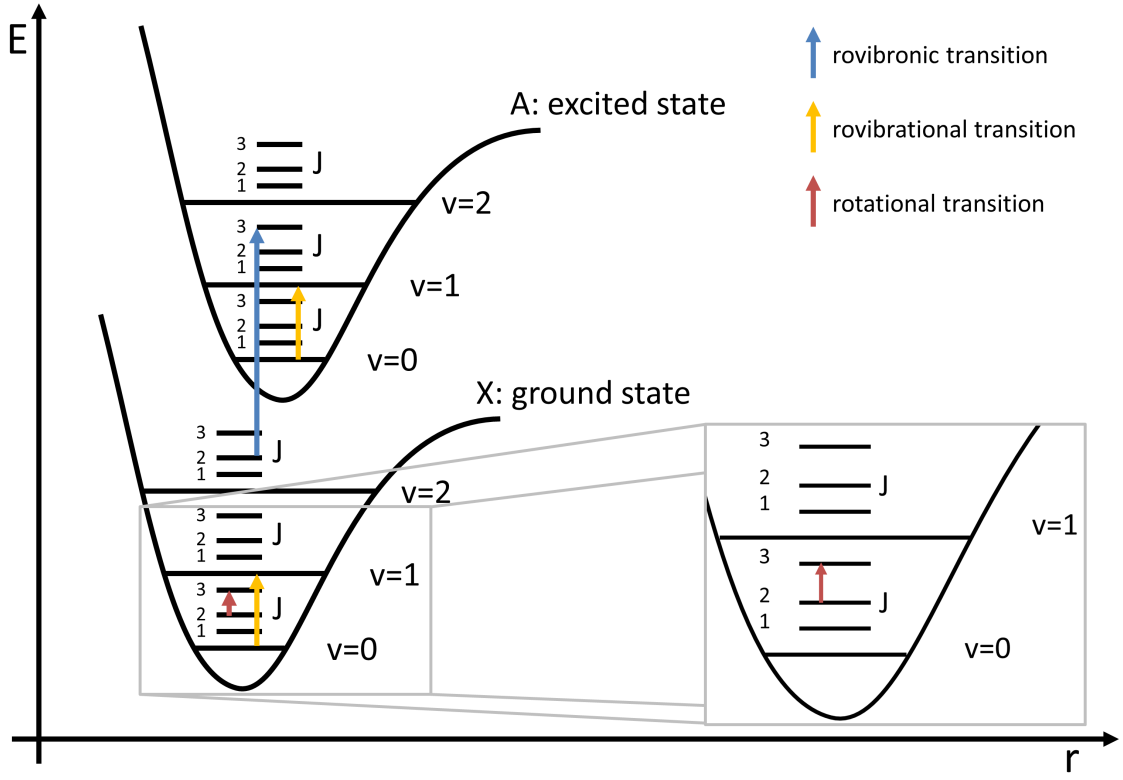

Figure 2.1: The potential energy curves of a ground and excited electronic state of a diatomic molecule as a function of internuclear distance, r. The arrows indicate various types of transitions between electronic, vibrational, and rotational energy levels.

As the work in this thesis is concerned with pure rotational spectroscopy, that is, transitions between the rotational quantum energy levels, the time-independent Schrödinger equation in focus is:

$$\hat{H}_{rot}\psi_{rot} = E_{rot}\psi_{rot}. \tag{2.5}$$

2.1 The Rigid Rotor Rotational Hamiltonian

The rotational energy of a molecule, E_{rot}, can be calculated using quantum mechanics by using the rigid rotor approximation in a similar way to classical mechanics [55]. The rigid rotor approximation states that the rotational energy can be calculated using the following:

$$E_{rot} = \frac{1}{2}\omega^{\dagger} I \omega, \tag{2.6}$$

where I is the inertial tensor and ω is the angular velocity. For a system consisting of N nuclei with mass m_i at coordinates x_i, y_i, and z_i, I can be written as:

$$I = \sum_{n=0}^{N} m_i \begin{pmatrix} y_i^2 + z_i^2 & -x_i y_i & -x_i z_i \\ -y_i x_i & x_i^2 + z_i^2 & -y_i z_i \\ -z_i x_i & -z_i y_i & x_i^2 + y_i^2 \end{pmatrix} = \begin{pmatrix} I_{xx} & I_{xy} & I_{xz} \\ I_{yx} & I_{yy} & I_{yz} \\ I_{zx} & I_{zy} & I_{zz} \end{pmatrix} \tag{2.7}$$

If the coordinate system is adjusted such that the origin is placed at the centre of mass of the molecule, the molecule is said to be in its principal axis system. The axes are labelled a, b, and c, such that the principal moments of inertia I follow the condition $I_a \leq I_b \leq I_c$. There are six ways that the (x, y, z) coordinate frame can be transformed into the (a, b, c) principal axis system, and the different representations are tabulated in Table 2.1 [55].

Table 2.1: The six representations for the adjustment of the (x, y, z) coordinate system into the (a, b, c) principal axis system.

	I^r	I^l	II^r	II^l	III^r	III^l
x	b	c	c	a	a	b
y	c	b	a	c	b	a
z	a	a	b	b	c	c

In the principal axis system, the rotational energy can be written as:

$$E_{rot} = \frac{1}{2}\left(I_a \omega_a^2 + I_b \omega_b^2 + I_c \omega_c^2\right) = \frac{1}{2}\left(\frac{J_a^2}{I_a} + \frac{J_b^2}{I_b} + \frac{J_c^2}{I_c}\right), \tag{2.8}$$

where J is the classical angular momentum. In quantum mechanics, the angular momentum operator $\hat{J}$ is equivalent to J. It follows that the rotational Hamiltonian for a molecule in the principal axis system within the rigid rotor approximation can be written as:

$$\hat{H}_{rig} = \frac{\hbar^2 \hat{J}_a^2}{2I_a} + \frac{\hbar^2 \hat{J}_b^2}{2I_b} + \frac{\hbar^2 \hat{J}_c^2}{2I_c}, \tag{2.9}$$

where $\hbar$ is the reduced Planck's constant.

A molecule can be described by a set of rotational constants, A, B, and C, which are related to the molecule's moments of inertia and are defined as:

$$A = \frac{\hbar^2}{2I_a}, B = \frac{\hbar^2}{2I_b}, C = \frac{\hbar^2}{2I_c}. \tag{2.10}$$

Because of the condition governing the definition of the axis labels, the rotational constants follow the condition $A \geq B \geq C$. Considering the definition of the rotational constants, the rotational Hamiltonian in Equation 2.9 can be rewritten as:

$$\hat{H}_{rig} = A\hat{J}_a^2 + B\hat{J}_b^2 + C\hat{J}_c^2. \tag{2.11}$$

Although this Hamiltonian is defined in the molecule's (a, b, c) principal axis system and is dependent on the angular momentum operator $\hat{J}$ in the molecule's principal axis system, the rotational energy can only be determined if there is a relation to the (x, y, z) laboratory axis system. It is necessary to perform a set of three axis rotations, an example of which is shown in Figure 2.2, to perform this transformation.

The transformation begins with the molecule's (a, b, c) principal axis system. The steps in the transformation are:

- an anti-clockwise rotation around c by an angle of ϕ;
- an anti-clockwise rotation around b_ϕ by an angle of θ;
- an anti-clockwise rotation around c_θ by an angle of χ.

The categorisation of molecules into a number of different categories can be done by considering the effects of molecular symmetry on the moments of inertia. This categorisation leads to different ways of calculating the energies of rotational levels and to varying patterns of transitions in the rotational spectra.

- **Linear top molecules** have $I_a = 0$ and $I_b = I_c$, which results in the rotational constants $A = \infty$ and $B = C$. Examples include hydrogen cyanide, HCN, and carbonyl sulfide, OCS. For linear molecules, the rotational constant conventionally used is B, and the energy of a rotational energy level J in the rigid rotor approximation is given by:

$$E = BJ(J + 1). \tag{2.12}$$

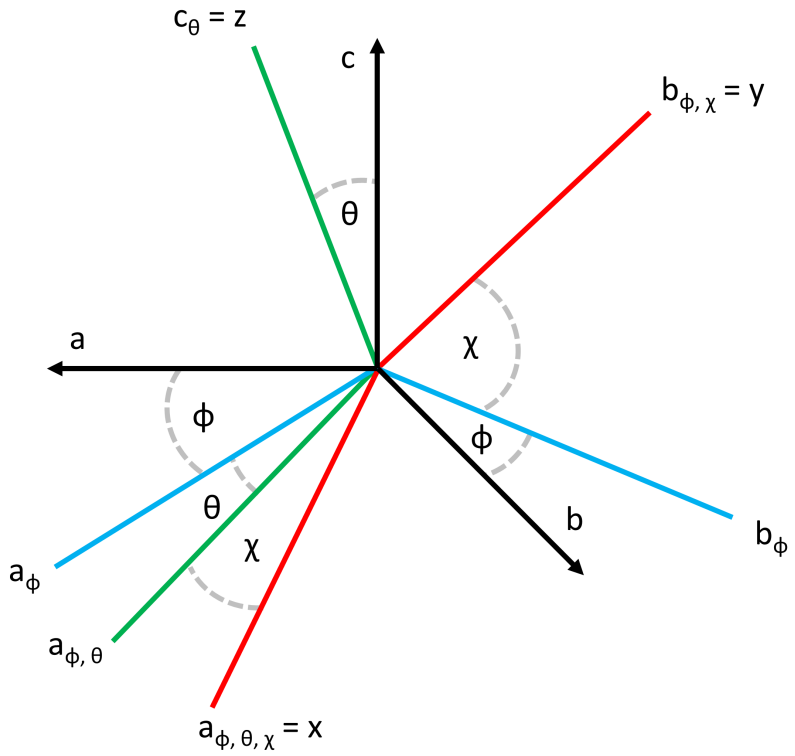

Figure 2.2: The transformation from the molecule's (a, b, c) principal axis system to the (x, y, z) laboratory axis system. Beginning with the (a, b, c) molecular principal axis system, the first step is an anti-clockwise rotation around c by an angle of ϕ, which results in the blue lines. The second step is an anti-clockwise rotation around b_ϕ by an angle of θ, which results in the green lines. The final step is an anti-clockwise rotation around c_θ by an angle of χ, which results in the red lines.

- **Spherical top molecules** have $I_a = I_b = I_c$ and hence have rotational constants $A = B = C$. Examples include sulfur hexafluoride, SF_6 and methane, CH_4. Because of their high degree of symmetry, spherical top molecules do not possess a permanent electric dipole moment. They therefore have no pure rotational spectrum, as the excitation electromagnetic radiation has no electric dipole moment to interact with.

- **Symmetric top molecules** have $I_a = I_b < I_c$ $(A = B > C)$ or $I_a < I_b = I_c$ $(A > B = C)$. The former case defines pancake-shaped oblate tops, such as benzene, C_6H_6; the latter case defines cigar-shaped prolate tops, such as chloroform, CH_3Cl. The energies of the rotational energy levels are defined as:

$$E_{prolate} = BJ(J+1) + (A-B)K^2, \tag{2.13}$$

$$E_{oblate} = AJ(J+1) + (C-A)K^2. \tag{2.14}$$

The quantum number K accounts for the projection of the total angular momentum onto the symmetry axis of the molecule. It takes values from $-J$ to $+J$ in integer steps.

- **Asymmetric tops** have $I_a \neq I_b \neq I_c$, which gives the rotational constants $A \neq B \neq C$. This is the largest category of molecules. Although the energy levels are not defined by simple expressions, as they are for the other classes of molecules, the equations describing their energies are known, and the Hamiltonians can be numerically solved. All molecules studied in this thesis belong to this category. It is also worthy to note that for asymmetric top molecules, the K quantum number becomes an insufficient parameter for describing a rotational energy level, as the K component of the angular momentum is not constant along the symmetry axes of the rotating asymmetric top [55]. The labels K_a (or K_{-1}) and K_c (or K_1) are used instead, which represent the projection of the total angular momentum onto the symmetry axis of the molecule in the prolate and oblate limiting cases, respectively [57]. Rotational energy level labels of asymmetric tops take the form $J_{K_aK_c}$. The degree of asymmetry of a molecule can be characterised by Ray's asymmetry parameter [58], which can be calculated using the molecule's rotational constants:

$$\kappa = \frac{2B - A - C}{A - C}. \tag{2.15}$$

The limiting case of $\kappa = -1$ represents a symmetric prolate top, while the limiting case of $\kappa = +1$ represents a symmetric oblate top. If $\kappa = 0$, the molecule has the highest possible degree of asymmetry. The value of κ plays a part in determining which of Watson's reduced Hamiltonians (the A- or S-reduced Hamiltonian [59]; discussed in more depth in Section 2.2) is used to describe the molecule in question.

Rotational spectra are observable when the molecule in question has a permanent electric dipole moment. The rotational transition arises from the interaction (or exchange of energy) between the electric dipole moment and the electric field component of the electromagnetic radiation [54]. The molecules studied in this thesis are asymmetric tops, and the selection rules governing the allowed transitions for asymmetric tops is summarised in Table 2.2. The transitions with $\Delta J = -1$ form a P-branch, $\Delta J = 0$ form a Q-branch, and $\Delta J = +1$ form an R-branch.

Table 2.2: A summary of the selection rules for rotational transitions in an asymmetric top for each dipole moment component type.

dipole moment component	transition type	ΔJ	ΔK_a	ΔK_c
μ_a	a-type	0, ± 1	0, ± 2,...	± 1, ± 3,...
μ_b	b-type	0, ± 1	± 1, ± 3,...	± 1, ± 3,...
μ_c	c-type	0, ± 1	± 1, ± 3,...	0, ± 2,...

2.2 The Non-rigid Rotor Hamiltonian

Centrifugal Distortion Constants

In reality, because of their flexibility, molecules can rarely be described with the rigid rotor Hamiltonian alone. The non-rigid rotor Hamiltonian takes into account a molecule's flexibility. Centrifugal distortion, or centrifugal stretching, occurs as a consequence of this flexibility causing nuclear position distortion during rotation. The effect of centrifugal distortion is to lower the frequency of rotational transitions relative to that predicted by the rigid rotor Hamiltonian. Centrifugal distortion constants account for this shift. This has a particularly marked effect in the higher frequency regimes, since the distortion scales with J. The Hamiltonians that are used to describe systems in this way were formulated by Watson in 1977 [59], and the choice of Hamiltonian depends on the symmetry of the molecule.

The A-reduced Hamiltonian in the I^r representation is most suited for asymmetric top molecules, and the quartic centrifugal distortion constants that can be determined under this reduction are Δ_J, Δ_{JK}, Δ_K, δ_J, and δ_K. The S-reduced Hamiltonian in the III^l representation is most suited for symmetric and slightly asymmetric top molecules, and the quartic centrifugal distortion constants that can be determined under this reduction are D_J, D_{JK}, D_K, d_1, and d_2. Table 2.3 gives a summary of the centrifugal distortion constants up to the octic order for both the A- and S-reduced Hamiltonians.

Large Amplitude Motions

Large amplitude motions (LAMs) with an amplitude on the order of a bond length can significantly alter the structure of a molecule or convert the molecule from one

Table 2.3: A comparison of the centrifugal distortion constant labels in Watson's A- and S-reduced Hamiltonians up to the octic order [55].

A-reduction	S-reduction
quartic order	
Δ_J	D_J
Δ_{JK}	D_{JK}
Δ_K	D_K
δ_J	d_1
δ_K	d_2
sextic order	
Φ_J	H_J
Φ_{JK}	H_{JK}
Φ_{KJ}	H_{KJ}
Φ_K	H_K
ϕ_J	h_1
ϕ_{JK}	h_2
ϕ_K	h_3
octic order	
L_J	L_J
L_{JJK}	L_{JJK}
L_{JK}	L_{JK}
L_{KKJ}	L_{KKJ}
L_K	L_K
l_J	l_1
l_{JK}	l_2
l_{KJ}	l_3
l_K	l_4

equivalent structure to another via tunnelling. Examples of LAMs include proton tunnelling, inversion motions (such as the inversion of ammonia), and ring puckering.

Methyl group internal rotation is another LAM that is commonly observed in rotational spectra. The rotation of the methyl group, -CH_3, relative to the rest of the molecule couples with the overall rotation of the molecule. In an asymmetric top, this can lead to three equivalent minimum positions. The coupling of the methyl group rotation and the molecular rotation has the effect that each rotational transition exhibits a fine structure. In the case of an asymmetric top, each transition is split into a doublet, the splitting of which is dependent on the height of the barrier and the transition being considered. The doublet consists of a non-degenerate A state and a doubly-degenerate E state. The corresponding rotational Hamiltonian, $\hat{H}$, must be extended to include the effect of the methyl internal rotation, and this extension includes the Hamiltonian of the internal rotation, $\hat{H}_I$:

$$\hat{H}_{rot} = \hat{H}_{rig} + \hat{H}_I. \tag{2.16}$$

The Hamiltonian of the internal rotation is defined as:

$$\hat{H}_I = F(\hat{j}_\alpha - \hat{J})^2 - V(\alpha), \tag{2.17}$$

where F is the rotational constant for the internal rotor, $\hat{j}$ is the angular momentum operator of the internal rotation, J is the total angular momentum operator, and V(α) is the potential energy with the internal rotation angle α. In the case of the methyl top, which has $2\pi/3$ periodicity, the potential energy can be expressed as:

$$V(\alpha) = \frac{1}{2}V_3(1 - cos(3\alpha)) + \frac{1}{2}V_6(1 - cos(6\alpha)) + ... \tag{2.18}$$

It is typically the case that the calculation of V(α) can be performed by considering only the first term, as V_3, the three-fold barrier, is usually much greater than V_6, the six-fold barrier. As the splitting of the rotational transition is a function of the internal rotation barrier, evaluation of the potential barrier is possible from rotational spectral analysis [55].

2.3 Nuclear Quadrupole Coupling

When a molecule contains one or more nuclei with a nuclear spin, I, greater than 1/2, the electric quadrupole moment of the nucleus or nuclei interacts with the molecular electric field gradient. This nuclear quadrupole coupling effect manifests itself as hyperfine splitting of the transitions in the rotational spectrum [60].

Nuclei with $I = 0$ or $I = \frac{1}{2}$ have spherical electronic charge distributions and hence no quadrupole moment. Nuclei with $I \geq 1$ have non-spherical electronic charge distributions and possess a quadrupole moment, Q. In this case, the nuclear spin angular momentum, $\mathbf{I}$, couples with the rotational angular moment, $\mathbf{J}$. This coupling results in a new total angular moment vector, $\mathbf{F}$, and the new quantum number, F, describes the energy levels of the hyperfine structure, where the values of F are:

$$F = J + I, J + I - 1, ..., J - 1. \tag{2.19}$$

Analysis of the hyperfine structure in the spectrum results in the determination of quadrupole coupling constants, χ, from the quadrupole coupling tensor:

$$\chi = \begin{pmatrix} \chi_{aa} & \chi_{ab} & \chi_{ac} \\ \chi_{ba} & \chi_{bb} & \chi_{ba} \\ \chi_{ca} & \chi_{cb} & \chi_{cc} \end{pmatrix}. \tag{2.20}$$

For the weaker coupling nuclei, such as ^{14}N (where $I_{^{14}N} = 1$), which is present in many of the molecules studied within this thesis, usually only the diagonal elements can be determined. The three nuclear quadrupole coupling constants are not linearly independent, and they follow with the condition:

$$\chi_{aa} + \chi_{bb} + \chi_{cc} = 0. \tag{2.21}$$

So, from the experimental spectrum of such weakly coupling nuclei, χ_{aa} and $\chi_{bb} - \chi_{cc}$ can be directly determined.

A relationship between the elementary charge, e, the electric field gradient, q, and the atomic nuclear quadrupole moment, Q, can further define χ_0:

$$\chi_0 = eqQ. \tag{2.22}$$

This makes the value of χ_0 useful for characterising the local electronic environment of the quadrupolar nucleus in the molecule [61]. It is also of use in confirming potential astronomical observations of molecules that contain nuclei with $I \geq 1$ [53].

The hyperfine splitting decreases with increasing J. For a number of molecules in this thesis that have been studied across a large frequency range, analysis has entailed a global fit encompassing transitions from the low frequency regime (with low J, and hence resolvable hyperfine splitting) and the high frequency regime (with higher J, and hence a collapsed hyperfine splitting). Examples of this type of analysis can be found in the studies of alaninol and valinol (studied between 2 - 110 GHz; Chapter 6), and imidazole (between 2 - 295 GHz; Chapter 7).

2.4 Rotational Partition Function

The molecular partition function, Q_{mol} (not to be confused with the atomic nuclear quadrupole moment from the previous section), is a representation of how the total number of molecules are distributed over the available microstates. The value of Q_{mol} gives an indication of the range of states in a molecule that are populated at a given temperature [62]. It can be derived from the consideration that the energy, E, of a molecule is the sum of a number of contributions, as defined in Equation 2.3.

As the energy is a sum of independent contributions, the partition function can be defined as a product of partition functions of these same contributions, such that:

$$Q_{tot} = Q_{trans}Q_{rot}Q_{vib}Q_{elec}. \tag{2.23}$$

The general form of these independent contributions is [62]:

$$Q = \sum_i g_i exp(-\frac{E_i}{k_B T}), \tag{2.24}$$

where g_i is the degeneracy of level i, E_i is the energy of level i, k_B is the Boltzmann constant, and T is the temperature.

Hence, the form of the rotational partition function is:

$$Q_{rot} = \sum_i g_i exp(-\frac{E_{rot}}{k_B T}). \tag{2.25}$$

The rotational partition function requires knowledge of the rotational energy levels. Evaluation of the rotational partition functions can be achieved upon analysis of the rotational spectrum, as doing so determines the energies of the rotational energy levels. For linear, symmetric prolate, and symmetric oblate tops, with the energy of the rotational levels defined by Equation 2.12, 2.13, and 2.14, the rotational partition function can be written in relatively straightforward ways [62]:

$$Q_{rot}^{linear} = \sum_J (2J+1) exp(-\frac{hBJ(J+1)}{k_B T}), \tag{2.26}$$

$$Q_{rot}^{prolate} = \sum_{K=-\infty}^{\infty} exp(-\frac{h(A-B)K^2}{k_B T}) \sum_{J=|K|}^{\infty} (2J+1) exp(-\frac{hBJ(J+1)}{k_B T}), \tag{2.27}$$

$$Q_{rot}^{oblate} = \sum_{K=-\infty}^{\infty} exp(-\frac{h(C-A)K^2}{k_BT}) \sum_{J=|K|}^{\infty} (2J+1)exp(-\frac{hAJ(J+1)}{k_BT}). \quad (2.28)$$

The factor of Planck's constant, h, is added to the expression for the rotational energy level. One can note the complexity in the formulae for symmetric tops, which is introduced because of the additional K quantum number. This becomes more complicated for asymmetric tops, as the energy levels do not have simplified energy equations. In practice, the rotational partition functions can be calculated using analysis software, such as the SPCAT programme [63]. This programme performs the direct summation across the rotational energy levels that are predicted from the experimentally determined rotational and centrifugal distortion constants (and, if applicable, nuclear quadrupole coupling constants).

If the assumption that the temperature is so high that numerous states are occupied is made, then the summation formulae can be approximated by integrals. Evaluation of these integrals leads to semi-empirical approximations for the rotational partition functions, which for the asymmetric top case is [62]:

$$Q_{rot}^{asymmetric} = \frac{1}{\sigma}\sqrt{(\frac{k_BT}{h})^3}\sqrt{(\frac{\pi}{ABC})}. \quad (2.29)$$

The additional σ term accounts for the symmetry of the molecule and indicates the number of ways a molecule can be rotated to overlap itself in an indistinguishable way. For example, for asymmetric molecules, when there is no exchange of identical nuclei with the turning of the rigid molecule, then $\sigma = 1$. The semi-empirical functions are valid at high temperatures, but can be unreliable in low temperature regimes. As discussed in Ref. [64], it is much more reliable to calculate the rotational partition functions using the direct summation method. The authors also conclude that the lack of accuracy of the semi-empirical method can be significant when compared to the direct summation method, even at high temperatures.

The rotational partition function has particular relevance when considering the intensity information in a rotational spectrum. According to Brown *et al.*, the signal, S, that comes from chirped pulse excitation can be described as [65]:

$$S \propto \omega\mu^2 E_{pulse}\Delta N_0(\frac{\pi}{\alpha})^2. \quad (2.30)$$

The signal strength resulting from chirped pulse excitation is directly proportional to the frequency of the transition, ω, the square of the transition dipole moment, μ^2, the electric field strength, E_{pulse}, the population difference, ΔN_0, and inversely proportional to the linear sweep rate of the chirped pulse, α.

The population difference can be described as a fractional population, that is, the ratio of the population of energy level m to the total population of the system is defined as:

$$F_m = \frac{N_m}{N_{tot}} = \frac{g_m exp(-\frac{E_m}{k_B T})}{\sum_i g_i exp(\frac{-E_i}{k_B T})}. \tag{2.31}$$

This is governed by the Boltzmann distribution, and one will notice that the denominator of this expression is precisely the total partition function, as defined in Equation 2.24. Because of the relationship between the total partition function and the rotational partition function, any change in the rotational partition function will affect the total function and hence the intensity of the transition.

The two variables directly affecting the rotational partition function are temperature and the energies of the rotational energy levels. The effect of changing these on the intensity profiles of rotational spectra are shown in Figure 2.3. On the left panel, it can be seen that increasing temperature shifts the Boltzmann distribution of a molecule to higher frequencies. On the right panel, it can be seen that, at a given temperature, decreasing the rotational constants, modelled as increasing the molecule size, shifts the Boltzmann distribution to lower frequencies. The work on the family of amino alcohols used to illustrate this can be found in Chapter 6. The direct proportion relationship of temperature and the inverse proportion relationship of the rotational constants can be seen directly in the semi-empirical expressions describing the rotational partition functions; as seen, for example, in the asymmetric top semi-empirical expression in Equation 2.29.

Application of the rotational partition function in astronomy allows the column density of a detected species to be determined, which is defined as the number of molecules per unit area along a line of sight. The procedure requires knowing the converged values of the partition function at a given temperature, where converged values of the rotational partition function are obtained from the summation of sufficiently high rotational energy levels such that the i^{th} exponential term in Equation 2.25 negligibly contributes to the value [64]. Plotting the so-called rotational temperature diagram yields the total molecular column density and the rotational temperature from the y-intercept and gradient of the line, respectively [24, 66]. Accurate estimates of the column density are only achieved when accurate, converged values of the rotational partition function are known [67].

2.5 Vibrationally Excited States

Rotational spectra can be recorded with the gaseous sample at different temperatures. In experiments which use a supersonic expansion, the molecules are typically cooled to the lowest vibrational energy level (for more details, see Section 3.4). This means that the rotational spectrum consists of rotational transitions as shown in Figure 2.1. In contrast, molecules in a room temperature gas cell are not cooled; higher vibrational levels in the ground electronic state are occupied. Therefore, the

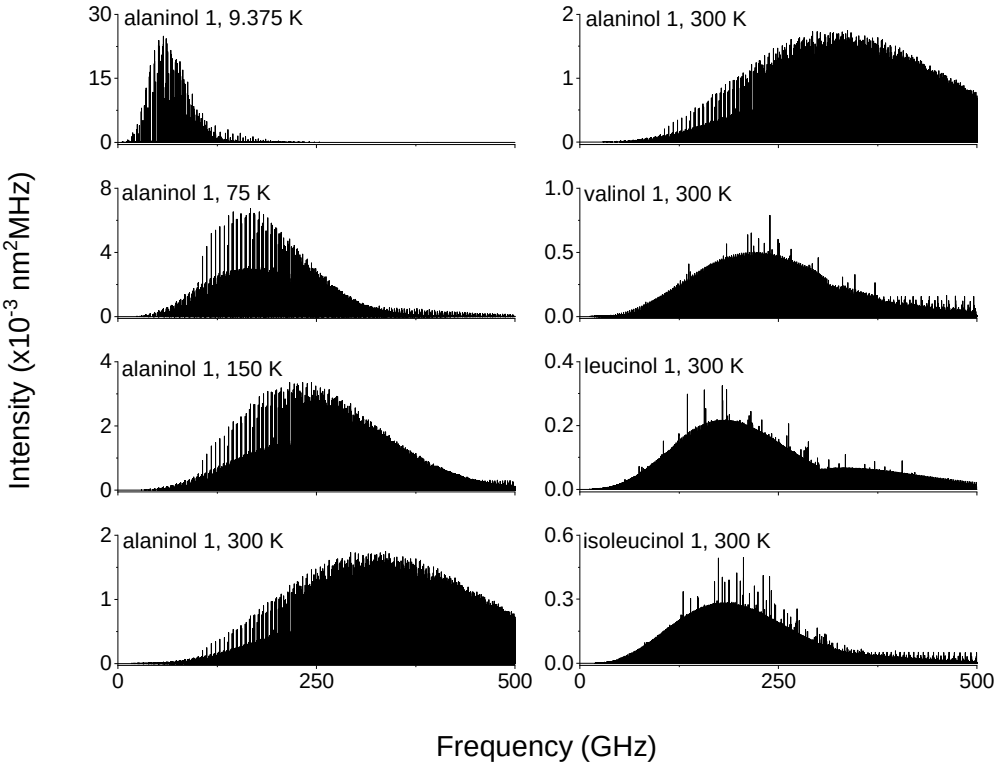

Figure 2.3: Left: The effect of increasing temperature on the distribution of the rotational transitions in the rotational spectrum of alaninol 1, g'Gg'. Right: The effect of decreasing the rotational constants, modelled as increasing the size of the molecule, on the distribution of the rotational transitions at 300 K. Note the different scales on the y-axes across the different panels.

low-lying vibrationally excited states are accessible for probing, as shown in Figure 2.4. Practically, the rotational spectra of these vibrational states can be analysed using the same programmes and theories that are used to analyse those of the ground state.

At temperatures where vibrationally excited states may be populated, the value of the vibrational partition function should be considered. This can then be incorporated into the evaluation of Q_{tot} (see Equation 2.23). The vibrational contribution to the total partition function in the harmonic approximation can be calculated by considering the harmonic vibrational frequency, $\bar{\nu}$, and it takes the form [62]:

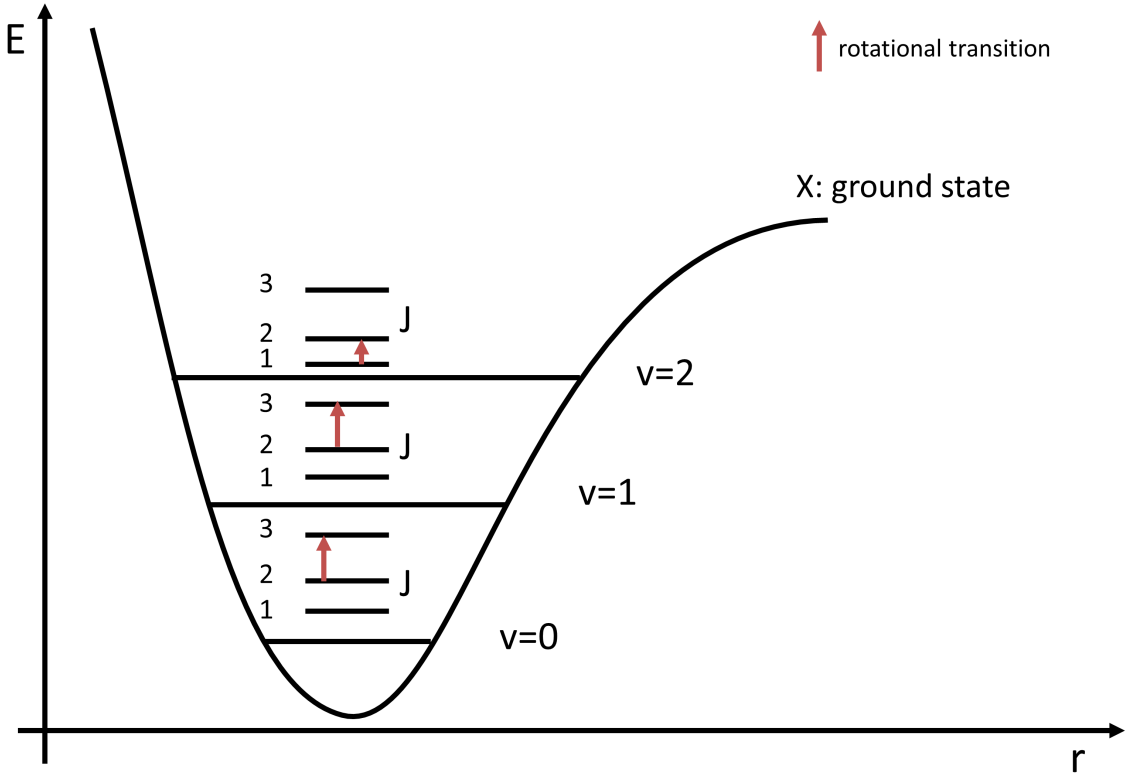

Figure 2.4: The potential energy curve of the ground electronic state of a diatomic molecule as a function of internuclear distance, r. The arrows indicate pure rotational transitions within a number of vibrationally excited states.

$$Q_{vib} = \prod_i \frac{1}{1 - exp(\frac{E_{vib}}{k_B T})} = \prod_i \frac{1}{1 - exp(\frac{hc\bar{\nu}}{k_B T})}. \tag{2.32}$$

The anharmonic energies of the vibrational states can be obtained from frequency calculations, and the vibrational partition function can be calculated with these values using the general form of partition functions (Equation 2.24). The aspects of quantum-chemical calculations to aid in the analysis of vibrationally excited states are expanded on in Section 2.7.

The analysis of the rotational spectrum of vibrationally excited states can be complicated by when the states interact and perturb each other. One such perturbation is the mixing of the wavefunctions of energetically close vibrational states whose symmetries are the same. This is known as Fermi coupling or Fermi resonance. The resulting effect on the rotational spectrum is stark - both the frequencies and intensities of the rotational transitions are affected [55]. The regularity of the frequencies of the transitions is destroyed, which is caused by the repulsion of nearby

energy levels. This shifted energy levels result in shifted transition frequencies relative to the expected rotational spectrum. More precisely, the transitions from the higher energy mode increase in frequency, and the transitions from the lower energy mode decrease in frequency. The second effect is that the weaker transitions increase in intensity, as they become more allowed, and the stronger transitions therefore decrease in intensity. Despite this, the contribution of each state to the perturbation is difficult to ascertain. The analysis of the rotational spectrum is not straightforward, but it is possible. The effective rotational constants can be determined, which are linear combinations of the constants for the parent (unperturbed) states [68].

Ro-vibrational coupling, or Coriolis coupling, is defined as the interaction of rotational and vibrational energy levels, and this may also have an effect on a rotational spectrum. This interaction causes the splitting of energy levels, meaning that there are more transitions present in the experimental spectrum than expected. This differs from Fermi resonances, in which no new lines lines are seen in the spectrum, but instead expected lines are shifted. Examples of systems in which Coriolis coupling is induced include the degenerate normal vibrational modes of linear molecules and the bending of non-linear triatomic molecules. For asymmetric top molecules, Coriolis coupling can occur when there are accidental vibrational degeneracies [55]. Coriolis coupling constants can be used to describe the effect of the ro-vibrational coupling on the rotational spectrum. These constants take into account the coupling of the overall rotation of the system with the coordinate system of the motion or interaction, and they measure the angular momentum caused by the vibration-rotation interaction.

2.6 Spectral Analysis

Analysis of a rotational spectrum is an iterative process, and it involves assigning quantum numbers to experimental frequencies and fitting the experimental frequencies to the parameters of an appropriate Hamiltonian. The choice of the Hamiltonian depends on factors such as the symmetry properties of the molecule under analysis, the need to consider centrifugal distortion constants in the analysis, and if the transitions in the spectrum exhibit splitting due to large amplitude motions or nuclear quadrupole coupling. Several programmes have been developed to assist in the analysis. For the work in this thesis, rotational spectra were initially fit using JB95 [69] or PGOPHER [70]. The fits were then refined using Pickett's SPFIT/SPCAT programmes as implemented in the AABS programme suite [63, 71]. A detailed description of these programmes can be found in the corresponding literature. In short, they facilitate the assignment of rotational quantum numbers to experimental frequencies, and the rotational constants (and further parameters, such as the centrifugal distortion constants, quadrupole coupling constants, etc.) are fit to the

assigned transitions in a least-squares manner. The spectrum is fit with the minimum number of constants required, thus keeping the error of the fit within a few kHz and in the order of experimental accuracy [72].

2.7 Quantum-chemical Calculations

Quantum-chemical calculations are often used to assist in the assignment of a rotational spectrum. In this work, the two main types of calculations performed were structure optimisation calculations and anharmonic frequency calculations. All the calculations were performed with the Gaussian programme suite [73] on the GWDG High-performance Computing Cluster.

Where relevant, for example in the work with the amino alcohols in Chapter 6, initial conformational searches were performed. The conformational searches were performed with the SPARTAN 14 programme [74], in which semi-empirical methods to calculate electronic structures were utilised. These were complemented with manual dihedral scans with the Gaussian programme suite.

Structure optimisation calculations were performed in order to obtain theoretical rotational constants and dipole moments (and where relevant, nuclear quadrupole coupling constants) of molecular structures at equilibrium positions in the molecule's potential energy surface. These constants were used to initially simulate the rotational spectrum to guide the assignment procedure.

For molecules that were studied in a room temperature flow cell, the performance of anharmonic frequency calculations on the optimised structures was necessary in order to obtain theoretical rotational constants for low-lying vibrationally excited states. These calculated rotational constants were adjusted by applying the difference between the experimental and theoretical rotational constants for the ground state of the molecule at the same level of theory and basis set, yielding A_{adj}, B_{adj}, and C_{adj}. The utilisation of this procedure can be found throughout the thesis. The anharmonic frequency calculations also determined the associated motions, the energies, in both the harmonic and anharmonic approximations, and theoretical centrifugal distortion constants.

A number of different levels of theory were used throughout this thesis. Predominantly, the B3LYP and MP2 functionals were used. The B3LYP functional (Becke, 3 parameter, Lee Yang Parr) is a density functional theory method and is a hybrid functional. It describes the molecular system with a linear combination of the exact Hartree-Fock functional and the electron-electron and exchange correlations [75, 76]. In some cases, a dispersion correction (D3) with Becke-Johnson (BJ) damping was included [77, 78]. The M06-2X functional is a hybrid exchange correlation energy functional that is also based on density functional theory [79]. MP2 corresponds to second order Møller-Plesset perturbation theory [80]. It is based on the Hartree-Fock

method [81] and includes electron correlation.

A number of different basis sets, which model the orbitals of the molecular system, were also used throughout the work. The basis sets are collections of Gaussian functions which describe the atomic wavefunctions of the atoms in the molecule. The molecular wavefunction is made up of these atomic wavefunctions. The construction of the molecular wavefunction is performed by the simulation software. Extending the basis sets to consider changes to the atomic orbitals when the atom becomes part of a molecule can be done by adding separate functions, such as polarisation and diffuse functions. The def2-TZVP basis set is a polarised triple zeta basis set, where the def stands for default in Turbomole [82]. The basis sets of the form 6-311G++(d, p) are Pople basis sets. The 6-311G represents the split-valence triple zeta basis set, and the basis set can be adjusted with diffuse functions (++) and/or polarisation functions ((d,p) or **) [83, 84]. The Dunning-type basis sets (cc-pVnZ) were also used, which include correlation corrections, and they can be augmented (aug) with diffuse functions [85].

In the work on imidazole [86], a collaborating partner used the coupled cluster method CCSD(T) for the structure optimisation calculation [87]. This method considers single and double electron excitations and estimates the effects of triple excitations with a perturbative treatment. The basis set used was a composite basis set, consisting of a Dunning-type foundation with a number of corrections and approximations. The thorough details of the computation procedure can be found in Refs. [88] and [86].

Comparisons between experimental and theoretical constants are made throughout this work. In the absence of isotopologue assignments, and hence where an experimental structure determination cannot be performed, these comparisons provide the basis for allocating an assignment to a molecular structure.

2.8 Structure Determination

Where the rotational spectra of singly-substituted rare isotopologues can be assigned in the experimental spectrum, experimental gas-phase structures can be determined. This is a consequence of the high resolution and high sensitivity of rotational spectroscopy and, in particular, the sensitivities of the rotational spectrometers utilised in this thesis. The observation of rare isotopologues occurs in natural abundance, providing the signal-to-noise ratio of the parent species is high enough, and the most commonly observed isotopes are ^{13}C (1.1% naturally abundant), ^{15}N (0.4% naturally abundant), and ^{18}O (0.2% naturally abundant). Where this is not feasible, isotopically enriched samples can be used.

Each isotopologue has its own set of rotational constants, which are a result of the change in moment of inertia that occurs upon isotopic substitution of a nuclei in

the parent molecule. Spectral analysis, therefore, delivers a unique set of rotational constants for each isotopologue. Because of the relationship between the mass of the molecule, the moments of inertia, and the rotational constants, detailed in Equations 2.6, 2.7, 2.8, 2.9, and 2.10, the isotopologue assignments can be used to construct molecular structures [89]. Two different types of structures were determined using isotopologue data throughout this work - the effective structure and the substitution structure.

The Effective Structure (r_0)

The effective structure of a molecule, r_0, is the ground state structure of the molecule observed in rotational spectroscopy. It is the structure of the molecule in the ground vibrational state and thus includes the contributions from the molecule's zero point motions. The r_0 structure can be determined by calculating the bond lengths and angles which reproduce the experimental rotational constants of the ground state and the rotational constants of the assigned isotopologues in a least squares manner. In this thesis, this is achieved with the use of the STRFIT programme [90].

The Substitution Structure (r_s)

The substitution structure, r_s, is based on the application of Kraitchman's equations [91]. Further, the method assumes that there is no change in molecular structure upon isotopic substitution. The moments of inertia of the parent molecule (I_a, I_b, and I_c) and the isotopologue (I'_a, I'_b, and I'_c) in the principal axis system can then reveal the coordinates of the substituted atom. The equations for determining the coordinates of the atom in asymmetric top molecules are:

$$|a| = \left[\frac{\Delta P_a}{\mu}\left(1+\frac{\Delta P_b}{I_a - I_b}\right)\left(1+\frac{\Delta P_c}{I_a - I_c}\right)\right]^{1/2} \tag{2.33}$$

$$|b| = \left[\frac{\Delta P_b}{\mu}\left(1+\frac{\Delta P_c}{I_b - I_c}\right)\left(1+\frac{\Delta P_a}{I_b - I_a}\right)\right]^{1/2} \tag{2.34}$$

$$|c| = \left[\frac{\Delta P_c}{\mu}\left(1+\frac{\Delta P_a}{I_c - I_a}\right)\left(1+\frac{\Delta P_b}{I_c - I_b}\right)\right]^{1/2} \tag{2.35}$$

where P_i are the planar moments of inertia, which can be defined for each i as:

$$\Delta P_a = \frac{1}{2}(-\Delta I_a + \Delta I_b + \Delta I_c) \tag{2.36}$$

$$\Delta P_b = \frac{1}{2}(-\Delta I_b + \Delta I_a + \Delta I_c) \tag{2.37}$$

$$\Delta P_c = \frac{1}{2}(-\Delta I_c + \Delta I_a + \Delta I_b) \tag{2.38}$$

The reduced mass for the isotopic substitution, μ, is given by:

$$\mu = \frac{M\Delta m}{M + \Delta m} \tag{2.39}$$

where M is the total mass of the molecule and Δm is the change in mass on isotopic substitution [55].

One can see from Equations 2.33, 2.34, and 2.35 that the absolute values of the coordinates are determined. The sign of the values can be confirmed by comparing the experimentally determined coordinates with those from structure optimisation calculations. When the substituted atom lies close to or on an inertial axis, the analysis yields imaginary coordinates. It is common practice to artificially designate these coordinates as zero along the relevant axes. The coordinates of the isotopically substituted atoms are calculated in this way with the KRA programme [90]. The experimental gas-phase structure can then be built up atom-by-atom.

Chapter 3

Experimental Details

The work in this thesis was performed on broadband chirped-pulse Fourier transform rotational spectrometers developed and maintained at the Deutsches Elektronen-Synchrotron (DESY) facility in Hamburg, Germany.

The spectrometers cover frequency regimes in the 2-110 GHz range. This, along with the different experimental conditions, as will be discussed throughout this thesis, has the advantage of being able to record the rotational spectrum of a molecule across a large frequency range and allow the:

- identification of gas-phase structures of vibronic ground states;
- characterisation of vibrationally excited states;
- accurate determination of centrifugal distortion constants, which are important for astrochemical applications.

This chapter describes the instrumentation, the different methods of sample introduction, which leads to the two distinct experimental methods, and the development of an electrical discharge source for initiating and studying chemical reactions of astrochemical interest.

3.1 The Hamburg COMPACT Spectrometer

The instrument components can be split into excitation electronics, detection electronics, and the molecule-radiation interaction zone. In Figures 3.1, 3.2, 3.3, and 3.4, the excitation components are labelled in blue, the detection components are labelled in orange, and the instrument infrastructure is labelled in black. The working of the various components during the spectroscopic investigation is detailed for the COMPACT in this section and for the other spectrometers in the following sections.

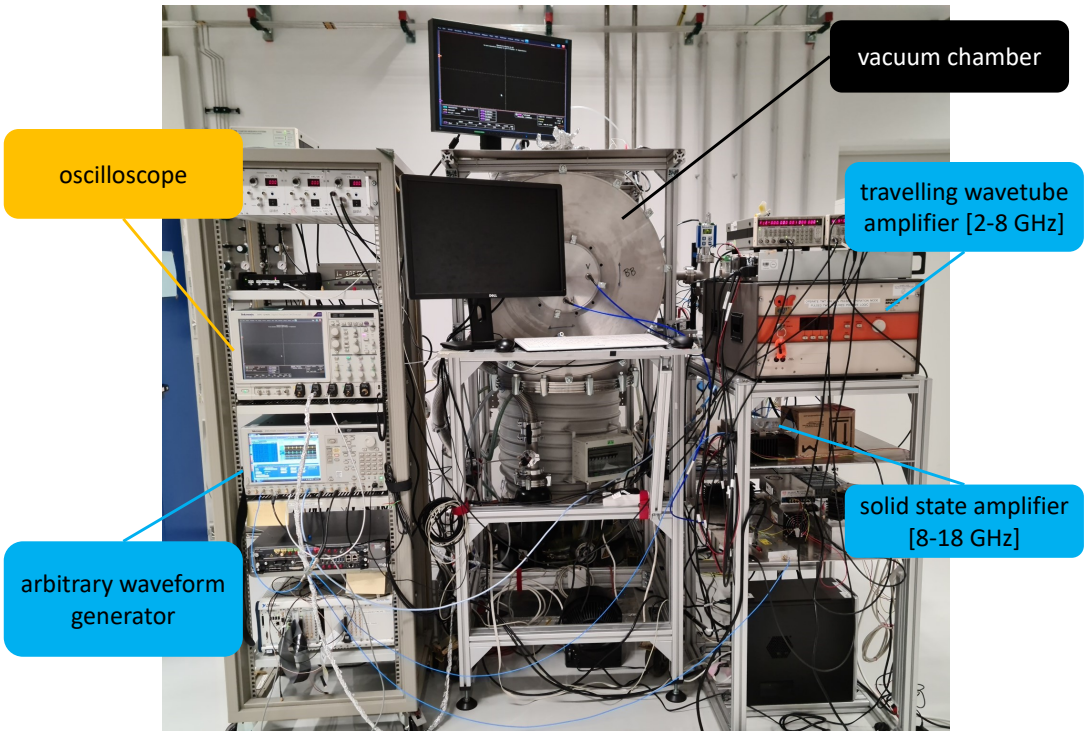

Figure 3.1: The Hamburg COMPACT Spectrometer, which operates in the region 2-18 GHz. The vacuum chamber stands between two racks containing the electronic components of the spectrometer.

The Hamburg COMPACT Spectrometer, shown in Figures 3.1 and 3.2, operates in the regions 2-8 GHz [92, 93] and 8-18 GHz [94]. With this spectrometer, the rotational levels of a molecule in a supersonic expansion are probed (see Section 3.4).

The excitation pulse trains are produced by an arbitrary waveform generator (AWG, Tektronik 7122C), where each pulse train consists of a number of excitation chirps spanning the region of interrogation. Each excitation pulse train usually consists of eight excitation chirps. The 2-8 GHz region is interrogated directly by a 6 GHz wide excitation chirp, usually 4 μs in length. The 8-18 GHz region is covered in four individual experiments, where each separate experiment deals with the rotational spectrum across the 8-10.5, 10.5-13, 13-15.5, and 15.5-18 GHz regions. The excitation pulse trains are produced by the same AWG as the 2-8 GHz experiments, and the excitation chirps span the region 4-9 GHz and are usually 2 μs long. The pulse trains are then frequency up-converted to the 8-18 GHz bandwidth. The pulse trains are fed through an amplifier - a 300 W travelling wavetube amplifier

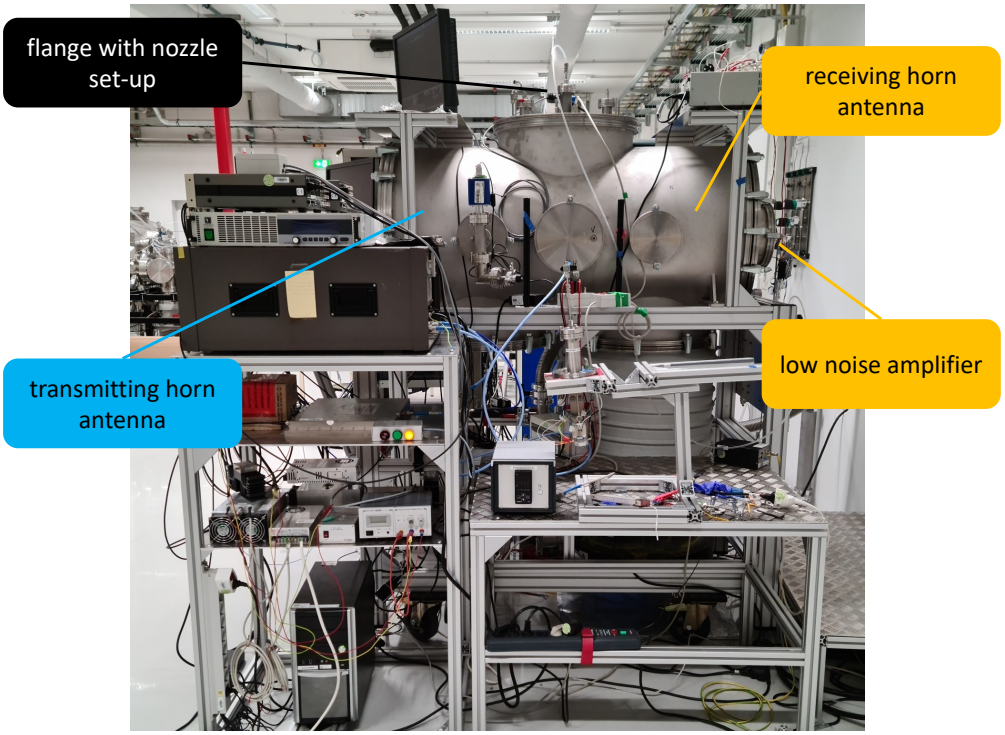

Figure 3.2: The Hamburg COMPACT Spectrometer shown from the side. The vacuum chamber is equipped, on the top, with a removable flange which houses the nozzle set-up. The radiation path is from the left to the right of the picture, which is perpendicular to the molecular beam.

(TWTA) in the case of the 2-8 GHz experiment, and a 50 W solid state amplifier (SSA, Mercury Systems L0618-46-T680) in the case of the 8-18 GHz experiment. The pulse trains are then broadcast into the vacuum chamber via a horn antenna. Inside the chamber, the excitation pulses induce a macroscopic dipole moment in the molecular sample, which is in the form of a supersonic molecular beam. The decay of this macroscopic dipole moment is collected in the form of a free induction decay (FID) by a receiving horn antenna, passed through a positive-intrinsic-negative (PIN) diode limiter and a low noise amplifier, and recorded on a 100 GS/s oscilloscope (Tektronik DPO 72004C). The oscilloscope is able to process multiple FIDs per molecular pulse, which is referred to as the fast frame method. This allows for the excitation pulse train to consist of multiple excitation chirps, and the method has the advantages of higher repetition rate and lower sample consumption during the experiment. The adjustable digitisation rate of the oscilloscope is set to 25 GS/s for the 2-8 GHz experiment and to 50 GS/s for the 8-18 GHz experiment. Fast Fourier transformation yields the rotational spectrum in the frequency domain. The FID is usually recorded for 40 μs and 20 μs for the 2-8 and 8-18 GHz experiments, respectively. Under these conditions, the spectra in the respective regions have a frequency resolution of 25 and 50 kHz.

The gas pulse has an adjustable repetition rate, which is usually set to 9 Hz for the 2-8 GHz experiments. This, in combination with eight excitation chirps per pulse train, results in an effective repetition rate of 72 Hz. The 8-18 GHz region is run with an effective repetition rate of 32 Hz. The increased digitisation rate of the oscilloscope in this set-up reduces the working memory, meaning the gas pulse repetition rate is reduced to 4 Hz as compensatory measure.

3.2 The 18-26 GHz Spectrometer

The 18-26 GHz Spectrometer, shown in Figure 3.3, is a spectrometer that was developed in order to exploit the advantages of chirped-pulse Fourier transform microwave spectroscopy and the lower capital costs associated with building an instrument with the so-called segmented approach. The full details of the design and characterisation of the instrument can be found in Ref. [94].

The spectrometer utilises the same multi-train method as the Hamburg COMPACT Spectrometer, meaning that multiple pulse trains can be associated with each gas pulse. The 18-26 GHz Spectrometer also uses the segmented approach, whereby the total bandwidth of the instrument is covered by a number of shorter segments, which are stitched together in an automatic manner in order to obtain the whole spectrum. The segments are 400 MHz wide, and a collection of ten of these segments, spanning the 7-3 GHz range is produced by a 25 GS/s AWG (Textronix AWG70000A series). This collection of chirped pulses, with each chirped pulse being

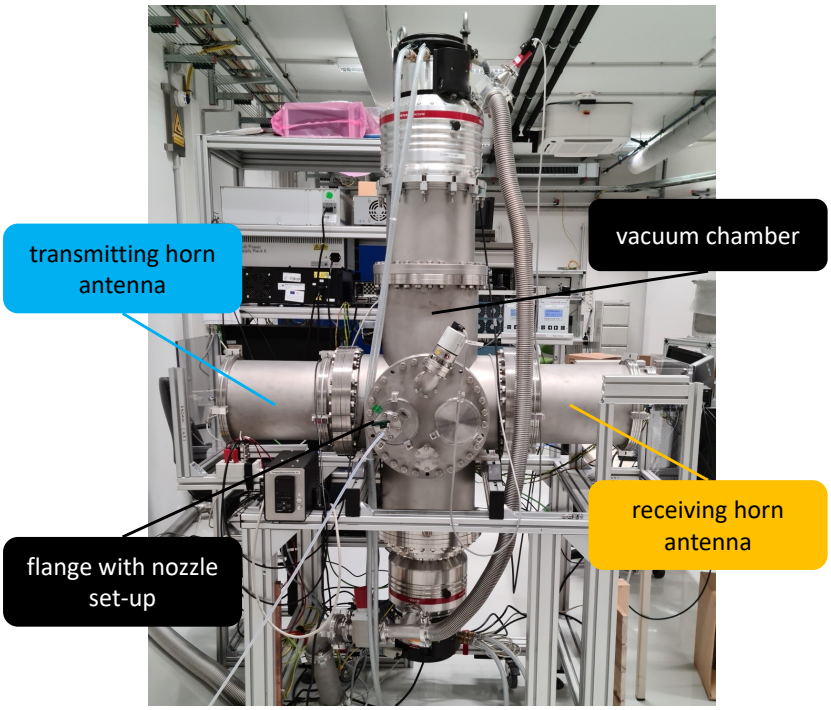

Figure 3.3: The 18-26 GHz spectrometer.

1.5 μs long, is the pulse train. The pulse train is then frequency up-converted to 9-13 GHz and doubled to 18-26 GHz. Each pulse is then amplified by a 6 W SSA (Quinstar QPP-18273840MPI) and transmitted into the vacuum chamber with a horn antenna. Each FID is collected, amplified, frequency down-converted, digitised on a high-speed digitiser card (Keysight U5303A), and fast Fourier transformed into the frequency domain. Usually, 10 μs of FID are collected and Fourier transformed per segment, which results in a resolution of approximately 100 kHz. Segment concatenation gives the spectrum across the whole bandwidth. The multi-frame method allows for three pulse trains per gas pulse to be utilised, and a gas pulse rate of 10 Hz gives an effective repetition rate of 30 Hz.

3.3 The BrightSpec W-band Spectrometer

The W-band Spectrometer, shown in Figure 3.4, operates in the region 75-110 GHz, and it was developed by BrightSpec, Inc. It is based on the work from the University of Virginia, in which the chirped-pulse technique was extended into the millimeter-wave regime [95]. The spectrometer operates in much the same way as the 18-26 GHz spectrometer in that it uses the segmented approach to cover the 35 GHz of bandwidth. This spectrometer was predominantly used to probe the molecules in a room-temperature slow flow cell configuration, with supersonic expansion capabilities being implemented later, in particular for the electrical discharge experiments detailed in Section 3.5. The electronic components of the instrument are controlled by the Edgar programme and user interface developed by BrightSpec.

For the room-temperature slow flow cell configuration, the instrument has two ways in which it can effectively record the rotational spectrum between 75-110 GHz: the Fast Mode and the High Dynamic Range (HDR) Mode. A 12 GS/s AWG (Keysight M8190A) produces excitation pulses initially in the range 1.56-2.28 GHz, which are then frequency up-converted and multiplied by mixing and an active multiplier chain (AMC, x6). The millimeter-wave radiation is then broadcast into the vacuum chamber via a horn antenna and through a first Teflon window. In the Fast Mode, the 35 GHz of bandwidth is covered by 48 segments of 720 MHz each. A graph showing the frequency input into the chamber against the time of the experiment is shown in Figure 3.5. It can be seen that the first segment covers the first 720 MHz of the bandwidth, and the excitation chirp can be seen to be 250 ns in length, which is the excitation pulse length for the Fast Mode. There is then a 2.35 μs pause in the input to allow for the collection of the FID of the first segment, following which the next segment's excitation chirp is transmitted into the chamber. The complete spectrum is covered in one average in a time of 131 μs. The FID of the molecular response is coupled out of the chamber through a second Teflon window, collected by a receiving horn antenna, frequency down-converted, digitised on a 4

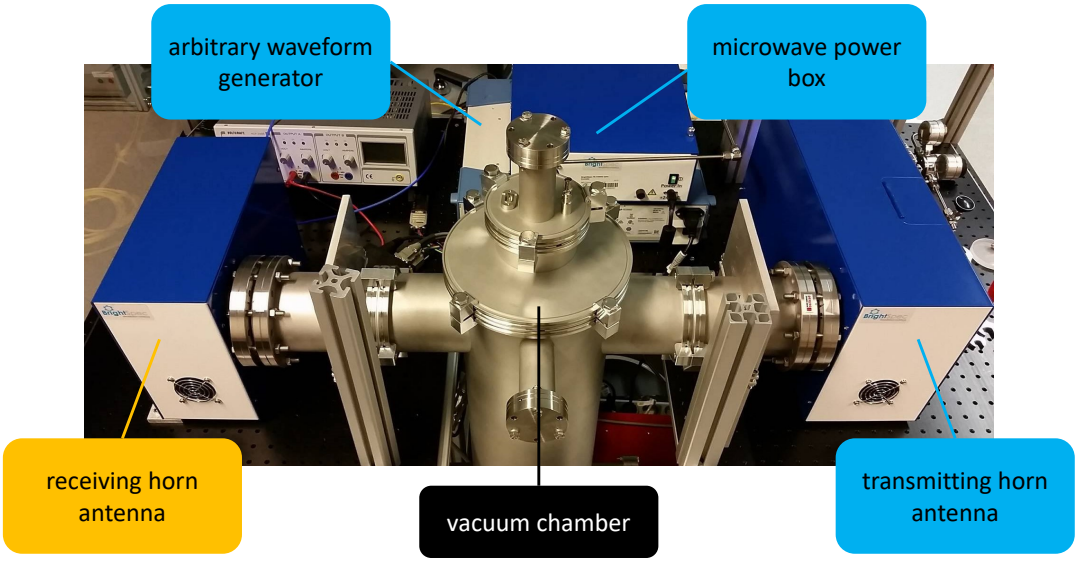

Figure 3.4: The BrightSpec W-band Spectrometer with the custom vacuum chamber.

GS/s real-time digitiser (Keysight U1084), and fast Fourier transformed into the frequency domain. The time- and frequency-domain data can then be handled and saved using the BrightSpec-developed Edgar user interface and software.

In the HDR Mode, each 720 MHz segment is further sub-divided into 30 MHz segments, thus increasing the measurement time, but decreasing the number of spurious signals in the spectrum. The HDR mode allows for more customisation of the parameters, and a typical excitation pulse duration for an HDR experiment is 500 ns, and the FID is usually collected for 4 μs. The achieved frequency accuracy of the instrument is approximately 30 kHz with line widths (full width at half maximum, FWHM) of about 550 kHz.

A typical measurement strategy is to use the Fast Mode to optimise the conditions of the experiment, such as the pressure in the slow flow cell or temperature, if the sample requires heating to be vapourised. Once the ideal conditions are set, a spectrum using the HDR Mode can be obtained, increasing the signal-to-noise ratio and decreasing the number of spurious signals relative to the spectrum recorded in the Fast Mode.

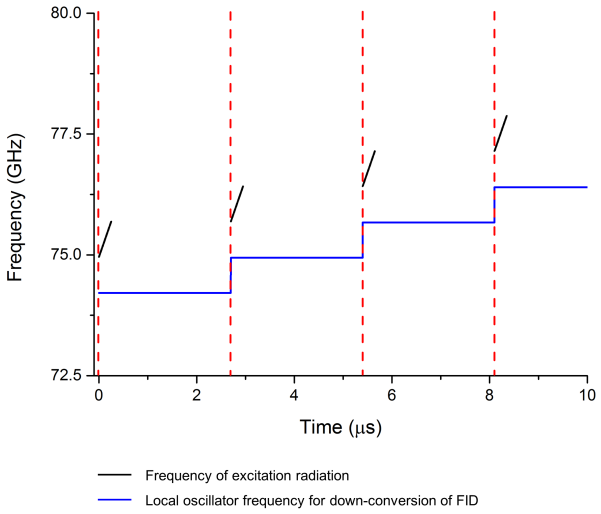

Figure 3.5: The segmented scheme of the W-band Spectrometer, where the frequency of the output of the up-conversion stages is plotted against the time of the experiment. The black lines show the frequency sweeps of the excitation chirps, and the blue lines show the local oscillators used for the frequency down-conversion of the FID. The segments are demarcated by the dashed red lines.

The spectrometer was initially combined with a stainless-steel single-pass vacuum chamber, 67 cm in length and sealed with a Teflon window at each side. Upon the implementation of the supersonic expansion apparatus, a custom chamber was constructed and installed. This custom chamber maintained the horizontal cylinder design of the BrightSpec chamber, but introduced vertical space to allow for the propagation of a molecular beam perpendicular to the radiation path.

For the implementation of the supersonic expansion regime on the W-band spectrometer, the Synchronised HDR Mode can be used. This mode runs the same experiment as the HDR Mode, but requires an external trigger, to which the working of the electronic components of the instrument is synchronised. A delay generator takes the place of the instrument's internal timing system and acts as the required external trigger. This allows for the excitation radiation to be transmitted into the vacuum chamber such that it coincides in the chamber with the molecular beam produced from the pulsed nozzle set-up.

3.4 The Supersonic Expansion vs. the Room-Temperature Cell

The Hamburg COMPACT Spectrometer and the 18-26 GHz Spectrometer work exclusively in the supersonic expansion regime. The capabilities of the W-band Spectrometer were extended to work in such a regime, though most of the work in this thesis was completed with the W-band's vacuum chamber acting as a room-temperature slow flow or static cell. These two regimes present distinct experimental environments, which have consequences on the rotational spectra recorded, as outlined in the following sections.

The Supersonic Expansion

The use of an atomic or molecular beam as the medium in which spectroscopic investigations take place has been widespread in gas-phase spectroscopy since the 1920s [96].

A schematic of a beam in the form of a supersonic expansion, first described in Ref. [97], is shown in Figure 3.6. The molecule of interest and the atomic carrier gas are mixed in the pre-expansion region, so that a few percent of molecular sample is present in the mixture. In this region, the atoms and molecules have a wide velocity distribution, which is described by the Maxwell-Boltzmann distribution, P(ν):

$$P(\nu) = 4\pi \left(\frac{m}{2\pi k_B T} \right)^{\frac{3}{2}} \nu^2 e^{-\frac{m\nu^2}{2k_B T}}. \tag{3.1}$$

As can be seen in Equation 3.1, where m is the mass of the particle, T is the temperature, k_B is the Boltzmann constant, and ν is the particle velocity, the distribution is dictated by the kinetic energies of the gaseous particles. This, in turn, is affected by the temperature. The maximum velocity can be calculated using the expression:

$$\nu_{max} = \sqrt{\frac{5k_B T}{m}}. \tag{3.2}$$

Equation 3.2 is only valid when the particles in question are those of an ideal gas, and for a real system, an approximation must be made.

The supersonic expansion occurs through a small orifice, from the high pressure of the pre-expansion region, P_0, into the low pressure of the vacuum chamber, P_B.

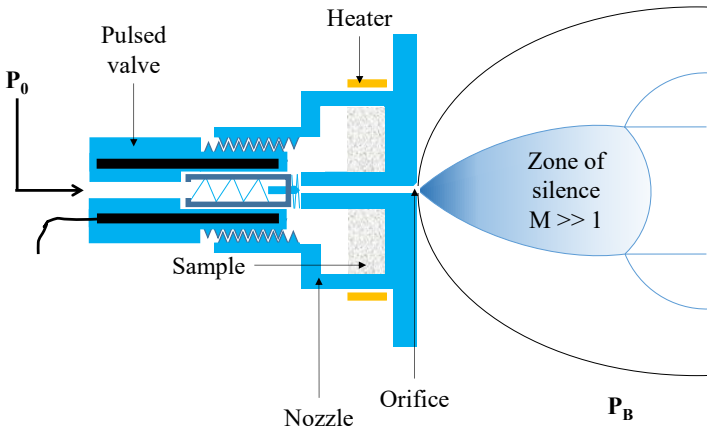

Figure 3.6: A schematic of the supersonic expansion propagating from a pulsed nozzle set-up.

The random motions of the particles are converted into a directed flow, in which the velocity distribution is reduced. This reduction in velocity distribution can be used to define the decrease in the so-called translational temperature of the ensemble. The resulting beam is known as a supersonic expansion because the Mach number, M, of the expansion, defined in Equation 3.3, is much greater than 1:

$$M = \frac{\nu_{gas}}{c_{local}}, \tag{3.3}$$

where ν_{gas} is the velocity of the gas and c_{local} is the local speed of sound.

In a supersonic expansion, the vibrational and rotational energy of a molecule is transferred to the surrounding inert carrier gas in which it is seeded. This occurs due to the many inelastic collisions that occur between the molecule of interest and the carrier gas atoms in the very early stages of the expansion. The extent of the vibrational and rotational cooling is dependent on the carrier gas with which the molecule undergoes these two-body collisions. A larger collision energy is associated with the heavier carrier gas atoms, and they hence produce lower vibrational and rotational temperatures.

Using the supersonic expansion method brings a number of important advan-

tages. Firstly, the low translational temperature leads to narrow spectral line width. Secondly, the low vibrational and rotational temperatures reduce the number of populated states. This simplifies the eventual spectrum recorded and, by increasing the population of the low-energy states, it increases the intensity of the observed transitions relative to a higher-temperature experiment.

In the experimental set-ups presented in the previous sections, the pre-expansion region and the expansion itself are separated by a pulsed nozzle. This allows for pulses or packets of molecules seeded in the carrier gas to be introduced into the vacuum chambers, and it is these defined molecular pulses which undergo spectroscopic interrogation. Specifically, the excitation radiation should interrogate the zone of silence (as shown in Figure 3.6), so-called because of the low density of particles and the lack of collisions between the particles that are present. The length of the zone of silence, x, can be calculated by considering the diameter of the orifice separating the pre- and post-expansion zones, D, as well as the pre-expansion pressure, P_0, and the post-expansion pressure, P_B:

$$x = 0.67D\sqrt{\frac{P_0}{P_B}}. \tag{3.4}$$

From Equation 3.4, it can be seen that the pressure gradient between the pre- and post-expansion regions is important in facilitating the zone of silence. This consideration lends itself to the experimental conditions, wherein the pumping system of the spectrometer should be adequate enough to allow a zone of silence to propagate, that is sufficiently long for spectroscopy to take place. For example, for a backing pressure P_0 in the region of 1-2 bar, a vacuum chamber with a pressure in the order of 10^{-5} mbar would typically be sufficient for a supersonic expansion to propagate.

The Room-Temperature Cell

In the supersonic expansion regime, which was outlined in the previous sub-section, the population of high rotational and vibrational energy levels are reduced. In other words, there is rotational and vibrational cooling. In contrast to the supersonic expansion regime, the W-band spectrometer was operated for the majority of experiments with the vacuum chamber acting as a room-temperature cell. This configuration allows access to the pure rotational spectra of low-lying vibrationally excited states, as outlined in Section 2.5.

For experiments in which commercial liquid samples were used, the sample was loaded into a reservoir external to the vacuum chamber, and a freeze-pump-thaw

procedure was carried out prior to the spectroscopic investigation. The method, as the name suggests, involves three stages: the freezing of the sample with liquid nitrogen, the pumping of the external reservoir such that the surrounding air is removed and the frozen sample remains, and the thawing of the sample back to room temperature. This was primarily performed in order to remove the air from the sample reservoir, thus ensuring that any increase in pressure in the chamber upon sample introduction was due to the molecular sample. The external reservoir can also be heated in order to increase the vapour pressure of the sample, if required.

Where experiments on solid samples were performed, for example imidazole (see Chapter 7), the solid sample was placed in an internal reservoir nozzle, heated, and the resulting vapours were allowed to pulse into the chamber without the presence of a carrier gas.

Considering it to be the thermodynamic system in which spectroscopy takes place, the supersonic expansion can be described as being adiabatic (thermally isolated). This is because neither heat nor mass is exchanged between the supersonic expansion and the surroundings. Energy is only transferred in a collisional sense, between the molecule of interest and the carrier gas, both of which are components of the thermodynamic system. As this exchange could occur in the reverse, the supersonic expansion regime can also be described as isentropic (adiabatic and reversible). In contrast to this, the room-temperature flow cell is an open system where the molecule of interest could transfer heat (energy) to the surroundings via the walls of the vacuum chamber and/or transfer matter to the surroundings through the active pumping system. If the room-temperature cell is used as a static cell, the system is no longer an open system, but rather a closed one. The static cell can still exhibit energy exchange, but does not exchange matter with the surroundings.

3.5 The Development of an Electrical Discharge Source

In order to experimentally explore the possible reaction pathways that lead to interstellar complex organic molecules, an electrical discharge set-up was developed and optimised. This section details this development across the two operating regimes of the W-band spectrometer; that is, as a room-temperature flow cell and with a supersonic expansion.

The electrical discharge source is based on that which has been reported previously, versions of which were designed as early as the 1990s [45]. In short, it is an extension to the Parker General Valve that consists of two oxygen-free high conductivity (OFHC) copper electrodes, which are separated by Teflon spacers, encased in a Teflon housing. This can be seen in Figure 3.7. The Teflon housing extension

is secured onto the pulsed nozzle such that the molecular beam passes from the orifice of the nozzle and through the electrodes. As this proceeds, the molecules are subjected to the potential applied between the electrodes. The bonds in the molecules break apart, which produces a broth of reactive species. These species can then react or recombine to form the discharge products, which, along with any remaining reactive species, adiabatically expand into the vacuum chamber in the form of a supersonic expansion. In order to facilitate the supersonic expansion, the molecules of interest are seeded in an inert carrier gas.

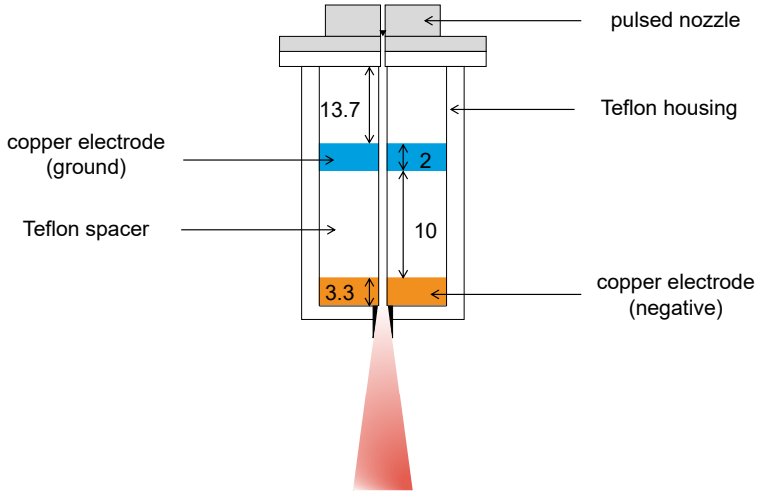

Figure 3.7: A sketch showing the discharge nozzle attached to a pulsed nozzle. The height of each component is labelled in mm. The nozzle forms a pulsed jet of molecules, which are further passed through a discharge nozzle, across which a potential is applied. The molecules pass through the discharge zone (the area between the two electrodes), where bonds can be broken and reactive species can be formed. The reactive species can then react and recombine directly after the second electrode set-up, which produces a mixture of products.

The physical mechanism by which the electrical discharge is initiated and propagated begins with the ionisation of a carrier gas atom, releasing an electron with kinetic energy, E_k. Because the electron is released into an electric field, the kinetic energy of the electron can increase due to its acceleration. This increase in kinetic energy gives the electron sufficient total energy to break the molecule of interest apart or to ionise another carrier gas atom, which can lead to an 'avalanche breakdown'. This breakdown results in the electron ionising more carrier gas atoms, thus

releasing more electrons into the discharge plasma. The breaking of the molecules of interest produces reactive species, which can then react with neutral molecules or recombine with other reactive species to produce discharge products.

Two methods of performing the electrical discharge experiments are employed in this thesis. The first method of discharge product analysis involves allowing the gas from the discharge nozzle to flow through a cold trap (cooled to 77 K with liquid nitrogen), where the neutral products formed in the discharge plasma are frozen. This allows the organic matter to remain in the cold trap while the carrier gas is pumped away. After a pre-determined volume of gas has been pulsed through the discharge nozzle, the contents of the isolated cold trap are allowed to return to room temperature, after which the contents are reintroduced into the vacuum chamber. The mixture of products is then characterised with the spectrometer acting as a room-temperature static cell as described above. The advantage of this method is the ability to concentrate on the neutral products formed in the discharge experiment, which can be advantageous as it avoids the potentially congested rotational spectra of free radicals, for example, which contain a hyperfine structure caused by the coupling of the unpaired electron to the Earth's magnetic field via the Zeeman effect. It also allows for the observation of the rotational spectra of the vibrationally excited states of any products formed.

The second method of discharge product analysis involves probing the supersonic expansion directly. This is achieved by using the Synchronised HDR Mode as described above. The advantage of this method is that the supersonic expansion is being directly probed - this means that, as well as the neutral products, the reactive species produced can be studied. This can hint towards the reaction pathways or mechanisms from reactant to product. The lower temperature of the expansion compared to the static cell means that vibrationally excited states are not as prevalent in the spectrum, which often simplifies spectral analysis.

The discharge components are controlled by the same delay generator used to control the Synchronised HDR Mode. The additional channels on the delay generator are used to control a switch, which completes a circuit containing the electrodes and the high voltage supply. This is programmed such that the switch is closed, and hence the potential is applied between the electrodes, for a short time before, the whole time during, and a short time after the molecular pulse is traversing the nozzle set-up.

Characterisation and Optimisation

The characterisation and optimisation of the discharge system was performed using acetonitrile, CH_3CN, as the test molecule. Acetonitrile was chosen due to the discharge products of it being well-characterised [98]. This prior knowledge was

essential in determining whether the discharge set-up was producing the expected products, a list of which is shown in Table 3.1.

Table 3.1: A direct comparison of the observed discharge products of acetonitrile from Ref. [98] and this work. The final column indicates if the species has been detected in the interstellar medium (ISM).

Molecule	Ref. [98] 260-295 GHz cold trap	Ref. [98] 6-18 GHz expansion	This work 75-110 GHz cold trap	This work 75-110 GHz expansion	Detected?
HCN	Yes	No	Yes	Yes	Yes
HCN ν_2=1	Yes	No	Yes	No	Yes
HCN ν_2=2	Yes	No	No	Yes	Yes
HNC	No	No	No	Yes	Yes
CH_3CN	Yes	Yes	Yes	Yes	Yes
HNC_3	No	No	No	No	Yes
HCCNC	No	Yes	No	No	Yes
HC_3N	Yes	Yes	Yes	Yes	Yes
HC_3N ν_7=1	Yes	No	Yes	Yes	Yes
HC_3N ν_7=2	Yes	No	Yes	Yes	Yes
HC_3N ν_6=1	Yes	No	Yes	Yes	Yes
HC_3N ν_6=2	Yes	No	Yes	Yes	Yes
HC_3N ν_6=1, ν_7=1	Yes	No	Yes	Yes	Yes
HC_3N ν_4=1	Yes	No	Yes	No	Yes
HC_3N ν_4=1, ν_7=1	Yes	No	Yes	No	Yes
HC_3N ν_5=1/ν_7=3	Yes	No	Yes	Yes	Yes
$H^{13}CCCN$	Yes	No	Yes	No	Yes
$HC^{13}CCN$	Yes	No	Yes	No	Yes
$HCC^{13}CN$	Yes	No	Yes	No	Yes
$HCCC^{15}N$	Yes	No	Yes	No	Yes
$H^{13}CCCN$ ν_7=1	Yes	No	Yes	No	Yes
$HC^{13}CCN$ ν_7=1	Yes	No	Yes	No	Yes
$HCC^{13}CN$ ν_7=1	Yes	No	Yes	No	Yes
CH_2CHCN	Yes	Yes	Yes	Yes	Yes
E- & Z-CH_3CHNH	No	Yes	No	No	Yes
CH_3CH_2CN	Yes	Yes	No	No	Yes

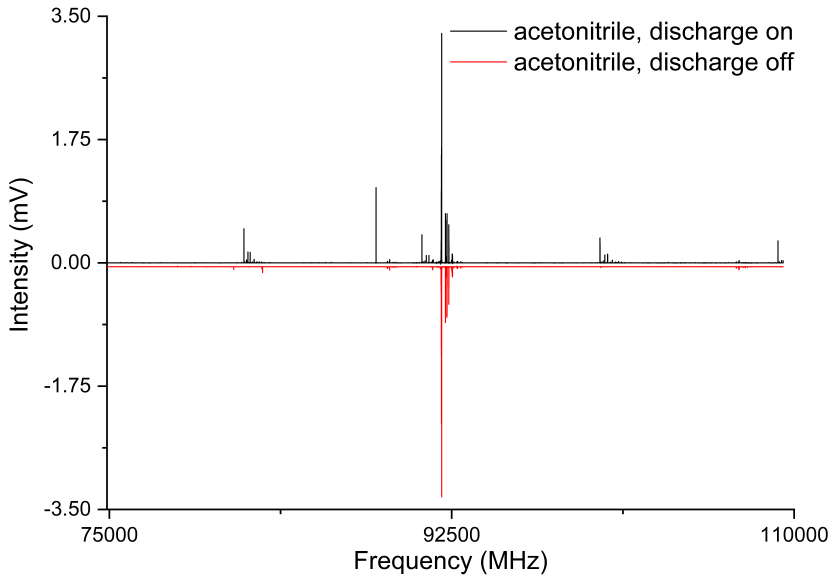

Figure 3.8: A comparison of the discharge on and the discharge off experiments for acetonitrile using the cold trap method.

Figure 3.8 shows the comparison of HDR spectra of a discharge off and discharge on experiment, herein referred to as the OFF and ON experiments respectively, using the cold trap method. A full comparison between the products seen in this work and the products reported in the discharge spectrum of acetonitrile in Ref. [98] can be found in Table 3.1. From the production of new molecules, indicated by the presence of new lines in the ON spectrum, and the comparison presented in Table 3.1, it is clear that the discharge apparatus was effectively breaking up the acetonitrile molecule in the intended way. It should be noted that the production of E- & Z-CH_3CHNH in Ref. [98] was achieved through the discharge of a mixture of acetonitrile and hydrogen sulfide [51]. Further steps to explore and optimise the experiment were taken, including varying the concentration of acetonitrile in the gas mixture, the polarity of the working electrode, and the variance of the current and voltage settings on the high voltage supply. Figures 3.9-3.13 provide a graphical summary of some of the findings from these investigations.

The effect of the composition of the gas mixture on the performance of the discharge apparatus was explored. Figure 3.9 shows the similarity in the signal levels recorded for cyanoacetylene, HC_3N, and hydrogen cyanide, HCN, as discharge products of 0.2 % and 2 % acetonitrile gas mixtures. The left panel shows the 81881.46 MHz transition ($J' \leftarrow J = 9 \leftarrow 8$) of cyanoacetylene, and the right panel shows the 88630.41, 88631.87, and 88633.95 MHz transitions ($J' \leftarrow J = 0 \leftarrow 1$; $F' \leftarrow F = 1 \leftarrow 1$, $2 \leftarrow 1$, and $0 \leftarrow 1$, respectively) of hydrogen cyanide. It can be concluded

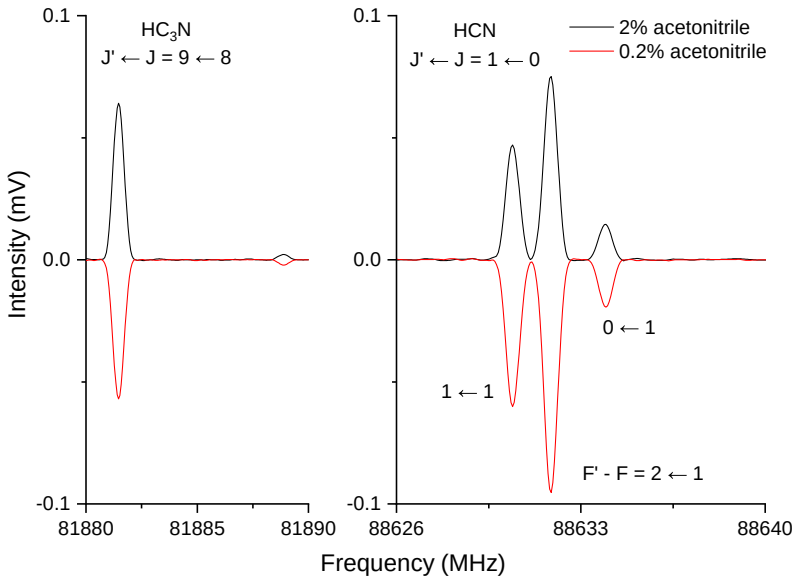

Figure 3.9: A comparison of the ON spectra for acetonitrile using the cold trap method with varying concentrations of acetonitrile. The left panel shows the 81881.46 MHz transition of cyanoacetylene, and the right panel shows the 88630.41, 88631.87, and 88633.95 MHz transitions of hydrogen cyanide. Each discharge experiment was performed to ensure the same total concentration of acetonitrile had passed through the discharge nozzle.

that the percentage composition of the gas mixture did not significantly affect the production of the expected discharge products. The similarity in the signal levels can also support the trapping efficiency of the cold trap and the reproducibility of product formation with respect to the number of 'discharge cycles' that each experiment requires in the cold trap method. As mentioned above, the cold trap discharge experiments were performed until a pre-determined volume of sample had been passed through the discharge nozzle. For acetonitrile, this pre-determined volume, where pressure was used as a proxy for the volume, was 3 mTorr. This means, for the 2 % acetonitrile tank, 150 mTorr of total gas was pulsed through the discharge nozzle and into the vacuum chamber in two aliquots of 75 mTorr, which was then passed through the cold trap; this is referred to as two discharge cycles. For the 0.2 % acetonitrile tank, a total of 1500 mTorr total gas mixture was pulsed through the discharge nozzle in twenty discharge cycles of 75 mTorr each. This increase in discharge cycles shows little effect on which products are formed, as well as little effect on the quantity of the products formed.

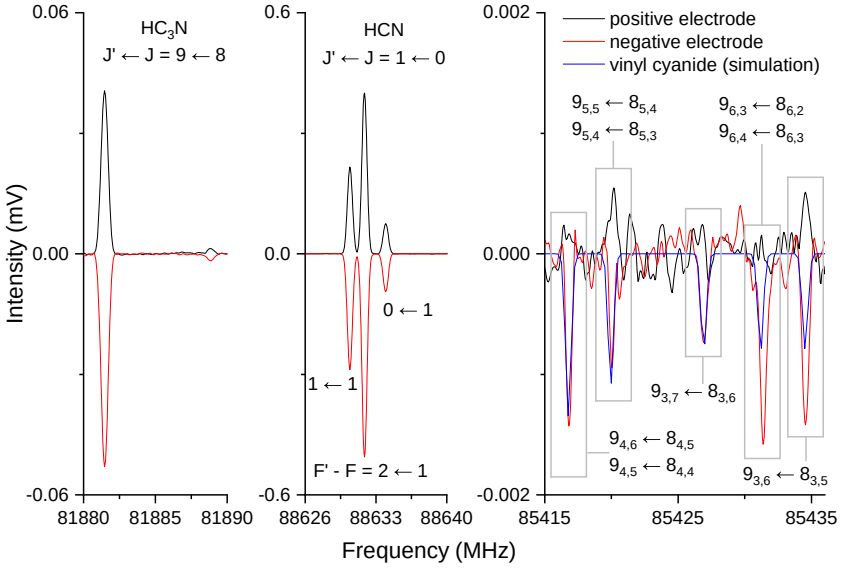

Figure 3.10: A comparison of the ON spectra for acetonitrile using the cold trap method with the working electrode varying in polarity. The left panel shows the 81881.46 MHz transition of cyanoacetylene, the middle panel shows the 88630.41, 88631.87, and 88633.95 MHz transitions of hydrogen cyanide, and the right panel contains the prediction of the rotational spectrum of vinyl cyanide (transitions labelled as $J'_{K'_a,K'_c} \leftarrow J_{K_a,K_c}$.

Figure 3.10 compares the ON spectra for acetonitrile using the cold trap method in two different scenarios - one in which the working electrode of the discharge system is positive and one in which the working electrode of the discharge system is negative. The negative electrode set-up was used for all further experiments due to chemical diversity in the discharge products. As can be seen in Figure 3.10, the negative electrode set-up allowed for the detection of vinyl cyanide, CH_2CHCN, while the positive electrode set-up did not allow for this observation to be made.

Figure 3.11 shows a comparison of a number of ON spectra for acetonitrile using the cold trap method with varying current parameters. As can be seen, the current setting of 4 mA was optimal for the production of the two major discharge products. As above, the left panel shows the 81881.46 MHz transition ($J' \leftarrow J = 9 \leftarrow 8$) of cyanoacetylene, and the right panel shows the 88630.41, 88631.87, and 88633.95 MHz transitions ($J' \leftarrow J = 0 \leftarrow 1$; $F' \leftarrow F = 1 \leftarrow 1$, $2 \leftarrow 1$, and $0 \leftarrow 1$, respectively) of hydrogen cyanide.

Figures 3.12 and 3.13 show a comparison of a number of ON spectra for acetonitrile using the cold trap method with varying voltage parameters. Note that the

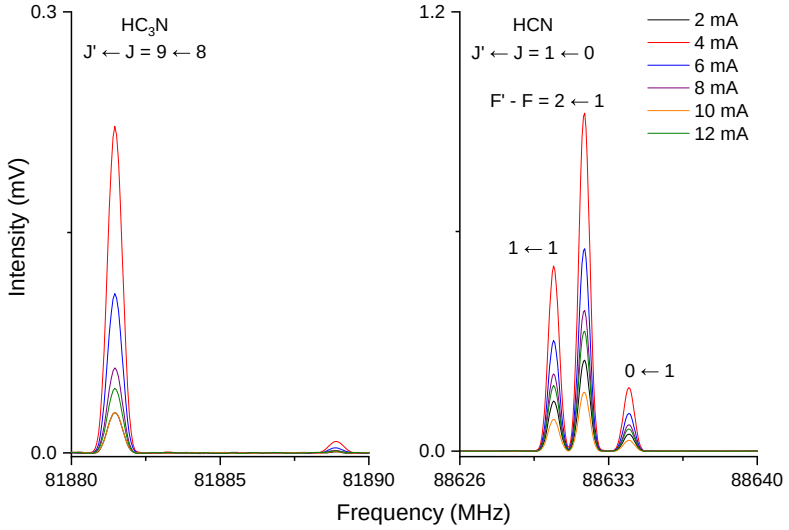

Figure 3.11: A comparison of the ON spectra for acetonitrile using the cold trap method with varying current settings. The voltage was set to 1 kV. The left panel shows the 81881.46 MHz transition of cyanoacetylene, and the right panel shows the 88630.41, 88631.87, and 88633.95 MHz transitions of hydrogen cyanide.

scales on the y-axes are different for both figures. The current was set and maintained at 4 mA whilst the voltage was varied. Again, the left panels of both figures show the 81881.46 MHz transition ($J' \leftarrow J = 9 \leftarrow 8$) of cyanoacetylene, and the right panels show the 88630.41, 88631.87, and 88633.95 MHz transitions ($J' \leftarrow J = 0 \leftarrow 1$; $F' \leftarrow F = 1 \leftarrow 1$, $2 \leftarrow 1$, and $0 \leftarrow 1$, respectively) of hydrogen cyanide. It is clear from these figures that the voltage also plays a pivotal role in the production of discharge products.

Many of the parameters for the discharge experiments were carried forward from the cold trap method to the supersonic expansion method. The major difference between the experiments is the molecular pulse duration, which is limited in the supersonic expansion experiments by the pumping capabilities of the turbo pump. The delay generator was set to operate at 5 Hz, which established as best a compromise as possible between the repetition rate of the molecular pulse and the opening time of the pulsed nozzle (the molecular pulse duration). The pumping system generally allowed for a molecular pulse duration of 260 μs at 5Hz. The comparison of the ON and OFF spectra using this method is shown in Figure 3.14. Table 3.1 identifies some of the discharge products of acetonitrile using this method. From Table 3.1, it can be seen that the molecular beam in the current work is warmer than that probed in Ref. [98] - this can be concluded from the observation of vibrational states

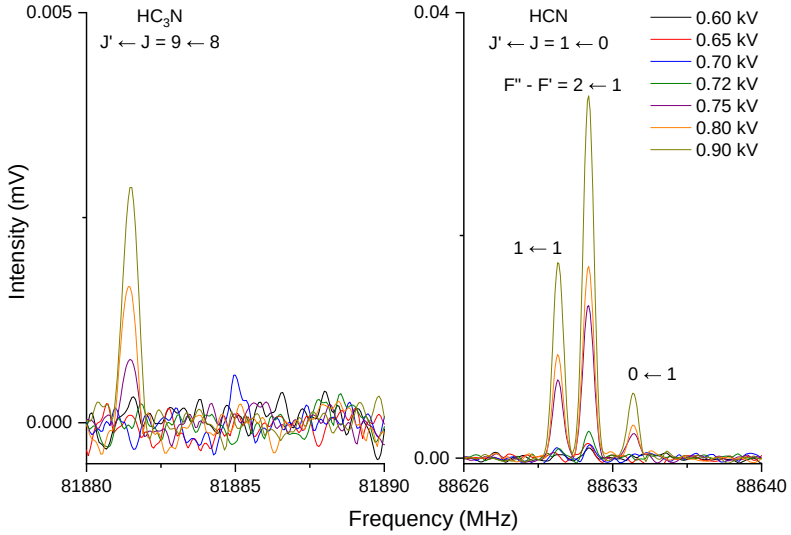

Figure 3.12: A comparison of the ON spectra for acetonitrile using the cold trap method with varying low voltage settings. The current was set to 4 mA. The left panel shows the 81881.46 MHz transition of cyanoacetylene, and the right panel shows the 88630.41, 88631.87, and 88633.95 MHz transitions of hydrogen cyanide.

of cyanoacetylene in this work. Table 3.2 lists some of the molecules and species observed in this work, and not reported in the previous discharge experiments of acetonitrile in Ref [98]. The majority of the species in Table 3.2 are isotopologues or vibrationally excited states of hydrogen cyanide and cyanoacetylene. This, rather than point to specific differences in product formation, instead likely points towards a higher temperature of the product gas mixture (for the vibrationally excited states) and higher sensitivity of the spectrometer used in this work (for the isotopologues).

There were a number of differences between the two types of experiments that are particularly worthy to note at this stage. The first is related to the composition of the gas flowing through the discharge nozzle. As can be seen from Figure 3.9, the composition of the gas in the acetonitrile tests for the cold trap method were initially 0.2% and 2% acetonitrile in neon, which was controlled by pre-mixing the required concentration of acetonitrile with neon in a gas bottle. For the experiments in the supersonic expansion regime, pure acetonitrile was loaded into an external reservoir, over which the neon carrier gas was flowed over en route to the vacuum chamber. This method, commonly utilised in the supersonic expansion experiments for the COMPACT and 18-26 GHz spectrometers, was required in this case, as the pre-mixed 0.2% and 2% acetonitrile in neon gas bottles did not allow for the

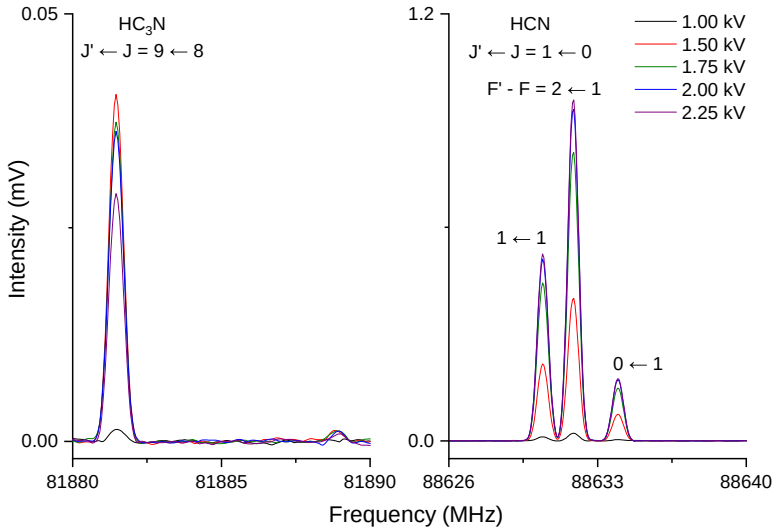

Figure 3.13: A comparison of the ON spectra for acetonitrile using the cold trap method with varying high voltage settings. The current was set to 4 mA. The left panel shows the 81881.46 MHz transition of cyanoacetylene, and the right panel shows the 88630.41, 88631.87, and 88633.95 MHz transitions of hydrogen cyanide.

Table 3.2: A list of molecular species observed from the discharge of acetonitrile in this work, but which were not reported in the previous discharge experiments of acetonitrile in Ref. [98].

Molecule
$H^{13}CN$
$HC^{15}N$
HC_3N ν_4=1/ν_7=2, ν_5^{0e}
$HC^{13}CCN$ ν_6=1
$HC^{13}CCN$ ν_7=2
$HCC^{13}CN$ ν_7=2
$HCC^{13}CN$ ν_6=1
$HCCC^{15}N$ ν_7=1
$^{\bullet}CH_2CN$

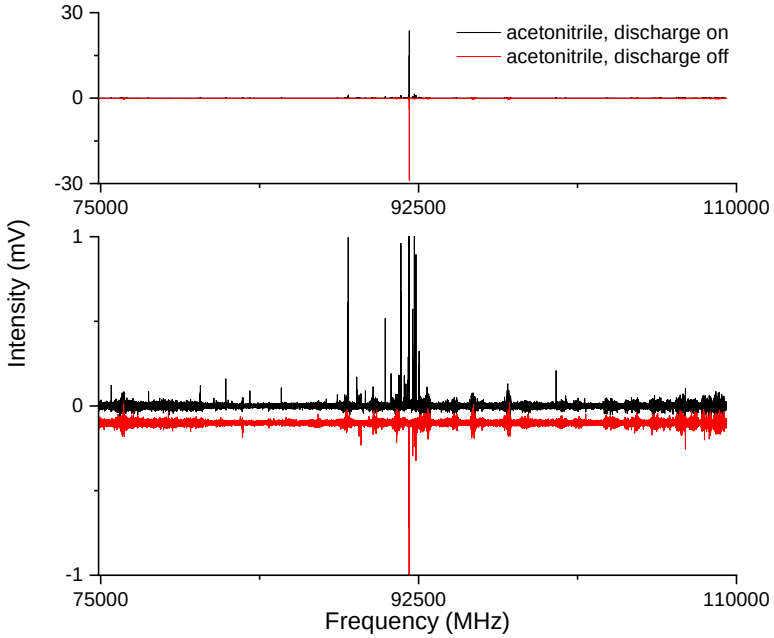

Figure 3.14: A comparison of the ON and OFF spectra for acetonitrile using the supersonic expansion method. The lower plot is a zoom-in of the upper plot, showing more clearly the new lines in the ON spectrum.

observation of the known discharge products in the spectrum. It is likely that, at these concentrations, there are not sufficient numbers of molecules in the expansion, which is being directly probed, for clear observation. This would not be a problem in the cold trap method, as the discharge products are frozen in the cold trap after production and re-introduced into the chamber for interrogation later, giving ample opportunity for the discharge products to accumulate a large enough concentration for observation. As the experiment requires a build-up of discharged gas to be collected before passing it through the cold trap, it could also be the case that the discharge affects the bulk gas load, and not just the gas passing through the discharge nozzle. That is, the discharge creates an electric arc to the molecules in the chamber as well as the gas being pulsed through the electrode set-up. This could further explain the proliferation of the discharge products from the low-concentration gas bottles.

A second difference in the two types of experiment is the discharge parameters as defined on the high voltage supply. This is particularly true for the value of the current, which was set to be higher for the supersonic expansion experiments. A current value of 4 mA was set in the cold trap method experiments, and this was sufficient for the production of discharge products. In the supersonic expan-

sion experiments, a current value of 100 mA was set. This change was made in conjunction with other acetonitrile discharge experiments being done on the other rotational spectrometers in the supersonic expansion regime. The difference in current could also be rationalised with the point raised above - that in the cold trap method, the discharge could be affecting the bulk gas load in the cell, as opposed to being confined between the electrodes in the discharge nozzle. The higher current could be required to trigger the production of the discharge plasma in the packets of molecules and buffer gas atoms in the supersonic expansion, but the lower current in the cold trap method is able to do the same, as it begins to act not on a dilute packet of gas but rather a cell of increasing concentration. As mentioned earlier, the cell is filled with up to 100 mTorr of sample and carrier gas per discharge cycle. A discharge plasma in this increased concentration of molecules and buffer gas could be more easily produced and maintained due to the higher availability of electrons, which are required to generate further electrons and the reactive species.

The difference between the methods is also clear in terms of the results that the experiments yield. As mentioned above, the cold trap method focusses the analysis on the neutral products formed. However, the method relies on the trapping of the molecular species in a cold trap, before the warming of the frozen organic species back into the gas phase. As much as effort can be placed in trying to mitigate any reactive processes occurring in this period of time, for example, allowing the cold trap to warm up using a room-temperature water bath, and the exclusion of any "excessive" heating sources such as heat guns, it is impossible to fully eliminate the possibility that products observed in the resulting spectra were not formed during the discharge process, but instead inside the cold trap. This is remedied in the supersonic expansion experiments, where the expansion is directly probed, effectively eliminating the possibility of detecting products not formed in the discharge plasma. Probing the supersonic expansion also ensures the products and reactive species observed are produced directly in the discharge zone (between the electrodes), and not produced because of the discharge acting on the bulk gas load accumulated in the cold trap method.

The probing of the molecular pulse directly has the further advantage that the detection of reactive intermediates is possible. For example, the cyanomethyl radical ($^{\bullet}CH_2CN$) is formed in the discharge of acetonitrile in neon; see Table 3.1 and Figure 3.15. This is a particularly important characteristic for the aims of the work of this thesis. Knowledge of the radical species produced in the discharge plasma can be used to guide the formulation of reaction pathways or mechanisms. These pathways or mechanisms can be supported by quantum-chemical calculations, and the presence of specific reactive species experimentally can better define or constrain the system being considered theoretically. For example, knowing that the cyanomethyl radical is produced from the discharge of acetonitrile suggests that it

could play a role in the pathway towards other discharge products.

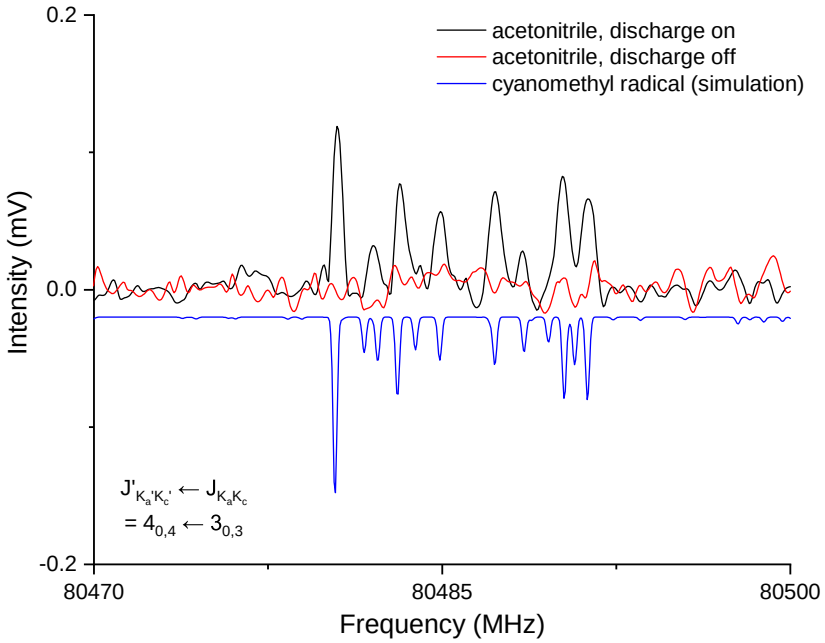

Figure 3.15: A comparison of the ON and OFF spectra for acetonitrile using the supersonic expansion method. The transitions shown are those belonging to the cyanomethyl radical, the predicted spectrum of which is shown in blue. The transition shown is the $J'_{K'_a,K_c} \leftarrow J_{K_a,K_c} = 4_{0,4} \leftarrow 3_{0,3}$ transition, and the extensive hyperfine structure is caused by the unpaired radical electron causing Zeeman splitting of the spectral lines, the interaction of the electron spin with the hydrogen nuclei, and the nuclear quadrupole of the nitrogen nucleus [99].

Chapter 4

The W-band Spectrum of *iso*-Propyl Cyanide and a Search for its Vibrationally Excited States in the Interstellar Medium

This chapter is based on the following publication:

- B. E. Arenas, S. Gruet, A. L. Steber, B. M. Giuliano, M. Schnell *Chirped-pulse Fourier transform millimeter-wave spectroscopy of ten vibrationally excited states of i-propyl cyanide: Exploring the far-infrared region*, Physical Chemistry Chemical Physics **19**, 1751-1756 (2017).

4.1 Introduction

The family of cyanide-containing molecules constitutes a considerable fraction (approximately 10%) of the almost 200 molecules detected in the interstellar medium (ISM). The most recent detections of complex cyanides have been performed toward the Galactic center source Sagittarius B2 (Sgr B2), identifying a variety of cyanide species (such as aminoacetonitrile, *n*-propyl cyanide [100–102], isotopologues of vinyl cyanide and ethyl cyanide [103], E-cyanomethanimine [104], methyl isocyanate and methyl cyanate [105, 106]).

Recently, Belloche *et al.* detected the first branched alkyl molecule, *iso*-propyl cyanide (*i*-propyl cyanide, $(CH_3)_2CCN$, *i*-C_3H_7CN), toward Sgr B2, with an abundance 0.4 times that of its straight-chain structural isomer *n*-propyl cyanide [107]. Based on astrochemical models, the authors proposed that both isomers, *i*-propyl cyanide and *n*-propyl cyanide, are produced on dust grain ice mantles through the

addition of molecular radicals. For the branched *i*-propyl cyanide species, the addition of a functional group to the non-terminal carbon would be required. This detection was based on an extensive laboratory spectroscopy investigation of *i*-propyl cyanide in selected regions between 6 and 600 GHz [108].

A considerable proportion of complex molecules resides in low-lying vibrationally excited states at the elevated temperatures that were determined for *i*-propyl cyanide towards Sgr B2 (around 150 K). These vibrationally excited states, along with isotopologues that can often be seen in natural abundance, are associated with the so-called 'weeds' in radioastronomy data [109]. These weeds can occupy many channels in a complex, warm, dense astronomical data set. Therefore, it is important that the vibrationally excited states and isotopologues of astronomically abundant species are characterised. In 1974, Durig and Li reported the analysis of the ground state and three low-lying vibrational states of *i*-propyl cyanide in a room-temperature microwave spectroscopy study (26.5–40 GHz) [110].

In this chapter, ten vibrationally excited states of *i*-propyl cyanide are identified and characterised with a segmented chirped-pulse W-band instrument. The energies of the vibrationally excited states ranged up to 500 cm^{-1}, reinforcing how millimeter-wave spectroscopy of room temperature samples can provide detailed molecular parameters of low-lying vibrationally excited states. The ^{13}C isotopologues of the vibronic ground state of *i*-propyl cyanide were also observed in natural abundance (1.1%) in the millimeter-wave frequency range. This allowed for the precise determination of the ground-state structure of the molecule.

4.2 Experimental and Theoretical Details

The rotational spectrum of *i*-propyl cyanide was recorded using the W-band chirped-pulse Fourier transform millimeter-wave spectrometer purchased from BrightSpec, Inc. The full description of the instrument can be found in Chapter 3. The *i*-propyl cyanide (99% pure, purchased from Alfa Aesar and used without further purification) was placed in a sample reservoir. A flow of about 4 μbar of *i*-propyl cyanide was maintained inside the chamber during the experiment. The typical excitation pulse duration of 500 ns was used, and the FID was collected for 4 μs. For this experiment, 500,000 FIDs were recorded and averaged in the High Dynamic Range (HDR) mode, which corresponds to a measurement time of 50 minutes. In the following, only spectra recorded using the HDR mode are shown.

The overall dipole moment of *i*-propyl cyanide is large, with μ_a = 4.02 D and μ_c = 0.62 D. Because of the fact that *i*-propyl cyanide is of C_s symmetry and the Ray's asymmetry parameter value is κ = -0.57, the molecule is a near-prolate asymmetric top molecule. However, to be consistent with previous data sets [108], the data were fit to a Watson's *S*-reduction Hamiltonian in an I^r representation.

The spectral assignment was performed with the AABS package [71, 90] and fit with Pickett's programs (SPFIT/SPCAT) [63]. The experimental analysis was supported with harmonic and anharmonic quantum-chemical calculations using the program package Gaussian 09 [73]. The anharmonic frequency calculations, performed at the B3LYP/aug-cc-pVTZ level of theory, provided the rotational constants of the individual vibrationally excited states. For facilitating the assignment of the rich experimental spectrum, the calculated rotational constants for the vibrationally excited states were shifted by the difference obtained between the calculated and the experimental rotational constants for the ground state.

For the rotational spectra of the non-perturbed vibrational states, between 66 to 128 transitions were assigned, with a signal to noise ratio of 1200:1 for the strongest transitions, and they were fit to a rigid-rotor Hamiltonian including centrifugal distortion within experimental accuracy (30 kHz). The transitions involved rotational quantum numbers J ranging between 11 and 17 and K_a values in the range 0 to 12 for R-type transitions, i.e., those following the selection rule ΔJ = +1. K_a is the quantum number associated with the projection of the rotational angular momentum onto the inertial axis a in the limit of the prolate symmetric top. Note that weak Q-type transitions with higher J values (obeying the selection rule ΔJ = 0) were also observed. The rotational constants A, B, and C, and the quartic centrifugal distortion rotational parameters of each state are well determined (see Table 4.1). The precision on the D_K values is limited by the range of K_a values observable in this spectral region. For the perturbed vibrational states (those that lie close in energy), only transitions with low K_a values (up to 7) were included in the fit, which impacts the accuracy of the D_K values. Therefore, in order to determine reliable rotational constants for those states, the D_K constant has been kept fixed to its ground state value. The additional rotational constants due to ^{13}C isotopic substitution in natural abundance were used to determine the substitution structure of *i*-propyl cyanide using Kraitchman's equations [91] as implemented in the KRA program package [90].

4.3 Results and Discussion

The broadband spectrum covering 75–110 GHz for *i*-propyl cyanide is shown in Figure 4.1, illustrating the high line density arising from the large number of vibrational states. Despite the spectrum's richness, the high resolution and sensitivity of the spectrometer result in well separated and distinguishable rotational transitions. This is illustrated in the zoom-in (Figure 4.2) of the $J'_{K'_a,K'_c} \leftarrow J_{K_a,K_c} = 16_{2,15} \leftarrow 15_{2,14}$ rotational transition (left component of the doublets) and the $16_{1,15} \leftarrow 15_{1,14}$ rotational transition (right component of the doublets) for the vibronic ground state and several vibrational states. Note that no ^{14}N nuclear quadrupole coupling was

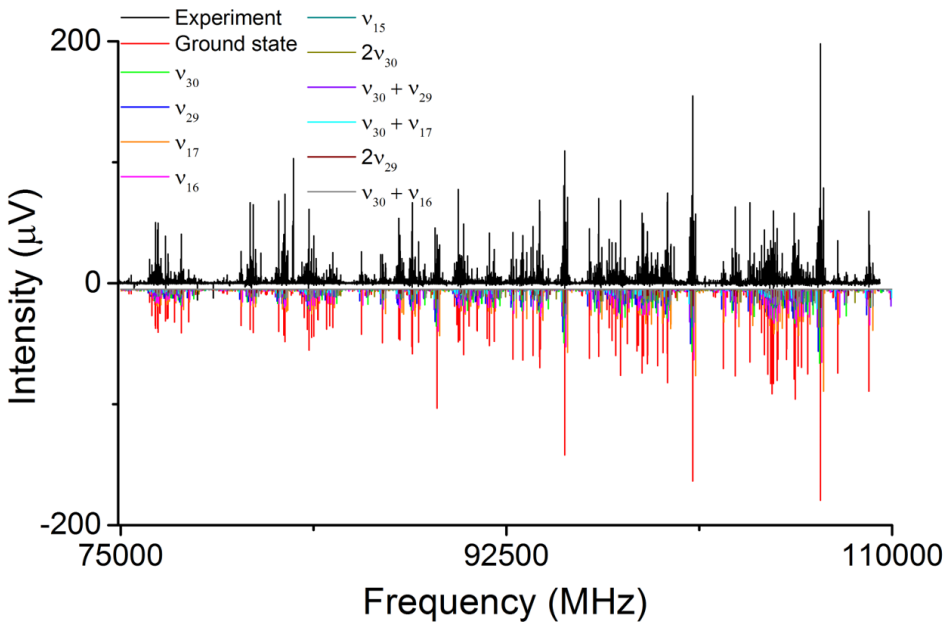

Figure 4.1: Broadband rotational spectrum of *i*-propyl cyanide. The upper trace is the experimental spectrum, consisting of 500,000 co-added FIDs, while the lower traces are simulations of the fitted rotational parameters (see Table 4.1 and the text for more details).

observed because it collapses for the high J, K_a, and K_c values populated at the elevated temperatures used in the experiment and observed in this high frequency range. As in previous rotationally resolved spectroscopy studies on *i*-propyl cyanide, no line splittings due to methyl group internal rotation were observed [108, 110]. The calculated barriers associated with this motion amount to 13.1 kJ mol^{-1} (B3LYP/6-311G++ level of theory) and are too high to cause detectable line splittings in the present experiment.

Based on the shifted calculated rotational constants, the assignment of most of the vibrationally excited states was straight forward. Ten energetically low-lying vibrationally excited states were unambiguously identified and their rotational transitions fit to a Watson's S-reduction Hamiltonian in an I^r representation, as described earlier. The rotational constants for the ground state and the vibrationally excited states are summarised in Table 4.1. The calculated vibrational frequencies of the respective states are also included (B3LYP/aug-cc-pVTZ level of theory with and without anharmonic corrections). However, for some pairs of states, such as ν_{29}/ν_{17} as well as $(\nu_{30} + \nu_{29})/(\nu_{30} + \nu_{17})$, the analysis was more challenging. It was found that these vibrationally excited states, which are within only a few cm^{-1}

Table 4.1: Molecular parameters for the ground state and vibrationally excited states of *i*-propyl cyanide, which has C_s symmetry. Ten vibrationally excited states were experimentally observed, two further states were predicted, but not observed. ΔE_a and ΔE_h are based on ab initio calculations with and without anharmonic corrections (B3LYP/aug-cc-pVTZ), respectively. Note the larger rms values for states ν_{17}, ν_{30} + ν_{29} and $2\nu_{29}$, which might arise from coupling with the near-degenerate states ν_{29}, ν_{30} + ν_{17}, and ν_{29} + ν_{17}, respectively. Perturbed states are marked with a *. J_m and $K_{a,m}$ are the maximum values included in the fits.

	GS	ν_{30}	ν_{29}*	ν_{17}*	ν_{16}	ν_{15}	$2\nu_{30}$	$(\nu_{30}+\nu_{29})$*	$(\nu_{30}+\nu_{17})$*	$(\nu_{29}+\nu_{17})$*	$2\nu_{29}$*	$2\nu_{17}$*	$(\nu_{30}+\nu_{16})$
Symmetry		A"	A"	A'	A'	A'	A'	A'	A"	A"	A'	A'	A"
ΔE_a (cm^{-1})	0	191.2	216.7	218.9	281.7	357.8	383.2	408.8	411.2	429.6	430.3	437.3	473.7
ΔE_h (cm^{-1})	0	189.7	220.9	218.3	281.9	353.2	379.3	410.6	408.0	439.3	441.8	436.7	471.6
A (MHz)	7940.8746(16)	7896.7463(15)	7932.513(51)	7993.882(26)	7923.1764(24)	7928.435(15)	7853.1241(69)	7879.481(28)	7945.628(27)		7926.817(25)		7875.091(21)
B (MHz)	3968.08888(52)	3980.03092(59)	3964.9749(93)	3971.8633(50)	3970.27231(63)	3978.7235(14)	3991.94840(76)	3976.7219(54)	3983.3608(56)		3963.9296(49)		3981.9721(22)
C (MHz)	2901.05458(53)	2899.86118(61)	2898.2195(46)	2904.7205(20)	2902.82671(69)	2900.5124(14)	2898.60041(73)	2896.9396(33)	2903.4154(23)		2896.3754(36)		2901.5706(16)
D_J (kHz)	0.6127(12)	0.6386(13)	0.630(16)	0.6085(79)	0.6129(14)	0.6155(16)	0.6603(15)	0.6349(75)	0.6205(82)		0.5585(60)		0.6320(34)
D_{JK} (kHz)	12.1698(43)	11.4510(21)	11.38(24)	13.162(99)	11.9422(17)	12.2310(37)	10.7860(38)	10.363(50)	12.519(92)		11.231(95)		11.279(13)
D_K (kHz)	-5.231(27)	-7.869(10)	[-5.231]	[-5.231]	-5.236(10)	-4.07(11)	-9.356(85)	[-5.231]	[-5.231]		[-5.231]		-7.20(55)
d_1 (kHz)	-0.24393(11)	-0.25602(18)	-0.2637(72)	-0.2486(39)	-0.25187(18)	-0.25600(83)	-0.27202(36)	-0.3044(60)	-0.2550(48)		-0.2516(46)		-0.2556(22)
d_2 (kHz)	-0.189404(63)	-0.183884(73)	-0.1774(31)	-0.2025(13)	-0.185515(88)	-0.19630(55)	-0.17902(17)	-0.1983(24)	-0.1934(15)		-0.1929(25)		-0.1760(10)
H_{JK} (Hz)	0.0347(16)		-2.55(77)	-1.55(31)					-1.59(26)				
h_2 (Hz)	0.000931(72)												
h_3 (Hz)	0.000326(33)												
No. lines	173	128	45	71	109	88	89	42	68		37		66
rms (kHz)	26.9	32.3	58.5	44.1	33.1	33.7	32.0	64.4	50.3		51.9		32.7
$J_m/K_{a,m}$	40/10	35/12	16/6	17/8	40/14	40/13	38/12	17/8	17/8		17/6		17/11

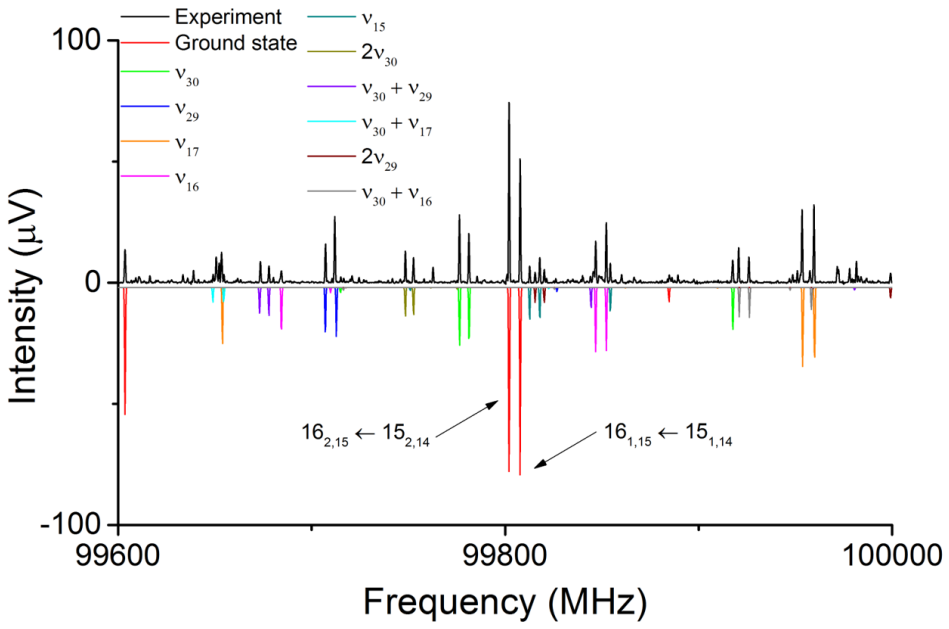

Figure 4.2: Zoom-in of the broadband rotational spectrum of *i*-propyl cyanide showing the $J'_{K'_a,K'_c} \leftarrow J_{K_a,K_c} = 16_{2,15} \leftarrow 15_{2,14}$ and $16_{1,15} \leftarrow 15_{1,14}$ transitions of the vibronic ground and ten vibrationally excited states as labelled in the spectrum. The upper trace is the experimental spectrum, while the lower traces are simulations of the fitted rotational parameters (see also Table 4.1 and the text for more details). The SNRs for these transitions correspond to 475:1 for the $16_{2,15} \leftarrow 15_{2,14}$ transition and to 324:1 for the $16_{1,15} \leftarrow 15_{1,14}$ transition for the vibronic ground state.

energetically, perturb each other. Without being able to identify the band centres, this perturbation cannot be analysed in detail. Such a study would require high-resolution far-infrared data, where vibrational transitions are probed, and the anharmonic frequency calculations predict the relevant vibrational transitions to be too weak to be observed. Due to the perturbation, the standard deviation for these states of the corresponding fits are larger than the frequency accuracy of the spectrometer. Despite this, the fits are still sufficiently determined to obtain useful molecular parameters to support their radioastronomic detection. And, indeed, the delivered line lists can be directly compared to astronomical data sets, facilitating the unambiguous identification of these perturbed states.

The results of the quantum-chemical calculations allowed for the assignment of motions for some of the vibrational states. The lowest frequency vibrational state, ν_{30}, corresponds to the C–CN out-of-plane bending motion, and ν_{17} can be assigned to the associated in-plane motion. The ν_{16} and ν_{29} modes concern the symmetric and asymmetric methyl torsional modes, respectively. Finally, the last fundamental mode assigned, ν_{15}, refers to a CC_2 deformation involving a bending motion between the two C–CH_3 bonds. All the other modes observed in this study are combinations of the previously described motions. The (ν_{29} + ν_{17}) and $2\nu_{17}$ modes could not be observed experimentally - they are likely too strongly perturbed because they are involved (with $2\nu_{29}$) in a three-party perturbation.

Note that three of the vibrationally excited states (namely ν_{29}, ν_{17}, and ν_{16}) were also observed in the previous study by Durig et al. (Table 3 of Ref. [110]). By comparing the respective rotational constants, the following correlation can be made: the ν_α, ν_β and ν_γ states from Ref. [110] correspond to the ν_{29}, ν_{17}, and ν_{16} states presented here, respectively. Based on transition intensities, the authors of Ref. [110] ordered their states according to ν_β, ν_α, and ν_γ, which the present findings generally agree with. However, they did not report on the lowest vibrational state, i.e., ν_{30} in Table 4.1.

The authors of Ref. [110] also derived an approximate molecular structure for *i*-propyl cyanide. The length of the C–CN bond is particularly interesting since it is expected to be rather short as a result of the strong electron-withdrawing cyano group. In Ref. [110], the bond length r(C–CN) was determined to be 1.501 Å and the angle between the C-N bond and the CCC plane was estimated to be $\sigma = 53.8°$. In the present work, the rotational spectra of all three singly substituted ^{13}C isotopologues of the vibronic ground state of *i*-propyl cyanide were recorded. These additional sets of rotational constants, which are listed in Appendix 1, allowed for the determination of the substitution structure (r_s) of the carbon backbone using the Kraitchman's equations. This method exploits mono-isotopic substitution information and provides a straightforward way to use the isotopic changes in the moments of inertia to determine the atom coordinates in the principal axis frame.

The determined coordinates for *i*-propyl cyanide are also tabulated in Appendix 1.

Figure 4.3 shows a comparison between the calculated structure of *i*-propyl cyanide (B3LYP/aug-cc-pVTZ) and the experimentally determined r_s structure. As can be seen, the experimental atom positions match those from the calculated structure with small deviations. The substitution structure yields the following structural parameters: r(C–CN) = 1.4600(46) Å, which is 0.04 Å shorter than determined in Ref. [110], and r(C–CH_3) = 1.5359(42) Å. The angle between the C-N bond and the CCC plane was determined to be $\sigma = 51.52(32)°$, which is also smaller than in Ref. [110]. This is in line with the qualitative discussions in Ref. [110] that a shorter C–CN bond results in smaller σ angles. The discrepancy between the structural parameters determined here and those from Ref. [110] might arise from the various assumptions the authors had to adopt for their analysis. Their data only allowed them to produce a partial structure, and they presented parameters that were determined with the aid of *i*-propyl chloride [110]. In the present work, the complete carbon backbone structure is determined solely based on the experimental data.

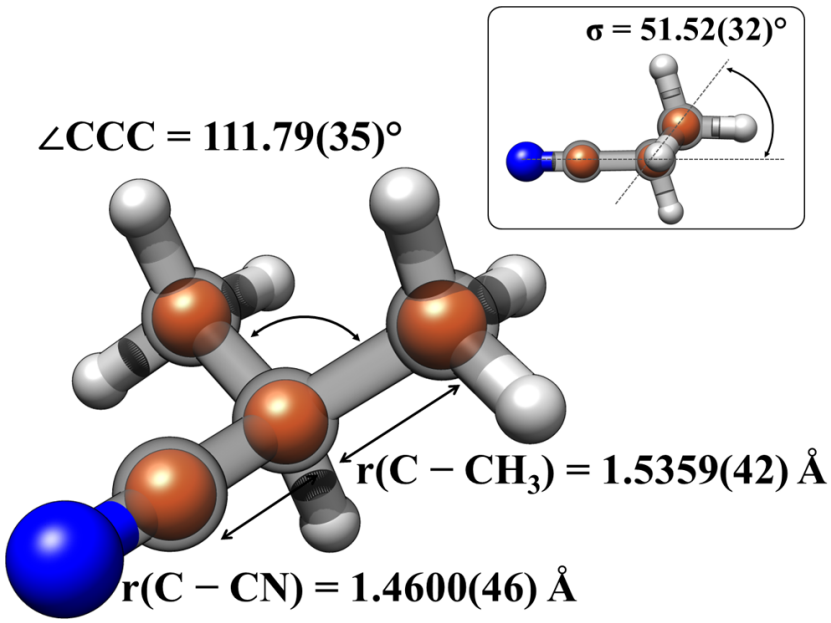

Figure 4.3: Comparison between experimentally determined (r_s) structure and calculated structure (B3LYP/aug-cc-pVTZ) at the equilibrium for *i*-propyl cyanide. The calculated structure is comprised of the transparent gray carbon atoms, while the orange spheres represent the r_s atom positions. Experimental values for selected bond lengths and angles are also given.

The comparison of the C–CN bond length obtained for *i*-propyl cyanide can be extended to other cyanide containing molecules. Keeping in mind that the electron-

Table 4.2: A comparison of the C–CN bond length in a variety of alkyl cyanides. Included in the table, for reference, are average C–C bond lengths for different orbital hybridisation regimes as well as calculated bond lengths (this work, B3LYP/aug-cc-pVTZ level of theory).

Compound	r(C–CN)$_{exp}$ (Å)	r(C–CN)$_{calc}$ (Å)
Methyl cyanide	1.4594(6) [111]	1.455
Ethyl cyanide	1.459(1) [112]	1.460
n-Propyl cyanide	1.4621(43) [113]	1.459
i-Propyl cyanide	1.501 [110]	1.466
i-Propyl cyanide	1.4600(46) (this work)	1.466
n-Butyl cyanide	-	1.459
t-Butyl cyanide	1.46(2) [114]	1.472
Benzonitrile	1.4509(6) [115]	1.430
C(sp^3)–C(sp^3)	1.53 [116]	-
C(sp^3)–C(sp)	1.47 [116]	-

withdrawing cyano group is expected to produce a shortening of that C–CN single bond, Table 4.2 compares the C–CN bond length in *i*-propyl cyanide with analogous, short-chain cyanides as well as with average C–C bond lengths for different orbital hybridisation regimes. The C–CN bond in *i*-propyl cyanide is on the same order of magnitude as an average C(sp^3)–C(sp) bond, being only slightly shorter by 0.01 Å. Indeed, the bond is substantially shorter than a typical C–C single bond (C(sp^3)–C(sp^3)) by 0.07 Å. In addition, the C–CN bond length in *i*-propyl cyanide is in keeping with those of analogous alkyl cyanides – it amounts to 1.46 Å (when errors are considered), regardless of the adjacent alkyl chains. The shortest C–CN bond is the one in benzonitrile, likely due to electronic effects of the aromatic ring giving it some double bond character. The experimental data are compared to computed bond distances at the B3LYP/aug-cc-pVTZ level of theory. The similar bond lengths in the alkyl cyanides and the respective shorter value for benzonitrile are well reproduced by the calculations.

4.4 Astrochemical Implications

The vibrationally excited states of *i*-propyl cyanide were searched for in the Re-exploring Molecular Complexity with ALMA (ReMoCA) survey [117]. This survey has an approximately three times higher angular resolution (approximately 0.5") than the previous Exploring Molecular Complexity with ALMA (EMoCA) survey (approximately 1.6") [118], which has the consequence of allowing smaller regions of the ISM to be probed. This results in lower spectral confusion, owing to the lower velocity dispersion, and this facilitated the detection of urea, $CO(NH_2)_2$, in Sgr B2(N1S), which is slightly offset from the main hot core of Sgr B2(N) [117].

The vibrational states of *i*-propyl cyanide were searched for in Sgr B2 at the N2b position. The Sgr B2(N2b) position is one which is slightly offset from the N2 core, and in this position, the linewidths, and hence the spectral confusion, is substantially reduced.

A number of transitions for the ν_{30}, ν_{29}, ν_{17}, ν_{16}, ν_{15}, $2\nu_{30}$, $\nu_{30}+\nu_{29}$, and $\nu_{30}+\nu_{17}$ vibrational states were detected towards Sgr B2(N2b). These vibrational states have been detected in the ISM for the first time. The overlays in Figures 4.4-4.14 show these detected transitions in the observational data set [119]. In all of the figures, the black trace is the observed spectrum, the red trace is the spectrum simulated from the rotational constants of the vibrational states, and the blue trace is the synthetic spectrum of the region, which is built up from the emission from all molecules already detected. All of these spectra assume local thermodynamic equilibrium (LTE) conditions. The dashed line contained in each panel signifies the 3σ noise level. The x-axes are the frequency axes, where the central frequency and the frequency range is indicated (in MHz), and the y-axes show the intensity as brightness temperature T_B (in K).

The unambiguously detected transitions are identified in Figures 4.4-4.14 with green stars. This is an indication that the line in the observational data set is above the 3σ noise level, and that it is not significantly blended with another line. Some panels for the ν_{29} state are labelled with a red triangle. This indicates a 'missing' transition; a transition which is not detected in the observational data set, but given the presence of other lines, is expected to be present. More work to investigate the reasons behind this phenomenon is ongoing, but it could be related to the fact that the ν_{29} state is perturbed. The other panels show transitions that are detected, showing the consistency of the LTE model with the observation, but whose line profiles are blended with emissions from other molecules.

The line intensities of the vibrational states are well reproduced in the LTE regime, and the states are consistent with a Boltzmann distribution at 150 K under LTE conditions. In total, nine transitions of the ν_{30} state, four transitions of the ν_{29} state, six transitions of the ν_{17} state, and three transitions of the ν_{16} state are

securely detected (see Table 4.3). This discovery has increased the degree to which the Sgr B2(N2b) region can be chemically characterised. The transitions can now be excluded from consideration when attempting to detect new molecular species in the same observational data set. Their presence reiterates the importance of vibrationally excited states of detected molecules in the ISM.

Table 4.3: Spectroscopic parameters and integrated intensities of rotational transitions of *i*-propyl cyanide in its vibrationally excited states detected toward Sgr B2(N2b) in the ReMoCA survey [119]. These unambiguously detected frequencies are indicated in Figures 4.4-4.14 with a green star.

State	Transition	Frequency	Δf [a]	A_{ul} [b]	E_u [c]	g_u [d]	I_{obs} [e]	I_{mod} [f]	I_{all} [g]
	J_{K_a,K_c}	(MHz)	(kHz)	(10^{-5} s^{-1})	(K)		(K km s^{-1})	(K km s^{-1})	
ν_{30}	$13_{2,11} - 12_{2,10}$	87615.609	40	5.65	315.2	27	9.2(9)	5.5	5.7
ν_{30}	$14_{1,13} - 13_{1,12}$	88205.086	40	5.95	317.1	29	5.8(10)	6.5	6.9
ν_{30}	$14_{2,12} - 13_{2,11}$	93200.766	40	6.85	319.7	29	13.2(10)	7.8	6.0
ν_{30}	$16_{2,15} - 15_{2,14}$	99776.391	40	8.70	326.4	33	19.8(21)	16.9	25.7
ν_{30}	$16_{1,15} - 15_{1,14}$	99781.266	40	8.70	326.4	33	18.8(21)	17.0	22.4
ν_{30}	$17_{0,17} - 16_{0,16}$	100910.008	40	9.27	327.9	35	42.1(21)	36.2	40.9
ν_{30}	$17_{1,17} - 16_{1,16}$	100910.008	40	9.27	327.9	35	–	–	–
ν_{30}	$14_{5,9} - 13_{5,8}$	102741.578	40	8.67	324.6	29	9.8(6)	7.6	7.6
ν_{30}	$14_{4,10} - 13_{4,9}$	103739.234	40	9.38	323.3	29	11.9(9)	9.5	13.9
ν_{29}	$14_{2,12} - 13_{2,11}$	93153.549	11	6.84	348.0	29	10.4(9)	6.2	6.4
ν_{29}	$14_{4,11} - 13_{4,10}$	96593.994	11	7.42	350.3	29	8.8(6)	8.7	10.0
ν_{29}	$17_{1,17} - 16_{1,16}$	100849.213	51	9.25	356.2	35	25.1(21)	30.4	32.6
ν_{29}	$17_{1,17} - 16_{1,16}$	100849.213	51	9.25	356.2	35	–	–	–
ν_{17}	$14_{2,12} - 13_{2,11}$	93417.257	9	6.90	351.3	29	3.9(8)	6.2	6.4
ν_{17}	$17_{2,16} - 16_{2,15}$	105758.815	15	10.40	363.1	35	9.7(10)	9.7	12.1
ν_{17}	$17_{1,16} - 16_{1,15}$	105761.575	15	10.40	363.1	35	–	–	–
ν_{17}	$16_{3,13} - 15_{3,12}$	110392.411	18	11.30	363.7	33	17.2(6)	11.8	19.0
ν_{17}	$19_{1,19} - 18_{1,18}$	112696.100	35	13.00	370.0	39	49.8(31)	37.0	45.2
ν_{17}	$19_{0,19} - 18_{0,18}$	112696.108	35	13.00	370.0	39	–	–	–
ν_{16}	$15_{1,15} - 14_{1,14}$	89395.075	5	6.40	440.4	31	5.6(11)	6.7	6.8
ν_{16}	$15_{0,15} - 14_{0,14}$	89395.325	5	6.40	440.4	31	–	–	–
ν_{16}	$17_{2,16} - 16_{2,15}$	105648.523	9	10.40	453.4	35	7.0(9)	4.9	5.5

(a)Frequency uncertainty. (b)Einstein coefficient for spontaneous emission. (c)Upper-level energy. (d)Upper-level degeneracy. (e)Integrated intensity of the observed spectrum in brightness temperature scale. The statistical standard deviation is given in parentheses in unit of the last digit. (f)Integrated intensity of the synthetic spectrum of *i*-C_3H_7CN. (g)Integrated intensity of the model that contains the contribution of all identified molecules, including *i*-C_3H_7CN. In the last three columns, a value followed by dashes in the following lines represents the intensity integrated over a group of transitions that are not resolved in the astronomical spectrum.

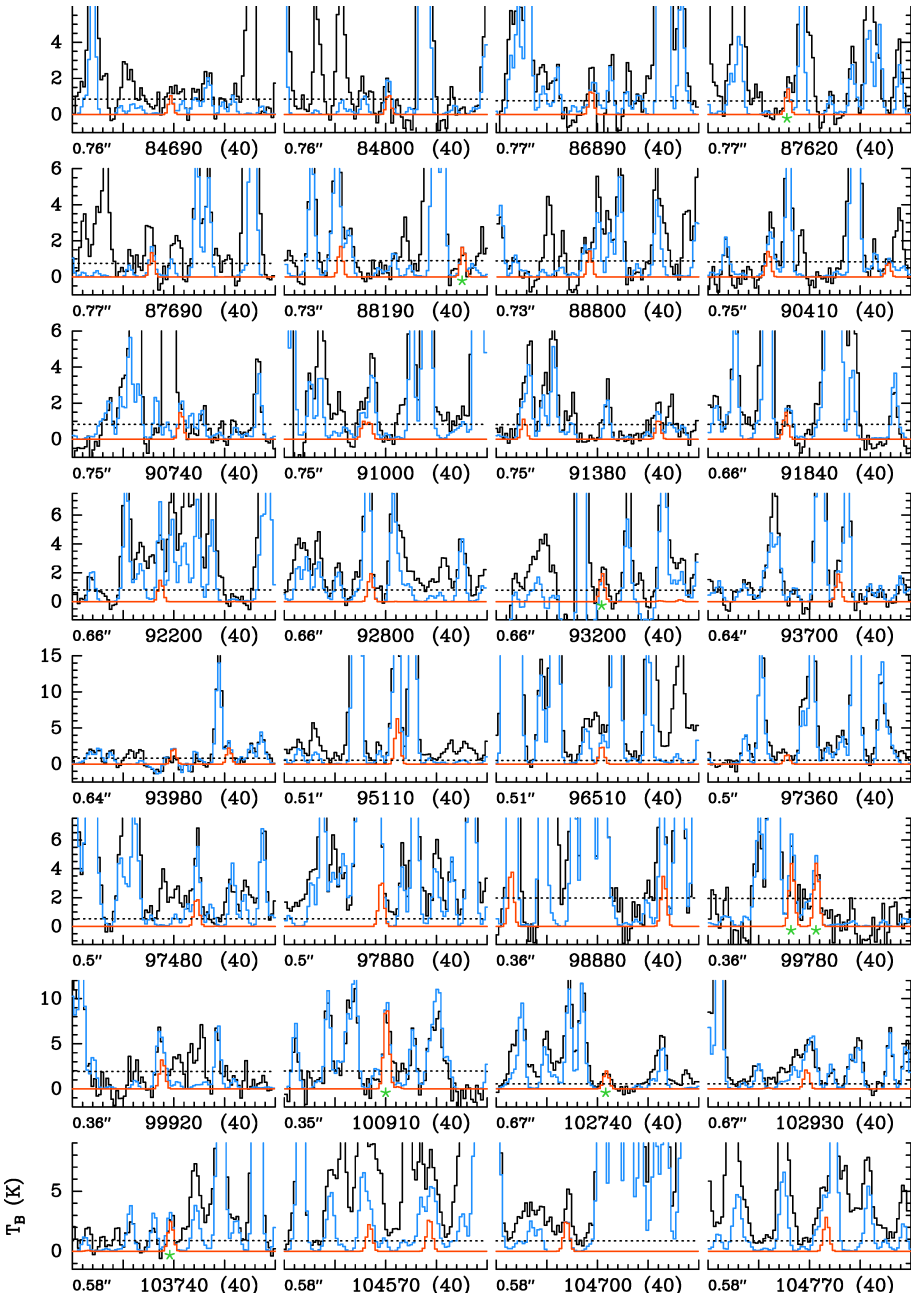

Figure 4.4: Each panel shows the ALMA spectrum of Sgr B2(N2b) in black, the synthetic model that contains all species identified so far in blue, and the synthetic model for the ν_{30} state of *i*-propyl cyanide in red. The dotted line indicates the 3σ noise level. The green stars indicate unambiguously detected transitions (see text for criteria).

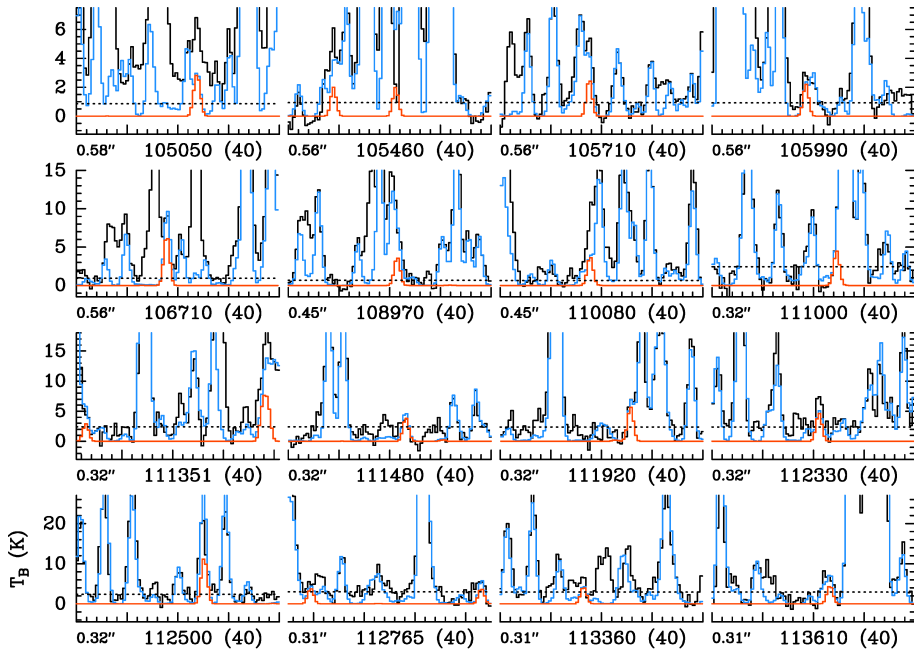

Figure 4.5: Each panel shows the ALMA spectrum of Sgr B2(N2b) in black, the synthetic model that contains all species identified so far in blue, and the synthetic model for the ν_{30} state of *i*-propyl cyanide in red. The dotted line indicates the 3σ noise level.

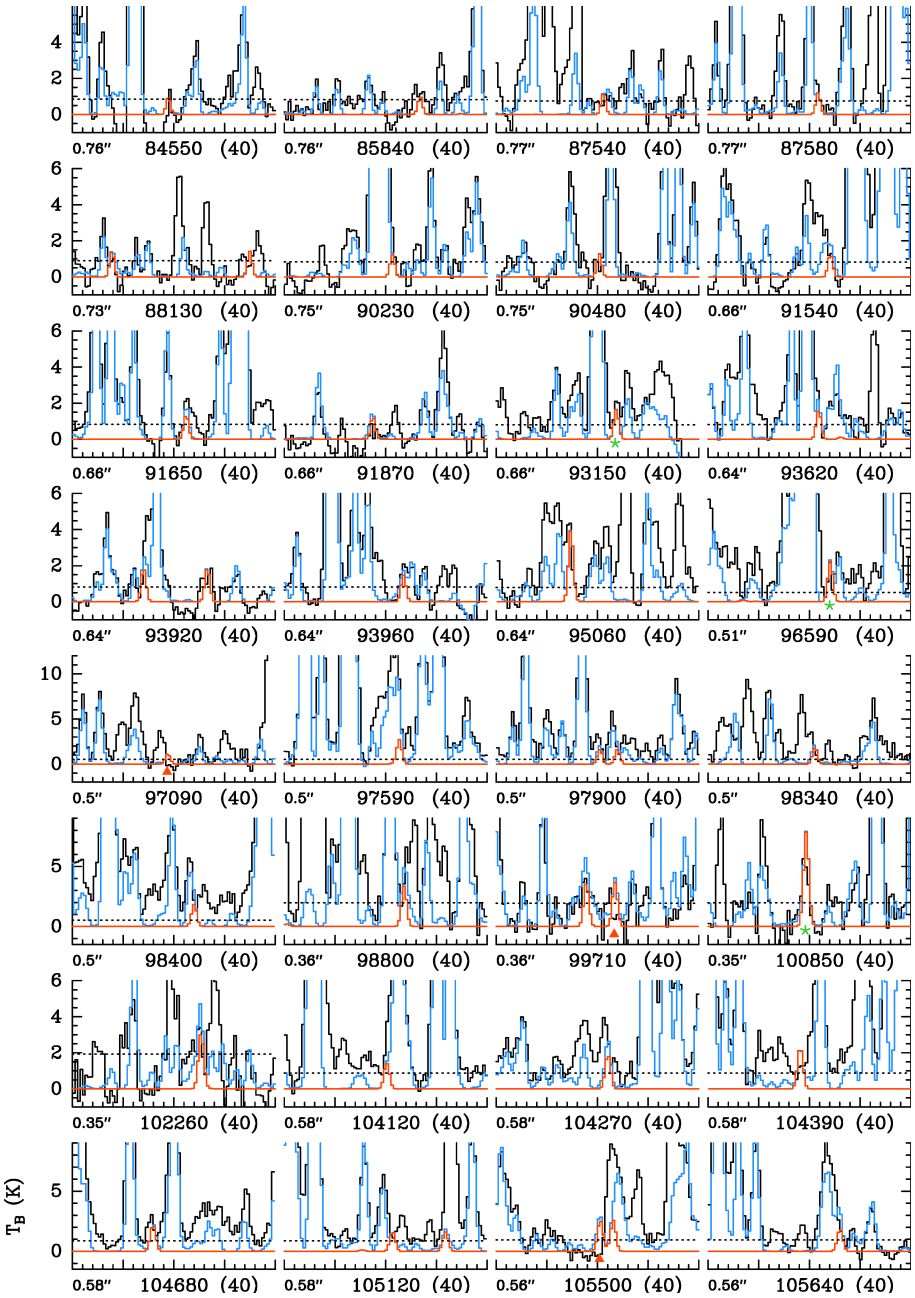

Figure 4.6: Each panel shows the ALMA spectrum of Sgr B2(N2b) in black, the synthetic model that contains all species identified so far in blue, and the synthetic model for the ν_{29} state of *i*-propyl cyanide in red. The dotted line indicates the 3σ noise level. The green stars indicate unambiguously detected transitions, and the red triangles indicate 'missing' transitions (see text for criteria).

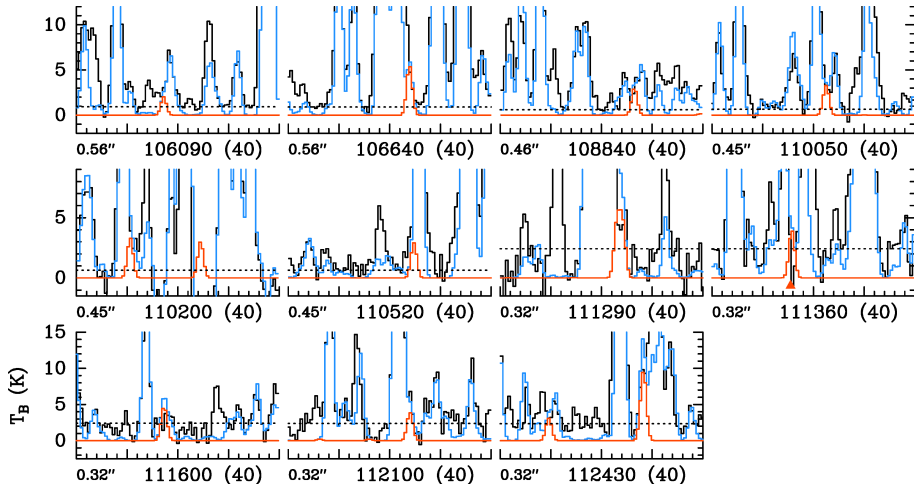

Figure 4.7: Each panel shows the ALMA spectrum of Sgr B2(N2b) in black, the synthetic model that contains all species identified so far in blue, and the synthetic model for the ν_{29} state of *i*-propyl cyanide in red. The dotted line indicates the 3σ noise level. The red triangles indicate 'missing' transitions (see text for criteria).

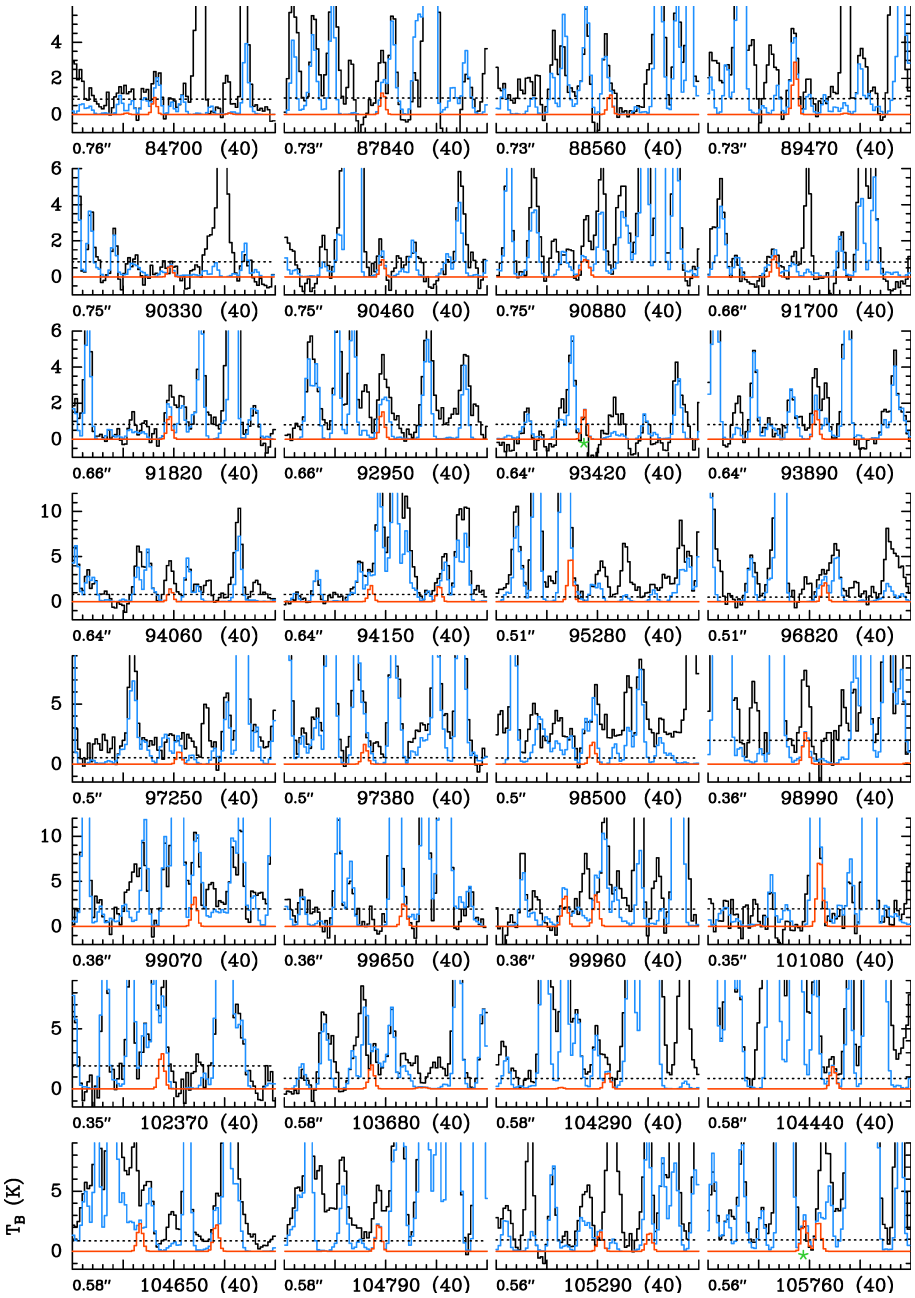

Figure 4.8: Each panel shows the ALMA spectrum of Sgr B2(N2b) in black, the synthetic model that contains all species identified so far in blue, and the synthetic model for the ν_{17} state of *i*-propyl cyanide in red. The dotted line indicates the 3σ noise level. The green stars indicate unambiguously detected transitions (see text for criteria).

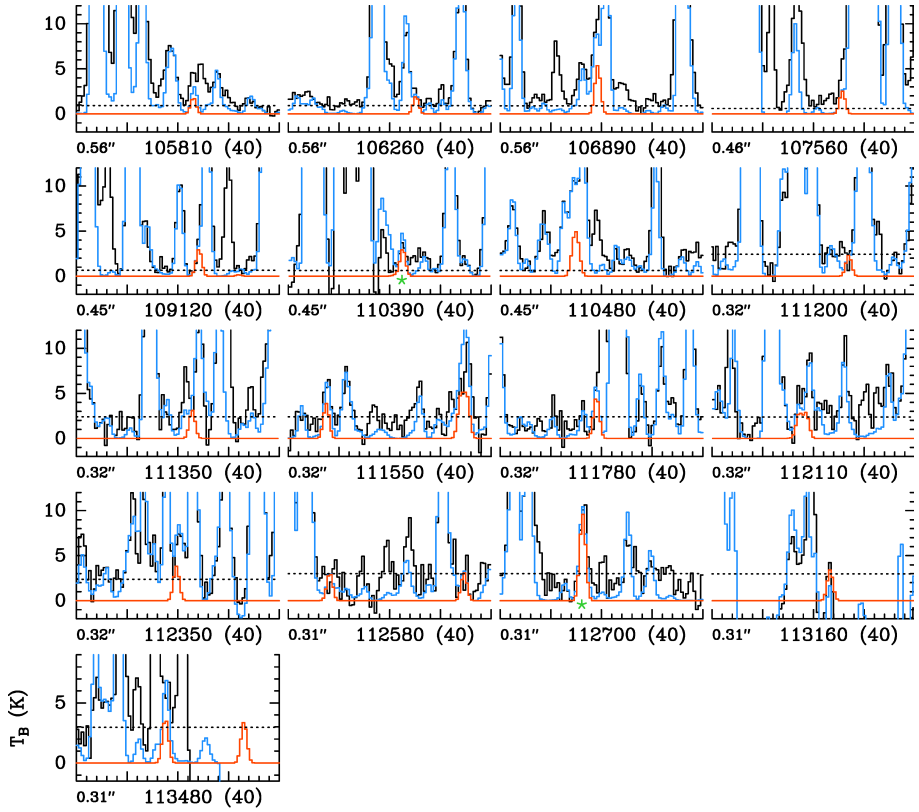

Figure 4.9: Each panel shows the ALMA spectrum of Sgr B2(N2b) in black, the synthetic model that contains all species identified so far in blue, and the synthetic model for the ν_{17} state of *i*-propyl cyanide in red. The dotted line indicates the 3σ noise level. The green stars indicate unambiguously detected transitions (see text for criteria).

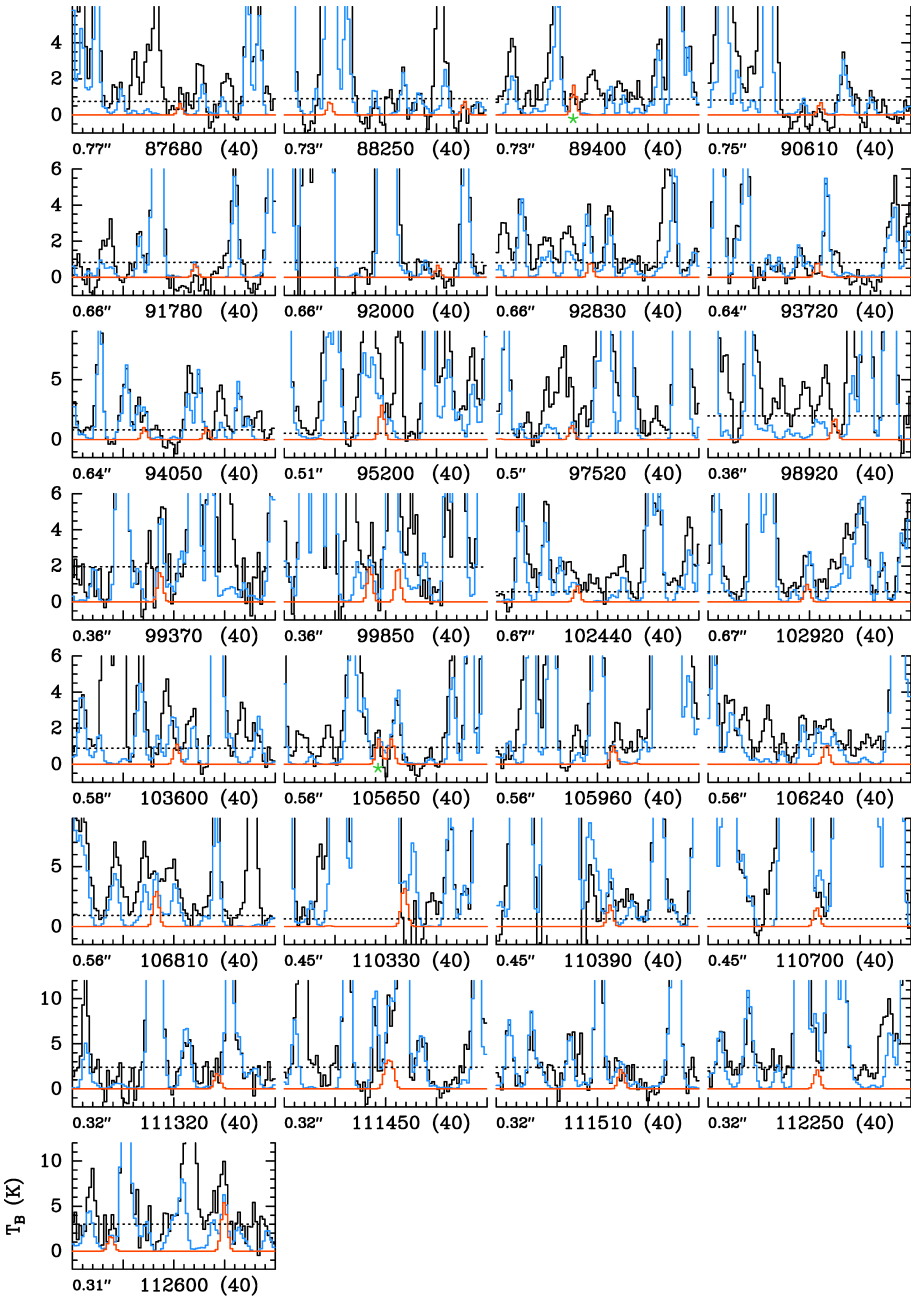

Figure 4.10: Each panel shows the ALMA spectrum of Sgr B2(N2b) in black, the synthetic model that contains all species identified so far in blue, and the synthetic model for the ν_{16} state of *i*-propyl cyanide in red. The dotted line indicates the 3σ noise level. The green stars indicate unambiguously detected transitions (see text for criteria).

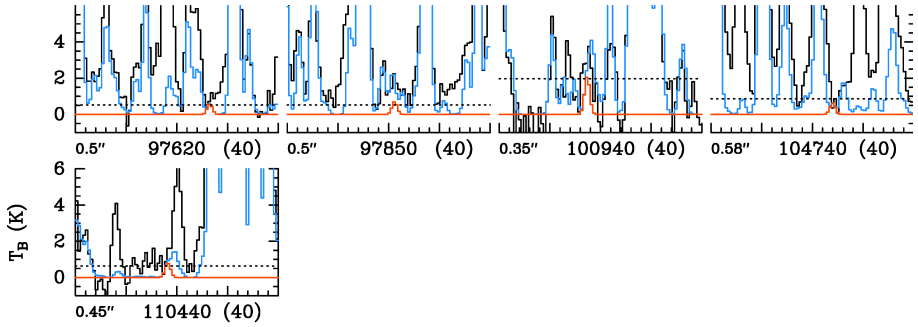

Figure 4.11: Each panel shows the ALMA spectrum of Sgr B2(N2b) in black, the synthetic model that contains all species identified so far in blue, and the synthetic model for the ν_{15} state of *i*-propyl cyanide in red. The dotted line indicates the 3σ noise level.

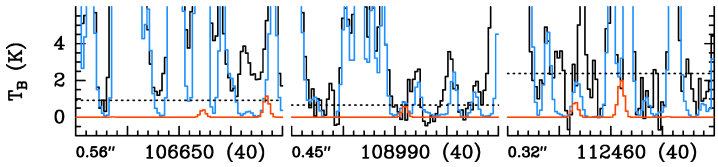

Figure 4.12: Each panel shows the ALMA spectrum of Sgr B2(N2b) in black, the synthetic model that contains all species identified so far in blue, and the synthetic model for the $2\nu_{30}$ state of *i*-propyl cyanide in red. The dotted line indicates the 3σ noise level.

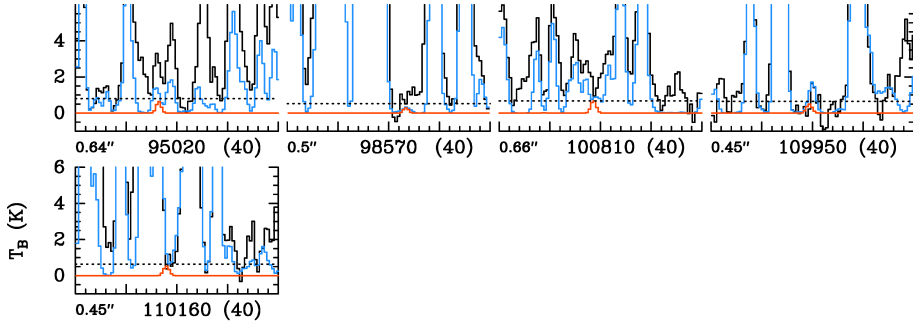

Figure 4.13: Each panel shows the ALMA spectrum of Sgr B2(N2b) in black, the synthetic model that contains all species identified so far in blue, and the synthetic model for the $\nu_{30}+\nu_{29}$ state of *i*-propyl cyanide in red. The dotted line indicates the 3σ noise level.

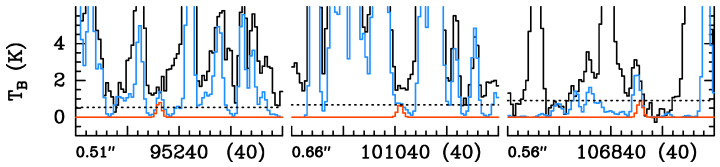

Figure 4.14: Each panel shows the ALMA spectrum of Sgr B2(N2b) in black, the synthetic model that contains all species identified so far in blue, and the synthetic model for the ν_{30}+ν_{17} state of *i*-propyl cyanide in red. The dotted line indicates the 3σ noise level.

4.5 Conclusions

High-resolution chirped-pulse Fourier transform rotational spectroscopy between 75–110 GHz was performed on *i*-propyl cyanide, a branched molecule of astronomical interest. Because of the high resolution and sensitivity of the spectrometer employed, the identification and characterisation of ten vibrationally excited states up to 500 cm^{-1} could be achieved. Further, the rotational signatures of the three singly substituted ^{13}C isotopologues of the vibronic ground state in the millimeter-wave frequency range were recorded. Spectral information for the isotopologues allowed for the carbon backbone structure of *i*-propyl cyanide to be determined and to be compared with similar molecules and previous studies.

This rather complete data set supported astronomical searches for the vibrational states of *i*-propyl cyanide in the ReMoCA survey. A number of frequencies were unambiguously detected towards Sgr B2(N2b), which is a position slightly offset from the Sgr B2(N2) core. The intensities of the vibrational states are well modelled by considering LTE conditions. The confirmed presence of these states in the observational data sets increases the degree to which the Sgr B2(N2b) region is characterised, and these first-time detections reiterate the importance of vibrationally excited states in interstellar space.

Chapter 5

A Global Study of the Conformers of 1,2-Propanediol and New Vibrationally Excited States

This chapter is based on the following publication:

- B. E. Arenas, S. Gruet, A. L. Steber, M. Schnell *A global study of the conformers of 1,2-propanediol and new vibrationally excited states*, Journal of Molecular Spectroscopy **337**, 9-16 (2017).

5.1 Introduction

The molecules that comprise the family of alcohols are of general interest to the astrochemistry community due to the importance of terrestrial oxygen chemistry. Oxygen-containing compounds are typically precursors to prebiotic molecules, and through a series of reactions, they can be incorporated into larger complex organic molecules (COMs) that are important for sustaining life, such as amino acids and nucleobases. The alcohols are an extensive family of molecules that have been studied in an astrochemical context; methanol, ethanol, and vinyl alcohol have already been detected in the ISM [5, 120–122]. The concept that smaller organic molecules can undergo reactions to form more biologically relevant COMs can be applied to interstellar environments, and reactions that explain the constituents of particular environments can be outlined. However, in many cases, the proposed reactions fail to account for the presence of particular species that have been observed in that environment. It can also be that one of the proposed reactants/products has yet to be detected - this is the case for 1,2-propanediol, $C_3H_8O_2$. This molecule could evolve into larger prebiotic molecules. Further, it is a chiral molecule, and chiral molecules

have an important role in terrestrial life. The homochirality of biomolecules in all living organisms is even referred to as a 'signature of life' [123].

Previously, 1,2-propanediol has been searched for, but it has yet to be detected in any interstellar environment. Based on the column density predicted by their calculations, Lovas *et al.* explained that instrumentation with increased sensitivity would be required to observe 1,2-propanediol [124]. Ref. [124] was published in 2009, and over a decade later, with the increased broadband capability, sensitivity, and resolution of facilities such as the Atacama Large Millimeter/submillimeter Array (ALMA), new laboratory and observational work is warranted. The laboratory work required to prepare for such an observational campaign is presented here.

The plausibility of 1,2-propanediol being present in interstellar environments comes from the fact that one of its possible precursors, 1,2-ethanediol, has already been detected in the molecular core Sagittarius B2(N-LMH) [125]. The ethane analogue (also known as ethylene glycol, $HOCH_2CH_2OH$) could react with the methyl radical, among others, to form 1,2-propanediol. The presence of 1,2-propanediol in this region would then allow for the consideration of reactions with other smaller abundant molecules present in such an environment. This, in turn, could result in the formation of important and complex hydroxyl-containing species, such as glycerol, lactic acid, and pyruvic acid.

Because of the biological and astrochemical importance of this molecule, it has already been studied extensively in the laboratory using rotational spectroscopy in the gas phase. The molecule is conformationally rich - the computational study by Vázquez *et al.* considered 23 conformations and even state that their conformation selection was limited [126]. The conformer-specificity of rotational spectroscopy makes it an ideal technique for studying 1,2-propanediol. Low frequency data from 6-40 GHz has been reported across a number of publications in which up to seven conformers were assigned [124, 127, 128]. Higher frequency data was added by Bossa *et al.*, who reported assignments in the ranges 38-70, 200-230, and 297-400 GHz for the three lowest energy conformers [129]. Alongside the preparation of this work, further analysis of conformers 4-6 was being performed by Zakharenko *et al.*, which provided refined fits for these conformers in the same frequency regions as Bossa *et al.* [130].

The nomenclature used to differentiate between and identify the different possible conformers of 1,2-propanediol is taken directly from the computational study by Vázquez *et al.*, and it consists of a three letter code which indicates the conditions of three dihedral angles. The atomic numbering scheme, using the lowest energy conformer of 1,2-propanediol as a model, is shown in Figure 5.1. The first (lower case) letter refers to the C4-C3-O2-H1 dihedral angle, the second (upper case) letter refers to the O5-C4-C3-O2 dihedral angle, and the third (lower case) letter refers to the H6-O5-C4-C3 dihedral angle. The letter t/T indicates a *trans* conformation, a

g/G indicates a +*gauche* conformation, and a g'/G' indicates a -*gauche* conformation [126]. The three letter code for the lowest energy conformer shown in Figure 5.1 is tG'g. The various names given to the conformers of 1,2-propanediol over previous publications are summarised in Table 5.1 to allow for easy comparison.

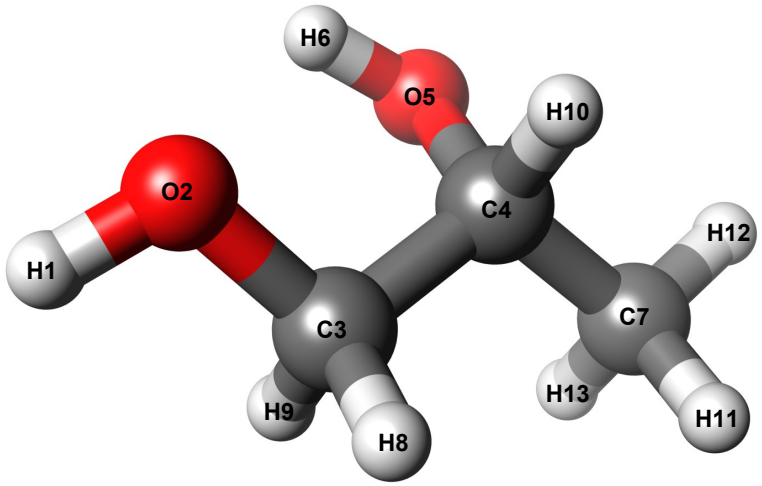

Figure 5.1: The equilibrium structure, optimised at the MP2/aug-cc-pVTZ level of theory, of the lowest energy conformer of 1,2-propanediol (tG'g) with atom labels. The labels are defined to be in keeping with Vázquez *et al.* [126].

In the initial assessment of 1,2-propanediol in 1981, three vibrationally excited states of the second lowest energy conformer, gG't, were assigned [127]. The centrifugal distortion constants of these vibrationally excited states were fixed to those of the ground state. Since this first study from the early 1980s, vibrationally excited states have not been a point of interest.

The aim of the work in this chapter is to provide refined global rotational constants for the first six vibronic ground state conformers of 1,2-propanediol. These fits encompass all previously reported transitions and the results of the new investigation in the 75-110 GHz region, which was performed in the framework of this thesis. Further, rotational constants for newly observed vibrationally excited states are reported. The data presented, particularly the new experimental line lists of the vibrationally excited states, can be used to search for these species in the ISM, especially as the frequency range of the W-band spectrometer overlaps with the Band 3 regime of ALMA (86-114 GHz).

5.2 Experimental and Theoretical Details

The rotational spectrum of 1,2-propanediol was acquired from 75-110 GHz with the segmented chirped-pulse Fourier transform millimeter-wave spectrometer described in Chapter 3. The spectrum shown here was measured using the High Dynamic Range (HDR) mode and utilised 500 ns long excitation pulses. The free induction decays (FIDs) were collected for 4 μs each. The full width at half maximum was approximately 550 kHz. A total of 500,000 FIDs were acquired and co-added, totalling a measurement time of approximately 50 minutes to cover the whole 75-110 GHz frequency range.

The 1,2-propanediol sample was purchased from Sigma Aldrich (>99.5 % chemical purity), and it was used without any further purification. The liquid sample was heated to 45 °C in a reservoir external to the vacuum chamber to produce sufficient vapour pressure. A pressure of about 6 μbar was maintained in flow conditions in the room temperature chamber during data acquisition.

The initial assignment of the ground state conformers was based on the experimental rotational constants reported in Ref. [124]. Quantum-chemical calculations performed with the Gaussian 09 package [73] were used to predict the rotational constants of the vibrationally excited states - structure optimisation and anharmonic frequency calculations were performed at the MP2/aug-cc-pVTZ level of theory. The optimised structures are depicted in Figure 5.2. After obtaining the fit of the ground states, the frequency calculations were used to obtain the theoretical rotational constants of the vibrational states. These were shifted by the same difference that was observed between the calculated and experimental rotational constants for the respective ground state conformers in order to support the assignment process. The energy diagram of the conformers and selected vibrational states is also shown in Figure 5.2.

Spectral assignment was performed with the AABS software package [71, 90], and the data were fit using Pickett's SPFIT/SPCAT [63]. The values of Ray's asymmetry parameter indicated the conformers are all asymmetric near-prolate tops ($\kappa = -0.51$ to $\kappa = -0.71$), hence data were fit to a Watson's A-reduction Hamiltonian in an I^r representation. Note that the studies by Bossa *et al.* and Zakharenko *et al.* differed from the other reports in that Watson's S-reduction was used [129, 130].

5.3 Results and Discussion

Using previous studies as a guide, six ground state conformers were assigned in the spectrum between 75-110 GHz. The structures of these six conformers are shown in Figure 5.2. The carbon backbone is the same in conformers 1 (tG'g), 2 (gG't), 3 (g'G'g), and 5 (gG'g'). These structures differ only in the relative orientations

Table 5.1: A comparison of the names given to the various conformers of 1,2-propanediol.

Caminati [127]	Vásquez *et al.* [126]	Lockley *et al.* [128]	Lovas *et al.* [124]	Bossa *et al.* [129]	Zakharenko *et al.* [130]	This work
-	tG'g	m-ga-c	3, tG'g	aG'g	-	1, tG'g
T-form	gG't	o-ga-α	2, gG't	gG'a	-	2, gG't
-	g'G'g	m-ga-β	5, g'G'g	g'G'g	-	3, g'G'g
G-form	g'Gt	o-gg-β	1, g'Gt	-	g'Ga	4, g'Gt
-	gG'g'	-	6, gG'g'	-	gG'g'	5, gG'g'
-	tGg'	-	4, tGg'	-	aGg'	6, tGg'
-	g'Gg	-	7, g'Gg	-	g'Gg	-

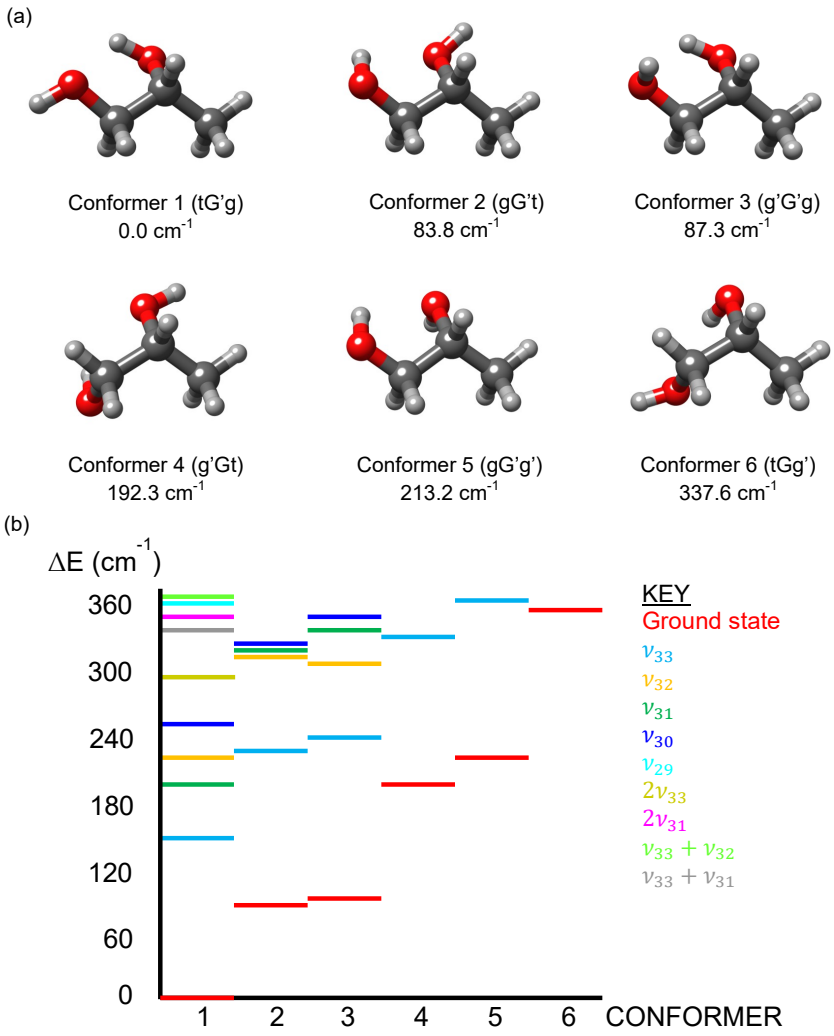

Figure 5.2: (a) The structures of six vibronic ground state conformers of 1,2-propanediol optimised at the MP2/aug-cc-pVTZ level of theory, and their energies, in cm^{-1}, with respect to the lowest energy conformer. (b) Diagram illustrating the energies of the conformers and selected vibrationally excited states up to 360 cm^{-1}. The energy values were determined with anharmonic frequency calculations at the MP2/aug-cc-pVTZ level of theory.

of the hydrogen atoms in the hydroxyl groups; the O5-C4-C3-O2 dihedral angle is the same. These lower energy conformers are stabilised by intramolecular hydrogen bonds. Conformers 4 (g'Gt) and 6 (tGg') have similar backbones to each other. Their backbone differs from the other backbone structure by the position of the terminal hydroxyl group. This different position relates to a different O5-C4-C3-O2 dihedral angle. Again, the conformers differ from each other only by the relative orientations of the hydroxyl hydrogen atoms. The relative energies of the conformers, calculated at the MP2/aug-cc-pVTZ level of theory, can be seen in Figure 5.2. These six ground state conformers have been previously observed in the microwave region; all six were studied in Ref. [124], and two, one, three, and three of the six conformers were studied, respectively, in Refs. [127], [128], [129], and [130].

The recorded spectrum, shown in Figure 5.3, has approximately 6,500 lines with a minimum signal-to-noise ratio (SNR) of 3:1, though there are many more lines with a SNR lower than 3:1. The total number of assigned lines in the spectrum was 1,350. The remaining lines most likely arise from high energy vibrational states and higher energy conformers. The highest SNR of 80:1 was observed for the conformer second highest in energy, gG't, which has a larger dipole moment than the lowest energy conformer. The lowest SNR of approximately 5:1 was observed for the highest energy conformer, tGg'. This can be seen in Figure 5.3. In previous studies, no effect of methyl rotation was observed on the spectrum [15]. This was also the case here, and it is consistent with a calculated barrier of 13.1 kJ mol^{-1} at the MP2/6-311++G(d,p) level of theory.

Between 68 and 307 distinct transitions could be assigned for the six lowest energy conformers in their vibronic ground states in the W-band frequency range. The transitions observed in the spectrum were combined with the transitions reported by Zakharenko *et al.* [130], Bossa *et al.* [129], Lovas *et al.* [124], Lockley *et al.* [128], and Caminati [127]. The global rotational constants of the six observed conformers are shown in Table 5.2. Two microwave root mean square (mw RMS) values are included in Table 5.2 - the global RMS and the W-band transition RMS. The W-band RMS was obtained by first fitting global rotational constants with all the available transitions, then fitting the W-band transitions to the fixed global constants in order to check the validity of the assigned W-band transitions.

The lowest three energy conformers (tG'g, gG't, and g'G'g) were fit with centrifugal distortion constants up to the octic level because the high J and K_a values (up to $J = 71$, $K_a = 45$) obtained by Bossa *et al.* [129] warranted the use of these higher order constants. The remaining conformers were initially fit using only the quartic centrifugal distortion constants, as the additional transitions used for the global fit were all low frequency transitions. Later, the high frequency data reported by Zakharenko *et al.* was incorporated, which allowed for the same extensive analysis to be performed on the higher three energy conformers (g'Gt, gG'g', and

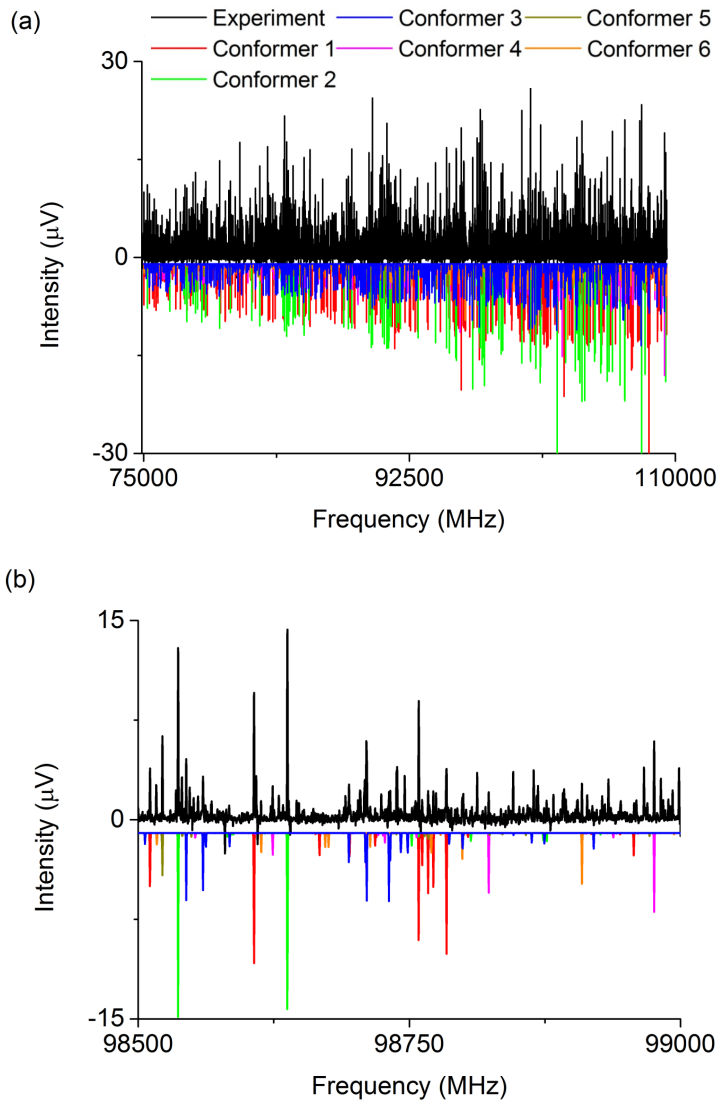

Figure 5.3: (a) The broadband rotational spectrum of 1,2-propanediol in the W-band region. The experimental trace is black, and the simulated spectra of the experimentally fitted rotational constants are in colour. A total of 831 distinct transitions were assigned for the vibronic ground state conformers - the breakdown of number of assigned lines per conformer is tabulated in Table 5.2. (b) A zoom-in of the broadband spectrum showing assignments of the six conformers.

tGg') as was performed for the lower three energy conformers.

The fits agree well with the previously published rotational constants, and the values of the W-band RMS for each conformer show that the W-band transitions fit well into the sets of global rotational constants. All of the ground state conformers have been studied across a large frequency range and hence have transitions with a large range of J values. The J_{max} included in the analysis performed by Bossa *et al.* [129] was $J_{max} = 71$, and the value from the analysis conducted by Zakharenko *et al.* [130] was $J_{max} = 59$. The global fits presented here encompass all experimental transitions assigned for the six lowest energy conformers of 1,2-propenadiol.

Full comparisons of the determined global rotational constants and those reported by Lovas *et al.* [124], Bossa *et al.* [129], and Zakharenko *et al.* [130] for the ground state conformers are tabulated in Tables 5.3 and 5.4. There is a difference in the values for the rotational constants between the A-reduction and the previously published S-reduction, particularly for $\delta_K[d_2]$, $\phi_{JK}[h_2]$, and $\phi_K[h_3]$. The differences can be attributed solely to using the different reductions. As was described by Kisiel and Pszczółkowski in 1997, changing between reductions can substantially alter the values of distortion constants without affecting the quality of the overall fit [131]. Upon fitting the global data with the S-reduction, performed to confirm the validity of the present global fit across both reductions, it is found that the aforementioned rotational constants agree well with those reported by Bossa *et al.* [129] and Zakharenko *et al.* [130]; see Table 5.5 for a comparison of the fit of conformer 1, tG'g between the two reductions.

The rotational constants of the observed vibrationally excited states of 1,2-propanediol are summarised in Table 5.6, and they are presented alongside the predicted rotational constants from the anharmonic frequency calculations. Figure 5.4 shows the assigned states in the W-band spectrum plotted with their respective ground state assignments. Analysis yielded assignments of two vibrational states of the lowest energy conformer, tG'g, and one vibrational state of the conformer second highest in energy, gG't. These states are denoted as $\nu_{33}(1)$, $\nu_{32}(1)$, and $\nu_{33}(2)$ where the notation takes the form ν_{mode}(conformer). There was some evidence of a third vibrational state of conformer 1, $\nu_{31}(1)$, and two vibrational states of conformer 2, $\nu_{32}(2)$ and $\nu_{31}(2)$, being present, but they were subject to a perturbation that did not allow for full assignment of these species in the spectrum. There is currently not a large enough data set to treat these perturbed states; further work should allow for this perturbation to be characterised. It is also worthy to note here that the labelling of the vibrational states follows the harmonic energy order - anharmonic corrections causes the $\nu_{32}(1)$ and $\nu_{31}(1)$ states to reverse in energy order.

The calculations yielding the rotational constants allow the assignment of specific vibrational motions to the fundamental modes that were observed. The motion of the first vibrationally excited state of conformer tG'g, $\nu_{33}(1)$, is calculated to be

Table 5.2: The global rotational constants of six conformers of 1,2-propanediol. Two mw RMS values are tabulated. The first is the global mw RMS, and the second is the mw RMS of the W-band transitions. The experimental dipole moments (shown in italics) from Lovas *et al.* are reported [124]. The remaining dipole moments are taken from the structure optimisation calculations performed at the MP2/aug-cc-pVTZ level of theory.

	Conformer 1	Conformer 2	Conformer 3	Conformer 4	Conformer 5	Conformer 6
	tG'g	gG't	g'G'g	g'Gt	gG'g'	tGg'
ΔE /cm^{-1}	0.0	83.8	87.3	192.3	213.2	337.6
A /MHz	8572.056757(89)	8393.40052(19)	8536.77122(10)	6642.44779(17)	8327.59369(34)	6634.76143(25)
B /MHz	3640.106085(30)	3648.565503(44)	3604.198352(50)	4163.594484(66)	3641.99965(12)	4160.63319(11)
C /MHz	2790.966689(30)	2778.296552(43)	2778.331494(51)	3365.363518(59)	2776.903906(95)	3377.907502(92)
Δ_J /kHz	0.736926(15)	0.782561(21)	0.737825(22)	1.777210(37)	0.787937(80)	1.726054(77)
Δ_{JK} /kHz	5.33332(12)	4.59878(20)	5.38677(18)	6.37322(15)	4.54331(75)	8.35543(63)
Δ_K /kHz	2.49067(15)	2.9998(29)	2.46290(29)	-4.75173(50)	2.6139(18)	-6.7370(20)
δ_J /kHz	0.1630055(28)	0.1826860(40)	0.1570564(52)	0.252414(18)	0.179665(38)	0.236086(42)
δ_K /kHz	3.16441(21)	2.93491(49)	3.11024(34)	1.56639(28)	2.8352(10)	2.18140(73)
Φ_J /Hz	-0.0000278(27)	-0.0000285(31)	-0.0000324(36)	0.0000666(79)	0.000305(25)	-0.000387(24)
Φ_{JK} /Hz	-0.007155(61)	-0.00905(12)	-0.00775(17)	0.02274(11)	-0.00482(83)	-0.02212(53)
Φ_{KJ} /Hz	-0.06019(25)	-0.04311(40)	-0.05801(53)	0.07720(40)	-0.0546(30)	0.0762(22)
Φ_K /Hz	0.08057(18)	-	0.08052(40)	0.04881(47)	0.0772(35)	-
ϕ_J /Hz	-	-	-	0.0001578(42)	0.000178(13)	-0.000004(13)
ϕ_{JK} /Hz	-0.003074(49)	-0.004247(74)	-0.003494(96)	0.005159(71)	0.00206(31)	0.00868(30)
ϕ_K /Hz	0.01995(54)	0.01166(94)	0.0155(12)	0.05824(52)	0.0694(62)	0.0952(21)
L_{JK} /mHz	-0.000262(25)	-0.000471(31)	-	-	-	-
No. lines $_{global}$	1479	1026	917	1043	563	507
mw RMS $_{global}$ /kHz	21.3	20.8	27.0	27.3	37.1	37.3
No. lines $_{W-band}$	307	100	200	83	73	68
mw RMS $_{W-band}$/ kHz	22.0	16.2	36.1	32.0	38.1	35.7
κ	-0.71	-0.69	-0.71	-0.51	-0.69	-0.52
μ_a /D	*1.20**	*2.50**	0.41	*2.20**	2.26*	2.00*
μ_b /D	*1.92**	*0.31*	1.87*	*0.00*	0.70	1.01
μ_c /D	*0.37*	*0.45*	1.52	*0.62*	1.19	1.00

Experimental dipole moments

*Transitions observed

Table 5.3: The global rotational constants determined from the present analysis compared with those reported by Lovas *et al.* [124] and Bossa *et al.* [129] for conformers 1-3. The *S*-reduction rotational constants from Ref. [129] are shown in square brackets.

Conformer 1, tG'g			
	This work	Lovas *et al.*	Bossa *et al.*
A /MHz	8572.056757(89)	8572.0553(8)	8572.057374 (95)
B /MHz	3640.106085(30)	3640.1063(5)	3640.099657 (37)
C /MHz	2790.966689(30)	2790.9666(4)	2790.972773 (33)
Δ_J [D_J] /kHz	0.736926(15)	0.738(7)	0.6116173 (186)
Δ_{JK} [D_{JK}] /kHz	5.33332(12)	5.276(30)	6.085380 (133)
Δ_K [D_K] /kHz	2.49067(15)	2.53(10)	1.863902 (170)
δ_J [d_1] /kHz	0.1630055(28)	0.1631(16)	-0.1630629 (72)
δ_K [d_2] /kHz	3.16441(21)	3.180(31)	-0.0627055 (46)
Φ_J [H_J] /Hz	-0.0000278(27)	-	0.0001462 (33)
Φ_{JK} [H_{JK}] /Hz	-0.007155(61)	-	-0.0129991 (310)
Φ_{KJ} [H_{KJ}] /Hz	-0.06019(25)	-	-0.043356 (153)
Φ_K [H_K] /Hz	0.08057(18)	-	0.069320 (103)
ϕ_J [h_1] /Hz	-	-	-0.00001021 (169)
ϕ_{JK} [h_2] /Hz	-0.003074(49)	-	-0.00007342 (118)
ϕ_K [h_3] /Hz	0.01995(54)	-	0.00002505 (36)
L_{JK} /mHz	-0.000262(25)	-	-0.0002276 (274)
Conformer 2, gG't			
	This work	Lovas *et al.*	Bossa *et al.*
A /MHz	8393.40052(19)	8393.4003(16)	8393.400915 (198)
B /MHz	3648.565503(44)	3648.5661(7)	3648.559609 (45)
C /MHz	2778.296552(43)	2778.2963(6)	2778.302133 (44)
Δ_J [D_J] /kHz	0.782561(21)	0.797(15)	0.6593872 (172)
Δ_{JK} [D_{JK}] /kHz	4.59878(20)	4.485(70)	5.337883 (204)
Δ_K [D_K] /kHz	2.9998(29)	3.16(35)	2.38752 (275)
δ_J [d_1] /kHz	0.1826860(40)	0.1827(60)	-0.18278504 (284)
δ_K [d_2] /kHz	2.93491(49)	3.14(21)	-0.0616642 (103)
Φ_J [H_J] /Hz	-0.0000285(31)	-	0.00018016 (230)
Φ_{JK} [H_{JK}] /Hz	-0.00905(12)	-	-0.013913 (37)
Φ_{KJ} [H_{KJ}] /Hz	-0.04311(40)	-	-0.030218 (183)
ϕ_{JK} [h_2] /Hz	-0.004247(74)	-	-0.00008575 (171)
ϕ_K [h_3] /Hz	0.01166(94)	-	0.00002179 (69)
L_{JK} /mHz	-0.000471(31)	-	-0.0004312 (309)
Conformer 3, g'G'g			
	This work	Lovas *et al.*	Bossa *et al.*
A /MHz	8536.77122(10)	8536.770(2)	8536.771860 (108)
B /MHz	3604.198352(50)	3604.198(1)	3604.192077 (50
C /MHz	2778.331494(51)	2778.331(1)	2778.337515 (52)
Δ_J [D_J] /kHz	0.737825(22)	0.751(14)	0.6178250 (226)
Δ_{JK} [D_{JK}] /kHz	5.38677(18)	5.29(7)	6.107365 (207)
Δ_K [D_K] /kHz	2.46290(29)	2.75(22)	1.862365 (315)
δ_J [d_1] /kHz	0.1570564(52)	0.152(6)	-0.1571335 (44)
δ_K [d_2] /kHz	3.11024(34)	3.34(14)	-0.0600612 (70)
Φ_J [H_J] /Hz	-0.0000324(36)	-	0.0001637 (37)
Φ_{JK} [H_{JK}] /Hz	-0.00775(17)	-	-0.012932 (104)
Φ_{KJ} [H_{KJ}] /Hz	-0.05801(53)	-	-0.043284 (211)
Φ_K [H_K] /Hz	0.08052(40)	-	0.070809 (222)
ϕ_{JK} [h_2] /Hz	-0.003494(96)	-	-0.00007860 (217)
ϕ_K [h_3] /Hz	0.0155(12)	-	0.00002229 (75)

Table 5.4: The global rotational constants determined from the present analysis compared with those reported by Lovas *et al.* [124] and Zakharenko *et al.* [130] for conformers 4-6. The *S*-reduction rotational constants from Ref. [130] are shown in square brackets.

Conformer 4, g'Gt			
	This work	Lovas *et al.*	Zakharenko *et al.*
A /MHz	6642.44779(17)	6642.4488(9)	6642.44480(184)
B /MHz	4163.594484(66)	4163.5949(9)	4163.591188(73)
C /MHz	3365.363518(59)	3365.3627(7)	3365.366481(65)
Δ_J [D_J] /kHz	1.777210(37)	1.774(29)	1.668650(40)
Δ_{JK} [D_{JK}] /kHz	6.37322(15)	6.354(82)	7.024940(168)
Δ_K [D_K] /kHz	-4.75173(50)	-4.51(12)	-5.29467(54)
δ_J [d_1] /kHz	0.252414(18)	0.267(13)	-0.2524108(192)
δ_K [d_2] /kHz	1.56639(28)	1.74(18)	-0.0542950(104)
Φ_J [H_J] /Hz	0.0000666(79)	-	-0.0002571(84)
Φ_{JK} [H_{JK}] /Hz	0.02274(11)	-	-0.034964(45)
Φ_{KJ} [H_{KJ}] /Hz	0.07720(40)	-	0.123285(180)
Φ_K [H_K] /Hz	0.04881(47)	-	-0.08233(46)
ϕ_J [h_1] /Hz	0.0001578(42)	-	0.0000329(47)
ϕ_{JK} [h_2] /Hz	0.005159(71)	-	0.00016435(275)
ϕ_K [h_3] /Hz	0.05824(52)	-	0.00012506(99)
Conformer 5, gG'g'			
	This work	Lovas *et al.*	Zakharenko *et al.*
A /MHz	8327.59369(34)	8327.599(5)	8327.59433(37)
B /MHz	3641.99965(12)	3642.001(4)	3641.993885(136)
C /MHz	2776.903906(95)	2776.902(3)	2776.909427(106)
Δ_J [D_J] /kHz	0.787937(80)	0.76(12)	0.668243(77)
Δ_{JK} [D_{JK}] /kHz	4.54331(75)	5.1(6)	5.26167(83)
Δ_K [D_K] /kHz	2.6139(18)	[2.9]	2.01566(199)
δ_J [d_1] /kHz	0.179665(38)	0.24(11)	-0.179685(40)
δ_K [d_2] /kHz	2.8352(10)	[2.8]	-0.0598907(236)
Φ_J [H_J] /Hz	0.000305(25)	-	0.0002344(221)
Φ_{JK} [H_{JK}] /Hz	-0.00482(83)	-	-0.01512(36)
Φ_{KJ} [H_{KJ}] /Hz	-0.0546(30)	-	-0.01922(177)
Φ_K [H_K] /Hz	0.0772(35)	-	0.0526(32)
ϕ_J [h_1] /Hz	0.000178(13)	-	0.0001287(126)
ϕ_{JK} [h_2] /Hz	0.00206(31)	-	0.0000465(70)
ϕ_K [h_3] /Hz	0.0694(62)	-	0.0000574(43)
Conformer 6, tGg'			
	This work	Lovas *et al.*	Zakharenko *et al.*
A /MHz	6634.76143(25)	6634.7621(7)	6634.762363(282)
B /MHz	4160.63319(11)	4160.6347(9)	4160.628511(136)
C /MHz	3377.907502(92)	3377.9063(8)	3377.911550(106)
Δ_J [D_J] /kHz	1.726054(77)	1.751(31)	1.577265(80)
Δ_{JK} [D_{JK}] /kHz	8.35543(63)	8.21(11)	9.24444(79)
Δ_K [D_K] /kHz	-6.7370(20)	-6.51(12)	-7.46489(243)
δ_J [d_1] /kHz	0.236086(42)	0.244(17)	-0.236082(49)
δ_K [d_2] /kHz	2.18140(73)	2.72(23)	-0.0744081(272)
Φ_J [H_J] /Hz	-0.000387(24)	-	-0.0007746(259)
Φ_{JK} [H_{JK}] /Hz	-0.02212(53)	-	-0.04326(56)
Φ_{KJ} [H_{KJ}] /Hz	0.0762(22)	-	0.13678(286)
ϕ_J [h_1] /Hz	-0.000004(13)	-	-0.0001915(139)
ϕ_{JK} [h_2] /Hz	0.00868(30)	-	0.0002002(121)
ϕ_K [h_3] /Hz	0.0952(21)	-	0.0001910(39)

Table 5.5: A comparison of global rotational constants for Conformer 1, tG'g, in the S-reduction from this work and Bossa *et al.* [129]. The A-reduction rotational constants from the global fit analysis are also tabulated.

	This work, Watson's S-reduction	Bossa *et al.*, Watson's S-reduction		This work, Watson's A-reduction
A /MHz	8572.057378(86)	8572.057374(95)	A /MHz	8572.056757(89)
B /MHz	3640.099653(33)	3640.099657(37)	B /MHz	3640.106085(30)
C /MHz	2790.972776(29)	2790.972773(33)	C /MHz	2790.966689(30)
D_J /kHz	0.611614(16)	0.6116173(186)	Δ_J /kHz	0.736926(15)
D_{JK} /kHz	6.08543(12)	6.085380(133)	Δ_{JK} /kHz	5.33332(12)
D_K /kHz	1.86386(15)	1.863902(170)	Δ_K /kHz	2.49067(15)
d_1 /kHz	0.1630610(65)	0.1630629(72)	δ_1 /kHz	0.1630055(28)
d_2 /kHz	0.0627043(40)	0.0627055(46)	δ_2 /kHz	3.16441(21)
H_J /Hz	0.0001453(29)	0.0001462(33)	Φ_J /Hz	-0.0000278(27)
H_{JK} /Hz	-0.012989(28)	-0.0129991(310)	Φ_{JK} /Hz	-0.007155(61)
H_{KJ} /Hz	-0.04333(13)	-0.043356(153)	Φ_{KJ} /Hz	-0.06019(25)
H_K /Hz	0.069287(92)	0.069320(103)	Φ_K /Hz	0.08057(18)
h_1 /Hz	-0.0000107(15)	-0.00001021(169)	ϕ_J /Hz	-
h_2 /Hz	-0.0000738(10)	-0.00007342(118)	ϕ_{JK} /Hz	-0.003074(49)
h_3 /Hz	0.00002496(32)	0.00002505(36)	ϕ_K /Hz	0.01995(54)
L_{JK} /mHz	-0.000234(24)	-0.0002276(274)	L_{JK} /mHz	-0.000262(25)

143.9 cm^{-1} above the ground state and involves a motion dominated by a rocking in the carbon backbone. The next assigned state of the lowest energy conformer is the $\nu_{32}(1)$ mode, which is a rotation in the methyl group, at 213.6 cm^{-1} above the ground state. Also assigned was the $\nu_{33}(2)$ state - the lowest energy vibration of conformer gG't. This resides 142.6 cm^{-1} above its ground state conformer, and it has an analogous motion to the $\nu_{33}(1)$ state.

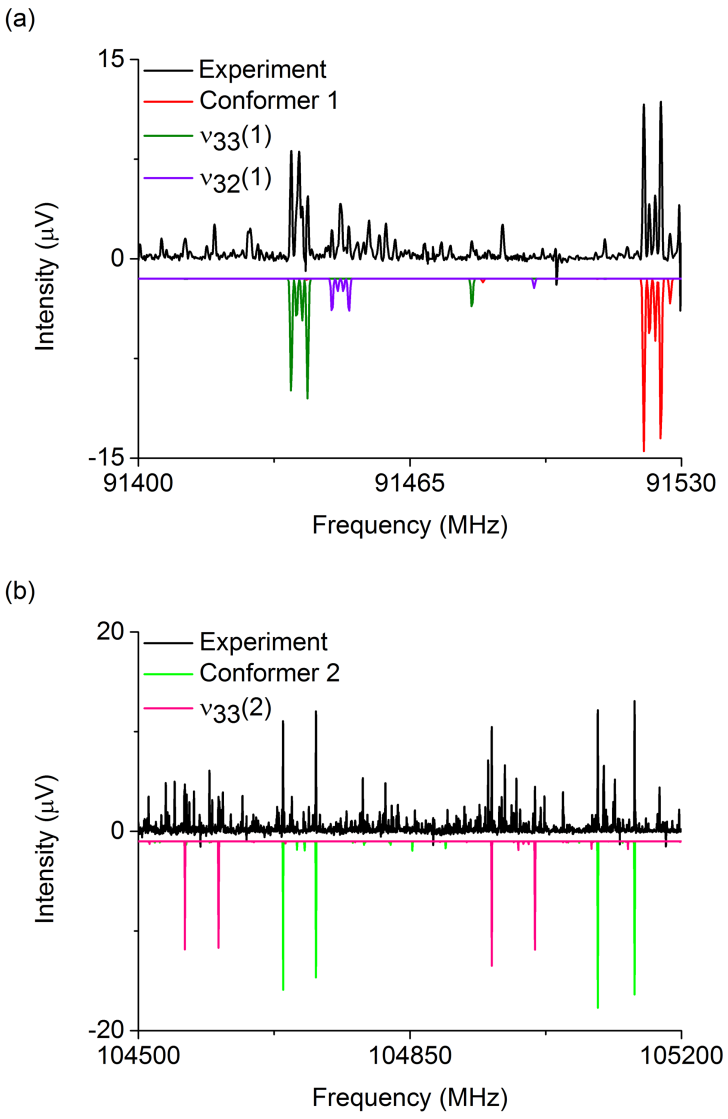

Figure 5.4: Zoom-in of the experimental spectrum of 1,2-propanediol, in black, and the simulated spectra of the experimentally fitted rotational constants for the observed vibrationally excited states and their respective ground states, in colour.

Table 5.6: The experimental rotational constants of the vibrationally excited states of 1,2-propanediol observed in this study. The calculated rotational constants, shown in bold, include anharmonic corrections at the MP2/aug-cc-pVTZ level of theory and were shifted by the same difference found between the experimental and computed rotational constants for the ground state. The shift values are - for conformer 1, tG'g: A = 36.73 MHz, B = 7.85 MHz, C = 7.30 MHz and for conformer 2, gG't: A = 35.55 MHz, B = 11.03 MHz, C = 8.93 MHz. The energies included are relative energies with respect to the relevant ground state conformer, with harmonic (ΔE^h) and anharmonic (ΔE^a) corrections.

	$\nu_{33}(1)$		$\nu_{32}(1)$		$\nu_{33}(2)$	
ΔE^h /cm^{-1}	150.2		222.5		146.2	
ΔE^a /cm^{-1}	143.9		213.6		142.6	
A /MHz	8524.4048(12)	**8520.16**	8557.4679(21)	**8556.23**	8348.173(22)	**8344.38**
B /MHz	3635.49161(78)	**3635.58**	3636.81102(36)	**3636.39**	3643.0369(21)	**3643.17**
C /MHz	2788.69875(84)	**2788.63**	2788.75729(42)	**2788.57**	2775.7901(17)	**2775.66**
Δ_J /kHz	0.7422(18)		0.74018(58)		0.7819(32)	
Δ_{JK} /kHz	5.34751(65)		5.3103(29)		4.518(14)	
Δ_K /kHz	1.8561(93)		2.044(15)		[2.9999]	
δ_J /kHz	0.162380(68)		0.160119(99)		0.1810(19)	
δ_K /kHz	3.0811(13)		3.0313(17)		2.887(44)	
Φ_{JK} /Hz	-0.00862(54)		-0.0147(18)		-	
Φ_{KJ} /Hz	-0.0466(58)		-0.069(20)		-	
No. lines	202		220		57	
mw RMS /kHz	35.6		48.4		28.3	

Caminati previously reported the observation of three vibrationally excited states [127]. Upon searching for them in the W-band spectrum, some inconsistencies were observed between those previously reported states and those being fit in the present data. In his work in 1981, performed on an 8400 C Hewlett-Packard spectrometer with which frequency measurements had an accuracy of 0.1 MHz, Caminati was able to assign the second lowest ground state conformer (conformer 2, gG't). He also reported three vibrationally excited states: $\nu_{t1} = 1$, $\nu_{t2} = 1$, and $\nu_{t1} = 2$ with energies respective to the gG't conformer of 105, 180, and 215 cm^{-1} [127]. Of these three reported vibrationally excited states for conformer 2, the two higher energy species $\nu_{t2} = 1$ and $\nu_{t1} = 2$ were unable to be observed/fully assigned in this work. This could be attributed to the $\nu_{t2} = 1$ state being perturbed (which was potentially already identified in Caminati's work; the standard deviations of the rotational constants for this state are higher than the others by an order of magnitude) and the low signal-to-noise ratio (below 3:1) of the high-energy $\nu_{t1} = 2$ state (284.8 cm^{-1} above its ground state conformer). It is noteworthy that these vibrational states were observed in Ref.[127], suggesting that the temperature of the cell was higher than the -5 °C than is detailed in the publication. It was further concluded that the first vibrationally excited state of conformer gG't that Caminati assigned ($\nu_{t1} = 1$) was, in fact, the conformer fifth highest in energy, gG'g'. It was a challenge to differentiate between the conformer gG'g' and the vibrationally excited state $\nu_{33}(2)$ because many of the features between the two are blended. This can be seen in Figure 5.5, which shows two small sections from the full spectrum - (a) has distinct peaks from each species, whilst (b) has peaks from both species blending and becoming indistinguishable. The resulting constants from the $\nu_{33}(2)$ fit can be assigned as a vibrationally excited state of gG't for two reasons: (i) the **fitted** distortion constants are of a similar order of magnitude to those fitted to the ground state conformer second highest in energy gG't and (ii) the relative intensity of the lines is what would be expected of the vibrational state. The similarity of the spectra might have led to the allocation of Caminati's rotational constants to a vibrationally excited state when, in fact, they belong to conformer 5, gG'g'. This is now untangled by fitting the high-energy conformer and the vibrational state in the same spectrum over a large bandwidth of 35 GHz. For the $\nu_{33}(2)$ state, the centrifugal distortion constant Δ_K has been fixed to the ground state value - it was not defined when left to float during the fitting process.

Only the three lowest energy conformers (tG'g, gG't, and g'G'g) were considered for the search of vibrationally excited states, as the most intense transitions of the vibrational satellites are likely caused by these low energy conformers. The SNR of the third lowest energy conformer is approximately 10:1. This means that the likelihood of identifying vibrationally excited states belonging to higher energy conformers is small. They may be present, but would be below a SNR of 3:1. This is

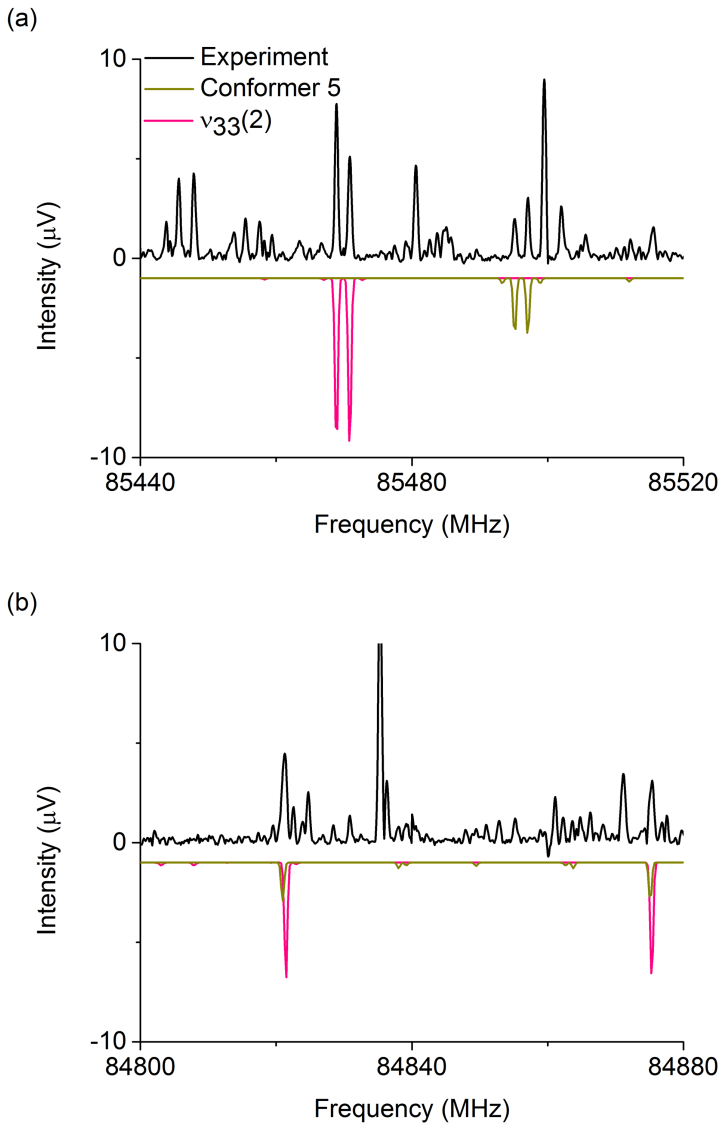

Figure 5.5: An overlay of conformer 5, gG'g', and the first vibrationally excited state of conformer 2, gG't ($\nu_{33}(2)$). The similarity in rotational constants causes line blending in some regions. Panel (a) shows a region where the transitions can be easily distinguished, whereas panel (b) shows a region where blending does not allow distinct peaks to be resolved.

probable as the spectrum is confusion limited due to the high number of conformers and vibrationally excited states present.

The calculations that aided in the spectral assignments were performed at both the MP2/aug-cc-pVTZ and the B3LYP/aug-cc-pVTZ level of theory. The MP2 calculations performed here mirrored the results of those performed by Lovas *et al.* [124], while the calculations done with the B3LYP functional failed to satisfactorily reproduce the energy landscape of the conformers. The energy order of the conformers calculated by B3LYP calculations is: conformer 1 (tG'g), conformer 5 (gG'g'), conformer 4 (g'Gt), conformer 6 (tGg'), conformer 2 (gG't), and conformer 3 (g'G'g). In 2009, Lovas *et al.* confirmed that the conformer that had the highest population in the supersonic expansion was conformer 1, tG'g, indicating it to be the lowest energy conformer [124]. These two sets of calculations agree that this is the case, and the experimental results presented here concur if the dipole-corrected signal intensity of the tG'g conformer compared to the other conformers is considered. The energy ordering of the conformers then continues to follow the order set out by the MP2 calculations and the experimental results of Lovas *et al.* [124], when the dipole-corrected signal intensities are considered. The B3LYP calculations underestimate, whilst the MP2 calculations generally overestimate, the magnitude of the experimental rotational constants. However, the B3LYP calculations fail to correctly report the energy landscape of the conformers.

5.4 Conclusions

The broadband rotational spectrum of the astrochemically relevant molecule 1,2-propanediol was recorded between 75-110 GHz under room temperature conditions. This facilitated the assignment of the first six conformers of the molecule. The data were globally fit with previously published line lists [124, 127–130], producing the most precise set of rotational constants for these conformers to date. Two vibrationally excited states of the lowest energy conformer and one vibrationally excited state of the conformer second highest in energy were observed for the first time. The assignment of the $\nu_{33}(2)$ state was reported previously by Caminati, but the broadband capabilities of the W-band instrument revealed that his assignment was actually conformer 5, gG'g' [127]. Three further vibrational states, one of the lowest energy conformer and two of the conformer second highest in energy, are observed, but they are perturbed and the current, limited data set does not allow for this to be fully accounted for. The astronomical search for this molecule and its vibrationally excited states will be supported with the new line lists,as the operating frequency of the W-band spectrometer overlaps directly with that of ALMA Band 3, data from which is expected to significantly increase the inventory of complex molecules detected in the ISM [25]. Further, the precise, global fits allow for the accurate

prediction of transitions into the submillimeter range, increasing the applicability of the data to observations at higher frequency bands.

Chapter 6

Facilitating Interstellar Searches for the Four Simple Amino Alcohols Alaninol, Valinol, Leucinol, and Isoleucinol

This chapter is based on the following publications:

- M. Fatima, C. Pérez, B. E. Arenas, M. Schnell, A. L. Steber *Benchmarking a new segmented K-band chirped-pulse microwave spectrometer and its application to the conformationally rich amino alcohol isoleucinol* Physical Chemistry Chemical Physics **22**, 17042-17051 (2020).*
- B. E. Arenas, M. Fatima, C. Pérez, S. Fischer, A. L. Steber, M. Schnell *Facilitating interstellar searches for simple amino alcohols with accurate rest frequencies into the millimeter-wave regime: Alaninol, valinol, and leucinol* **Under Review**.

6.1 Introduction

Many of the molecules detected in the interstellar medium (ISM) contain biologically relevant functional groups that could become incorporated into larger biomolecular motifs. Examples include alcohols and diols (important for their -OH groups), simple cyano-containing molecules (thought to be important for the incorporation of

*This publication also contributed to: M. Fatima, *A systematic study of intermolecular interactions in non-covalently bound complexes by using and expanding advanced broadband rotational spectroscopy* PhD Thesis, Universität Hamburg, Germany (2020).

nitrogen into complex molecules), and even the simple sugar glycolaldehyde [132]. As a consequence of increasingly sensitive observational facilities, larger and more complex molecules are becoming targets for interstellar searches. Amino alcohols and amino acids are appealing targets, as important questions in astrochemistry are whether an essential amino acid exists in the gas phase in the ISM, and if so, how it could have formed. Searches for amino acids in the ISM are not new, with the first reported observation of interstellar glycine in 2003 [133]. Despite this observation eventually being disconfirmed [134–136], amino acids are still of paramount interest in interstellar (bio-)chemistry.

The amino alcohols essentially represent a reduced state of the corresponding amino acid. That is, the acid can be produced from the alcohol in a one-step oxidation process. This could be made possible by the presence of gas-phase oxidising agents in the ISM, for example molecular oxygen, O_2, in Orion [137], hydrogen peroxide, H_2O_2, in ρ Oph A [138], or their relevant radical or ionic species, which may be more likely to participate in chemical reactions. Oxidation reactions could also occur on water ice surfaces upon irradiation because of the presence of, for example, hydroxyl radicals. Therefore, successful detection of these amino alcohols could act as sign posts towards regions of the ISM where their amino acid analogues are more likely to be observed.

Because of the potential importance of amino alcohols, there have been a number of previous studies on smaller examples for the purposes of supporting astronomical detections. For example, the millimeter wavelength experiment involving 2-aminoethanol [139], which determined rotational and centrifugal distortion constants for the ground state and a number of vibrationally excited states, extended previous work on the molecule [140, 141]. This molecule, also known as glycinol, is the simplest amino alcohol that is related to the proteinogenic α-amino acid glycine. A number of larger amino alcohols have also been examined by rotational spectroscopy, including serinol, which was used as a model system for the lipid sphingosine [142]. The authors of Ref. [142] focussed on describing intra-molecular hydrogen bonding within the conformers of the assigned species. Another extensive survey along these lines involved a group of molecules, consisting of D-allothreoninol, 2-amino-1,3-propanediol, and 1,3-diamino-2-propanol, being studied to analyse the competition between cyclic and chain hydrogen-bond motifs [143].

In a previous structural analysis of an amino alcohol that is analogous to the proteinogenic α-amino acid alanine, Ellingsen *et al.* reported a microwave investigation of alaninol with transitions between 18.6-39.7 GHz [144]. Their experimental analysis revealed the two lowest-energy conformers, each with an intra-molecular hydrogen bond. They also observed the pure rotational spectra of vibrationally excited states: four for Rotamer I and two for Rotamer II. Dipole moments determined from Stark measurements were also reported. The work was followed by a matrix-

isolation infrared spectroscopy and Raman spectroscopy study from Fausto *et al.* [145]. Five conformations of alaninol were experimentally observed, two of which were those reported in Ref. [144], and the experimental work was complemented with theoretical calculations.

A number of small proteinogenic α-amino acids have likewise been characterised by microwave spectroscopy, including alanine, valine, leucine, and isoleucine [146–149]. Each work deduced that the gas-phase structure of the lowest energy conformers of the amino acids contain a bifurcated hydrogen bond between the hydrogen atom of the amino group and the carboxyl oxygen. The portfolio of work also provides the rotational constants required to search for the respective amino acids in the ISM. This has been noteworthy recently because of the detection of glycine, the simplest amino acid, in the coma of the comet 67P/Churyumov-Gerasimenko [150].

The work in this chapter concerns four potential proteinogenic α-amino acid precursors - alaninol (2-amino-1-propanol), valinol (2-amino-3-methyl-1-butanol), leucinol (2-amino-4-methyl-1-pentanol), and isoleucinol (2-amino-3-methyl-1-pentanol) – and the analysis of their high-resolution, broadband rotational spectra. This will facilitate searches for these potential amino acid precursors and their heavy-atom isotopologues in the ISM by providing rotational constants and line lists, which are essential for astronomical detection of these complex organic molecules. Their presence would signify the observation of a new class of molecules not detected in the ISM before. Further, the assignments of the isotopologues have allowed for a comprehensive comparison between the amino alcohol structures and to their analogous amino acids.

6.2 Experimental and Theoretical Details

The rotational spectra of alaninol, valinol, leucinol, and isoleucinol were recorded with three chirped-pulse Fourier transform rotational spectrometers. The low-energy conformers were first identified using a supersonic expansion molecular beam on the Hamburg COMPACT spectrometer, between 2 - 8 GHz [92, 93] and 8 - 18 GHz [94], and the 18-26 GHz spectrometer [94]. The experiments in the millimeter-wave (mmw) regime were carried out on the W-band (75-110 GHz) spectrometer at room temperature in a slow flow cell configuration [151]. Individual details for each measurement are summarised in the following paragraphs, and extensive descriptions of the apparatuses can be found in Chapter 3 and in the corresponding publications.

The number of co-added FIDs collected within each frequency range per molecule varied between 0.5 and 5.6 million, and an exact breakdown is given in Table 6.1. The samples were obtained from Alfa Aesar (L-alaninol, 98 % purity), Biozol (L-valinol, 98 % purity), and Fisher Scientific (L-leucinol, 98 % purity and L-isoleucinol, 97 % purity) and were used without further purification. The samples were heated

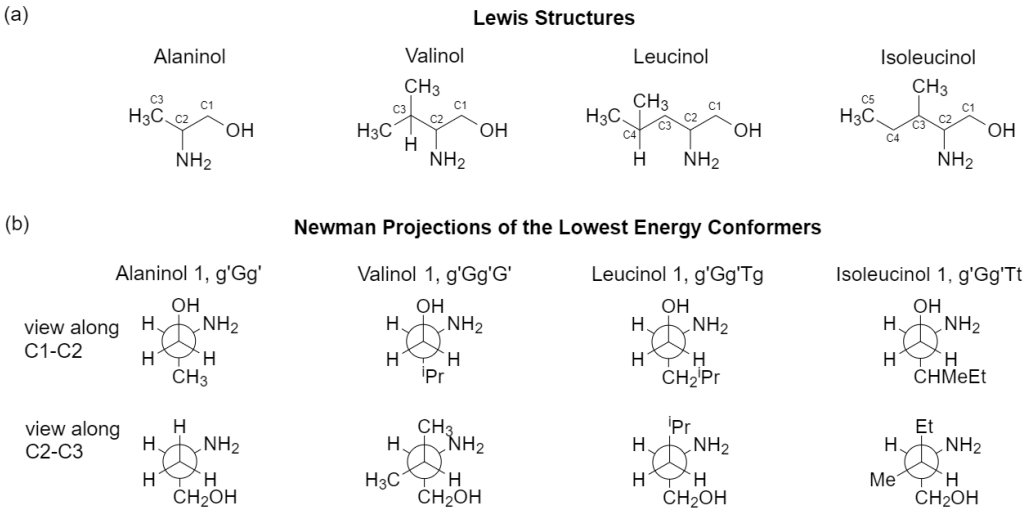

Figure 6.1: (a) The Lewis structures of the three amino alcohols alaninol, valinol, leucinol, and isoleucinol. (b) The Newman projections of the lowest energy conformers; see text for discussion.

to the following temperatures during the experiments: 80 °C for alaninol, 30 °C for valinol, 125 °C for leucinol, and 45 °C for isoleucinol.

For experiments conducted on the Hamburg COMPACT spectrometer, the excitation chirps were 4 μs (2-8 GHz) and 2 μs long (8-18 GHz), and the FIDs were recorded for 40 μs (2-8 GHz) or 20 μs (8-18 GHz). The instrument has a resulting resolution of 25 kHz for the 2-8 GHz band and 50 kHz for the 8-18 GHz band. The samples were placed in a heatable reservoir nozzle (Parker Series 9 nozzle), and the molecular vapour was supersonically expanded into the vacuum chamber with 3 bar of neon as the backing gas.

For experiments performed on the 18-26 GHz spectrometer, the excitation pulses were 1.5 μs in duration, and the FIDs were recorded for 10 μs per segment. The resulting resolution of the spectrometer is approximately 100 kHz. The sample was placed in a similar heatable reservoir nozzle as in the COMPACT. Neon, with a backing pressure of 1 bar, was used as the carrier gas.

The W-band spectrometer's High Dynamic Range mode [151] was used to collect the spectra in the 75-110 GHz region. The excitation pulse duration was 500 ns, and the FIDs were recorded for 4 μs. The spectrometer has a resolution of approximately 550 kHz. The room-temperature experiments were performed under slow flow cell conditions, with the sample being pre-treated in a freeze-pump-thaw manner to remove any air from the external reservoir. The samples were then heated, vapour was allowed to flow into the chamber without a backing gas, and a pressure of 10 μbar was maintained in the chamber for all samples.

Table 6.1: A summary of the number of co-added FIDs, in millions, collected per molecule for each frequency range investigated.

Frequency region / GHz	2-8	8-13	13-15.5	15.5-18	18-26	75-110
Alaninol	1.9	1.1	1.0	1.4	2.6	0.5
Valinol	5.6	1.4	1.0	2.3	2.0	0.5
Leucinol	1.0	1.2	1.0	3.0	2.1	0.5
Isoleucinol	4.2	1.0	1.0	1.0	2.9	0.5

All four molecules studied here are flexible; rotations around their C-C single bonds (see structures in Figure 6.1) can result in a number of different possible conformations. Conformational searches were conducted for each molecule in the same manner. First, automatic semi-empirical conformational searches were done on the SPARTAN programme using the Austin Model 1 (AM1) method, the Parameterization Method 3 (PM3), and the Parameterization Method 6 (PM6) [74]. After sorting through the structures to remove duplicates, each returned structure was re-optimised with the B3LYP-D3(BJ)/def2-TZVP level of theory as implemented in the Gaussian 09 package [73]. Structures from all three methods that were considered to be energetically accessible in the experiments were re-optimised at the B3LYP/aug-cc-pVTZ level of theory. The energetic considerations followed those made in Ref. [152] and focus the list of potential conformers to those which have energies within 6 kJ mol^{-1} of the lowest energy structure. The number of conformers of each molecule from each method were as follows: alaninol – two conformers from AM1, three conformers from PM3, two conformers from PM6; valinol - four conformers from AM1, four conformers from PM3, three conformers from PM6; leucinol - two conformers from AM1, five conformers from PM3, one conformer from PM6; isoleucinol - sixty four conformers from AM1, fifty six conformers from PM3, forty six conformers from PM6. This resulted in three distinct conformers for alaninol, four distinct conformers for valinol, five distinct conformers for leucinol, and seven distinct conformers for isoleucinol. The automatic conformational searches, which are summarised in Figure 6.2, were supplemented with manual dihedral angle scans along the carbon backbones of the molecules. The scans were performed at the B3LYP/6-311G++ level of theory, and each resulting minimum was re-optimised at the B3LYP/aug-cc-pVTZ level of theory. The results from both methods produced the same final list of conformers. The collated list of final conformers was used to aid in spectral assignment. For alaninol, the conformational landscape reported by Ref. [145] in their matrix-isolation infra-red study was an additional guide.

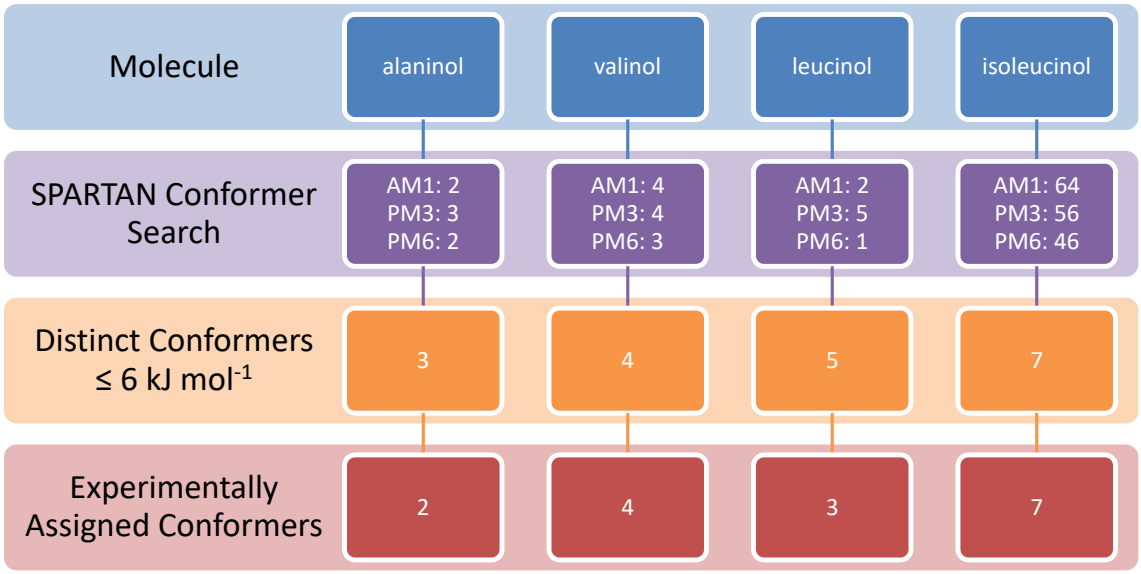

Figure 6.2: A summary of the results of the conformer searches for the amino alcohols using the SPARTAN programme.

In order to maintain consistency, the naming scheme of the conformers was based on the work in Refs. [144] and [145], and it is extended here to include the longer carbon chains of valinol, leucinol, and isoleucinol. The Lewis structures and the atom labelling scheme can be found in Figure 6.1. Each structure is named with a string of letters, for example alaninol 1 is named g'Gg', whereby each letter denotes the magnitude of a defined dihedral angle. In general, the names take the form aBcDe, where the letters refer to the following combinations: a is the dihedral angle N(lp)-N-C2-C1 (where N(lp) is the lone pair of electrons on the nitrogen atom), B is the N-C2-C1-O dihedral angle, and c refers to the C2-C1-O-H dihedral angle [144, 145]. The symbols D and e take different meanings depending on the molecule being considered. D is the C1-C2-C3-H dihedral angle in valinol. In leucinol and isoleucinol, D is the C1-C2-C3-C4 dihedral angle. In leucinol, e is the C2-C3-C4-H dihedral angle, and in isoleucinol, e is the C2-C3-C4-C5 dihedral angle. The letter

used and the dihedral angle sizes they denote are: g/G for a dihedral angle close to 60° (a *gauche* configuration), g'/G' for a dihedral angle close to -60° (a *gauche* configuration), t/T for a dihedral angle close to 180° (noted as a *trans* configuration in Refs. [144] and [145], though also commonly referred to as an *anti* configuration).

Anharmonic frequency calculations, at the B3LYP/aug-cc-pVTZ level of theory, were performed for each assigned conformer in order to obtain theoretical rotational constants for their vibrational states. To aid with the assignments, the calculated rotational constants for the vibrational states were shifted by the difference observed between the experimental and calculated rotational constants for the respective ground state conformer. The frequency calculations also provided theoretical quartic distortion constants to aid in the assignment of the ground state conformers in the W-band data sets.

The amino alcohols studied here are all asymmetric tops, where $A \neq B \neq C$. The theoretical and experimental values for Ray's asymmetry parameter, κ, for each conformer are given in Tables 6.2-6.5. All of the conformers are asymmetric, near-prolate tops, with the theoretical κ values ranging from -0.99 to -0.48. They were thus fit to a Watson's A-reduction Hamiltonian in the I^r representation. Spectral analysis was carried out using the PGOPHER programme [70] and the AABS programme package [71, 90]. The final fits were obtained from Pickett's suite of programmes (SPFIT/SPCAT) [63].

The low frequency data sets, up to 26 GHz, exhibited hyperfine splitting due to the nuclear electric quadrupole moment of the nitrogen nucleus. This hyperfine splitting was only relevant for these data sets, and not for the W-band spectra, as the splitting collapses for transitions with high rotational quantum number, J. In order to obtain a fit encompassing all of the measured transitions, a global fit was performed whereby the rotational constants and the quartic centrifugal distortion constants were fit to all assigned lines, and the nitrogen nuclear quadrupole coupling constants were fit only to those lines which exhibited the hyperfine splitting. That is, any transition exhibiting hyperfine splitting was labelled with the relevant F-state labels, and those which did not exhibit the splitting were assigned to a pure rotational Hamiltonian.

The substitution structures of some of the amino alcohols were determinable because singly-substituted isotopologues were observed in natural abundance. This analysis was performed using the KRA programme package, and further structural analysis, such as the determination of dihedral angles, was performed with the EVAL programme package [71, 90].

6.3 Results and Discussion

Vibronic Ground States and Structure Determination

The spectroscopic parameters for the observed ground state conformers of alaninol (g'Gg' and gG'g), valinol (g'Gg'G', g'Gg'G, g'Gg'T, and gG'gG'), leucinol (g'Gg'Tg, gG'gTg', and g'Gg'Gg'), and isoleucinol (g'Gg'Tt, g'Gg'G't, g'Gg'Tg', g'Gg'Gt, g'Gg'Gg, gG'gTt, and gG'gTg') are presented in Tables 6.2-6.5, respectively. In these tables, the experimentally determined constants are listed alongside those obtained from theory. The theoretical rotational constants agree with the experimental rotational constants within a 1 % difference for alaninol, a 2 % difference for valinol, a 3 % difference for leucinol, and a 1 % difference for isoleucinol. A comparison to the previously published rotational constants of alaninol [144] is also presented in Table 6.2. The improvement of the microwave root mean square (σ) between the current analysis of alaninol and that performed in Ref. [144] highlights the experimental frequency accuracy available from modern high-resolution rotational spectroscopy. The fits for alaninol 1, g'Gg', alaninol 2, gG'g, valinol 1, g'Gg'G', and valinol 2, g'Gg'G, combine data from the ranges 2-26 and 75-110 GHz.

For all systems, the spectra recorded with the COMPACT and the 18-26 GHz spectrometers showed hyperfine splitting, caused by the interaction of the ^{14}N I=1 spin with the electric field gradient. This is shown clearly in Figure 6.3, where a section of the rotational spectrum of alaninol is plotted against the simulated spectrum of the fitted rotational constants for the lowest energy conformer, g'Gg'. The hyperfine splitting generally spans 2-3 MHz for alaninol 1, g'Gg', and this holds true for all conformers of the other amino alcohols. Analysis of this effect has allowed for the determination of the nitrogen nuclear quadrupole coupling constants χ_{aa} and χ_{bb}-χ_{cc} for all ground state conformers and a number of isotopologues. Comparison of these experimental constants to those computed from theory provides a further confirmation of the structure designated to each assignment. These constants are of particular importance for interstellar searches, as the observation of nuclear hyperfine splitting can act as a further validation mechanism for interstellar detections [51, 53].

It is important to note that the level of theory reported for the isoleucinol structure optimisation calculations is different from the other three amino alcohols. Namely, the results of the B3LYP-D3(BJ)/aug-cc-pVTZ calculations are reported. The dispersion correction was necessary for the larger amino alcohol molecule for the correct prediction of the energy ordering of the conformers. The extra considerations of the B3LYP-B3(DJ) functional were not required to model the energy ordering of alaninol, valinol, and leucinol, likely due to their structures containing less propensity for secondary intermolecular interactions. Details of the analysis can

Table 6.2: The experimental and theoretical rotational constants for the observed ground state conformers of alaninol. The experimental values for both conformers are the result of global fits of the data in the regions 2-18, 18-26, and 75-110 GHz. The theoretical parameters were obtained at the B3LYP/aug-cc-pVTZ level of theory. The rotational constants reported by Ref. [144] are included for comparison.

	Conformer 1, g'Gg'			Conformer 2, gG'g		
	This work	Theory	Ellingsen *et al.* 1978	This work	Theory	Ellingsen *et al.* 1978
A / MHz	7948.48588(88)	7948.7	7948.403(77)	6461.60804(69)	6481.2	6461.620(32)
B / MHz	3640.57864(28)	3630.8	3640.570(11)	4144.43502(37)	4108.4	4144.442(30)
C / MHz	2747.73691(20)	2738.6	2747.727(11)	3336.16546(34)	3306.6	3336.163(30)
Δ_J / kHz	0.72345(80)	0.7	0.51(18)	1.6343(17)	1.7	1.65(69)
Δ_{JK} / kHz	3.4438(58)	3.5	3.84(63)	4.940(10)	5.4	6.35(15)
Δ_K / kHz	2.024(87)	2.4	1.5(3.2)	-3.701(48)	-4.0	-7.02(40)
δ_J / kHz	0.17391(29)	0.2	0.163(24)	0.24994(53)	0.3	0.3420(94)
δ_K / kHz	2.321(13)	2.4	3.23(56)	1.115(16)	1.2	-0.034(117)
χ_{aa} / MHz	-3.6734(33)	-4.1	-	-0.7119(50)	-0.7	-
χ_{bb}-χ_{cc} / MHz	-0.1108(68)	-0.16	-	4.0368(72)	4.4	-
μ_a, μ_b, μ_c / D	-	3.1, 0.5, 0.4	3.03(1), 0.54(3), 0.57(19)	-	2.4, 0.9, 1.3	2.19(3), 1.46(8), 1.172(3)
κ	-0.66	-0.66	-0.66	-0.48	-0.51	-0.48
No. of lines	258	-	39	251	-	36
σ / kHz	13.7	-	112	18.2	-	75.8

Table 6.3: The experimental and theoretical rotational constants for the observed ground state conformers of valinol. The experimental values for conformers 1, g'Gg'G', and 2, g'Gg'G, are the result of global fits of the data in the regions 2-18, 18-26, and 75-110 GHz. The experimental values for conformers 3, g'Gg'T, and 4, gG'gG', are the result of fits of the data in the regions 2-18 and 18-26 GHz. The theoretical parameters were obtained at the B3LYP/aug-cc-pVTZ level of theory. Values contained within square brackets were kept fixed to the theoretical values.

	Conformer 1, g'Gg'G'		Conformer 2, g'Gg'G		Conformer 3, g'Gg'T		Conformer 4, gG'gG'	
	This work	Theory	This work	Theory	This work	Theory	This work	Theory
A / MHz	4023.53359(37)	4023.6	4236.8058(15)	4227.0	3629.76830(45)	3640.8	3411.43927(47)	3425.8
B / MHz	1701.31802(14)	1691.7	1546.61067(26)	1534.3	1691.76050(54)	1677.5	2011.33242(29)	1975.2
C / MHz	1284.21089(12)	1277.0	1414.10206(23)	1405.8	1470.41499(43)	1456.1	1486.51765(23)	1471.5
Δ_J / kHz	0.108023(72)	0.1	0.22047(15)	0.2	0.2656(49)	0.3	0.3400(43)	0.4
Δ_{JK} / kHz	0.18277(36)	0.2	0.12889(98)	0.2	-	-	0.242(24)	0.06
Δ_K / kHz	0.724(22)	0.9	[1.039662972]	1.0	-	-	-	-
δ_J / kHz	0.026377(33)	0.03	0.043245(77)	0.04	0.0362(29)	0.04	0.1216(23)	0.1
δ_K / kHz	0.2496(16)	0.3	4.825(13)	5.2	3.05(15)	1.9	-	0.5
χ_{aa} / MHz	-4.1801(33)	-4.7	-3.9918(49)	-4.5	-4.2541(36)	-4.7	0.2715(30)	0.5
χ_{bb}-χ_{cc} / MHz	0.6928(64)	0.8	-0.6612(48)	-0.4	0.7028(76)	0.4	4.7808(52)	5.6
μ_a, μ_b, μ_c / D	-	3.0, 1.2, 0.7	-	3.0, 0.3, 0.7	-	2.7, 1.7, 0.4	-	1.5, 1.7, 1.5
κ	-0.70	-0.70	-0.91	-0.91	-0.79	-0.80	-0.45	-0.48
No. of lines	569	-	172	-	184	-	258	-
σ / kHz	20.1	-	15.7	-	12	-	11.8	-

Table 6.4: The experimental and theoretical rotational constants for the observed ground state conformers of leucinol. The experimental values for all three conformers are the result of fits of the data in the regions 2-18 and 18-26 GHz. The theoretical parameters were obtained at the B3LYP/aug-cc-pVTZ level of theory.

	Conformer 1, g'Gg'G'		Conformer 2, g'Gg'G		Conformer 3, g'Gg'T	
	This work	Theory	This work	Theory	This work	Theory
A / MHz	4047.45526(45)	4023.3	3438.92783(94)	3434.6	3338.49819(61)	3338.0
B / MHz	904.64031(11)	889.0	1044.55278(34)	1025.2	1017.18281(31)	993.3
C / MHz	876.84190(12)	874.2	945.90732(33)	937.6	919.14552(29)	912.0
Δ_J / kHz	0.07316(22)	0.08	0.1065(13)	0.1	0.1125(14)	0.1
Δ_{JK} / kHz	0.4674(20)	0.4	-0.0447(83)	-0.09	0.1639(80)	0.3
Δ_K / kHz	1.198(29)	1.5	1.307(72)	1.7	0.948(29)	1.0
δ_J / kHz	0.01315(11)	0.01	0.02794(70)	0.03	0.0357(10)	0.04
δ_K / kHz	7.583(44)	16.0	1.139(89)	1.8	1.272(74)	1.9
χ_{aa} / MHz	-3.8315(28)	-4.3	0.302(15)	0.3	-3.309(8)	-3.7
χ_{bb}-χ_{cc} / MHz	-1.0472(56)	-1.2	-1.1172(196)	-1.6	-0.1600(156)	-0.4
μ_a, μ_b, μ_c / D	-	3.0, 0.1, 1.2	-	1.8, 2.3, 0.0	-	2.2, 2.1, 0.2
κ	-0.98	-0.99	-0.92	-0.93	-0.92	-0.93
No. of lines	419	-	180	-	238	-
σ / kHz	12.8	-	18.3	-	17.2	-

Table 6.5: The experimental and theoretical rotational constants for the observed ground state conformers of isoleucinol. The experimental values for all seven conformers are the result of fits of the data in the regions 2-18 and 18-26 GHz. The theoretical parameters were obtained at the B3LYP-D3(BJ)/aug-cc-pVTZ level of theory.

	Conformer 1, g'Gg'Tt		Conformer 2, g'Gg'G't		Conformer 3, g'Gg'Tg'		Conformer 4, g'Gg'Gt	
	This work	Theory	This work	Theory	This work	Theory	This work	Theory
A / MHz	3759.34376(39)	3777.1	3170.22321(33)	3188.8	3067.56626(32)	3079.3	3234.58882(34)	3246.7
B / MHz	1062.44909(12)	1062.7	1103.61682(17)	1102.7	1213.42566(16)	1213.0	1083.52381(21)	1084.6
C / MHz	880.24579(13)	879.9	971.59291(15)	970.4	1010.54858(14)	1009.3	972.62991(22)	971.3
Δ_J / kHz	0.02663(55)	0.04	0.08475(84)	0.09	0.11429(88)	0.1	0.0881(11)	0.08
Δ_{JK} / kHz	0.3348(82)	0.1	-0.3651(58)	-0.3	-0.2067(55)	-0.2	-0.2216(76)	-0.2
Δ_K / kHz	-	-	-	-	-	-	2.158(17)	2.4
δ_J / kHz	-	-	0.01271(62)	0.02	0.02256(63)	0.02	0.02247(55)	0.02
δ_K / kHz	-	-	-	-	-	-	1.036(71)	0.9
χ_{aa} / MHz	-4.2152(31)	-4.7	-4.2156(33)	-4.7	-3.4897(33)	-3.9	-3.6859(30)	-4.1
χ_{bb}-χ_{cc} / MHz	0.4968(60)	0.4	-0.5144(60)	-0.4	0.4780(60)	0.4	0.1620(60)	-0.08
μ_a, μ_b, μ_c / D	-	3.2, 0.9, 0.5	-	3.0, 0.9, 0.8	-	3.1, 0.5, 1.3	-	2.5, 2.0, 0.4
κ	-0.87	-0.87	-0.88	-0.88	-0.80	-0.80	-0.90	-0.90
No. of lines	357	-	323	-	269	-	278	-
σ / kHz	12.5	-	11.4	-	11.2	-	11.0	-

	Conformer 5, g'Gg'Gg		Conformer 6, gG'gTt		Conformer 7, gG'gTg'	
	This work	Theory	This work	Theory	This work	Theory
A / MHz	2357.79993(38)	2361.0	3124.11041(36)	3142.3	3000.70059(60)	3017.9
B / MHz	1370.35475(21)	1375.8	1218.15680(11)	1213.8	1332.57586(26)	1327.5
C / MHz	1107.69103(20)	1107.4	1019.16409(12)	1016.5	1089.86075(21)	1087.0
Δ_J / kHz	0.4981(18)	0.4	0.10863(65)	0.1	0.1316(12)	0.1
Δ_{JK} / kHz	-1.377(10)	-1.0	-	-	-	-
Δ_K / kHz	1.797(20)	1.5	0.495(38)	1.7	-	-
δ_J / kHz	0.20951(91)	0.1	0.00966(26)	0.01	0.03128(91)	0.03
δ_K / kHz	0.970(24)	0.6	-	-	-	-
χ_{aa} / MHz	-3.0398(33)	-3.3	0.5847(25)	0.7	-0.4353(40)	-0.5
χ_{bb}-χ_{cc} / MHz	-0.8696(72)	-1.2	5.0264(44)	5.6	4.4336(68)	4.8
μ_a, μ_b, μ_c / D	-	2.3, 2.1, 0.9	-	1.5, 1.7, 1.6	-	2.1, 1.4, 1.1
κ	-0.58	-0.57	-0.81	-0.81	-0.75	-0.75
No. of lines	272	-	323	-	154	-
σ / kHz	11.2	-	10.3	-	10.5	-

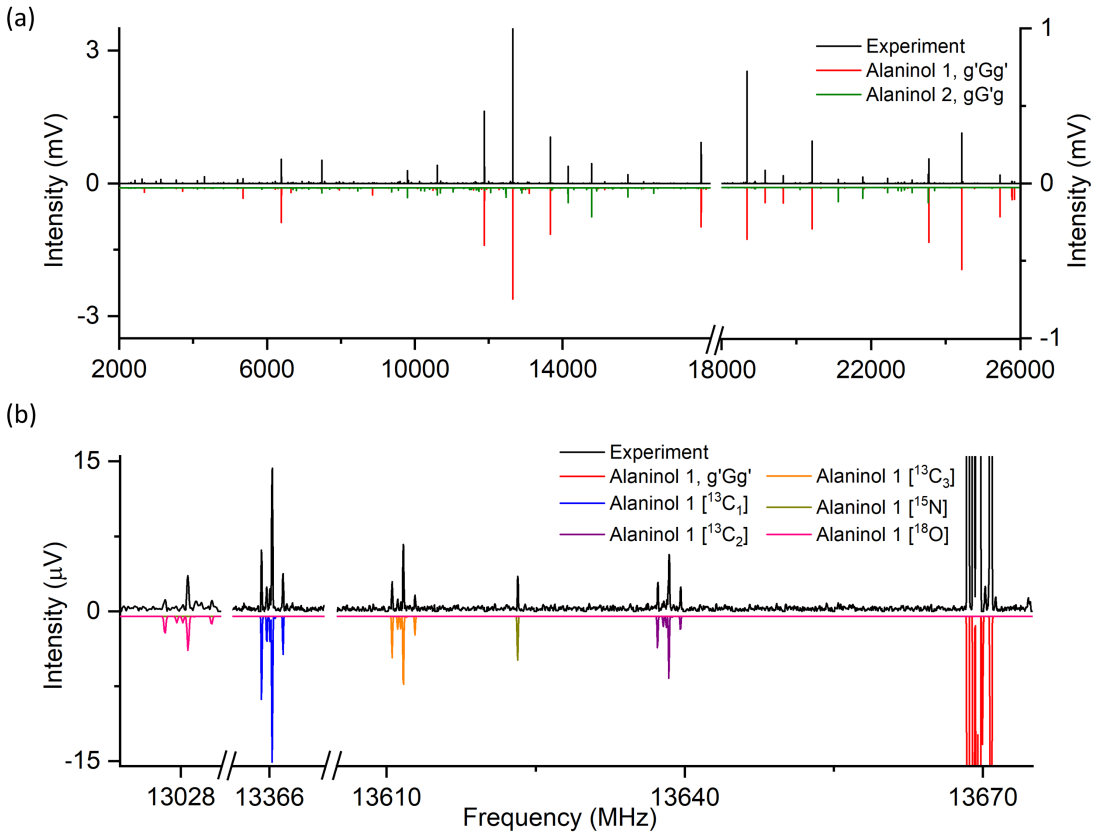

Figure 6.3: (a) The low-frequency (2-18 and 18-26 GHz) experimental data sets of the rotational spectrum of alaninol. The numbers of co-added FIDs, in millions, are 1.9, 1.1, 1.0, 1.4, and 2.6 in the 2-8, 8-13, 13-15.5, 15.5-18, and 18-26 GHz regions, respectively. Note the different intensity axes for the two different frequency ranges. (b) Zoom-ins to illustrate the assignments of the observed isotopologues for alaninol 1, g'Gg' in the 13-15.5 GHz region. In both, the black trace is the experimental spectrum, and the coloured traces are the simulated spectra based on the fitted rotational constants at 3 K.

be found in Ref. [94].

In addition to the low-energy conformers listed above, the rotational spectra of a number of isotopologues in natural abundance were also observed in the 2-26 GHz data sets. The application of Kraitchman's equations [91] allowed the experimental determination of the position of each isotopically substituted atom with respect to the molecule's centre of mass. A comparison of the experimentally determined substitution structures in the gas phase and the quantum-chemically optimised structures is presented in Figure 6.4 for those that were observed. The partially transparent molecular structure is the optimised structure at the B3LYP/aug-cc-pVTZ level of theory (or B3LYP-D3(BJ)/aug-cc-pVTZ for isoleucinol), and the coloured spheres are the experimentally determined atom positions. As shown, the theoretical structures match the experimental structures. Isotopologues were observed for the following conformers: ^{13}C, ^{15}N, and ^{18}O for alaninol 1 (g'Gg'), valinol 1 (g'Gg'G'), and isoleucinol 1 (g'Gg'Tt); ^{13}C and ^{15}N for alaninol 2 (gG'g), valinol 2 (g'Gg'G), and leucinol 1 (g'Gg'Tg); ^{13}C for isoleucinol 2 (g'Gg'G't) and isoleucinol 3 (g'Gg'Tg'). A full account of the rotational constants for the isotopologues observed is reported in Appendix 2. The analysis of the isotopologues allowed the unambiguous determination of the experimental backbones of the alaninol conformers, the two lowest energy conformers of valinol, the lowest energy conformer of leucinol, and the three lowest energy conformers of isoleucinol. Aside from the structural analysis that can be developed from this information, which follows below, this information can be useful to astronomers in the future for searches for these species in the ISM. Searches of this nature would rely on any parent-species conformer being detected in sufficient abundance, and the likeliness of detection would be increased with the continuously improving sensitivities of observational facilities. Isotopologue detections, despite currently being relatively rare in comparison to detections of parent species, could in the future provide information on isotopic fractionation and reveal reaction pathways in specific regions [31].

As can be seen from Figure 6.4, all of the low energy conformers of each amino alcohol can be categorised based on their backbone structures in terms of the relative positions of the amino and the alcohol groups. That is, the lowest energy conformers follow the structure of conformer 1 of alaninol, g'Gg', where the conformer is dominated by the hydrogen-bond stabilisation between the $-NH_2$ and the –OH groups. The second group of amino alcohol structures follow the backbone structure of alaninol 2, gG'g. This can be seen in the structures in Figure 6.4, where the g'Gg' conformers are boxed in blue, and the gG'g conformers are boxed in red. Following the depiction in Figure 6.1, looking at the molecules' most stabilised configuration, the view along the C1-C2 bond clearly shows that the relatively large -X substituent is *anti* to the –OH group (-X = -Me for alaninol, -^{i}Pr for valinol, -CH_2 ^{i}Pr for leucinol, and -CHMeEt for isoleucinol). This was first discussed for alaninol

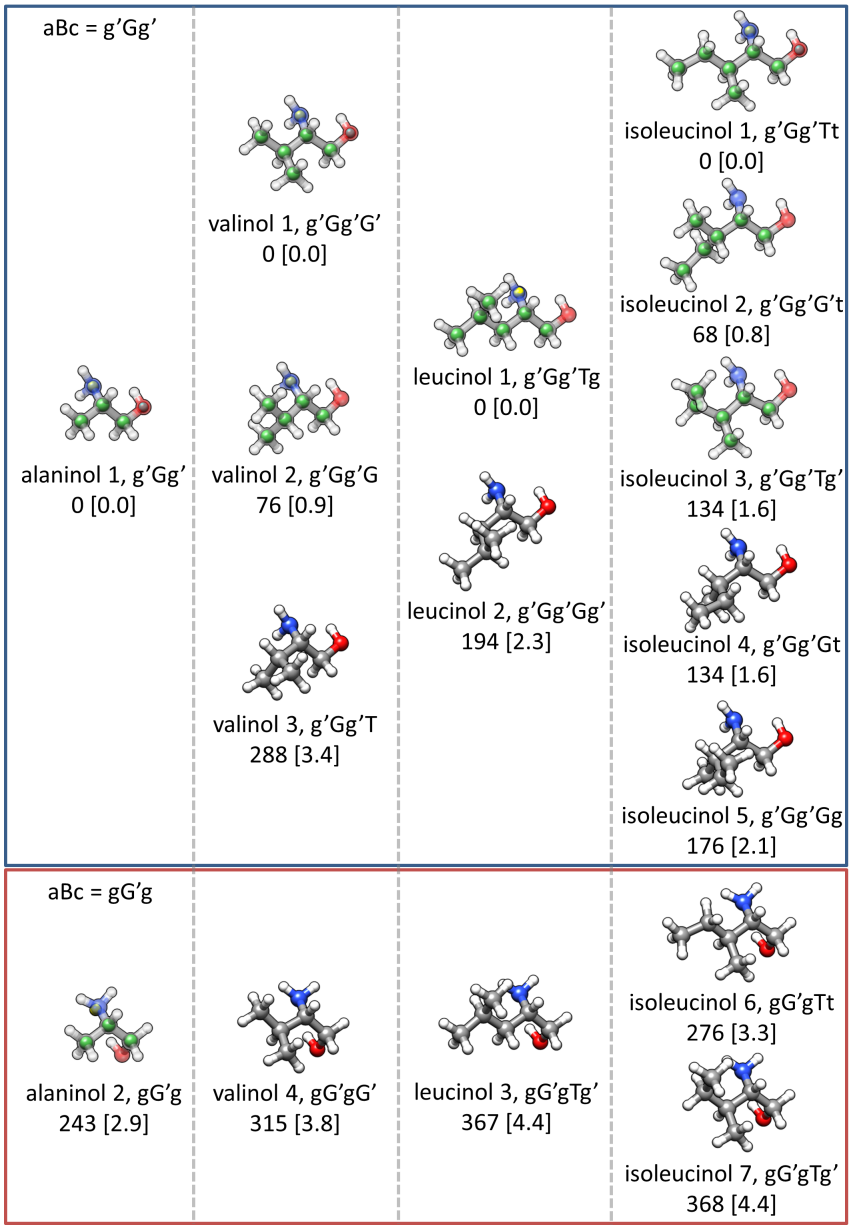

Figure 6.4: Alaninol, valinol, and leucinol (B3LYP/aug-cc-pVTZ), and isoleucinol (B3LYP-D3(BJ)/aug-cc-pVTZ), grouped by their aBc dihedral angle definitions. The zero-point energy corrected energy values, cm^{-1} [kJ mol^{-1}], are noted relative to the lowest energy conformer of each molecule. A comparison of the experimentally determined atom positions (carbon (green), nitrogen (yellow), and oxygen (cyan)) and the atom positions from the structure optimisation calculations (faded colour) are shown.

by the authors of Ref. [144]. If the molecule is viewed along the C2-C3 bond, the *anti* configuration for the $-CH_2OH$ on C2 and the bulkiest substituent on C3 can also be noted. Where there is more than one non-hydrogen substituent on the C3 position, the second is positioned *anti* to the $-NH_2$ group. This is seen most clearly in isoleucinol, where the *anti* pairs along the C2-C3 bond are $-CH_2OH$/-Et and $-NH_2$/-Me. The differences between the molecules arise from the various additions to the carbon chain at the C3 position. One would expect that as more extended carbon groups are added to the C3 position, the number of low-energy conformers increases due to the higher number of C-C single bonds around which bond rotations can occur. However, steric effects do play a role, and this can be seen by the fact that a number of 'expected' conformers are not observed; for example, the hypothetical structure of leucinol 1, g'Gg'Tg in which the C1-C2-C3-C4 dihedral angle is around -60° is not observed because of steric hindrance. Indeed, this hypothetical structure does not appear as a minimum in the conformational search performed, as it would likely interconvert to either leucinol 1, g'Gg'Tg, or leucinol 2, g'Gg'Gg'. Ref. [147] already noted steric effects as an important consideration in explaining 'missing' conformers. The structures of the amino alcohols follow chemical intuition when considering the *anti* configurations of the bulky substituents, but as already mentioned, steric effects should be considered as an important factor in determining if a structure will be observable in a supersonic expansion.

The studies on the rotational spectra of the relevant amino acids [146–149] allow for a comparison of the structural motifs with the amino alcohol structures observed here. The lowest energy structures of all the observed amino acids in the gas phase (Conformer I in the relevant publications) contain a bifurcated hydrogen bond between the amino group and the oxygen of the carbonyl group. With the lack of a carbonyl group in the amino alcohol analogues, it is not surprising that the lowest energy conformers of the amino alcohols are not structurally similar to those of the amino acids. However, in all cases, the lowest energy amino alcohol conformer resembles the motif of the next energetically favourable amino acid conformer observed; that is, alaninol 1, g'Gg' resembles alanine IIa, valinol 1, g'Gg'G' resembles valine IIa, leucinol 1, g'Gg'Tg resembles leucine IIb_1, and isoleucinol 1, g'Gg'Tt, resembles isoleucine IIa_1. The major differences between the similar structures can be explained by the constitutional difference regarding the carbonyl group. The amino acids contain the carbonyl group, which itself adopts a planar structure due to the sp^2-hybridised carbon. In the study on alanine, the authors of Ref. [146] state that "the amino acid backbone is nonplanar", and this non-planarity is further emphasised in alaninol, wherein the sp^2-hybridised carbon is now an sp^3-hybridised carbon. This results in a tetrahedral arrangement around the C1 atom, and, thus, a non-planar arrangement of the backbone. The hydrogen bond between the amino group and the alcohol group (-N$\cdots$H-) increases from 1.96(1) Å in alanine IIa [146]

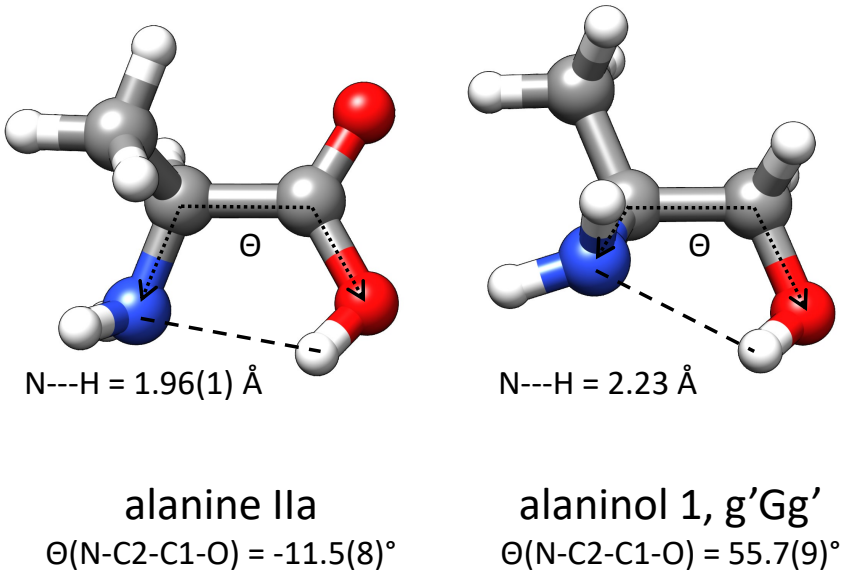

Figure 6.5: A summary of the structural comparison between alanine IIa and alaninol 1, g'Gg'. The structure of alanine IIa is taken from Ref. [146]. The alaninol 1, g'Gg' dihedral angle is experimentally determined, and the -N· · ·H- hydrogen bond distance is taken from the structure optimisation calculation at the B3LYP/aug-cc-pVTZ level of theory.

to 2.23 Å in alaninol 1, g'Gg' (from the structure optimisation calculation), and the N-C2-C1-O dihedral angle, the dihedral angle effectively defining the backbone planarity, increases from -11.5(8)° in alanine IIa [146] to 55.7(9)° in alaninol 1, g'Gg'. This comparison is summarised in Figure 6.5. The dihedral angle in alaninol is the same as that reported previously, 54(2)° [144], and it is in keeping with the dihedral angle from the theoretical structure at the B3LYP/aug-cc-pVTZ level of theory, which is 54.3°.

There is not as detailed an account of structural parameters in the studies of valine, leucine, or isoleucine. This means that valinol, leucinol, or isoleucinol cannot be directly compared to their amino acid analogues in the same manner as alaninol can be compared to alanine. The experimental N-C2-C1-O dihedral angle for valinol 1, g'Gg'G' is 50.5(7)°. This compares well with the dihedral angle in the optimised theoretical structure, which is 50.9°. The same angle was determined to be 50.9(8)° in isoleucinol 1, g'Gg'Tt, for which the theoretical value for the dihedral angle is 50.4° [94]. The full experimental substitution structure of leucinol 1, g'Gg'Tg is not currently available, as the ^{18}O isotopologue was not observed in natural abundance. The theoretical value (53.7°) is expected to be an adequate estimation because of the

Table 6.6: Summary of the N-C2-C1-O dihedral angles in the lowest energy conformers of alaninol, valinol, leucinol, and isoleucinol. Note that the value for leucinol is theoretical (at the B3LYP/aug-cc-pVTZ level of theory).

conformer	N-C2-C1-O dihedral angle / °
alaninol 1, g'Gg'	55.7(9)
valinol 1, g'Gg'G'	50.5(7)
leucinol 1, g'Gg'Tg	53.7*
isoleucinol 1, g'Gg'Tt	50.9(8)

agreement between experimental and theoretical values for the other amino alcohols in the series and the good agreement between experimental and theoretical rotational constants. All these values, which are summarised in Table 6.6, are in keeping with the dihedral angle in alaninol 1, g'Gg', and they show a 3.8 % average deviation from the mean value. Small deviations in the dihedral angles could originate from the different groups on the C3 atoms of the molecules. In valinol and isoleucinol, the groups on the C3 atom could exhibit steric hindrance with the groups on the C2 atom, which would make the N-C2-C1-O dihedral angle deviate more from 60°. This effect is less pronounced for alaninol and leucinol, which both have fewer bulky groups on the C3 atom. This can be seen in the Newman projections in Figure 6.1 and follows from the earlier discussion about the Newman projections. The dihedral angle N-C2-C1-O effectively defines the carbon backbone planarity in the amino alcohols studied, and the values reported here indicate non-planarity. Where data is available, an increase in the degree of non-planarity is seen when compared to the analogous amino acid.

Vibrationally Excited States

The spectroscopic data for the vibrational states of alaninol and valinol were accessible in the W-band experiments performed at room temperature. These states, like the isotopologues, could prove important if the ground state conformers are detected in warm regions of the ISM. The assignments of the vibrational states of alaninol conformer 1, g'Gg' are shown in the zoom-ins in Figure 6.6.

Figure 6.7 shows these motions alongside their energies with anharmonic corrections at the B3LYP/aug-cc-pVTZ level of theory. A short description of the fundamental modes follows: ν_{36} is the heavy atom torsion; ν_{35} is the rotation of the terminal methyl group; ν_{34} is a scissor motion of the carbon chain; ν_{33} is a motion in the $-NH_2$ group; ν_{32} is the $-CH_3$/-NH_2 scissor; ν_{31} is a wagging motion mainly af-

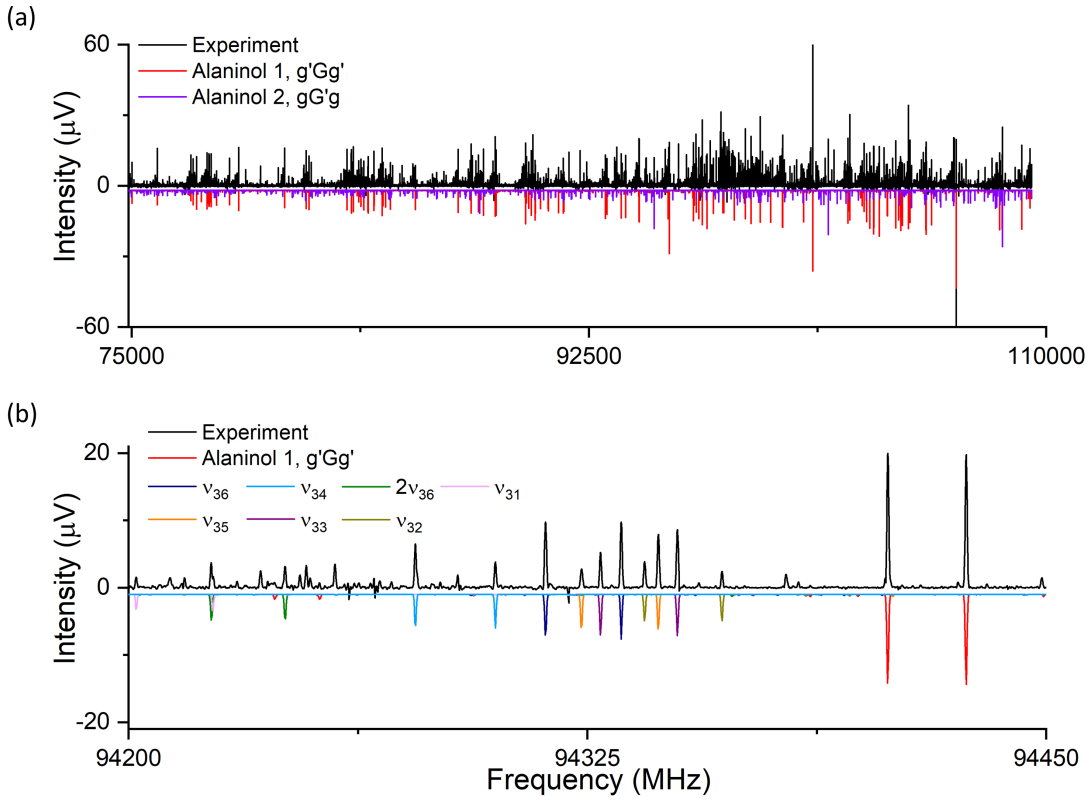

Figure 6.6: (a) High-frequency rotational spectrum of alaninol. The black trace is the experimental spectrum of 500,000 co-added FIDs, and the coloured traces are the simulated spectra based on the fitted rotational constants at 300 K. (b) Zoom-in illustrating the assignment of alaninol 1, g'Gg' and seven fundamental vibrational states of that conformer.

fecting the hydrogens on terminal atoms. The rotational constants derived for these, as well as the combination band $2\nu_{36}$, are detailed in Table 6.7. The experimental rotational constants for the observed vibrational state of alaninol 2, gG'g can be found in Table 6.8. The rotational spectra of three fundamental vibrational modes of valinol 1, g'Gg'G' were also assigned in this work. The rotational constants for these states are shown in Table 6.9. The ν_{54} fundamental mode of valinol 1, g'Gg'G' is a carbon backbone twist. The ν_{53} mode is an asymmetric rocking motion centred on the C1 nucleus. The third state is the overtone of ν_{54}. In total, the number of assigned vibrational states for each molecule, by conformer, is: 7 for alaninol 1, g'G'g; 1 for alaninol 2; gG'g; 3 for valinol 1, g'Gg'G'. The shifted theoretical rotational constants are included in the tables, which were gleaned from the anharmonic frequency calculations performed. A direct application of this work is that detected vibrational states could be used as temperature probes for regions where the ground state conformers are detected, for example in hot core regions. Further, the elimination of lines from vibrationally excited states (and isotopologues), which can occupy many channels in astronomical data sets, is an important step in making complex observational spectra more useful.

Partition Function Values

Searches for the assigned species in this work in observational data sets require not only accurate rest frequencies, but also information on the relative intensities of the rotational transitions. Partition functions, as described in Chapter 2, can be used to calculate transition intensities. This information can be further used to calculate column densities of detected species [66]. The rotational partition functions computed across the standard temperatures implemented in the JPL database [153] are reported in Table 6.10 for the lowest energy conformer of alaninol 1, g'Gg'. Two sets of rotational partition functions are tabulated: one for spin degeneracy equal to 1 ($2I+1=1$; the case where hyperfine splitting is not considered) and one for spin degeneracy equal to 3 ($2I+1=3$; the case where hyperfine splitting is considered). The rotational partition functions for the other assigned species - the ground state conformers alaninol 2, gG'g, valinol 1, g'Gg'G', valinol 2, g'Gg'G, valinol 3, g'Gg'T, valinol 4, gG'gG', leucinol 1, g'Gg'Tg, leucinol 2, g'Gg'Gg', leucinol 3, gG'gTg', the heavy-atom isotopologues, and the vibrationally excited states - can be found in Appendix 2. A consequence of varying temperature is the change in the intensity distribution of the observed rotational transitions. This can be seen in Figure 6.8, which shows the simulated spectra for alaninol 1, g'Gg' across a number of temperatures. This plot was made using the rotational partition functions determined for the case where the spin degeneracy is equal to 1. The general distribution of transitions is the same for the case where the spin degeneracy is equal to 3.

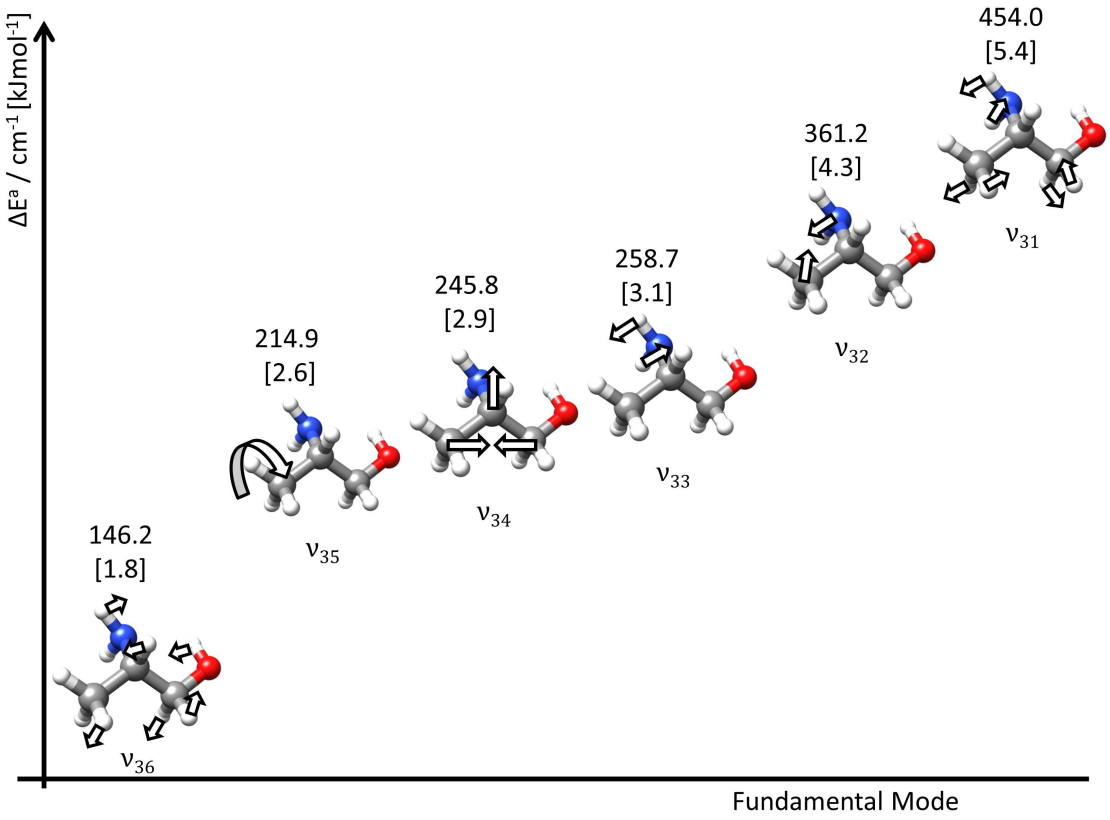

Figure 6.7: A summary of the assigned fundamental vibrations of alaninol 1, g'Gg'. The predominant motion for each mode is indicated by the arrows; a description can be found in the main text. The anharmonic energies presented are those calculated at the B3LYP/aug-cc-pVTZ level of theory.

Table 6.7: The experimental and theoretical rotational constants for the observed vibrational states of the lowest energy conformer of alaninol 1, g'Gg'. The theoretical parameters were obtained at the B3LYP/aug-cc-pVTZ level of theory and shifted by $\Delta A = 96.1$ MHz, $\Delta B = 52.7$ MHz, and $\Delta C = 43.0$ MHz to account for the differences in the experimental and theoretical rotational constants of the vibronic ground state. The harmonic and anharmonic energies (E^h and E^a respectively) of the vibrational states tabulated are relative to the energy of the alaninol 1, g'Gg' conformer.

	ν_{36}	ν_{35}	ν_{34}	ν_{33}	$2\nu_{36}$	ν_{32}	ν_{31}
E^h / cm^{-1} [kJ mol^{-1}]	143.8 [1.7]	226.5 [2.7]	254.2 [3.0]	265.3 [3.2]	287.7 [3.4]	362.9 [4.3]	449.6 [5.4]
E^a / cm^{-1} [kJ mol^{-1}]	146.2 [1.8]	214.9 [2.6]	245.8 [2.9]	258.7 [3.1]	294.8 [3.5]	361.2 [4.3]	454.0 [5.4]
A_{theory} / MHz	7906.6	7931.5	7959.9	7963.5	7864.8	7953.4	7941.4
B_{theory} / MHz	3636.6	3637.9	3639.0	3639.1	3632.6	3640.8	3637.8
C_{theory} / MHz	2745.7	2745.5	2742.6	2744.5	2743.8	2745.6	2747.0
A_{exp} / MHz	7907.215(19)	7930.202(22)	7971.968(21)	7948.078(15)	7873.565(20)	7946.558(21)	7922.836(21)
B_{exp} / MHz	3636.4881(14)	3638.1177(18)	3638.3710(15)	3641.2328(12)	3632.5727(16)	3640.4956(15)	3634.6192(19)
C_{exp} / MHz	2745.8447(13)	2745.4712(17)	2742.8480(13)	2744.8387(10)	2743.8372(13)	2745.4025(13)	2741.7037(13)
Δ_J / kHz	0.7308(17)	0.7200(23)	0.7151(19)	0.7222(17)	0.7393(22)	0.7202(22)	0.7209(28)
Δ_{JK} / kHz	3.4823(82)	3.581(12)	3.3912(93)	3.5434(83)	3.500(10)	3.442(13)	3.497(14)
Δ_K / kHz	1.77(51)	2.06(67)	2.49(58)	2.16(44)	2.06(62)	2.60(65)	2.27(69)
δ_J / kHz	0.1766(11)	0.1660(16)	0.1765(12)	0.1738(12)	0.1769(14)	0.1737(14)	0.1788(19)
δ_K / kHz	2.239(31)	2.191(39)	2.539(30)	2.373(26)	2.335(44)	2.294(46)	2.563(39)
No. of lines	78	53	69	68	65	55	51
σ / kHz	24.3	22.5	25.5	18.8	23.4	22.9	22.5

Table 6.8: The experimental and theoretical rotational constants for the observed vibrational state of alaninol 2, gG'g. The theoretical parameters were obtained at the B3LYP/aug-cc-pVTZ level of theory and shifted by the following values to account for the differences in the experimental and theoretical rotational constants of the vibronic ground state: ΔA = 41.8 MHz, ΔB = 94.4 MHz, ΔC = 80.6 MHz. The harmonic and anharmonic energies (E^h and E^a respectively) of the vibrational states are relative to the energy of the alaninol 2, gG'g conformer.

	ν_{36}	
	This work	Theory
E^h / cm^{-1} [kJ mol^{-1}]		137.9 [1.7]
E^a / cm^{-1} [kJ mol^{-1}]		136.6 [1.6]
A / MHz	6468.737(31)	6469.4
B / MHz	4138.1980(31)	4136.9
C / MHz	3323.3733(34)	3322.2
Δ_J / kHz	1.6329(51)	-
Δ_{JK} / kHz	5.433(29)	-
Δ_K / kHz	-4.28(72)	-
δ_J / kHz	0.2583(34)	-
δ_K / kHz	1.333(84)	-
No. of lines	46	-
σ / kHz	28.5	-

Table 6.9: The experimental and theoretical rotational constants for the observed vibrational states of valinol 1, g'Gg'G'. The theoretical parameters were obtained at the B3LYP/aug-cc-pVTZ level of theory and shifted by the following values to account for the differences in the experimental and theoretical rotational constants of the vibronic ground state: $\Delta A = 44.7$ MHz, $\Delta B = 28.6$ MHz, $\Delta C = 21.5$ MHz. The harmonic and anharmonic energies (E^h and E^a respectively) of the vibrational states are relative to the energy of the valinol 1, g'Gg'G' conformer. Distortion constants contained within square brackets were kept fixed to the values of the parent species.

	ν_{54}		ν_{53}		$2\nu_{54}$	
	This work	Theory	This work	Theory	This work	Theory
E^h / cm^{-1} [kJ mol^{-1}]		71.0 [0.9]		122.8 [1.5]		141.9 [1.7]
E^a / cm^{-1} [kJ mol^{-1}]		66.1 [0.8]		115.7 [1.4]		132.2 [1.6]
A / MHz	4020.001(11)	4019.2	4017.841(12)	4008.3	4009.515(11)	4015.0
B / MHz	1697.89013(67)	1698.1	1694.6255(21)	1702.3	1694.6859(12)	1694.9
C / MHz	1284.60788(48)	1284.8	1285.09357(59)	1284.8	1285.22224(98)	1285.4
Δ_J / kHz	0.10835(25)	-	0.10933(61)	-	0.11503(28)	-
Δ_{JK} / kHz	0.1909(11)	-	0.2163(16)	-	0.15858(80)	-
Δ_K / kHz	0.738(78)	-	[1.015838217]	-	[1.015838217]	-
δ_J / kHz	0.02641(13)	-	0.02709(36)	-	0.02221(23)	-
δ_K / kHz	0.2643(26)	-	[0.261615812]	-	[0.261615812]	-
No. of lines	100	-	31	-	34	-
σ / kHz	25.9	-	25.0	-	27.6	-

Table 6.10: The rotational partition functions (Q_{rot}) for alaninol 1, g'Gg' across standard temperatures as implemented in the JPL database [153] and as calculated by SPCAT [63] are tabulated to one decimal place, where $J_{max} = 220$ and $K_{max} = 40$. The vibrational partition function contributions were calculated by considering the theoretical anharmonic energies up to 500 cm^{-1}.

T / K	Q_{rot} [2I+1=1]	Q_{rot} [2I+1=3]	Q_{vib}
300	94350.6	283051.8	4.2
225	62723.5	188170.5	3.0
150	34638.3	103914.8	1.8
75	12292.0	36876.0	1.1
37.5	4347.6	13042.8	1.0
18.75	1538.7	4616.2	1.0
9.375	545.3	1635.8	1.0
1.5	-	107.3	1.0

The rotational partition functions were all calculated using the SPCAT program [63], which computes the values by direct summation over the rotational energy levels [90, 154]. It is important to ensure that the summation over the rotational energy levels converges, and this is done by ensuring that a sufficiently large number of rotational energy levels is taken into account. The maximum J and K values considered for each conformer for the summation calculation is detailed in the captions of the relevant tables of rotational partition functions. Further, the contribution of vibrationally excited states to the total partition function have been calculated, and the values are tabulated alongside the rotational partition functions. The vibrational partition function values were determined by considering the anharmonic energies from the calculations performed, up to the vibrational states with an energy of 500 cm^{-1} with respect to the ground state energy. This energy cut-off was chosen because of previous experiments showing the observation of vibrational states up to 500 cm^{-1} in the room-temperature cell of the W-band spectrometer. Combining intensity information, which is provided by these rotational partition function values, with line frequencies is paramount for confirming interstellar detections and calculating column densities in the ISM.

A study such as this, which covers a large frequency range and includes both low- and high-frequency data sets, is essential for facilitating comprehensive interstellar

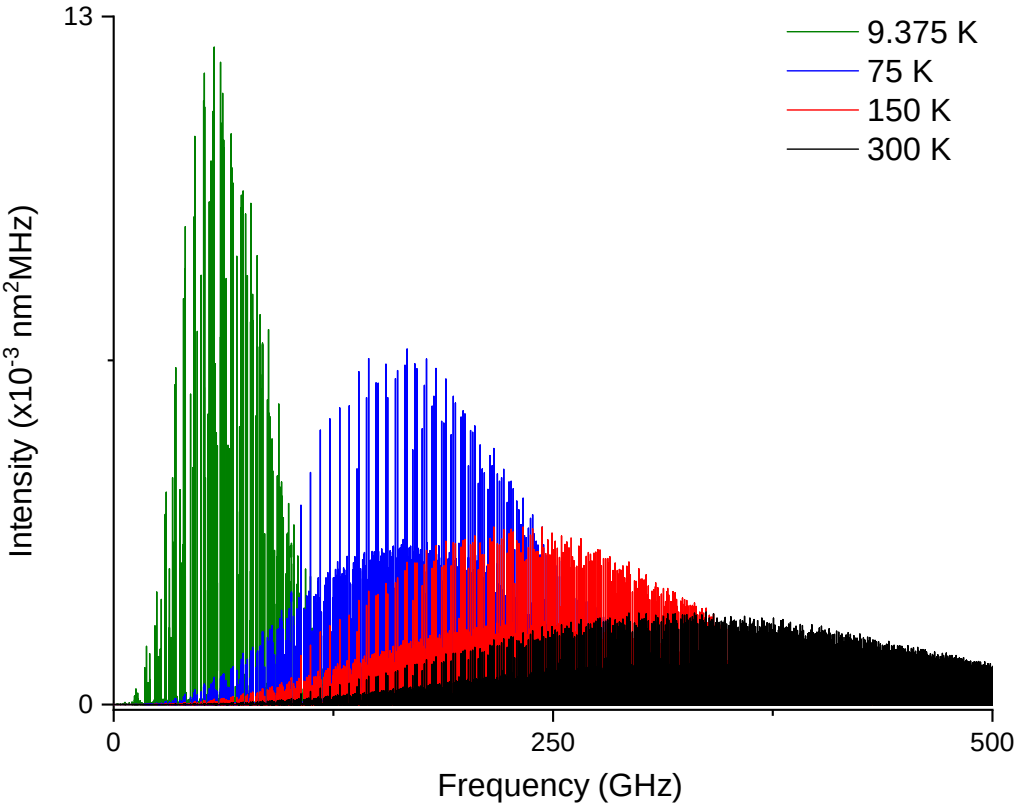

Figure 6.8: The distributions of rotational transitions of alaninol 1, g'Gg' across four of the standard temperatures implemented in the JPL database; 9.375 K, 75 K, 150 K, and 300 K [153]. The maximum frequency simulated here is 500 GHz, and the plot was made for the case where $2I+1=1$. Note that the intensity scale for the prediction at 9.375 K has been halved for a clearer comparison to the other predictions.

searches. The reason for this is two-fold. Firstly, the large frequency range allows experimental transition frequencies to be directly compared to observational spectra across a number of facilities. For example, data in the 18-26 GHz range could be used for future searches using data from the Next Generation Very Large Array (ngVLA), where nuclear quadrupole coupling could be relevant. Similarly, the line frequencies in the W-band (75-110 GHz) can be directly compared to those from ALMA Band 3 (84-116 GHz), where the hyperfine splitting has little-to-no effect for molecules similar in size to the amino alcohols presented here. Secondly, the high frequency data sets allow for the determination of accurately defined centrifugal distortion constants for the molecules studied. This can, in the absence of laboratory data higher than 110 GHz, provide more accurate predictions of transition frequencies into the THz regime than if predictions from rotational constants from centimetre-regime data, and thus typically involving low-J transitions, were simply extrapolated. The pitfalls of this were recently highlighted in Ref. [155] in a laboratory investigation and interstellar search for vinyl mercaptan. The potential issues presented there are reduced with this present study by providing high-level centrifugal distortion constants for alaninol, valinol, leucinol, and isoleucinol.

6.4 Conclusions

This extensive study of the rotational spectra of alaninol, valinol, leucinol, and isoleucinol resulted in the observation and assignment of a total of 76 species, including ground state conformers, isotopologues in natural abundance, and vibrationally excited states. The assignments, comprising of exact transition frequencies between 2-26 and 75-110 GHz and rotational constants up to the quartic centrifugal distortion constants, including the nitrogen nuclear quadrupole coupling constants, are accurately reported here for the first time for the majority of the species observed. The structures of the observed amino alcohols are confirmed with a combination of isotopologue data available in natural abundance and quantum-chemical calculations. The dominance of the intramolecular hydrogen bond in stabilising the lowest-energy conformers of each molecule is revealed, with each exhibiting similar dihedral angles between N(lp)-N-C2-C1, N-C2-C1-O, and C2-C1-O-H. This work provides the astronomical community with the extensive data necessary to search for these astrochemically important molecules. Their detection would establish a new class of compounds observed in the ISM and could point towards areas where their amino acid analogues could be present in the gas phase.

Chapter 7

Rotational Spectroscopy of Imidazole

This chapter is based on the following publications:

- B. M. Giuliano, L. Bizzocchi, A. Pietropolli Charmet, B. E. Arenas, A. L. Steber, M. Schnell, P. Caselli, B. J. Harris, B. H. Pate, J.-C. Guillemin, A. Belloche *Rotational spectroscopy of imidazole: Improved rest frequencies for astrophysical searches*, Astronomy and Astrophysics **628**, A53 (2019).

- B. E. Arenas, G. Batra, A. L. Steber, L. Bizzocchi, B. M. Giuliano, P. Caselli, B. J. Harris, B. H. Pate, A. Pietropolli Charmet, M. Schnell *Rotational spectroscopy of imidazole: three vibrationally excited states and a molecular structure based on an extended frequency range* **In Preparation**.

7.1 Introduction

Imidazole, *c*-$C_3H_4N_2$, is a relevant molecule for astrochemical studies due to the confirmed presence of N-heterocycles on meteors (see Ref. [156] and references therein), suggesting conditions exist in space for its formation in substantial abundance. Examples of N-heterocycles are also prevalent in biologically important motifs. For example, imidazole is present in the purine bases of DNA and RNA, as well as in the structures of the amino acid histidine and the neurotransmitter histamine. Despite a number of cyclic compounds already being observed in the interstellar medium (ISM), imidazole has yet to be detected [157].

Imidazole was studied with an astrochemical motivation by Schwell *et al.*, where the fragmentation patterns of imidazole with photoionisation mass spectrometry was studied. The fragments observed, such as H_2CCNH^+, $HCNH^+$, and $HCCN^+$, were

explained, for example, with the loss of H, HCN, and CH_2CH, H shifts, and ring-breaking processes [158]. The survival of imidazole, and other nitrogen-containing cyclic molecules, was discussed. In summary, the authors of Ref. [158] conclude that protection from vacuum ultraviolet (VUV) radiation is required for detectable quantities of the N-bearing molecules they studied to survive in the ISM. The molecules would likely undergo dissociative ionisation if irradiated with VUV radiation - the expected maximum ionisation yield of imidazole was estimated to be 54% in diffuse interstellar clouds [158]. Therefore, the authors suggest searches for imidazole in denser regions, such as hot molecular cores and in young circumstellar disks, where shielded conditions are likely to exist. The authors of Ref. [159] performed a computational study that looked at the formation of adenine in the ISM, which led to some potential pathways towards imidazole from simple building blocks. It was concluded that the nucleobase could be synthesised though a series of barrierless reactions in the gas phase and in water ice environments from HCN, HCCN, NH_2CN, and CN. A number of imidazole-like molecules appear as intermediates in the proposed reaction scheme towards adenine, and the termination or slight alteration of the reaction scheme could hint towards interstellar routes to imidazole.

Blackman *et al.* (1976) presented an analysis of the rotational spectrum of imidazole and N-deutero imidazole, which focussed on the characterisation of the quadrupole hyperfine structure [160]. Building on this, and their previous study in Ref. [161], Christen *et al.* (1982) provided a set of rotational constants for the molecule's parent species, as well as the deuterium, carbon-13, and nitrogen-15 isotopologues [162]. This allowed a comprehensive structure of imidazole in the gas phase to be constructed. Despite the considerable amount of data presented in the latter paper, only limited centrifugal distortion constants were derived because of the small frequency coverage ($\nu < 40$ GHz) and the use of an outdated pre-Watson Hamiltonian [59] to describe the rotational energy. In order for searches for imidazole in the ISM to be performed, in particular in the millimeter and sub-millimeter (sub-mm) ranges, new laboratory investigations are required. The present work addresses this and includes measurements in higher frequency regimes for the first time. The fits across the 2-295 GHz range facilitate targeted observational campaigns, for example, across a number of operating bands of the Atacama Large Millimeter/submillimeter Array (ALMA).

Whilst the main motivation behind this work is the astrochemical interest in imidazole, it is worthy to note that imidazole finds applications throughout a number of fields. For example, as already alluded to, the imidazole motif can be found throughout biological systems. The biological activity of imidazole and its derivatives are exploited in the pharmaceutical industry, for example in anti-fungal agents [163]. Imidazole is also at the forefront of the ionic liquid field, and as such, is used extensively for biphasic reaction catalysis (for example, polymer synthesis) and wa-

ter purification [164]. This non-exhaustive list of examples shows the prevalence of the imidazole ring in the chemical sciences.

In this chapter, the rotational spectra of the vibronic ground state, the low-lying vibrationally excited states, and the isotopologues of imidazole in the 2-295 GHz frequency region are investigated. The resulting rotational constants, quadrupole coupling constants, and high-order distortion constants allow for the accurate prediction of the rotational line lists for these species in the millimeter-wave (mmw) regime and beyond. This data is essential for observational searches, and an upper limit for the vibronic ground state of imidazole in the ISM, which was obtained from a search for the molecule in Sagittarius B2(N2) (Sgr B2(N2)), is also presented in this chapter.

7.2 Experimental and Theoretical Details

The experimental work was conducted across a number of high-resolution broadband chirped-pulse Fourier transform rotational spectrometers at the Deutsches Elektronen-Synchrotron (DESY, Germany), which are all described in detail in Chapter 3, and at the University of Virginia (USA). The work covers the frequency ranges 2-8, 12-15.5, 18-26, 75-110, and 260-295 GHz.

The Hamburg COMPACT spectrometer was used to record the spectrum of imidazole across the 2-8 GHz and 12-15.5 GHz regions [92–94]. For these measurements, solid imidazole (purchased from Sigma Aldrich and used without further treatment) was placed in a reservoir nozzle, which was heated to 90 °C. Neon, at a pressure of 3 bar, was used a backing gas, and the imidazole vapour was supersonically expanded into the vacuum chamber. For the 2-8 GHz experiment, 1.6 million free induction decays (FIDs) were co-added and fast Fourier transformed into the frequency domain, and 1.2 million FIDs were co-added and fast Fourier transformed for the 12-15.5 GHz experiment. The FIDs were recorded for 40 μs for the 2-8 GHz experiment and for 20 μs for the 12-15.5 GHz experiment.

The spectrum across the 18-26 GHz region was recorded using a segmented chirped-pulse Fourier transform microwave spectrometer [94]. The FIDs for each segment were recorded for 10 μs. The spectrum consisted of 1.8 million co-added FIDs. The imidazole sample was placed in a similar heatable reservoir nozzle as in the experiments with the Hamburg COMPACT spectrometer, and the sample was heated to 90 °C. Three bar backing pressure of neon was used as the carrier gas.

The spectrum in the 75-110 GHz region was recorded in a room temperature flow cell set-up with a BrightSpec, Inc. W-band spectrometer. This spectrometer's high dynamic range (HDR) mode was used. The excitation pulses were 500 ns in duration, and the FIDs were recorded for 4 μs. A total of 500,000 FIDs were co-added and fast Fourier transformed into the frequency domain. The imidazole

sample was heated to 90 °C in an external reservoir, and the vapours were pulsed into the sample chamber without a backing gas.

The 260-295 GHz spectrum was recorded at the University of Virginia. The instrument is described in detail in Refs. [40, 95, 165]. The operation of the 260-295 GHz spectrometer also follows the segmented operating regime. The arbitrary waveform generator (AWG) produces a pulse train in the region 2-4 GHz, which is then frequency up-converted by an active multiplier chain (AMC) to the 260-295 GHz range. The spectrum is split into fifty segments of 720 MHz bandwidth, where each 720 MHz bandwidth is made up of thirty 24 MHz chirps. The excitation pulse duration was 100 ns, and the FIDs, after collection and frequency down-conversion, were recorded for 1900 ns . The experiment was performed with imidazole crystals, which were sublimed, and the vapours were allowed to enter the sample chamber, where a pressure of 7 μbar was maintained in a slow-flow configuration. The number of co-added FIDs in this case was 10 000, which equates to approximately three minutes of measurement time.

Much of the structural optimisation work on imidazole was performed by a collaborating partner, and thorough details of the computation procedure can be found in Refs. [88] and [86]. In short, the CCSD(T) method was used for structure optimisation [87], and the basis set used was a composite basis set, consisting of a Dunning-type foundation with a number of corrections and approximations.

Quantum chemical calculations were also used to support the assignment of the vibrational states, which were accessible because of the room temperature experiments in the high frequency regimes. In particular, structure optimisation and anharmonic frequency calculations were performed at the MP2/aug-cc-pVTZ level of theory as implemented in Gaussian09 [73]. As well as allowing the visualisation of the associated motions, the frequency calculations provided theoretical rotational constants for the vibrational states. These theoretical rotational constants were adjusted by applying the difference between the theoretical rotational constants of the vibronic ground state species (at the same level of theory and basis set) and the experimentally determined values. These adjusted theoretical rotational constants were used as the starting point for the assignment of the vibrationally excited states.

The spectra were initially fit using the PGOPHER programme [70]. Global fits were obtained using Pickett's SPFIT/SPCAT suite of programmes [63]. The substitution structure analysis was performed using the KRA programme, and the EVAL programme was used to determine structural parameters and their associated errors [90].

7.3 Results and Discussion

Vibronic Ground State

Imidazole is a five-membered ring molecule containing two nitrogen atoms; its structure, the principal axes, and a conventional numbering of the skeleton atoms are depicted in Figure 7.1. The delocalisation of six electrons (four double-bond π and two of the N lone pair) provides improved stability of the ring skeleton (aromaticity) and constrains the molecule to a planar structure. From the spectroscopic point of view, imidazole is an oblate-type asymmetric top ($\kappa = 0.8581$) with dipole moment components of $\mu_a = 3.603$ D and $\mu_b = 0.680$ D [162].

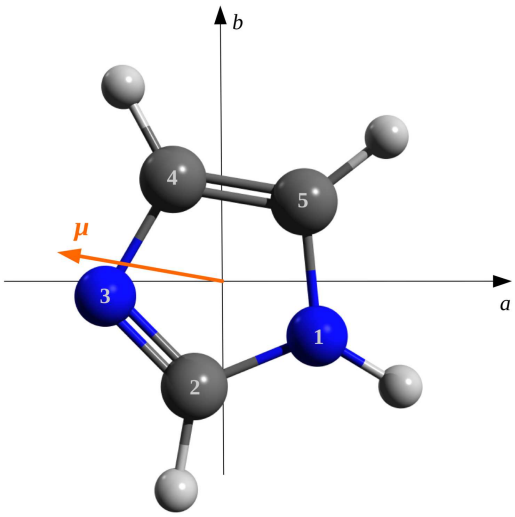

Figure 7.1: Molecular structure and principal inertial axes of imidazole. The c axis is perpendicular to the ab molecular plane. The orange arrow indicates the direction of the electric dipole moment μ and points towards the displacement of the notional negative charge.

The two nitrogen atoms (numbered as atoms 1 and 3 in Figure 7.1, hereafter N(1) and N(3)) generate the hyperfine structure (HFS) of the rotational transitions through the quadrupole coupling between the electric field gradient and the I=1 spin of the ^{14}N nuclei. This HFS is rather complex, and for low-J transitions, it consists of a crowded pattern of components spread over a frequency interval up to 4.5 MHz. Figure 7.2 presents two illustrative cases: the upper panel shows the crowded pattern of the a-type $1_{1,0}$ - $1_{1,1}$ transition, which consists of 36 hyperfine components. On the opposite extreme, the lower panel displays the fundamental b-type line $1_{1,1}$ - $0_{0,0}$, characterised by a loose HFS composed of only seven features. The difference in the number of hyperfine components originates from the transitions

involved; the latter transition shows fewer hyperfine components as the J=0 energy level does not split to the same extent as the J=1 energy levels.

Essentially, all the transitions recorded at frequencies below 26 GHz show a resolvable HFS. When possible, a single hyperfine transition has been assigned to a given resolved feature detected in the rotational spectrum. Measurements corresponding to tight line blends have instead been assigned to the subset of components that make up the dominant intensity contribution. In these cases, the intensity-averaged frequency is compared with the experimental datum in the least-squares fit. Loose blends of unresolved components, resulting in broad or distorted line profiles, have not been used in the analysis.

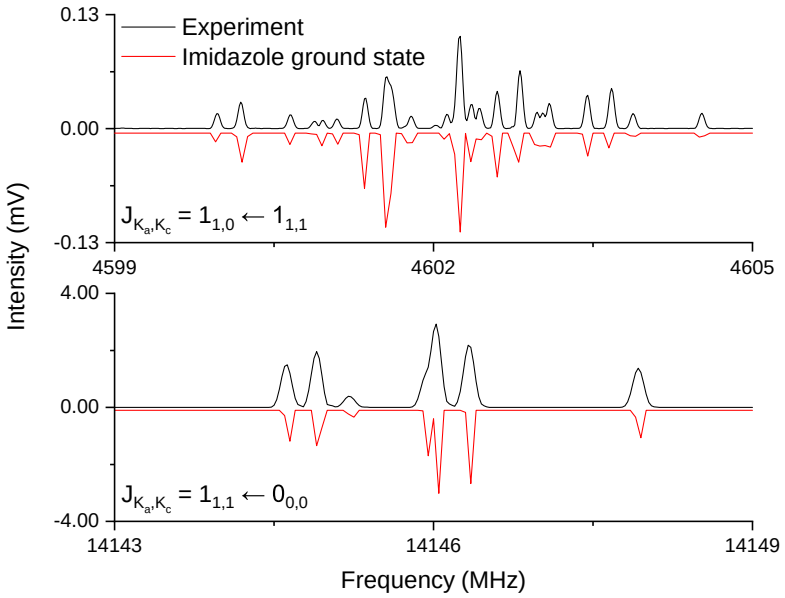

Figure 7.2: Recordings (black trace) of the $1_{1,0}$ - $1_{1,1}$ (upper panel) and $1_{1,1}$ - $0_{0,0}$ (lower panel) rotational transitions of imidazole. The red trace indicates the predicted position of the hyperfine components computed using the spectroscopic parameters found in Table 7.1.

The lines measured in the W band (75–110 GHz, shown in Figure 7.3) and in the sub-mm regime (260–295 GHz) generally do not show a detectable HFS of the rotational transitions for molecules of this size because nuclear quadrupole coupling decreases with increasing rotational quantum number. This subset constitutes the bulk of the experimental data set. For these data, the contribution due to the nuclear quadrupole coupling was not considered, and the experimentally measured frequencies were assigned to the corresponding pure rotational transitions.

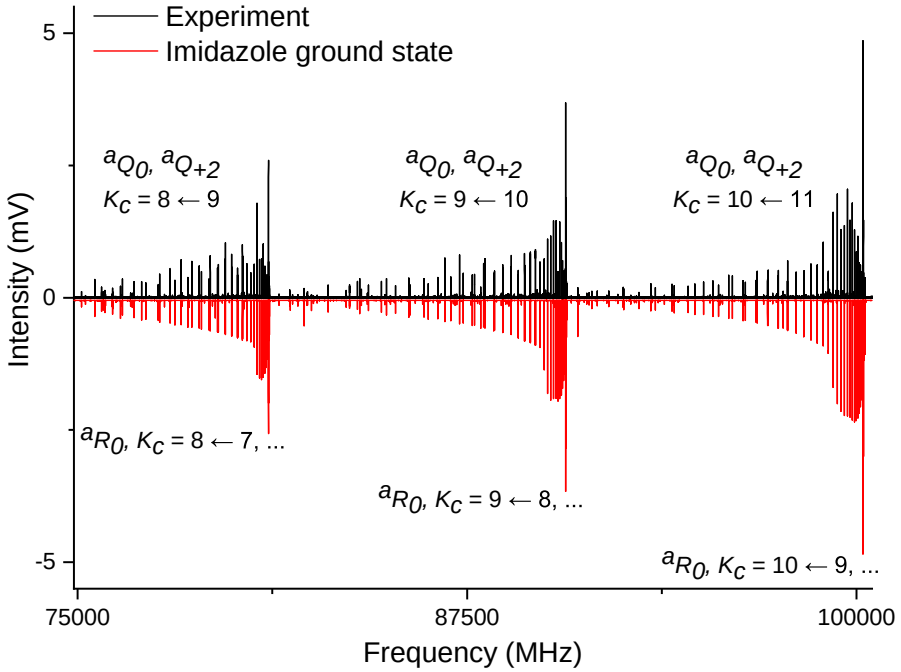

Figure 7.3: Recording (black trace) of the imidazole rotational spectrum in the 3 mm region taken with the segmented chirped-pulse W-band spectrometer. The red trace indicates the predicted positions of the lines computed using the spectroscopic parameters of Table 7.1. The symbol ${}^xM_{\delta K_a,\delta K_c}$ is used to label in a compact form the transition type for an asymmetric rotor: x=a, b, c indicates the dipole moment component involved, M = P, Q, R is the symbol for the transitions with Δ J = -1, 0, +1, respectively, and δK_a and δK_c refer to the (signed) change of the K_a and K_c pseudo-angular quantum numbers.

The spectroscopic parameters for imidazole resulting from the analysis of the full data set of 698 lines are reported in Table 7.1. Table 7.1 contains the results of two different fits, together with a compilation of theoretically computed spectroscopic constants. Precise determinations of the rotational constants A, B, and C were obtained, whose uncertainties are reduced by a factor of ~ 100 compared to previous findings [162]. A full set of quartic centrifugal distortion constants was obtained for the first time. In previous work, the Watson-reduced [59] form of the rotational Hamiltonian was not used (only three τ unreduced quartic coefficients were reported in Ref. [162]). The precision of the new quartic centrifugal distortion constants determined in this work is high, with relative 1σ errors ranging in the 10^{-3}-10^{-5} interval. A fair-to-good determination of the sextic constants H_{JK} ($\sim 1\%$), H_{KJ} ($\sim 5\%$), and h_2 ($\sim 7\%$) and of the octic correction parameter L_{JKK} ($< 10\%$) was also

obtained. The new values of the quadrupole coupling constants compare very well with those reported previously [160, 162], but the previously reported precisions are improved by factors of 6–10. For N(1) the anisotropy term χ_{bb}-χ_{aa} is too small to be determined from the present set of data. This is in agreement with the results of Ref. [162], where a quadrupole coupling analysis of several isotopic species of imidazole was performed and individual determinations of each diagonal element of the χ tensor were obtained. From their results, it holds that χ^1_{bb}-χ^1_{aa}=0.030(24) MHz, a value that is essentially zero within the quoted uncertainty.

The comparison of the experimentally derived spectroscopic parameters with those obtained from the theoretical calculations (reported in the rightmost column of Table 7.1) shows an excellent agreement. The ground-state rotational constants are predicted within 10 MHz, which corresponds to a 0.1% maximum discrepancy. Experimental and *ab initio* values of the quartic centrifugal distortion constants also compare well (within 1–2% for the diagonal D_J, D_{JK}, and D_K, 10–20% for the small d_1 and d_2). Furthermore, for the three determined sextic constants, the sign and the order of magnitude have been correctly predicted by theory.

Fit I and fit II (Table 7.1) differ for the different choice of the assumed values of the sextic centrifugal distortion constants which could not be adjusted in the least-squares analysis. These were the H_J, H_K, h_1, and h_3 constants. In fit I, these parameters were held fixed at the corresponding theoretically computed values (the column labelled "ab initio"), while in fit II, these constants were simply constrained to zero. As expected, the two sets of spectroscopic constants are slightly different, reflecting the existing correlations between the model parameters, for instance, H_J with C and D_K; H_K with A, B, C, and D_J.

A listing of the rotational (Q_{rot}), hyperfine (Q_{HFS}), and vibrational (Q_{vib}) partition functions of imidazole is provided in Table 7.2. They are computed for temperatures ranging in the 3-300 K interval. These values are computed by direct summation over the rotational levels whose energy position is accurately determined during the spectral analysis. The vibrational partition functions are obtained through direct summation on all energy levels (including combinations and overtones), which contribute to Q_{vib} higher than 10^{-7}. The vibrational energies were derived theoretically using a hybrid method that employs harmonic CCSD(T) calculations with complete basis set extrapolation, plus an MP2 estimate of the anharmonic contribution [166].

Vibrationally Excited States

The experiments in the 75-110 GHz and 260-295 GHz ranges were performed in room temperature flow cells, and thus the rotational spectra of low-lying vibrationally excited states could be observed and assigned. The assignment of three of these vibrationally excited states is presented here: ν_{21}, ν_{20}, and ν_{19}. The assign-

Table 7.1: Experimental and theoretical spectroscopic parameters of imidazole. Theoretical parameters (calculated using the CCSD(T) composite basis set method described in Section 7.2) are rounded to two decimal places. Values in square brackets were kept fixed.

Parameter		fit I	fit II	ab initio
A	/ MHz	9725.30651(18)	9725.30901(19)	9731.03
B	/ MHz	9373.99203(17)	9373.99319(18)	9387.36
C	/ MHz	4771.91599(18)	4771.91736(19)	4776.42
D_J	/ kHz	3.27363(15)	3.27806(15)	3.24
D_{JK}	/ kHz	-5.17552(17)	-5.17584(17)	-5.11
D_K	/ kHz	2.24932(14)	2.24728(14)	2.21
d_1	/ kHz	0.019825(17)	0.020145(17)	0.02
d_2	/ kHz	0.016675(10)	0.016700(10)	0.02
H_J	/ mHz	[1.367]	[0.0]	1.37
H_{JK}	/ mHz	-6.148(51)	-6.111(53)	-5.54
H_{KJ}	/ mHz	10.15(19)	9.02(19)	6.99
H_K	/ mHz	[-2.813]	[0.0]	-2.81
h_1	/ mHz	[0.0459]	[0.0]	0.05
h_2	/ mHz	-0.0757(51)	-0.1191(52)	-0.06
h_3	/ mHz	[-0.0147]	[0.0]	-0.01
L_{JKK}	/ μHz	-1.98(10)	-1.28(10)	–
$\chi_{cc}^{(1)}$	/ MHz	-2.5592(62)	-2.5599(63)	-2.67
$\chi_{bb}^{(1)} - \chi_{aa}^{(1)}$	/ MHz	[0.0]	[0.0]	-0.07
$\chi_{cc}^{(3)}$	/ MHz	2.2293(66)	2.2293(66)	2.21
$\chi_{bb}^{(3)} - \chi_{aa}^{(3)}$	/ MHz	5.727(12)	5.727(12)	5.74
No. of lines			698	
σ_{w}		0.76	0.76	

ment process was supported by anharmonic frequency calculations (see Section 7.2), and the adjusted theoretical rotational constants are tabulated alongside the experi-

Table 7.2: Rotational, hyperfine, and vibrational partition functions of imidazole.

T / K	Q_{rot}	Q_{HFS}	Q_{vib}
3	43.092	387.83	1.0000
5	91.766	825.90	1.0000
10	257.57	2318.09	1.0000
15	471.98	4247.77	1.0000
25	1013.48	9121.30	1.0000
50	2862.31	25760.8	1.0000
100	8090.49	72811.4	1.0008
150	14860.8	133638	1.0013
225	27293.2	244152	1.1051
300	41965.5	371478	1.3522

mentally determined rotational constants in Table 7.3. The motions associated with the assigned fundamental modes could also be inferred from the same anharmonic frequency calculations. The ν_{21} vibration is a stretch in the N(1)-H bond, resulting in an out-of-plane displacement of the hydrogen atom. The ν_{20} and ν_{19} vibrations are wagging motions along the C(4)-C(5)-N(1) and the N(1)-C(2)-N(3) sections of the ring, respectively, which manifest as the out-of-plane displacement of the hydrogen atoms connected to these heavy atoms. Table 7.3 also contains depictions of these fundamental modes. The experimental spectrum is shown in Figure 7.4, and it is compared to the simulated spectra of the fitted rotational constants for the assigned vibrational states. The spectra of these states, like those of the imidazole vibronic ground state and isotopologues in the same frequency region, are characterised by an intense Q-branch (ΔJ=0) ladder, which culminates with a set of R-branch (ΔJ=+1) transitions [86].

The assigned states could prove to be important targets for astronomical searches in regions where the parent imidazole species is detected, and these searches are facilitated by the rotational constants and line frequencies reported here. On one hand, the vibrational states could act as effective temperature probes for regions that they are detected in and could aid in the characterisation of, for example, hot core regions. On the other hand, eliminating lines in observational data sets that come from known species, and their associated isotopologues and vibrational states, is an important step in processing complex, confusion-limited spectra. Knowledge of these lines can draw attention to cases of blended transitions and prevent misassignments,

particularly in broadband, unbiased observational campaigns.

The rigidity of the imidazole ring motif may be hinted towards by the relatively high energy of the vibrationally excited states. The lowest energy vibrational state, ν_{21}, has ΔE^a=521.4 cm^{-1} relative to the imidazole ground state at MP2/aug-cc-pVTZ. In contrast, imidazolidine (c-$NHCH_2NH(CH_2)_2$), a fully saturated ring analogue, has its lowest energy vibrational state, ν_{33}, only 71.4 cm^{-1} above the ground state at MP2/aug-cc-pVTZ, pointing towards the increased flexibility of the fully saturated structure.

The vibrationally excited states of a number of other aromatic molecules have been characterised. The fundamental modes of the nitrogen-containing aromatic molecule indole, which is the simplest example of a N-substituted polycyclic aromatic hydrocarbon, have had energies reported following the analysis of their rotational spectra. The energies of the ν_{42} and ν_{41} states were determined as 207 and 241 cm^{-1}, respectively [167]. These states are substantially lower in energy compared to the lowest vibrational states of imidazole. One implication of this is to suggest that the imidazole structure, as alluded to earlier, is rather inflexible. When the vibrational motion is centred on a substituent, rather than the aromatic ring structure, the energies of the corresponding states are comparatively low. For example, in 2018, the two lowest vibrational states of benzonitrile were studied in the region 103-360 GHz. The authors of Ref. [168] report the energies of the ν_{22} and ν_{33} vibrational states, both of which are vibrations in the cyano group rather than the benzene ring, as being 141 and 163 cm^{-1}, respectively. In the publication, the authors also report on the interstate mixing of the vibrational states, a complete fit for which was only achievable with a Coriolis-coupled model. The second implication is the effect that these high energies may have on astronomical searches. The difference in the signal-to-noise ratio (SNR) between the experimental spectra of the imidazole ground state and the lowest energy vibrationally excited state, ν_{21}, is a factor of 10. For hydantoin (c-$NHC(O)NHCH_2C(O)$), a structurally similar molecule to imidazole, for which a structural comparison is laid out in the next section, the ratio of the SNR of the ground state to the first vibrationally excited state (140 cm^{-1} above the ground state) was found to be 1:0.6 [169]. This reinforces experimentally the higher relative energies of the imidazole vibrationally excited states, and it suggests the high temperature required in interstellar regions in which searches for these states should be carried out.

Isotopologues and Structure Determination

Using the rotational constants from Ref. [162] and the high-order distortion constants determined for the parent species [86] as a starting point, the spectra of the singly substituted isotopologues of imidazole were assigned. Table 7.4 shows the

Table 7.3: The experimentally determined rotational constants of the observed imidazole vibrational states, which are tabulated alongside the adjusted theoretical rotational constants for each state (ΔA = 22.97 MHz, ΔB = 72.66 MHz, ΔC = 24.97 MHz). Values contained in square brackets were kept fixed to the parent species values. The harmonic and anharmonic energies of each state relative to the ground state at the MP2/aug-cc-pVTZ level of theory are also shown. The structures show the associated motions of the states (see text for full descriptions). The figures depict the optimised structure of imidazole superimposed with the extreme positions of the atoms during the vibration.

mode assigned	ν_{21}		ν_{20}		ν_{19}	
associated motion	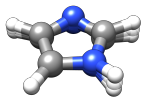		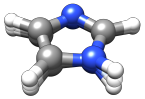		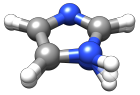	
	experimental	theoretical	experimental	theoretical	experimental	theoretical
ΔE^h / cm^{-1}		561.5		649.2		682.2
ΔE^a / cm^{-1}		549.3		637.9		669.1
A / MHz	9705.93562(85)	9708.4	9695.8454(17)	9697.0	9703.4261(18)	9701.4
B / MHz	9356.37255(79)	9357.4	9352.6015(19)	9353.9	9344.6215(14)	9345.1
C / MHz	4771.23603(40)	4772.4	4773.4111(12)	4773.5	4773.48988(67)	4773.4
D_J / kHz	3.26871(40)		3.2253(13)		3.21492(71)	
D_{JK} / kHz	-5.15120(53)		-5.0268(13)		-4.98702(63)	
D_K / kHz	2.23314(36)		2.14483(98)		2.11768(43)	
d_1 / kHz	0.01875(31)		[0.019825]		0.0512(15)	
d_2 / kHz	0.01779(69)		[0.016675]		0.0148(27)	
H_J / mHz	[1.367]		[1.367]		[1.367]	
H_{JK} / mHz	[-6.148]		[-6.148]		[-6.148]	
H_{KJ} / mHz	[-10.15]		[-10.15]		[-10.15]	
H_K / mHz	[-2.813]		[-2.813]		[-2.813]	
h_1 / mHz	[0.0459]		[0.0459]		[0.0459]	
h_2 / mHz	[-0.757]		[-0.757]		[-0.757]	
h_3 / mHz	[-0.0147]		[-0.0147]		[-0.0147]	
L_{JKK} / μHz	[1.98]		[1.98]		[1.98]	
No. of lines	234		119		115	
σ / kHz	20.6		21.6		27.4	

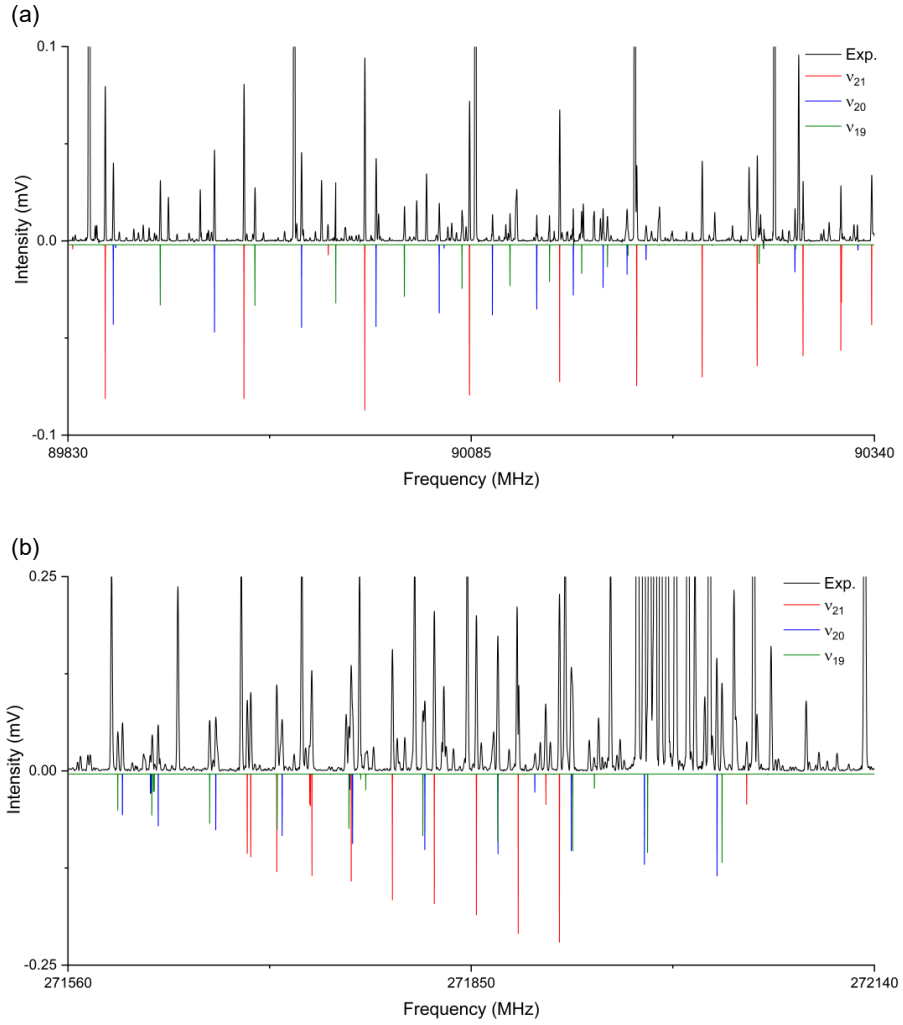

Figure 7.4: The spectrum of imidazole (black) with the simulated spectra of the experimentally determined rotational constants for the three assigned vibrationally excited states at 300 K (ν_{21} is shown in red, ν_{20} is shown in blue, and ν_{19} is shown in green). (a) A zoom-in of the W-band spectrum, showing a number of assigned Q-branch transitions. (b) Assigned R-branch transitions of the normal modes in the 260-295 GHz region.

experimentally determined constants and compares them to those reported in Ref. [162]. The J_{max} values assigned has increased from J=35, 30, 37, 29, 18 by Christen *et al.* to J_{max}=45, 48, 34, 52, 44 in this work for ^{15}N(1), ^{13}C(2), ^{15}N(3), ^{13}C(4), and ^{13}C(5), respectively. The maximum percentage difference between the rotational constants determined here and those from Ref. [162] is 0.007 % for A, 0.019 % for B, and 0.007 % for C. Figures 7.5 and 7.6 show the experimental spectrum compared with the simulated spectra of the fitted rotational constants for the assigned isotopologues.

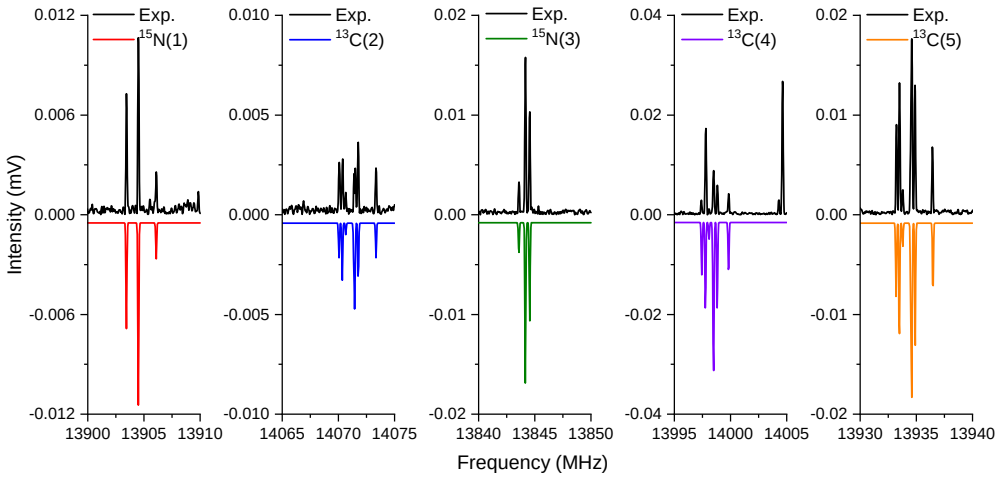

Figure 7.5: A zoom-in of the assigned spectra of the isotopologues of imidazole in the frequency range 12-15.5 GHz, where the $1_{0,1}$-$0_{0,0}$ transitions show hyperfine splitting. The experimental spectra are shown in black, and the simulated spectra of the fitted rotational constants at 3 K are shown in colour. The atom labelling scheme is detailed in Figure 7.7.

Note that Figure 7.5 shows a section of the low frequency data set (12-15.5 GHz), where the spectra of the isotopologues exhibit hyperfine splitting due to the presence of the ^{14}N nucleus/nuclei. Figure 7.6 shows a section of the high frequency data set (260-295 GHz), where this splitting is no longer present due to the collapse at the relatively high principal rotational quantum number, J. The constants in Table 7.4 are a result of fitting the rotational constants and centrifugal distortion constants to all the assigned line frequencies and fitting quadrupole coupling constants only to line frequencies in the 2 - 26 GHz region, as described in the previous sub-section.

The assigned isotopologues allowed for the determination of the structure of imidazole in the gas phase. Figure 7.7 shows an overlay of the theoretical structure optimised using the coupled-cluster composite method, shown in transparent

Table 7.4: A comparison of the experimental rotational constants for the heavy atom isotopologues of imidazole determined in this work and those reported in Ref. [162]. The values contained in square brackets were kept fixed to those determined in the fit of the imidazole parent species.

		^{15}N(1)		^{13}C(2)		^{15}N(3)	
		This work	Christen *et al.*	This work	Christen *et al.*	This work	Christen *et al.*
A	/ MHz	9695.27145(60)	9695.278(26)	9522.2430(12)	9522.309(62)	9721.5279(17)	9721.546(22)
B	/ MHz	9188.15484(59)	9188.170(26)	9353.9408(11)	9354.007(62)	9135.7461(12)	9135.778(22)
C	/ MHz	4716.17342(55)	4716.172(22)	4717.38675(32)	4717.455(62)	4708.48085(66)	4708.472(18)
D_J	/ kHz	3.21342(45)		3.19511(42)		3.2027(11)	
D_{JK}	/ kHz	-5.06379(40)		-5.05552(52)		-5.0522(15)	
D_K	/ kHz	2.19239(43)		2.19958(37)		2.1887(12)	
d_1	/ kHz	0.066142(99)		-0.04638(23)		0.04649(65)	
d_2	/ kHz	0.020931(47)		[0.016675]		0.00511(54)	
H_J	/ mHz	[1.367]		[1.367]		[1.367]	
H_{JK}	/ mHz	[-6.148]		[-6.148]		[-6.148]	
H_{KJ}	/ mHz	[10.15]		[10.15]		[10.15]	
H_K	/ mHz	[-2.813]		[-2.813]		[-2.813]	
h_1	/ mHz	[0.0459]		[0.0459]		[0.0459]	
h_2	/ mHz	[-0.0757]		[-0.0757]		[-0.0757]	
h_3	/ mHz	[-0.0147]		[-0.0147]		[-0.0147]	
L_{JKK}	/ μHz	[-1.98]		[-1.98]		[-1.98]	
χ^1_{cc}	/ MHz	-		-2.605(22)		-2.593(24)	
χ^1_{bb}-χ^1_{aa}	/ MHz	-		[0]		[0]	
χ^3_{cc}	/ MHz	2.265(39)		2.217(46)		-	
χ^3_{bb}-χ^3_{aa}	/ MHz	4.808(52)		5.716(68)		-	
No. of lines		248		399		244	
σ	/ kHz	32.3		31.2		32.8	
		^{13}C(4)		^{13}C(5)			
		This work	Christen *et al.*	This work	Christen *et al.*		
A	/ MHz	9573.80980(57)	9573.922(60)	9632.88165(65)	9632.227(74)		
B	/ MHz	9285.89510(44)	9286.009(60)	9223.79437(46)	9225.537(62)		
C	/ MHz	4712.53924(34)	4712.609(56)	4710.66717(33)	4710.987(54)		
D_J	/ kHz	3.20319(33)		3.19524(32)			
D_{JK}	/ kHz	-5.06608(37)		-5.04879(39)			
D_K	/ kHz	2.20186(31)		2.19354(39)			
d_1	/ kHz	0.069619(82)		-0.00520(14)			
d_2	/ kHz	0.021840(42)		-0.009358(42)			
H_J	/ mHz	[1.367]		[1.367]			
H_{JK}	/ mHz	[-6.148]		[-6.148]			
H_{KJ}	/ mHz	[10.15]		[10.15]			
H_K	/ mHz	[-2.813]		[-2.813]			
h_1	/ mHz	[0.0459]		[0.0459]			
h_2	/ mHz	[-0.0757]		[-0.0757]			
h_3	/ mHz	[-0.0147]		[-0.0147]			
L_{JKK}	/ μHz	[-1.98]		[-1.98]			
χ^1_{cc}	/ MHz	-2.565(26)		-2.538(36)			
χ^1_{bb}-χ^1_{aa}	/ MHz	[0]		[0]			
χ^3_{cc}	/ MHz	2.288(33)		2.173(34)			
χ^3_{bb}-χ^3_{aa}	/ MHz	3.020(52)		[5.727]			
No. of lines		422		360			
σ	/ kHz	27.6		25.9			

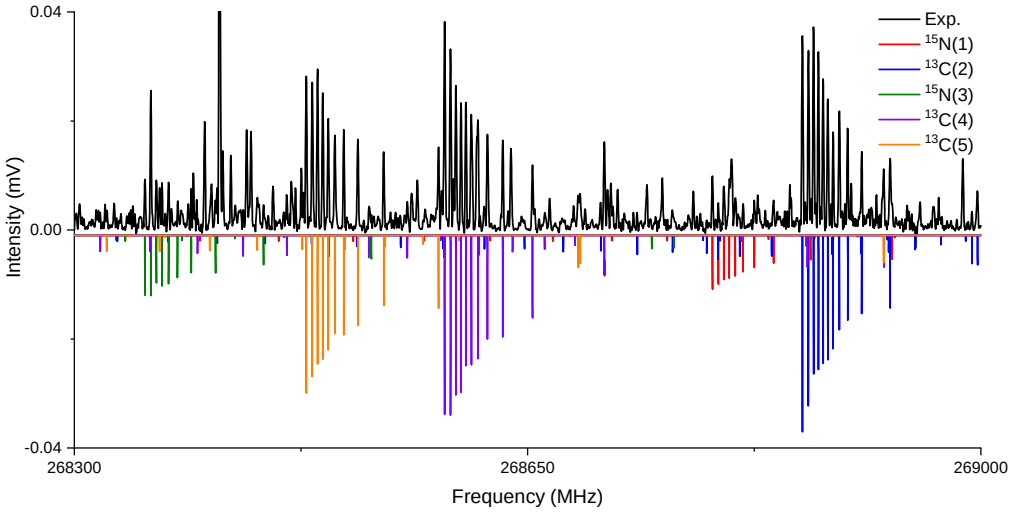

Figure 7.6: A zoom-in of the 260-295 GHz region, showing the imidazole isotopologue assignments, which do not exhibit a hyperfine structure. The experimental spectra are shown in black, and the simulated spectra of the fitted rotational constants at 300 K are shown in colour. The atom labelling scheme is detailed in Figure 7.7.

colour, with the experimentally determined atom positions, shown as solid spheres. The determined bond distances between the nuclei that make up the ring structure of imidazole and the determined internal angles of the five-membered ring are labelled in Figure 7.7. In Tables 7.5 and 7.6, the theoretical and experimental structural parameters are compared to the parameters presented in Ref. [162]. It can be seen that the substitution structure obtained from this analysis shows little deviation from that reported by Christen *et al.*, as can be expected from the fact that the rotational constants of each of the isotopologues also show little variation (see Table 7.4). The new line lists and rotational constants are nevertheless important, especially for astrophysical applications at higher frequencies.

This structure of imidazole can be compared directly to the structures of similar molecules. Indeed, in Ref. [162], the imidazole structure was discussed in comparison with those of oxazole, pyrrole, and pyrazole. To add to these comparisons, and to put the structure of imidazole in context with rings of the same elemental composition and connectivity, a comparison to the fully saturated ring analogues imidazolidine and hydantoin is considered here.

Figure 7.8 shows the ring structures of the three molecules along with the relevant bond lengths and internal angles, which are taken from the structure optimisation calculations at the MP2/aug-cc-pVTZ level of theory. These were performed for this work due to the absence of experimental gas-phase structures for imidazolidine

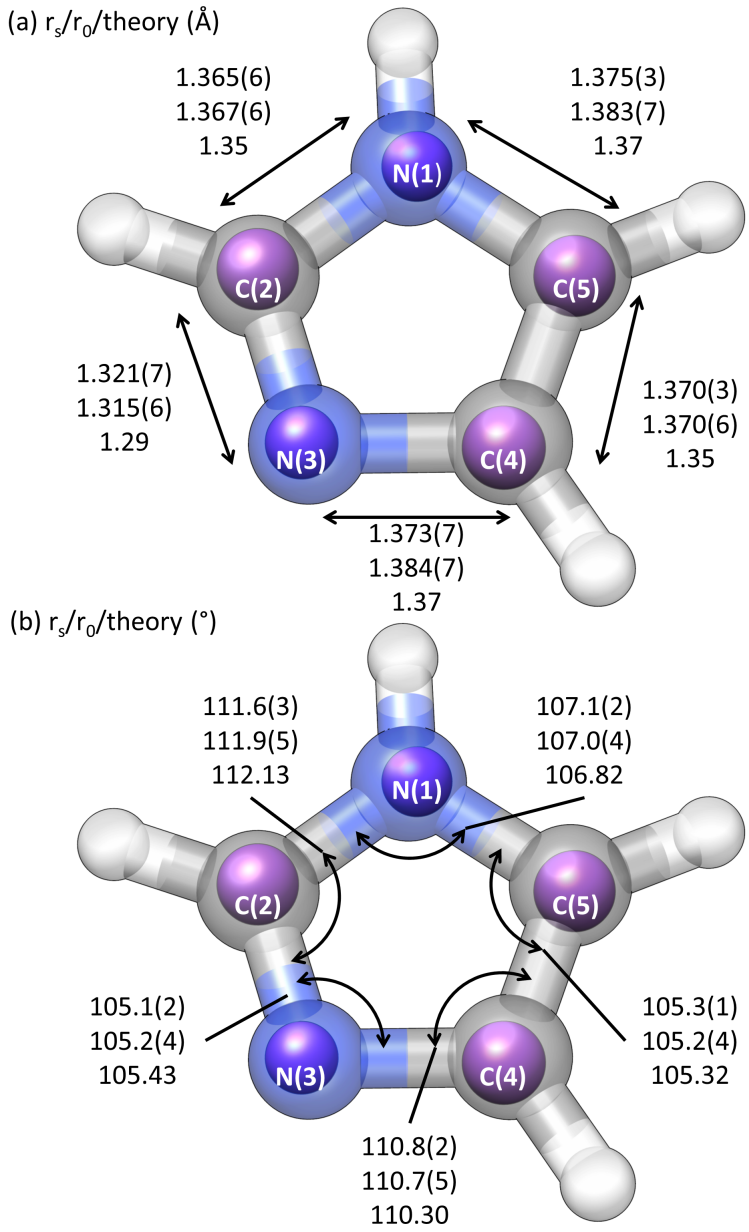

Figure 7.7: The theoretical structure, optimised using the coupled-cluster composite method [86] and shown in transparent colour, is compared to the experimentally determined atom positions from the r_s structure analysis, shown as solid spheres. Three sets of values are shown, which are from the r_s structure analysis, the r_0 structure analysis, and from the coupled-cluster composite method. The bond lengths between the heavy atoms of the ring are labelled in (a), and the internal angles of the ring are labelled in (b).

Table 7.5: A comparison of bond lengths, in Å, determined in this work and in Ref. [162] from the r_s and r_0 structure analysis, and those from the structure optimised using the coupled-cluster composite method [86].

Bond length / Å	r_s		r_0		Theory
	This work	Christen *et al.*	This work	Christen *et al.*	Giuliano *et al.*
N1-C2	1.365(6)	1.3643	1.367(6)	1.3704	1.35
C2-N3	1.321(7)	1.3135	1.315(6)	1.3164	1.29
N3-C4	1.373(7)	1.3822	1.384(7)	1.3875	1.37
C4-C5	1.370(3)	1.3638	1.370(6)	1.3676	1.35
N1-C5	1.375(3)	1.3774	1.383(7)	1.3788	1.37

Table 7.6: A comparison of the internal bond angles of the imidazole ring, in °, determined in this work and in Ref. [162] from the r_s and r_0 structure analysis, and those from the structure optimised using the coupled-cluster composite method [86].

Bond angles / °	r_s		r_0		Theory
	This work	Christen *et al.*	This work	Christen *et al.*	Giuliano *et al.*
N1-C2-N3	111.6(3)	111.99	111.9(5)	111.85	112.13
C2-N3-C4	105.1(2)	104.93	105.2(4)	105.08	105.43
N3-C4-C5	110.8(2)	110.69	110.7(5)	110.50	110.30
C4-C5-N1	105.3(1)	105.48	105.2(4)	105.65	105.32
C5-N1-C2	107.1(2)	106.90	107.0(4)	106.93	106.82

and hydantoin in the literature. The biggest difference between the structures is the degree of saturation of the ring bonds, and this can be seen in the bond lengths. The C(2)-N(3) bond illustrates this clearly. In the fully aromatic system, imidazole, where the bond is formally a carbon-nitrogen double bond, the bond length is 1.321(7) Å. This can be compared to the theoretical value for this bond length, which is 1.32 Å at the MP2/aug-cc-pVTZ level of theory. This demonstrates the excellent agreement between the MP2 calculation and the r_s structure, which can be exploited for further comparisons. The C(2)-N(3) bond increases to 1.37 Å in hydantoin, in which the bond has some double bond character due to resonance effects. The C(2)-N(3) bond is the longest in the fully saturated imidazolidine, where it is a carbon-nitrogen single bond, at 1.48 Å.

The C(5)-N(1) bond in hydantoin also has some double bond character, and this bond, at 1.38 Å, is similar in length to the same bond in imidazole (experimental = 1.375(3) Å; theoretical = 1.37 Å), despite the bond being formally a single bond in imidazole. The same bond in imidazolidine is longer, at 1.47 Å. Another consequence of unsaturation and aromaticity is structure planarity. This can be characterised by the dihedral angles between the atoms in the ring, where Θ_1 is the dihedral angle N(1)-C(2)-N(3)-C(4), Θ_2 is C(2)-N(3)-C(4)-C(5), Θ_3 is N(3)-C(4)-C(5)-N(1), Θ_4 is C(4)-C(5)-N(1)-C(2), and Θ_5 is C(5)-N(1)-C(2)-N(3). In the fully saturated, non-aromatic imidazolidine, the ring structure is non-planar. The dihedral angles in imidazolidine are: Θ_1=11.1°, Θ_2=-27.8°, Θ_3=34.5°, Θ_4=-27.8°, and Θ_5=11.1°. These values are in contrast to those of the other two structures, where the dihedral angles are essentially zero for both imidazole and hydantoin. This planar structure is expected for imidazole because of its aromatic nature and for hydantoin because of the carbonyl groups introducing resonance effects. The planarity can also be explained by the hybridisation of the atoms in the ring motif. The sp^2-hybridised molecular orbitals in the imidazole ring locks the planar structure, whilst the sp^3-hybridised molecular orbitals in imidazolidine cause some deviation from planarity. The internal angles of imidazole, as shown in Figure 7.7(b), are within 3.3% of 108°, which is the value of the internal angle of a regular pentagon. In contrast to this, the internal bond angles of the imidazolidine ring are within 4.3% of 108°, and they are within 5.6% of 109.5°, which is the ideal value between the substituents of an sp^3-hybridised atom.

Further structural information can be retrieved from the values of the nuclear quadrupole coupling constants, χ_i. In Ref. [170], there was discussion about the values and implications of χ_{cc} in the hydantoin structure. In short, the authors concluded that the hydantoin molecule contains two pyrrolic nitrogen nuclei. This was signified by the negative χ_{cc} values determined in their work: -4.7338(70) and -3.4635(75) MHz for N(1) and N(3), respectively [170]. In imidazole, the χ_{cc} values indicate that the N(1) nucleus is pyrrolic, and the N(3) nucleus is pyridinic. The

χ_{cc} values for the parent species were determined to be -2.5592(62) and 2.2293(66) MHz for N(1) and N(3), respectively (see Table 7.1 and Ref. [86]). This can also be seen in Table 7.4, where all of the values determined for χ^1_{cc} for the isotopologues are negative, and the χ^3_{cc} values are positive. The lone pair of electrons on N(1) is within the aromatic ring system. The electrons are, therefore, unavailable for bonding to an external electrophile, as is the case in pyrrole. The lone pair on N(3), however, lies outside of the ring structure, and it is available for bonding to an external electrophile, as is the case in pyridine.

From an astrochemical point of view, searches for these isotopologues are facilitated by the extended frequency ranges studied here compared to previous studies. In particular, the frequency ranges employed make the rest frequencies of the rotational transitions measured directly comparable to a number of observational facilities. For example, the lower frequency data sets overlap with the Effelsberg 100m Radio Telescope and the Robert C. Byrd Green Bank Telescope, the W-band data has overlap with the Band 3 operating regime (84-116 GHz) of ALMA, and the 260-295 GHz experiment overlaps with ALMA Bands 6 and 7 (211-275 GHz and 275-373 GHz respectively).

The search for and detection of the isotopologues in regions where imidazole is detected could be of importance for elucidating formation pathways of the parent species. Ref. [31] demonstrated with a gas-grain chemical network model that isotopic ratios can be used to deduce likely routes to interstellar molecules. In their study, they showed that the $^{12}C/^{13}C$ ratio for CCH and CCS differed from the elemental $^{12}C/^{13}C$ ratio, and it was dependent on whether the molecule was formed from the carbon ion or from carbon monoxide. One could postulate that constructing similar models with the nitrogen atom/ion, nitrogen monoxide, or other small nitrogen-containing species, could allow for the deduction of likely formation pathways for imidazole. The detection of imidazole isotopologues, made possible by this study, would provide the interstellar abundances and $^{14}N/^{15}N$ ratios required for such an analysis to be performed.

7.4 Astrochemical Implications

The best-fit model of the rotational spectrum of the vibronic ground state of imidazole was used to search for this molecule in the hot molecular core Sgr B2(N2). The Exploring Molecular Complexity with ALMA (EMoCA) imaging spectral line survey obtained with ALMA between 84.1 GHz and 114.4 GHz with a median angular resolution of 1.6" was used. A detailed account of the observations and data reduction can be found in Ref. [118]. The programme Weeds [171] was used to generate a synthetic spectrum of imidazole under the approximation of local thermodynamic equilibrium (LTE) and matching lines in the observed spectrum of Sgr B2(N2) were

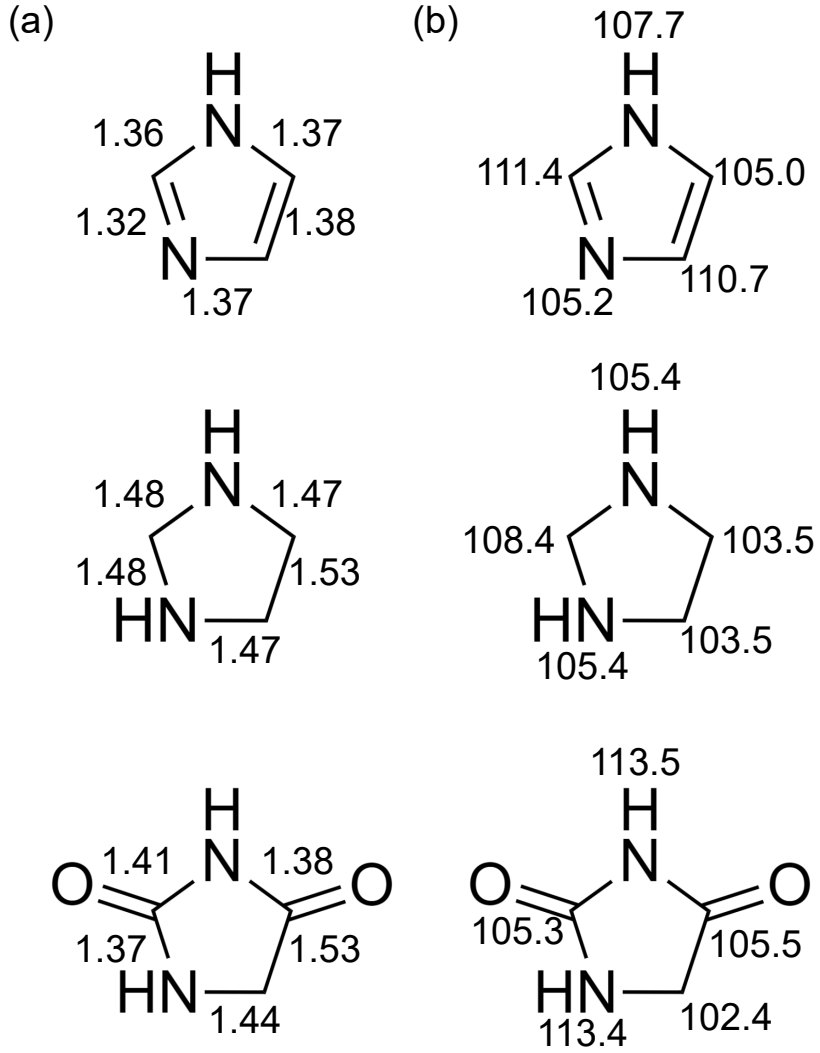

Figure 7.8: The Lewis structures of imidazole (top), imidazolidine (middle), and hydantoin (bottom). (a) The bond lengths between the atoms in the ring are shown in Å. (b) The internal angles are marked, in °, at the atom of the angle vertex. All values are from structure optimisation calculations at MP2/aug-cc-pVTZ.

searched for.

No evidence for imidazole was found in the EMoCA spectrum of Sgr B2(N2). The most stringent constraints were imposed by the transitions around 100.21 GHz, as is shown in Figure 7.9. The line detected at 100.21 GHz towards Sgr B2(N2) is a blend of transitions of $CH_3^{18}OH$, $^{13}CH_3CH_2OH$, and $CH_3C(O)CH_3$. There is little room left for imidazole emission at this frequency. Assuming the same LTE parameters as for ethyl cyanide (a source size of 1.2", a temperature of 150 K, a line width of 5 km s^{-1}, and a source velocity of 73.2 km s^{-1}), an upper limit of 1.8×10^{15} cm^{-2} for the column density of imidazole is obtained, which implies that this ring molecule is at least 3400 and 230 times less abundant than ethyl cyanide and vinyl cyanide in this source, respectively [118].

At a temperature of 150 K, the vibrational contribution to the partition function of imidazole would increase the derived value of the column density upper limit by only 0.1% (see Table 7.2). A column density of 4×10^{11} cm^{-2} was reported for benzonitrile (c-C_6H_5CN) in the Taurus Molecular Cloud (TMC-1) by Ref. [53], which is 15 times less abundant than vinyl cyanide in this source [172]. If imidazole and benzonitrile have similar abundances in Sgr B2(N2), then it may be concluded that aromatic molecules are less abundant towards Sgr B2(N2) than towards TMC-1 relative to aliphatic compounds.

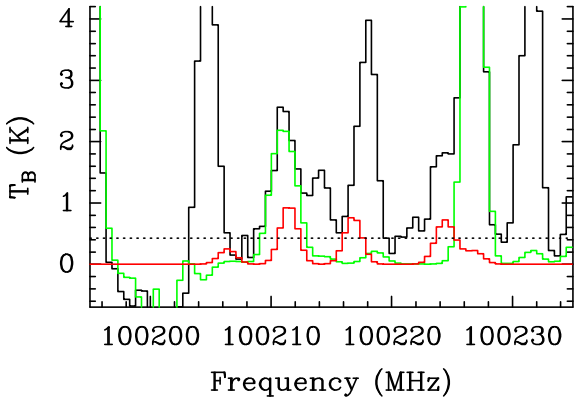

Figure 7.9: Portion of the EMoCA survey around 102.2 GHz. The best-fit LTE synthetic spectrum that contains the contributions of all molecules identified so far towards Sgr B2(N2) (green) is overlaid on the observational spectrum (black). The spectrum of imidazole used to derived the upper limit on its column density is shown in red. The y-axis is labelled in brightness temperature units. The dotted line indicates the 3σ noise level. [86]

7.5 Conclusions

This chapter presents a comprehensive laboratory study of the rotational spectrum of imidazole, extending the earlier microwave-band investigations into the millimetre-wave regime. The use of different broadband spectrometers allowed the sampling of wide portions of the spectrum to be achieved: at centimetre wavelength, the intervals 2–8 GHz, 13–15.5 GHz, and 18–26 GHz were covered, and in the mmw region, the full W-band (75–110 GHz) and the 260–295 GHz range were studied. The vibronic ground state of imidazole, three vibrationally excited states, and the ^{13}C and ^{15}N isotopologues in natural abundance were all observed, and their rotational spectra assigned in the regions studied.

The final analysis of the vibronic ground state comprises of 698 transitions, which were fit to the coefficients of the S-reduced rotational Hamiltonian, providing a very precise set of rotational and quartic centrifugal distortion constants. Three sextic and one octic parameters were also determined. The optimised values of the spectroscopic constants are in excellent agreement with the results of high-level theoretical calculations.

The low-lying vibrational states assigned in the room-temperature data can be designated as an N-H bond stretch (the fundamental mode ν_{21}) and wagging motions along the C-C-N and N-C-N sections of the ring (the fundamental modes ν_{20} and ν_{19}). Their high energies relative to the vibrationally excited states of imidazolidine reinforce the rigidity of the aromatic ring structure, and their low signal levels compared to the ground state suggest potential difficulties in searches for these species.

The gas-phase structure of imidazole was determined. When compared to the previous structure from Ref. [162], there were small, rather insignificant, changes in the bond lengths (within 0.67%) and bond angles (within 0.35%) with respect to the r_s structures. The effect of the aromatic character of the imidazole ring, in comparison to the similar molecules imidaolzidine and hydantoin, was also explored. The aromaticity is a satisfactory explanation for the decrease in lengths of the ring bonds in imidazole when compared to the other cyclic molecules.

Finally, using the improved spectral predictions that resulted from this analysis, a search for the vibronic ground state of imidazole was attempted in the hot core Sgr B2(N2) based on the observations of the EMoCA spectral line survey. This ring molecule was not detected. A column density upper limit of 1.8×10^{15} cm^{-2} was derived, which implies that imidazole is at least 3400 times less abundant than ethyl cyanide in this source. Given that the cyclic molecule benzonitrile was recently detected in the molecular cloud TMC-1 [53], the chances of detecting imidazole may be higher towards this source. A search for imidazole towards this source is therefore suggested.

Chapter 8

The Electrical Discharge of Acetaldehyde in the W-band Region: Product Identification and Towards Discharging Multi-component Mixtures

8.1 Introduction

Electrical discharge experiments have been used extensively for many years in the areas of combustion research and astrochemistry (see, among others, Ref. [173] and references therein). These experiments involve one or more precursors reacting together in high-energy plasma conditions, mimicking, for example, conditions relevant for fuel combustion. This results in the formation of product molecules, which can then be characterised by spectroscopic techniques. An added advantage of discharge reactions is the *in situ* production of reactive species that can undergo direct spectroscopic investigation. These species can include ions and radicals, as well as relatively unstable neutral species. Previous discharge experiments have resulted in interstellar detections of many species. For example, extensive studies on lengthy unsaturated carbon chains produced by the discharge of acetylene, HCCH, have been successful in leading to laboratory characterisation and observation (see, among many others, Refs. [47–50]). Therefore, discharge experiments can play, and have played in the past, a vital role in extending the complexity and type of molecules studied for characterising the inventory of interstellar molecules.

As was discussed in Chapter 3, the discharge of one molecular species can already produce a plethora of discharge products. In the set-up and optimisation of the dis-

charge apparatus, the discharge of acetonitrile was shown to produce, among other species, cyanoacetylene, vinyl cyanide, and the cyanomethyl radical. The discharge of two (or more) precursors could lead to interesting product formation, especially if there is incorporation of parts of both precursor molecules in the product. This becomes particularly relevant when considering the formation of doubly functional molecules, such as the amino alcohols presented in Chapter 6.

In 2013, Loomis *et al.* studied the discharge reaction between acetonitrile, CH_3CN, and hydrogen sulfide, H_2S. The production of ethanimine, CH_3CHNH, in the discharge plasma led to its spectroscopic characterisation and interstellar observation. Although, one may note that this product molecule does not contain sulfur, which is also an interesting substituent to consider for observational detection and has been studied in discharge experiments for such purposes, as in Ref. [174]. One major application of discharge experimental data is the hints that may be provided for potential pathways and mechanisms from the initial reactants to the discharge products. In Ref. [51], there was some exploration of the mechanisms that could result in the interstellar production of ethanimine from acetonitrile via hydrogen addition reactions, but the analysis focussed on the chemistry occurring on interstellar ices. This reaction was recently revisited in a publication by Baiano *et al.*, which involved the theoretical exploration of the gas-phase formation route of ethanimine. Their considerations concentrated on the reaction between the NH and C_2H_5 radicals [175], which could be more relevant to the discharge experiments that were previously performed.

Though it is not a new notion, this brings into the fore the need for the collaboration between experimentalists, theoreticians, and observational astronomers. The experimental work can identify potential interstellar molecules, their rotational signatures, and their potential precursors. Theoreticians and modellers can help to elucidate the pathways and mechanisms that might play important roles in the interstellar transformation from reactants to products. Observational astronomers undertake the searches for the species in question. With the combination of knowledge from experiment and theory, the searches could incorporate multi-species spatial distribution maps, as will be discussed later, and thus bring more concrete evidence for pathway and mechanism suggestions.

In this chapter, in order to build a foundation for the type of analyses described above, the results of implementing the pulsed discharge nozzle on the W-band spectrometer are described. The results are discussed in the context of the discharge of acetaldehyde, CH_3CHO. This is an interstellar molecule that was first detected in the 1970s [176–178]. It has since been detected in a number of different interstellar environments [179–188]. In addition, the laboratory spectra of acetaldehyde and its various isotopologues have been analysed extensively, including analyses on internal rotation and of vibrationally excited (torsional) states [189–202]. Acetoni-

trile, CH_3CN, which was discussed in the context of the set-up and optimisation of the discharge nozzle in Section 3.5, is further utilised in this chapter in a multi-component mixture with acetaldehyde. Acetonitrile was first detected in the ISM in 1971 [203], and isotopologues and vibrationally excited states were subsequently detected (see, for example, Refs. [25, 118, 204]). Experiments with acetonitrile over the past 70 years or so have allowed for an extensive spectroscopic characterisation (see, for example, Refs. [205–219]).

The discharge products of acetaldehyde are identified, some plausible reaction pathways to these discharge products are discussed, and extending the discharge to multi-component mixtures is explored.

8.2 Experimental and Theoretical Details

The electrical discharge experiments were performed as described in Section 3.5. A short summary follows here.

In discharge experiments that involved probing the supersonic expansion that propagates from the discharge nozzle, the W-band spectrometer was operated in the synchronised high dynamic range (HDR) mode, wherein the working of the spectrometer was controlled by the Edgar software and an external delay generator. The delay generator was used to control and provide the triggers for the molecular pulse, the excitation radiation, and the discharge high voltage circuit. This method, as mentioned in Chapter 3, has the advantages that it can minimise the congestion of the recorded spectra by reducing the presence of vibrationally excited states and eliminate the possibility of reactions occurring on the surface of the cold finger used in the cold trap method.

The molecular pulse length was set to 260 μs, and the delay generator controlling this and the Edgar software for spectral acquisition was set to a repetition rate of 5 Hz. This was the best compromise achieved between a high repetition rate and the abilities of the pumping system to maintain a supersonic expansion. The high voltage supply had parameters set to 1 kV, 100 mA. The potential was applied between the electrodes 5 μs before, the whole time during, and 100 μs after the molecular pulse, which was the optimised timing system that ensured the molecular pulse was traversing the discharge nozzle whilst the potential difference existed between the electrodes. The geometry of the discharge nozzle was as described in Section 3.5 and in Figure 3.7. The synchronised HDR mode experiment was performed until 1,000 free induction decays (FIDs) per segment had been recorded, co-added, and fast Fourier transformed. This equated to a measurement time of approximately 3 hours. The acetaldehyde, which was purchased from Sigma-Aldrich (99% stated purity) was loaded into an external reservoir, over which 3 bar of neon backing gas was passed and supersonically expanded into the vacuum chamber. For the mix-

ture experiment, a 1:1 mixture of acetaldehyde, the same as above, and acetonitrile, which was also purchased from Sigma-Aldrich (99% stated purity), was loaded into the external reservoir and supersonically expanded into the chamber in the same way.

For the experiments performed using the cold trap method, the discharge parameters were optimised to be 1.75 kV and 20 mA. As the gaseous sample is reintroduced into the vacuum chamber from the cold trap, with the vacuum chamber acting as a static cell, the spectrometer can be run using the HDR method without the synchronisation to the external triggering system. The experiments were performed until 100,000 FIDs had been recorded, co-added, and fast Fourier transformed. The mixture of acetonitrile and acetaldehyde was prepared by seeding them into a gas bottle such that the gas bottle comprised of 0.5% of each precursor and 99% neon. During the experiment, a backing pressure of 3 bar was maintained behind the pulsed nozzle/discharge nozzle set-up, and 20 discharge cycles (total gas pressure discharged = 2000 mTorr, total sample pressure discharged = 20 mTorr) were performed.

Structure optimisation calculations were performed at the B3LYP/aug-cc-pVTZ level of theory. These were performed in order to consider the energy changes associated with the discharge reactions discussed. The zero-point energy (ZPE) corrections were calculated with harmonic frequency calculations at the same level of theory. The calculations were performed using Gaussian 09 [73].

8.3 Results and Discussion

The Discharge Spectrum of Acetaldehyde

The overview of the acetaldehyde spectrum with the electrical discharge on and the electrical discharge off, the ON and OFF experiments respectively, is shown in Figure 8.1(a). The action of the discharge on acetaldehyde resulted in a number of discharge products being produced, a summary of which can be found in Table 8.1.

The probing of the supersonic expansion allows for the observation of the reactive species produced in the discharge zone of the nozzle extension. Analysis of the spectrum from the ON experiment revealed the presence of the formyl radical, $^{\bullet}$COH. The transitions observed for the radical are shown in Figure 8.2, in which the spectra from the ON and OFF experiments are compared with the simulation of its rotational spectrum. The transitions were identified thanks to the work in Ref. [220] (which was an update on the work in Ref. [221]) and the transitions listed on the Splatalogue* database [153]; see Table 8.2. It is also worthy to note

*www.cv.nrao.edu/php/splat/

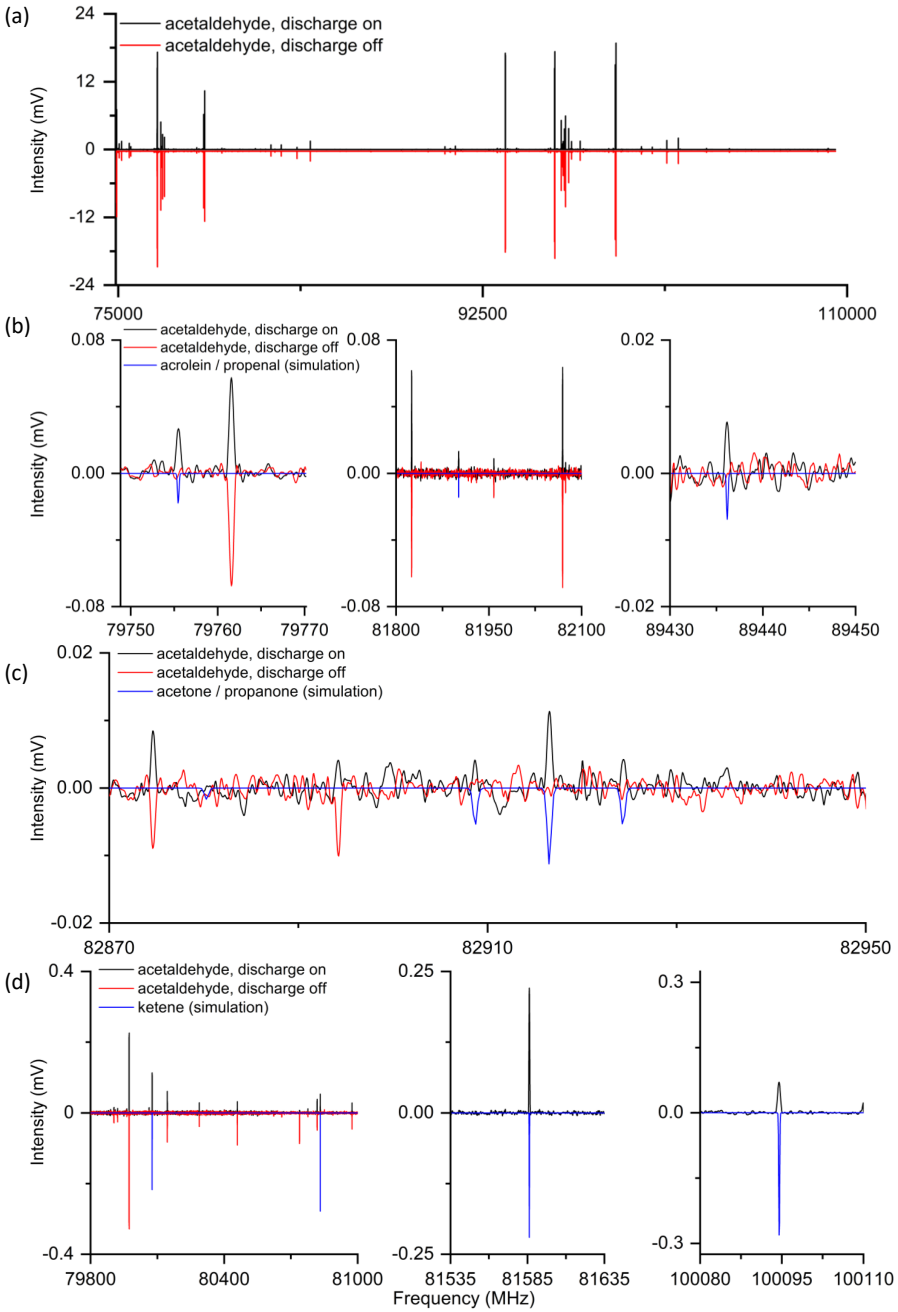

Figure 8.1: A comparison of the ON and OFF spectra from the acetaldehyde alone experiment (a), in black and red respectively, with the simulated rotational spectra of (b) acrolein, (c) acetone, and (d) ketene, all shown in blue in their respective panels.

Table 8.1: A list of species observed in this work from the discharge of acetaldehyde, CH_3CHO, in the supersonic expansion experiment.

Molecule
formyl radical, $^{\bullet}CHO$
ketene, H_2CCO
propyne, methyl acetylene, $HCCCH_3$
acrolein, propenal, acrylaldehyde, CH_2CHCHO
acetone, propanone, $(CH_3)_2CO$

that the formyl radical has been detected in the ISM [222]. The breakdown of the acetaldehyde molecule into the formyl radical should result in the production of the complementary radical $^{\bullet}CH_3$, the methyl radical. However, due to its planarity and symmetry, the methyl radical lacks electric dipole-allowed rotational transitions for detection to be possible [223]. Because of the detection of discharge products whose carbon chain is longer than that of acetaldehyde (described in the following paragraphs), the methyl radical is very likely produced and actively involved in the discharge plasma chemistry. The reaction pathway describing this has an energy difference between the reactant and products, ΔE, of +425 kJ mol^{-1}, suggesting that this is a barrier that can be overcome in the discharge plasma.

Table 8.2: A comparison of the transition frequencies for the formyl radical observed in this work and those observed in Ref. [220]. See Figure 8.2 for the ON spectrum showing the presence of these transitions.

Frequency from Ref. [220] (MHz)	Frequency from this work (MHz)
86670.82	86670.7610
86708.35	86708.0989*
86777.43	86777.9119**
86805.75	86805.1411

*partially blended with a line at 86708.5774 MHz

**partially blended with a line at 86777.2551 MHz

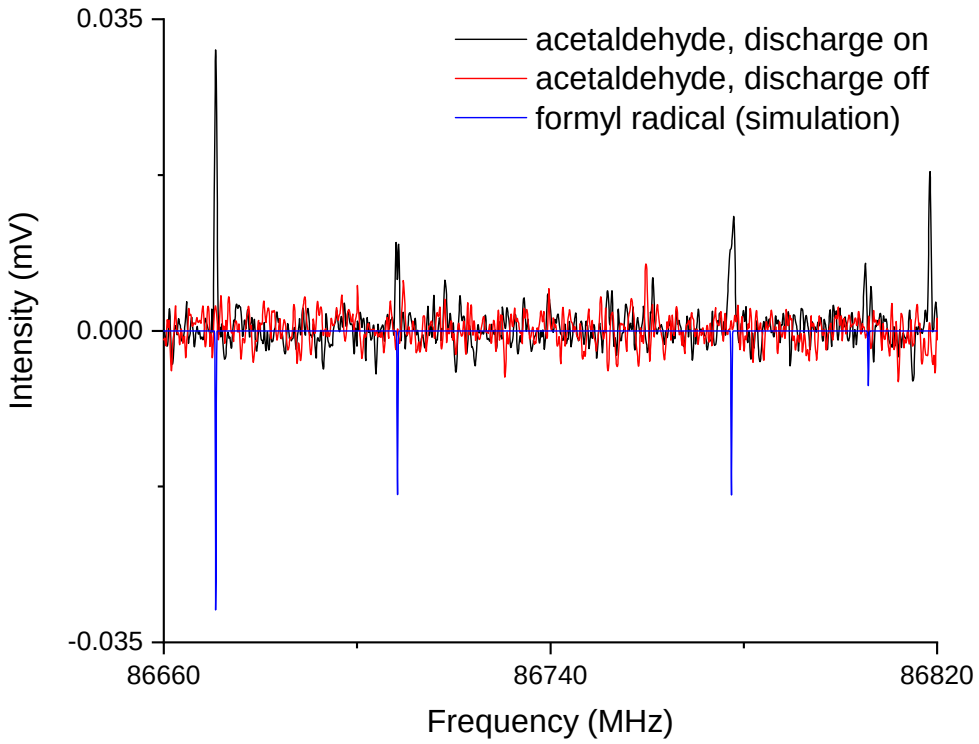

Figure 8.2: A comparison of the ON and OFF spectra from the acetaldehyde alone experiment, in black and red respectively, and the predicted spectrum of the formyl radical from the JPL database [153] is shown in blue. See Table 8.2 for a comparison between the observed frequencies and those reported in Ref. [220], confirming that the lines shown here can be attributed to the formyl radical; the spectral pattern is the hyperfine structure of the $J'_{K'_a,K'_c} \leftarrow J_{K_a,K_c} = 1_{0,1} \leftarrow 0_{0,0}$ transition.

Figure 8.1(b) shows the identification of acrolein, CH_2CHCHO, also known as propenal, in the ON experiment. The elongation of the two-carbon acetaldehyde molecule to the three-carbon acrolein molecule could be achieved by the recombination of a methyl radical with the $^{\bullet}CH_2CHO$ radical. The production of acrolein could also be explained by the attack of a carbon-based radical on the terminal carbon of an acetaldehyde molecule. If a methyl radical adds on at the terminal carbon, the presence of propanal should also be observed. However, because of the absence of propanal in the ON experiment spectrum, it can be concluded that this mechanism is not efficient, at least under the present experimental conditions. A carbon-based radical could also attack the acetaldehyde molecule at the carbonyl carbon. If this mechanism occurs, for example, if the methyl radical attacks the carbonyl carbon, the production of acetone (also known as propanone) could be prevalent. This, indeed, was found to be the case. Figure 8.1(c) shows the identification of acetone, $(CH_3)_2CO$, in the ON experiment.

Ketene, CH_2CO, was also identified in the ON spectrum, as shown in Figure 8.1(d). The presence of ketene could be explained by the loss of hydrogen atoms from the acetaldehyde molecule. This could be achieved directly via a dehydrogenation reaction, or hydrogen abstraction being initiated by a radical present in the discharge plasma. The removal of two hydrogen atoms to produce ketene from acetaldehyde has a calculated ΔE of $+530$ kJ mol^{-1}, with the discharge being the source of energy for this reaction.

In addition, there were some hints of the production of propyne, also called methyl acetylene, $HCCCH_3$. This is a particularly interesting product, as it does not contain an oxygen atom. This would suggest that either the carbon-oxygen double bond in acetaldehyde is broken in the discharge plasma, or that the propyne is produced by the recombination of a number of carbon-based radical entities. The recombination of carbon-based reactive species into longer carbon chains has already been show in discharge systems, for example, on the work on the discharge of acetylene, HCCH, as previously cited. However, with a signal-to-noise ratio (SNR) of 1.5:1 or lower for propyne in the ON spectrum, and only a handful of lines observed, it is clear that whichever production mechanism prevails, it is not effective under the current conditions. A summary of the suggested pathways from acetaldehyde to the observed discharge products is provided in Figure 8.3.

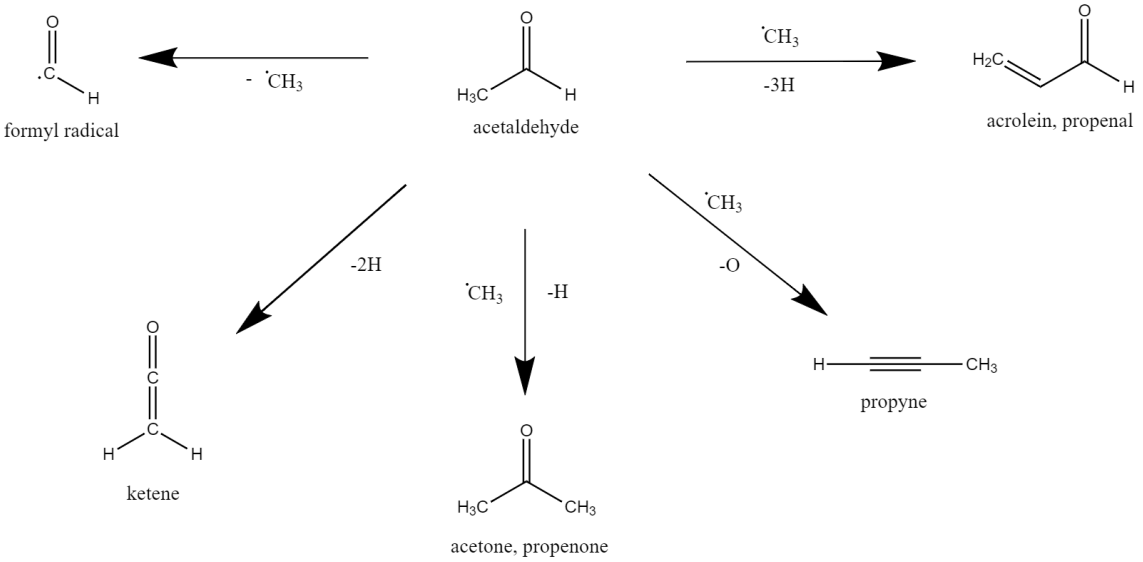

Figure 8.3: The pathways towards the observed discharge products in the acetaldehyde alone discharge experiments, where the net gain and loss of elements is shown above and below the arrows, respectively.

Another product that was searched for in the ON spectrum was vinyl alcohol, CH_2CHOH. Consideration of this molecule was particularly interesting because it is exactly the keto-enol tautomer of the molecule acetaldehyde. Vinyl alcohol, due to its presence in the ISM, is also astrochemically relevant [122]. Generally, the keto-enol tautomeric equilibrium lies towards the keto side, and the equilibrium is highly thermodynamically driven. The equilibrium constant for the acetaldehyde (keto) / vinyl alcohol (enol) keto-enol tautomerisation reaction is on the order of 10^{-7} at room temperature; that is, the relative amount of vinyl alcohol in a sample of acetaldehyde is very small [224]. There is no evidence of vinyl alcohol in either the ON or the OFF spectra, and this is consistent with the keto-enol equilibrium constant considerations.

One important application of this work is the comparison of these results to chemical models. This is particularly true for the comparison and interplay between gas-phase and grain-surface reaction pathways. For example, it was reported by Hollis *et al.* in Ref. [225] that "simple hydrogen addition on interstellar grains accounts for successively larger molecular species: from propynal to propenal and from propenal to propanal." This pathway is summarised in Figure 8.4. However, it could be possible that a gas-phase route plays an equally important role in the interstellar production of these molecules. In fact, it has already been noted that it is likely that the majority of molecules in the ISM are produced by an interplay of significant gas-phase and grain-surface reactions [226]. In the context of these results, it is clear that a potential gas-phase pathway to interstellar acrolein/propenal is very different from the surface-grain mechanism. Whilst the surface reactions rely on the hydrogenation of propynal, the gas-phase reactions could be reliant on the availability of acetaldehyde and the methyl radical. In fact, because of its absence in the ON experiment spectrum, it can be concluded that gas-phase propenal is independent of propynal, at least under the current conditions. Further, the hydrogenation of propenal to propanal in the gas phase is not efficient: this can be concluded due to the absence of the latter from the ON experiment spectrum.

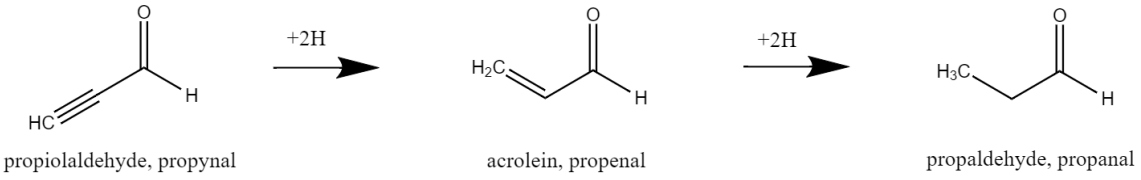

Figure 8.4: The pathways from Ref. [225] to explain the interstellar link between propynal, propenal, and propanal, which was suggested as being the addition of hydrogen to the molecules on ice grains. Only propenal (acrolein) was detected in the discharge ON experiment of acetaldehyde.

These hypotheses linking the discharge experimental results to potential pathways that could be important in the ISM can be tested for their interstellar applicability by taking advantage of the spatial resolution offered by observational facilities such as ALMA. As was demonstrated by Neill *et al.* in Ref. [227] for methyl formate, gas phase processes can be uncovered by considering the relative spatial distributions of the component parts of a chemical reaction. In the publication, Neill *et al.* note that the spatial distributions of methyl formate and formic acid in the Orion KL Region heavily suggest the reaction responsible for the production of methyl formate leads to the depletion of formic acid. Therefore, in the framework of Figure 8.3, the mapping of the spatial distributions of acetaldehyde, acrolein, acetone, the formyl radical, and ketene should be performed. The resulting multi-species spatial distribution maps would allow for pathways in the figure to be confirmed as relevant to interstellar chemistry.

Multi-component Mixtures

To explore the discharge of multi-component mixtures with the individual systems already studied in this work, a multi-component mixture of acetonitrile and acetaldehyde was passed through the discharge apparatus. This is particularly relevant as it addresses the potential presence of doubly functional molecules - in this case, the precursors have cyano, -CN, and carbonyl, -C=O, functionality, respectively. In the ISM, only about a dozen doubly functional molecules have been detected (see Refs. [105, 117, 228–239] for the detections of molecules with both a nitrogen and oxygen atom / functional group). A comparison of the ON and OFF experiment spectra is shown in Figure 8.5. Analysis of the ON spectrum shows the expected effect of the discharge on the acetonitrile and acetaldehyde molecules. That is, the discharge products previously characterised in the acetonitrile alone and the acetaldehyde alone ON spectra are observed in the mixture ON spectrum (seen in the zoom-ins of Figure 8.5).

There are two methods that can be used when considering such an experiment, and indeed, these principles are also true for single-component discharge experiments. As outlined by Zaleski *et al.*, the focus can either be the targeted generation of a molecule through careful choice of precursors or the use of the 'broadband reaction screening' method, wherein an unbiased survey of the produced species is undertaken [173]. In practice, these methods can work hand-in-hand, where an experiment can be designed with a target molecule in mind, but an unbiased survey can be carried out in order to fully characterise the products produced. A number of interesting molecules can be envisioned when considering the potential reactions between acetonitrile and acetaldehyde, and in particular, by taking into account the recombinations of likely radicals produced in the discharge plasma, possible hydro-

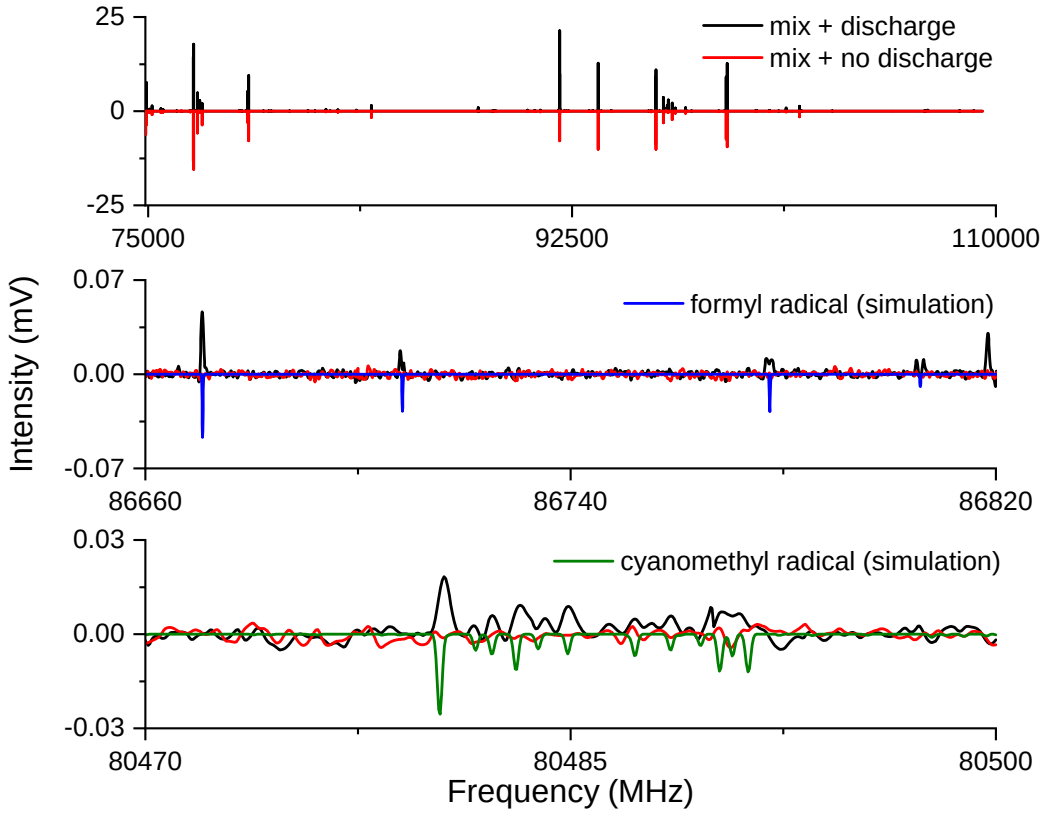

Figure 8.5: A comparison of the ON and OFF spectra recorded for the mixture of acetaldehyde and acetonitrile (top panel). The identifications of discharge products from each individual precursor molecule - the formyl radical from acetaldehyde (middle panel) and the cyanomethyl radical from acetonitrile (bottom panel).

genation and dehydrogenation reactions, and basic chemistry parameters such as valency. This can lead to large number of potential discharge products from one or two relatively simple precursors, and indeed McCarthy *et al.* report on the incorporation of substantial computational powers to fully predict and fit the spectra of the discharge of more complicated systems where a large number of potential products are studied [240]. The authors of Ref. [240] detailed a comprehensive analysis of the discharges of benzene, benzene and nitrogen, and benzene and oxygen which resulted, with the aid of automatic double resonance experiments and machine-learning spectral pattern recognition methods, in the characterisation of around 50 structures that were either entirely new or previously poorly characterised, including hydrocarbon structures that incorporated nitrogen and oxygen atoms [240].

A substantial list of potential discharge products from the acetonitrile and acetaldehyde mixture can be found in Table 8.3. These molecules have been compiled by considering the recombination of the hydrogen, methyl, cyano, formyl, cyanomethyl, and acetyl radicals. These are the radicals either confirmed, or assumed, as being produced from the discharge of the individual precursors. This list of potential products is, naturally, neither exhaustive nor exclusive. A number of potential discharge products which contain both a nitrogen and an oxygen atom can be found in Figure 8.6.

Table 8.3 also lists the calculated dipole moment components of the product molecules at the B3LYP/aug-cc-pVTZ level of theory. The molecules marked with a star (*) can act as an indicator that fragments from both acetonitrile and acetaldehyde are recombining. These molecules are formyl cyanide (also known as cyanoformaldehyde), acetyl cyanide, cyanoacetaldehyde, and 3-cyanopropenal (see Figure 8.6 and Table 8.4). The observation of the rotational spectrum of these molecules relies not only on the abundance of the molecule in the gas phase, but also the magnitude of their dipole moment components. As can be seen in Table 8.3, the four molecules have substantial dipole moment components. The formyl radical is one of the radicals produced in the discharge of the mixture (from the acetaldehyde) and is suggested to be involved in the incorporation of the oxygen into the potential indicator molecules listed in Figure 8.6. The μ_a dipole moment component of the formyl radical was determined experimentally to be 1.3626(39) D [241]. Botschwina calculated the μ_b dipole moment component to be approximately twice that of μ_a [242], and this was found to be in agreement with experimental findings [243]. The cyanomethyl radical (produced from the discharge of acetonitrile) was also found to have a strong dipole; Ref. [244] suggests a value of 3.5-4.0 D, which was confirmed with a number of private communications to the authors. These values of the dipole moment components of these two radicals are similar to those of a number of the products listed in Table 8.3, and in particular, to the four indicator molecules. This suggests that, if they are present in similar abundances, the four indicator molecules should be observable in the mixture ON spectrum.

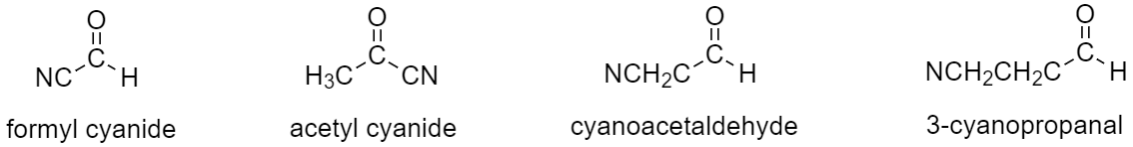

Figure 8.6: A number of potential products that could be obtained upon the discharge of acetonitrile and acetaldehyde. The molecules can be formed from the recombination of the hydrogen, methyl, cyano, formyl, cyanomethyl, and acetyl radicals.

The abundance of the molecules in the gas phase is then likely the limiting factor to their observation in the ON spectrum. Formyl cyanide and acetyl cyanide are products that could be synthesised from the cyano radical, one that is thought to be ubiquitous in the discharge plasma of acetonitrile. Neither of these potential products are formed in a high enough abundance for detection. Cyanoacetaldehyde is a difficult molecule to synthesise, and hence study spectroscopically, as noted in Ref. [245]. The transitions reported in Ref. [245] were used to search for the presence of cyanoacetaldehyde in the mixture ON spectrum, however this search was unsuccessful. A literature search for previous rotational spectroscopy studies on 3-cyanopropenal showed that it has not yet been characterised. An attempt to assign it in the mixture ON spectrum was performed using the theoretical rotational constants obtained from the structure optimisation calculation. This search was also unsuccessful. Therefore, searching for these four indicator species in the supersonic expansion experiment, which should indicate if the species from each reactant are reacting together, reveals no concrete evidence for such an occurrence.

The radical reactions for the formation of the four indicator molecules and their associated ΔE values, calculated at the B3LYP/aug-cc-pVTZ level of theory, are shown in Table 8.4. All of the reactions are exothermic. Of the four indicator species named in the previous paragraph, the order of molecule stability with respect to reaction energetics is: formyl cyanide > acetyl cyanide > cyanoacetladehyde > 3-cyanopropanal. Radical-radical recombination reactions are also known to be effectively barrierless, so the elusive nature of the products in the mixture spectrum, even with the relatively low number of co-added FIDs in the presented data, is puzzling. It is clear from the ON spectrum that the two precursor molecules are undergoing dissociation due to the action of the electrical discharge (see Figure 8.5). However, there is a lack of evidence that suggests that the reactive species produced are reacting together in a way that fulfils the potential applications for multi-species spatial distribution mapping. It appears that the problem does not lie in the discharge parameters, as both the acetonitrile and acetaldehyde are being efficiently broken into radical species. One consideration that could be taken into account is the configuration of the discharge nozzle. As shown in Figure 3.7 in Section 3.5, the discharge nozzle is arranged, in the order of the direction of gas flow, as a Teflon spacer, followed by the ground electrode, followed by a Teflon spacer, and completed by the working electrode. This limits the recombination zone, the volume in which the reactive species can interact, to the space directly after radical generation to the flare signalling the start of the supersonic expansion. Encouraging the recombination of the radicals could be achieved through altering this configuration. For example, by changing the configuration from spacer-electrode-spacer-electrode to electrode-spacer-electrode-spacer, the recombination zone can be elongated substantially. This has been previously shown to be effective in stimulating the formation

of long polyyne carbon chains, "presumably because a greater number of collisions prior to expansion allows time for long chains to assemble" [246]. The configuration with the elongated recombination zone was also the design used in, among others, Refs. [174] and [247], which showed significant growth of carbon chain molecules and polycyclic aromatic hydrocarbons, respectively.

A further point to note is that the ON experiment of the mixture was run under the same conditions and parameters as the ON experiments of the individual precursors. However, it could be the case that more optimisation of these are required. For example, the synchronised HDR experiments were performed until 1,000 FIDs per segment had been recorded, equating to a measurement time of approximately 3 hours. The generally low SNR of the discharge products can be improved by collecting, co-adding, and Fourier transforming more FIDs, which, in turn, could allow for some of the products in Figure 8.6 to be detected. The effect on the SNR of increasing the number of averages, $N_{averages}$, from $N^{A}_{averages}$ in experiment A to $N^{B}_{averages}$ in experiment B can be described by the relationship in Equation 8.1. Therefore, in order to see an increase in SNR of a factor of three, the number of averages would have to be increased by a factor of nine. This would equate to a measurement time of about 27 hours for the mixture ON experiment, which could prove difficult for factors such as sample availability and stability of the discharge plasma. In principle, though, this could be possible to perform with further improvements to the experimental set-up. The implementation of a larger reservoir system could curtail the issue of sample availability for longer experiments. Upgrading of the pumping system could allow for the rate of the pulsing of the molecular jet to be increased from 5 Hz, thus decreasing the time required to run the experiments.

$$\Delta_{SNR} = \sqrt{\frac{N^{B}_{averages}}{N^{A}_{averages}}} \tag{8.1}$$

To begin to explore the effect of longer integration time, the mixture discharge experiments were performed using the cold trap method. The aim of this was to ascertain if any of the neutral molecules deemed 'missing' from the supersonic expansion experiments could be observed, albeit under different experimental conditions. Despite the different conditions, the cold trap method has the advantage that recording more FIDs, thus resulting in longer experiments, is presently more easily achieved than in the supersonic expansion method. As discussed in Chapter 3, the cold trap method allows for the accumulation of neutral discharge products in the cold trap, and the spectroscopic probing of these molecules once they are re-introduced into the vacuum chamber acting as a static gas cell.

For the cold trap experiments here, the total number of FIDs recorded, co-added, and Fourier transformed was 100,000. This, according to Equation 8.1, should result

in an increase in SNR of a factor of ten compared to the supersonic expansion experiment. Care should be taken here, though, as the two experiments are not so easily compared. The different temperatures of the experiments, among other factors, will also have an effect on the line intensities. So the direct comparison in this way may not be as applicable as is first suggested. However, the elongated experiments nonetheless allow for the possibility to detect weaker species without modifying the current infrastructure of the set-up.

The spectrum of the cold trap ON experiment showed, as expected, products that can be assigned to the discharge of the individual precursors. These products have been detailed in Chapter 3 for the discharge of acetonitrile and in the preceding paragraphs for the discharge of acetaldehyde. The products identified as indicator species for the reaction of the two precursor molecules were also searched for in the ON experiment spectrum, in particular those which contain both a nitrogen and oxygen atoms. The presence of acetyl cyanide, cyanoacetaldehyde, or 3-cyanopropanal is of significant relevance, especially in terms of the application of the discharge experimental data to observational searches, as these molecules have not yet been detected in the ISM, and acetonitrile and acetaldehyde have been. The production of any of these, then, could provide evidence and motivation for searches for the molecules in areas of high abundance of acetonitrile and acetaldehyde. The cold trap ON experiment, and the concurrent increased number of recorded FIDs, did not show transition frequencies for any of the four indicator species. As the production of these molecules could not be identified, it seems likely that the longer integration time with the supersonic expansion method would also not show their presence in the current set-up, though this cannot be completely ruled out because of the aforementioned differences in the experimental procedures. It is worth noting, then, that the best strategy in moving forwards would be to explore different nozzle designs in order to facilitate the production of these molecules. Targeted experiments could be performed, where the concentration is the production of the doubly functional molecules. This is discussed above in the context of elongating the recombination zone, and is supported by the fact that the molecules of interest are not detected in the cold trap experiment.

It should also be noted that the pathways and mechanisms presented here are suggestions as to what may be occurring in the discharge plasma. As mentioned earlier, they are constructed from chemical intuition, and by considering the presence of various radicals indicated by the spectral analysis. Experiments with isotopically enriched precursors could be performed to confirm some of these pathways. Using rotational spectroscopy as the analytical tool in this experiment would allow for the distinction between the isotopically enriched discharge products, meaning that a refined breakdown of which precursor molecules the radicals originate from, and which radicals react together to form the discharge products, can be achieved.

Table 8.3: The radical-radical recombinations and resulting product molecules compiled by considering the hydrogen, methyl, cyano, formyl, cyanomethyl, and acetyl radicals. The molecules marked with a star (*) are those which contain both nitrogen and oxygen atoms and can act as an indicator that fragments from both precursors are recombining; see Table 8.4 and Figure 8.6. The dipole moment components listed, in Debye (D), are from structure optimisation calculations at the B3LYP/aug-cc-pVTZ level of theory.

Radical recombination	Product	μ_a / D	μ_b / D	μ_c / D
hydrogen + hydrogen	dihydrogen	0.0	0.0	0.0
hydrogen + methyl	methane	0.0	0.0	0.0
hydrogen + cyano	hydrogen cyanide	0.0	3.0	0.0
hydrogen + formyl	formaldehyde	2.4	0.0	0.0
hydrogen + cyanomethyl	acetonitrile	0.0	3.0	0.0
hydrogen + acetyl	acetaldehyde	2.7	1.1	0.0
methyl + methyl	ethane	0.0	0.0	0.0
methyl + cyano	acetonitrile	0.0	3.0	0.0
methyl + formyl	acetaldehyde	2.7	1.1	0.0
methyl + cyanomethyl	ethyl cyanide	4.0	1.3	0.0
methyl + acetyl	propanal	1.8	2.1	0.0
cyano + cyano	cyanogen	0.0	0.0	0.0
cyano + formyl	formyl cyanide*	1.1	2.2	0.0
cyano + cyanomethyl	malononitrile	0.0	3.8	0.0
cyano + acetyl	acetyl cyanide*	2.5	2.6	0.0
formyl + formyl	glyoxal	0.0	0.0	0.0
formyl + cyanomethyl	cyanoacetaldehyde*	2.5	4.6	0.0
formyl + acetyl	malondialdehyde; keto	0.0	3.0	0.0
formyl + acetyl	malondialdehyde; enol	4.8	2.4	0.0
cyanomethyl + cyanomethyl	succinonitrile	0.0	0.0	0.0
cyanomethyl + acetyl	3-cyanopropanal*	2.6	1.6	0.0
acetyl + acetyl	succinaldehyde	0.0	0.0	0.0

Table 8.4: The zero-point energy corrected energy differences between the products and radical reactants, calculated at the B3LYP/aug-cc-pVTZ level of theory. The molecules are those which contain both nitrogen and oxygen atom and can act as an indicator that fragments from both precursors are recombining. The Lewis structures of the molecules can be found in Figure 8.6.

Radical recombination	Product	ΔE / kJ mol^{-1}
cyano + formyl	formyl cyanide	-525
cyano + acetyl	acetyl cyanide	-429
formyl + cyanomethyl	cyanoacetaldehyde	-364
cyanomethyl + acetyl	3-cyanopropanal	-243

8.4 Conclusions

The discharge spectrum of acetaldehyde was recorded in the W-band region under supersonic expansion conditions. This revealed the production of a number of astrochemically interesting species, including the formyl radical, acrolein, ketene, and propyne. The results were discussed in the context of the possible pathways that could lead to these products being formed. The spatial distribution mapping of acetaldehyde with the discharge products would unveil whether the pathways suggested by the discharge experiments are relevant to interstellar chemistry. As a next step, spatial distribution maps using data from the discharge of multi-component mixtures could be used to study the complex reaction networks in the ISM and bring together experimentalists, theoreticians, and observers to help answer some of the pressing questions in interstellar chemical evolution.

Chapter 9

Summary and Outlook

The detection of molecules in the interstellar medium (ISM) is achieved through the interplay of laboratory spectroscopy and observational astronomy. Advancements in observational astronomy, in particular in the bandwidth, sensitivity, and spatial resolution of radio astronomical facilities, has led to an unprecedented throughput of observational data. In order to meet the challenge of analysing this data, and to answer fundamental questions in astronomy and astrochemistry, there needs to be a concurrent increase in the volume of data produced from laboratory spectroscopy. The detection of ever-increasingly complex organic molecules (COMs) and understanding the reactions that occur in the ISM that produce these COMs are current aspects at the forefront of the field. The focus of this thesis has been to contribute to this effort with the application of high-resolution broadband chirped-pulse rotational spectroscopy to molecules of astrochemical relevance.

Pure rotational spectroscopy is perfectly suited to meeting the demand for laboratory data. Analysis of rotational spectra delivers line lists and rotational constants for the molecules studied. Application of these to observational data sets allows astronomers to search for the molecules in interstellar space. The fingerprint nature of rotational spectra means that the unambiguous identification of molecules is made. This specificity is not only molecule-specific, but also conformer- and isotopologue-specific. Further, the use of rotational transitions for detections allows for quantitative information on the density and temperature of molecules in the ISM to be obtained.

The experimental set-ups used to meet the aims of this thesis were introduced in Chapter 3. The Hamburg COMPACT Spectrometer, the 18-26 GHz Spectrometer, and the BrightSpec W-band Spectrometer allow for the recording of rotational spectra in the frequency ranges 2-18 GHz, 18-26 GHz, and 75-110 GHz, respectively. These spectrometers can be utilised under two different conditions. The COMPACT and 18-26 GHz spectrometers involve probing molecules in a supersonic expansion. The environment of the supersonic expansion leads to the study of the vibrationally-

and rotationally-cooled low-energy conformers of the molecules. In addition to this functionality, the W-band spectrometer can also operate with the vacuum chamber acting as a room-temperature static or slow flow cell. The experiments at room temperature allow for the observation and assignment of the pure rotational spectra of low-lying vibrationally excited states of molecules. The frequency ranges that the spectrometers cover are particularly relevant for comparison to observational data sets. For example, the low-frequency data overlaps with facilities such as the Jansky Very Large Array and the Effelsberg 100m Radio Telescope. The W-band spectrometer has substantial overlap with the Band 3 operating regime (86-114 GHz) of the Atacama Large Millimeter/submillimeter Array (ALMA), which makes the laboratory data presented in this thesis applicable to the cutting edge of observational astronomy. The chapter also details the implementation and optimisation of an electrical discharge nozzle on the W-band spectrometer. The discharge nozzle facilitates the *in situ* investigation of reactive species and the production of new molecules from these species. The discharge nozzle's performance was benchmarked against the performance of similar systems with acetonitrile as the test molecule.

The analyses of the rotational spectra of *iso*-propyl cyanide, 1,2-propanediol, the amino alcohols alaninol, valinol, leucinol, and isoleucinol, and imidazole are presented in Chapters 4-7. These molecules are interesting in a chemical sense due to the presence of nitrogen- and oxygen-containing functional groups, which are important in terrestrial chemistry. In Chapter 8, the application of the electrical discharge apparatus on the W-band spectrometer to acetaldehyde and the resulting astrochemical implications are discussed, as is the prospect of its use for multi-component mixtures.

In Chapter 4, the rotational spectrum of *iso*-propyl cyanide, the first branched molecule detected in the ISM [107], was analysed. The experiment was performed in the room-temperature flow cell of the W-band spectrometer, and the analysis focused on the characterisation of the ground state of the molecule, the energetically available vibrationally excited states, and the singly substituted isotopologues. Ten vibrationally excited states were identified and assigned, and all of the states were within 500 cm^{-1} of the ground state structure, as revealed by anharmonic frequency calculations. The rotational constants and line lists determined by this analysis allowed for a search for the vibrationally excited states in the Re-exploring Molecular Complexity with ALMA survey [117]. Four of the low-lying states were detected towards the molecular cloud Sagittarius B2 (Sgr B2), in a region called Sgr B2(N2b), which is offset from the main hot core Sgr B2(N). The states ν_{30}, ν_{29}, ν_{17}, and ν_{16} were detected with nine, four, six, and three securely identified features, respectively. A number of other features were identified in the observational spectrum, but were unable to be securely assigned due to blending of emissions from other molecules. The line profiles were accurately described under local thermodynamic equilibrium

(LTE) conditions at 150 K. Because of the sensitivity of the W-band spectrometer, the singly substituted isotopologues of *iso*-propyl cyanide were assigned in natural abundance, which allowed the experimental gas-phase structure of the molecule to be determined. From this analysis, it was found that the C-CN bond length is somewhat independent of the alkyl chains attached to the -CN group; the bond length was determined to be 1.4600(46) Å for *i*-propyl cyanide, which is in keeping with analogous molecules whose C-CN bond length was determined in other work [111–115].

The broadband rotational spectrum of 1,2-propanediol between 75-110 GHz was presented in Chapter 5. The six lowest energy conformers of the molecule were assigned in the spectrum, and the line frequencies were globally fit with line lists available in the literature [124, 127–130]. This augmentation of data delivered the most comprehensive set of rotational constants for the conformers available to date. The rotational constants, which were determined with experimental data extending up to 400 GHz, will facilitate searches for these conformers in the ISM, and, due to their substantial frequency overlap, the line lists from the W-band spectrometer are particularly applicable to observational data from ALMA Band 3. Vibrational states of the lowest two energy conformers were also assigned - two states were assigned for conformer 1 and one state was assigned for conformer 2. The assignment of the lowest energy vibrational state of conformer 2, $\nu_{33}(2)$, was reported previously by Caminati [127], but the broadband capabilities of this work allowed the determination of his assignment as actually being the ground state conformer fifth highest in energy, gG'g'.

A family of simple amino alcohols - alaninol, valinol, leucinol, and isoleucinol - were studied across the 2-110 GHz frequency range, using all three spectrometers described in Chapter 3. The myriad of conformers, isotopologues, and vibrationally excited states observed is discussed in Chapter 6. The rotational constants of these species, which are effectively a reduced form of their amino acid analogues, include accurately determined nuclear quadrupole coupling constants, determinable from the low-frequency data, and centrifugal distortion constants, important for the high-frequency data. This extensive description, reported for the majority of the species for the first time in this work, is necessary for searching for these molecules across a large number of observational facilities. The quadrupole coupling constants will be important for searches in the low frequency regimes, where hyperfine patters can be used as a further validation mechanism for interstellar detections [53]. The centrifugal distortion constants will be important for searches that go deeper into the mmw regime. In total, two vibronic ground state conformers for alaninol, four for valinol, three for leucinol, and seven for isoleucinol were assigned in the experimental spectra. The experiments also produced a wealth of data regarding the isotopologues of these structures, which allowed for detailed structural parameters

to be determined and compared. The analysis definitively showed that the lowest energy conformers of all of the amino alcohols studied had structures that were stabilised by a hydrogen bond between the hydroxyl hydrogen and the nitrogen of the amino group. The motif, characterised by similar N(lone pair)-N-C2-C1, N-C2-C1-O, and C2-C1-O-H dihedral angles, is seen across all four of the amino alcohols. Vibrational states of alaninol and valinol were also assigned in the room-temperature W-band spectrum, and with these assignments, they can now be searched for upon the successful detection of the parent species. The observation of any one of these molecules, made possible by the data presented in Chapter 6, would establish a new type of compound observed in the ISM and could act as signposts to regions where their amino acid analogues could be present in the gas phase.

Chapter 7 discusses the rotational spectrum of the nitrogen-containing heterocycle imidazole. The molecule was studied across a number of rotational spectrometers, including the ones described in Chapter 3 and the 260-295 GHz spectrometer at the University of Virginia [40, 95, 165]. The vibronic ground state of the molecule was assigned, including the extensive hyperfine splitting pattern observed because of the nuclear quadrupole coupling of the two nitrogen nuclei. The singly substituted isotopologues were also assigned, and allowed for the gas-phase structure to be determined with the extended frequency range covered in this work compared to the literature [160–162]. Both the 75-110 GHz and 260-295 GHz regions were probed at room temperature, and three vibrationally excited states were observed and assigned. The high energies of the vibrational states reinforce the rigidity of the imidazole ring structure. The parent species was searched for towards Sgr B2(N2) with the Exploring Molecular Complexity with ALMA line survey [118]. The heterocycle was not detected towards this source, and a search towards the Taurus Molecular Cloud TMC-1, where the aromatic molecule benzonitrile was detected [53], is suggested.

The discharge set-up that was implemented and optimised in Chapter 3 was used to study the discharge products of acetaldehyde, the results of which are discussed in Chapter 8. Subjecting acetaldehyde to the action of the discharge produced a number of astrochemically relevant molecular species, the presence of which was confirmed by the W-band spectrometer. The discharge of acetaldehyde produced the formyl radical, acrolein, acetone, ketene, and propyne. A number of reaction pathways from acetaldehyde to these discharge products were explored. For example, the elongation of the two-carbon molecule acetaldehyde to the three-carbon molecules acrolein and acetone is suggested to proceed by the reaction of acetaldehyde with the discharge-produced methyl radical. Further, the production of ketene is likely due to acetaldehyde dehydrogenation, and propyne is likely produced by the recombination of smaller carbon-based radicals. The relevance of these pathways to the ISM could be determined by mapping the spatial distributions of acetaldehyde

and the identified discharge products simultaneously, where the production of such data from observational campaigns is becoming the norm because of the broadband capabilities, increased sensitivity, and high spatial resolution of facilities such as ALMA. The foundation was also laid for application of this method to the discharge of multi-component mixtures. The discharge of the mixture of acetaldehyde and acetonitrile was performed, and a number of experimental modifications were suggested in order for the experiment to be optimised for the detection of molecules that contain the oxygen atom from acetaldehyde and the nitrogen atom from acetonitrile. The discharge should enable the production of transient molecular species that can be characterised by rotational spectroscopy and subsequently searched for in interstellar space. And the further application of multi-species spatial distribution maps from observational data will determine whether the species are chemically linked in the ISM.

Further work in the direction of the aims of this thesis can be centred around the detection of the studied molecules in the ISM. Work on this has already begun, with a number of vibrational states of *iso*-propyl cyanide being detected towards Sgr B2(N2b) and searches for imidazole towards Sgr B2. Inspiration can be gained from the studied systems for new laboratory measurements, especially in the high-frequency regime. For example, other simple amino alcohols can be studied, where two such examples include prolinol, interesting because of its ring structure, or sulfur-containing cysteinol, which may have important structural side-effects because of the presence of the thiol group. Other heteroatom-containing cyclic compounds can also be investigated, such as purines, pyrimidines, and further derivatives. This can, and should, be influenced by collaboration with astronomers, so that the data can directly meet their needs. This can also be applied to the discharge experiments, whereby systematic studies of the incorporation of other functional groups into COMs could be studied. Interstellar phosphorus and sulfur are two such examples that could be focal points of these future projects.

The work showcased in this thesis focused on the characterisation of the rotational spectra of astrochemically relevant molecules. In particular, the molecules studied encompass a number of nitrogen- and oxygen-containing COMs, which are important classes of compounds for characterising the chemical complexity of the ISM. The experimental data is paramount for performing searches for these molecules, including isotopologues and vibrationally excited states, in molecular clouds, thus allowing the chemical inventory of interstellar space to be better determined. The study of isotopologue chemistry can allow for the chemical evolution of such regions to be traced, as well as providing structural information on the molecules themselves. And the presence of vibrational states can aid in the characterisation of the physical conditions of the regions they are detected in. Reaction pathways to molecules can also be considered with the use of electrical discharge ex-

periments, the relevance of which can be extended to observational data sets in the form of multi-species spatial distribution maps, thus deepening the understanding of chemical evolution in the ISM. Increasing the chemical knowledge of interstellar structures will allow for these fundamental questions in astronomy and astrochemistry to be answered.

Bibliography

[1] S. Weinreb, A. Barrett, M. Meeks, and J. Henry, "Radio observations of OH in the interstellar medium", Nature **200**, 829–831 (1963).

[2] A. Cheung, D. Rank, C. Townes, D. Thornton, and W. Welch, "Detection of NH_3 molecules in the interstellar medium by their microwave emission", Physical Review Letters **21**, 1701–1705 (1968).

[3] A. Cheung, D. Rank, C. Townes, D. Thornton, and W. Welch, "Detection of water in interstellar regions by its microwave radiation", Nature **221**, 626–628 (1969).

[4] L. Snyder, D. Buhl, B. Zuckerman, and P. Palmer, "Microwave detection of interstellar formaldehyde", Physical Review Letters **22**, 679–681 (1969).

[5] J. Ball, C. Gottlieb, A. Lilley, and H. Radford, "Detection of methyl alcohol in Sagittarius", The Astrophysical Journal **162** (1970).

[6] H. Kroto, C. Kirby, D. Walton, L. Avery, N. Broten, J. MacLeod, and T. Oka, "The detection of cyanohexatriyne in Heile's Cloud 2", The Astrophysical Journal **219**, L133 (1978).

[7] J. Cami, J. Bernard-Salas, E. Peeters, and S. Malek, "Detection of C_{60} and C_{70} in a young planetary nebula", Science **329**, 1180–1182 (2010).

[8] B. A. McGuire, "2018 Census of interstellar, circumstellar, extragalactic, protoplanetary disk, and exoplanetary molecules", Astrophysical Journal Supplement Series **239**, 17 (2018).

[9] E. Herbst, "Chemistry in the interstellar medium", Annual Review of Physical Chemistry **46**, 27–54 (1995).

[10] T. P. Snow and B. J. McCall, "Diffuse atomic and molecular clouds", Annual Review of Astronomy and Astrophysics **44**, 367–414 (2006).

[11] NRAO - National Radio Astronomy Observatory.

[12] NASA - National Aeronautics and Space Administration.

[13] ALMA - Atacama Large Millimeter/submillimeter Array.

[14] Schmiedeke, A., Schilke, P., Möller, Th., Sánchez-Monge, Á., Bergin, E., Comito, C., Csengeri, T., Lis, D. C., Molinari, S., Qin, S.-L., and Rolffs, R., "The physical and chemical structure of Sagittarius B2 - I. Three-dimensional thermal dust and free-free continuum modeling on 100 au to 45 pc scales", Astronomy and Astrophysics **588**, A143 (2016).

[15] Sánchez-Monge, Á., Schilke, P., Schmiedeke, A., Ginsburg, A., Cesaroni, R., Lis, D. C., Qin, S.-L., Müller, H. S. P., Bergin, E., Comito, C., and Möller, Th., "The physical and chemical structure of Sagittarius B2 - II. Continuum millimeter emission of Sgr B2(M) and Sgr B2(N) with ALMA", Astronomy and Astrophysics **604**, A6 (2017).

[16] Pols, S., Schwörer, A., Schilke, P., Schmiedeke, A., Sánchez-Monge, Á., and Möller, Th., "The physical and chemical structure of Sagittarius B2 - III. Radiative transfer simulations of the hot core Sgr B2(M) for methyl cyanide", Astronomy and Astrophysics **614**, A123 (2018).

[17] A. Schwörer, Á. Sánchez-Monge, P. Schilke, T. Möller, A. Ginsburg, F. Meng, A. Schmiedeke, H. S. P. Müller, D. Lis, and S.-L. Qin, "The physical and chemical structure of Sagittarius B2 - IV. Converging filaments in the high-mass cluster forming region Sgr B2(N)", Astronomy and Astrophysics **628**, A6 (2019).

[18] F. Meng, Á. Sánchez-Monge, P. Schilke, M. Padovani, A. Marcowith, A. Ginsburg, A. Schmiedeke, A. Schwörer, C. DePree, V. S. Veena, and T. Möller, "The physical and chemical structure of Sagittarius B2 - V. Non-thermal emission in the envelope of Sgr B2", Astronomy and Astrophysics **630**, A73 (2019).

[19] L. Pagani, C. Favre, P. F. Goldsmith, E. A. Bergin, R. Snell, and G. Melnick, "The complexity of Orion: An ALMA view - I. Data and first results", Astronomy and Astrophysics **604**, A32 (2017).

[20] C. Favre, L. Pagani, P. F. Goldsmith, E. A. Bergin, M. Carvajal, I. Kleiner, G. Melnick, and R. Snell, "The complexity of Orion: An ALMA view - II. gGg'-ethylene glycol and acetic acid", Astronomy and Astrophysics **604**, L2 (2017).

[21] L. Pagani, E. Bergin, P. F. Goldsmith, G. Melnick, R. Snell, and C. Favre, "The complexity of Orion: An ALMA view - III. The explosion impact", Astronomy and Astrophysics **624**, L5 (2019).

[22] S. L. Widicus Weaver, "Millimeterwave and submillimeterwave laboratory spectroscopy in support of observational astronomy", Annual Review of Astronomy and Astrophysics **57**, 79–112 (2019).

[23] J. K. Jørgensen, M. H. D. van der Wiel, A. Coutens, J. M. Lykke, H. S. P. Müller, E. F. van Dishoeck, H. Calcutt, P. Bjerkeli, T. L. Bourke, M. N. Drozdovskaya, C. Favre, E. C. Fayolle, R. T. Garrod, S. K. Jacobsen, K. I. Öberg, M. V. Persson, and S. F. Wampfler, "The ALMA Protostellar Interferometric Line Survey (PILS) - first results from an unbiased submillimeter wavelength line survey of the Class 0 protostellar binary IRAS 16293-2422 with ALMA", Astronomy and Astrophysics **595**, A117 (2016).

[24] P. F. Goldsmith and W. D. Langer, "Population diagram analysis of molecular line emission", The Astrophysical Journal **517**, 209–225 (1999).

[25] A. Belloche, H. S. P. Müller, K. M. Menten, P. Schilke, and C. Comito, "Complex organic molecules in the interstellar medium: IRAM 30 m line survey of Sagittarius B2(N) and (M)", Astronomy and Astrophysics **559**, A47 (2013).

[26] E. F. van Dishoeck, *Laboratory astrophysics: Key to understanding the universe*, 2019.

[27] V. Taquet, E. F. van Dishoeck, M. Swayne, D. Harsono, J. K. Jørgensen, L. Maud, N. F. W. Ligterink, H. S. P. Müller, C. Codella, K. Altwegg, A. Bieler, A. Coutens, M. N. Drozdovskaya, K. Furuya, M. V. Persson, M. L. R. van't Hoff, C. Walsh, and S. F. Wampfler, "Linking interstellar and cometary O_2: A deep search for $^{16}O^{18}O$ in the solar-type protostar IRAS 16293-2422", Astronomy and Astrophysics **618**, A11 (2018).

[28] N. Brickhouse, G. J. Ferland, S. Milam, E. Sciamma-O'Brien, A. Smale, A. Spyrou, P. Stancil, L. Storrie-Lombardi, and G. M. Wahlgren, "2018 NASA Laboratory Astrophysics Workshop: Scientific Organizing Committee Report", Bulletin of the American Astronomical Society **52** (2020).

[29] R. A. Motiyenko, B. Tercero, J. Cernicharo, and L. Margulès, "Rotational spectrum of formamide up to 1 THz and first ISM detection of its vibrational state", Astronomy and Astrophysics **548**, A71 (2012).

[30] C. Gottlieb, M. McCarthy, and P. Thaddeus, "Vibrationally excited C_6H", Astrophysical Journal Supplement Series **189**, 261–269 (2010).

[31] K. Furuya, Y. Aikawa, N. Sakai, and S. Yamamoto, "Carbon isotope and isotopomer fractionation in cold dense cloud cores", The Astrophysical Journal **731**, 38 (2011).

[32] J. K. Jorgensen, A. Belloche, and R. T. Garrod, "Astrochemistry during the formation of stars", arXiv e-prints, Invited review to be published in Annual Reviews of Astronomy and Astrophysics, arXiv:2006.07071 (2020).

[33] S. Fortman, I. Medvedev, C. Neese, and F. De Lucia, "How complete are astrophysical catalogs for the millimeter and submillimeter spectral region?", Astrophysical Journal Letters **725**, L11–L14 (2010).

[34] A. Wuttke and R. A. Mata, "Visualizing dispersion interactions through the use of local orbital spaces", Journal of Computational Chemistry **38**, 15–23 (2017).

[35] C. E. Cleeton and N. H. Williams, "Electromagnetic waves of 1.1 cm wavelength and the absorption spectrum of ammonia", Physical Review **45**, 234–237 (1934).

[36] T. J. Balle, E. J. Campbell, M. R. Keenan, and W. H. Flygare, "A new method for observing the rotational spectra of weak molecular complexes: KrHCl", The Journal of Chemical Physics **71**, 2723–2724 (1979).

[37] T. J. Balle and W. H. Flygare, "Fabry–Perot cavity pulsed fourier transform microwave spectrometer with a pulsed nozzle particle source", Review of Scientific Instruments **52**, 33–45 (1981).

[38] J. Grabow, W. Stahl, and H. Dreizler, "A multioctave coaxially oriented beam-resonator arrangement Fourier-transform microwave spectrometer", Review of Scientific Instruments **67**, 4072–4084 (1996).

[39] G. G. Brown, B. C. Dian, K. O. Douglass, S. M. Geyer, and B. H. Pate, "The rotational spectrum of epifluorohydrin measured by chirped-pulse Fourier transform microwave spectroscopy", Journal of Molecular Spectroscopy **238**, 200–212 (2006).

[40] J. L. Neill, B. J. Harris, A. L. Steber, K. O. Douglass, D. F. Plusquellic, and B. H. Pate, "Segmented chirped-pulse Fourier transform submillimeter spectroscopy for broadband gas analysis", Optics Express **21**, 19743 (2013).

[41] H. S. Gutowsky, J. Chen, P. J. Hajduk, J. D. Keen, C. Chuang, and T. Emilsson, "The silicon-carbon double bond: Theory takes a round", Journal of the American Chemical Society **113**, 4747–4751 (1991).

[42] M. D. Harmony, K. A. Beran, D. M. Angst, and K. L. Ratzlaff, "A compact hot-nozzle Fourier-transform microwave spectrometer", Review of Scientific Instruments **66**, 5196–5202 (1995).

[43] R. J. Levis, "Laser desorption and ejection of biomolecules from the condensed phase into the gas phase", Annual Review of Physical Chemistry **45**, 483–518 (1994).

[44] R. D. Suenram, F. J. Lovas, G. T. Fraser, and K. Matsumura, "Pulsed-nozzle fourier-transform microwave spectroscopy of laser-vaporized metal oxides: Rotational spectra and electric dipole moments of YO, LaO, ZrO, and HfO", The Journal of Chemical Physics **92**, 4724–4733 (1990).

[45] R. Schlachta, G. Lask, S. Tsay, and V. Bondybey, "Pulsed discharge source of supersonically cooled transient species", Chemical Physics **155**, 267–274 (1991).

[46] P. Thaddeus, M. C. McCarthy, M. J. Travers, C. A. Gottlieb, and W. Chen, "New carbon chains in the laboratory and in interstellar space", Faraday Discussions **109**, 121–135 (1998).

[47] P. Thaddeus and M. McCarthy, "Carbon chains and rings in the laboratory and in space", Spectrochimica Acta Part A: Molecular and Biomolecular Spectroscopy **57**, 757 (2001).

[48] H. Gupta, S. Brünken, F. Tamassia, C. A. Gottlieb, M. C. McCarthy, and P. Thaddeus, "Rotational spectra of the carbon chain negative ions C_4H^- and C_8H^-", The Astrophysical Journal **655**, L57 (2007).

[49] M. C. McCarthy and P. Thaddeus, "High-resolution rotational spectroscopy of the carbon chain anions C_3N^-, C_4H^-, and C_4D^-", The Journal of Chemical Physics **129**, 054314 (2008).

[50] M. C. McCarthy, K. N. Crabtree, M.-A. Martin-Drumel, O. Martinez, B. A. McGuire, and C. A. Gottlieb, "A laboratory study of C_3H^+ and the C_3H radical in three new vibrationally excited $^2\Sigma$ states using a pin-hole nozzle discharge source", Astrophysical Journal Supplement Series **217**, 10 (2015).

[51] R. A. Loomis, D. P. Zaleski, A. L. Steber, J. L. Neill, M. T. Muckle, B. J. Harris, J. M. Hollis, P. R. Jewell, V. Lattanzi, F. J. Lovas, O. Martinez, M. C. McCarthy, A. J. Remijan, B. H. Pate, and J. F. Corby, "The detection of interstellar ethanimine (CH_3CHNH) from observations taken during the GBT PRIMOS survey", The Astrophysical Journal **765**, L9 (2013).

[52] B. A. McGuire, P. B. Carroll, R. A. Loomis, I. A. Finneran, P. R. Jewell, A. J. Remijan, and G. A. Blake, "Discovery of the interstellar chiral molecule propylene oxide (CH_3CHCH_2O)", Science **352**, 1449–1452 (2016).

[53] B. A. McGuire, A. M. Burkhardt, S. Kalenskii, C. N. Shingledecker, A. J. Remijan, E. Herbst, and M. C. McCarthy, "Detection of the aromatic molecule benzonitrile (c-C_6H_5CN) in the interstellar medium", Science **359**, 202–205 (2018).

[54] J. M. Brown, *Molecular spectroscopy*, Oxford Chemistry Primers (Oxford University Press, 1998).

[55] W. Gordy and R. L. Cook, *Microwave molecular spectra* (New York: Wiley, 1984).

[56] M. Born and R. Oppenheimer, "Zur Quantentheorie der Molekeln", Annalen der Physik **389**, 457–484 (1927).

[57] S. A. Cooke and P. Ohring, "Decoding pure rotational molecular spectra for asymmetric molecules", Journal of Spectroscopy (2013).

[58] B. S. Ray, "Über die Eigenwerte des asymmetrischen Kreisels", Zeitschrift für Physik **78**, 74–91 (1932).

[59] J. K. G. Watson, *Vibrational spectra and structure*, 3rd ed., Vol. 6, 1, ed. J. Durig (Amsterdam: Elsevier, 1977).

[60] C. H. Townes and A. L. Schawlow, *Microwave spectroscopy* (New York: Dover Publications, 1975).

[61] J. B. Graneek, W. C. Bailey, and M. Schnell, "Electron-withdrawing effects on the molecular structure of 2- and 3-nitrobenzonitrile revealed by broadband rotational spectroscopy and their comparison with 4-nitrobenzonitrile", Physical Chemistry Chemical Physics **20**, 22210–22217 (2018).

[62] P. W. Atkins and D. P. J., *Atkins' physical chemistry*, 9th edition (Oxford: Oxford University Press, 2010).

[63] H. M. Pickett, "The fitting and prediction of vibration-rotation spectra with spin interactions", Journal of Molecular Spectroscopy **148**, 371–377 (1991).

[64] M. K. Sharma, M. Sharma, A. K. Sharma, and S. Chandra, "On partition function in astronomy & astrophysics", Astronomische Nachrichten **338**, 125–128 (2017).

[65] G. G. Brown, B. C. Dian, K. O. Douglass, S. M. Geyer, S. T. Shipman, and B. H. Pate, "A broadband Fourier transform microwave spectrometer based on chirped pulse excitation", Review of Scientific Instruments **79**, 053103 (2008).

[66] J. Mangum and Y. Shirley, "How to calculate molecular column density", Publications of the Astronomical Society of the Pacific **127**, 266 (2015).

[67] M. Carvajal, C. Favre, I. Kleiner, C. Ceccarelli, E. A. Bergin, and D. Fedele, "Impact of nonconvergence and various approximations of the partition function on the molecular column densities in the interstellar medium", Astronomy and Astrophysics **627**, A65 (2019).

[68] Y. Morino and C. Hirose, "Microwave spectra of methyl iodide in the excited vibrational states. The Fermi resonance between the ν_5 and $\nu_3 + \nu_6$ states", Journal of Molecular Spectroscopy **22**, 99–104 (1967).

[69] D. F. Plusquellic, R. D. Suenram, B. Maté, J. O. Jensen, and A. C. Samuels, "The conformational structures and dipole moments of ethyl sulfide in the gas phase", The Journal of Chemical Physics **115**, 3057–3067 (2001).

[70] C. M. Western, "PGOPHER: A program for simulating rotational, vibrational and electronic spectra", Journal of Quantitative Spectroscopy and Radiative Transfer **186**, 221–242 (2017).

[71] Z. Kisiel, L. Pszczółkowski, I. R. Medvedev, M. Winnewisser, F. C. De Lucia, and E. Herbst, "Rotational spectrum of trans-trans diethyl ether in the ground and three excited vibrational states", Journal of Molecular Spectroscopy **233**, 231–243 (2005).

[72] J. K. G. Watson, "Indeterminacies of fitting parameters in molecular spectroscopy", in *Handbook of high-resolution spectroscopy, vol. 1*, edited by M. Quack and F. Merkt (New York: John Wiley and Sons, Ltd., 2011), pp. 587–606.

[73] M. J. Frisch, G. W. Trucks, H. B. Schlegel, G. E. Scuseria, M. A. Robb, J. R. Cheeseman, G. Scalmani, V. Barone, G. A. Petersson, H. Nakatsuji, X. Li, M. Caricato, A. Marenich, J. Bloino, B. G. Janesko, R. Gomperts, B. Mennucci, H. P. Hratchian, J. V. Ortiz, A. F. Izmaylov, J. L. Sonnenberg, D. Williams-Young, F. Ding, F. Lipparini, F. Egidi, J. Goings, B. Peng, A. Petrone, D. Henderson T. andRanasinghe, V. G. Zakrzewski, J. Gao, N. Rega, G. Zheng, W. Liang, M. Hada, M. Ehara, K. Toyota, R. Fukuda, J. Hasegawa, M. Ishida, T. Nakajima, Y. Honda, O. Kitao, H. Nakai, T. Vreven, K. Throssell, J. A. Montgomery Jr., J. E. Peralta, F. Ogliaro, M. Bearpark, J. J. Heyd, E. Brothers, K. N. Kudin, V. N. Staroverov, T. Keith, R. Kobayashi, J. Normand, K. Raghavachari, A. Rendell, J. C. Burant, S. S. Iyengar, J. Tomasi, M. Cossi, J. M. Millam, M. Klene, C. Adamo, R. Cammi, J. W. Ochterski, R. L. Martin, K. Morokuma, O. Farkas, J. B. Foresman, and D. J. Fox, *Gaussian 09*, 2009.

[74] Spartan 14.

[75] A. D. Becke, "Density-functional thermochemistry. III. The role of exact exchange", The Journal of Chemical Physics **98**, 5648–5652 (1993).

[76] C. Lee, W. Yang, and R. G. Parr, "Development of the Colle-Salvetti correlation-energy formula into a functional of the electron density", Physical Review B **37**, 785–789 (1988).

[77] S. Grimme, J. Antony, S. Ehrlich, and H. Krieg, "A consistent and accurate ab initio parametrization of density functional dispersion correction (DFT-D) for the 94 elements H-Pu", The Journal of Chemical Physics **132**, 154104 (2010).

[78] S. Grimme, S. Ehrlich, and L. Goerigk, "Effect of the damping function in dispersion corrected density functional theory", Journal of Computational Chemistry **32**, 1456–1465 (2011).

[79] Y. Zhao and D. G. Truhlar, "The M06 suite of density functionals for main group thermochemistry, thermochemical kinetics, noncovalent interactions, excited states, and transition elements: Two new functionals and systematic testing of four M06-class functionals and 12 other functionals", Theoretical Chemistry Accounts **120**, 215–241 (2008).

[80] C. Møller and M. S. Plesset, "Note on an approximation treatment for many-electron systems", Physical Review **46**, 618–622 (1934).

[81] D. R. Hartree, "The wave mechanics of an atom with a non-coulomb central field. Part II. Some results and discussion", Mathematical Proceedings of the Cambridge Philosophical Society **24**, 111–132 (1928).

[82] F. Weigend and R. Ahlrichs, "Balanced basis sets of split valence, triple zeta valence and quadruple zeta valence quality for H to Rn: Design and assessment of accuracy", Physical Chemistry Chemical Physics **7**, 3297–3305 (2005).

[83] R. Ditchfield, W. J. Hehre, and J. A. Pople, "Self-consistent molecular-orbital methods. IX. An extended Gaussian-type basis for molecular-orbital studies of organic molecules", The Journal of Chemical Physics **54**, 724–728 (1971).

[84] R. Krishnan, J. S. Binkley, R. Seeger, and J. A. Pople, "Self-consistent molecular orbital methods. XX. A basis set for correlated wave functions", The Journal of Chemical Physics **72**, 650–654 (1980).

[85] T. H. Dunning, "Gaussian basis sets for use in correlated molecular calculations. I. The atoms boron through neon and hydrogen", The Journal of Chemical Physics **90**, 1007–1023 (1989).

[86] B. M. Giuliano, L. Bizzocchi, A. Pietropolli Charmet, B. E. Arenas, A. L. Steber, M. Schnell, P. Caselli, B. J. Harris, B. H. Pate, J.-C. Guillemin, and A. Belloche, "Rotational spectroscopy of imidazole: Improved rest frequencies for astrophysical searches", Astronomy and Astrophysics **628**, A53 (2019).

[87] K. Raghavachari, G. W. Trucks, J. A. Pople, and M. Head-Gordon, "A fifth-order perturbation comparison of electron correlation theories", Chemical Physics Letters **157**, 479–483 (1989).

[88] A. Gambi, A. Pietropolli Charmet, P. Stoppa, N. Tasinato, G. Ceselin, and V. Barone, "Molecular synthons for accurate structural determinations: The equilibrium geometry of 1-chloro-1-fluoroethene", Physical Chemistry Chemical Physics **21**, 3615–3625 (2019).

[89] J. Demaison, "Accurate structures of non-rigid molecules by microwave spectroscopy", in *Structures and conformations of non-rigid molecules*, edited by J. Laane, M. Dakkouri, B. van der Veken, and H. Oberhammer (Springer Netherlands, Dordrecht, 1993), pp. 239–256.

[90] Z. Kisiel, *PROSPE - Programs for Rotational Spectroscopy*, 2015.

[91] J. Kraitchman, "Determination of molecular structure from microwave spectroscopic data", American Journal of Physics **21**, 17–24 (1953).

[92] D. Schmitz, V. A. Shubert, T. Betz, and M. Schnell, "Multi-resonance effects within a single chirp in broadband rotational spectroscopy: The rapid adiabatic passage regime for benzonitrile", Journal of Molecular Spectroscopy **280**, 77–84 (2012).

[93] C. Pérez, A. Krin, A. L. Steber, J. C. López, Z. Kisiel, and M. Schnell, "Wetting camphor: Multi-isotopic substitution identifies the complementary roles of hydrogen bonding and dispersive forces", The Journal of Physical Chemistry Letters **7**, 154–160 (2016).

[94] M. Fatima, C. Pérez, B. E. Arenas, M. Schnell, and A. L. Steber, "Benchmarking a new segmented K-band chirped-pulse microwave spectrometer and its application to the conformationally rich amino alcohol isoleucinol", Physical Chemistry Chemical Physics **22**, 17042–17051 (2020).

[95] A. L. Steber, B. J. Harris, J. L. Neill, and B. H. Pate, "An arbitrary waveform generator based chirped pulse fourier transform spectrometer operating from 260 to 295 GHz", Journal of Molecular Spectroscopy **280**, 3–10 (2012).

[96] H. Kallmann and F. Reiche, "Über den Durchgang bewegter Moleküle durch inhomogene Kraftfelder", Zeitschrift für Physik, 352–375 (1921).

[97] D. H. Levy, "The spectroscopy of very cold gases", Science **214**, 263–269 (1981).

[98] A. L. Steber, "Millimeter wave and microwave instrumental development for analytical and astrochemical applications", PhD thesis (Department of Chemistry, University of Virginia, 2014).

[99] S. Saito and S. Yamamoto, "The microwave spectrum of the cyanomethyl radical $CH_2CN(^2B_1)$", The Journal of Chemical Physics **107**, 1732–1739 (1997).

[100] A. Belloche, K. Menten, C. Comito, H. Müller, P. Schilke, J. Ott, S. Thorwirth, and C. Hieret, "Detection of amino acetonitrile in Sgr B2(N)", Astronomy and Astrophysics **482**, 179–196 (2008).

[101] A. Belloche, R. Garrod, H. Müller, K. Menten, C. Comito, and P. Schilke, "Increased complexity in interstellar chemistry: Detection and chemical modeling of ethyl formate and n-propyl cyanide in Sagittarius B2(N)", Astronomy and Astrophysics **499**, 215–232 (2009).

[102] H. S. P. Müller, A. Walters, N. Wehres, A. Belloche, O. H. Wilkins, D. Liu, R. Vicente, R. T. Garrod, K. M. Menten, F. Lewen, and S. Schlemmer, "Laboratory spectroscopic study and astronomical detection of vibrationally excited n-propyl cyanide", Astronomy and Astrophysics **595**, A87 (2016).

[103] H. Müller, A. Belloche, K. Menten, C. Comito, and P. Schilke, "Rotational spectroscopy of isotopic vinyl cyanide, H_2CCHCN, in the laboratory and in space", Journal of Molecular Spectroscopy **251**, 319–325 (2008).

[104] O. Martinez Jr., D. Zaleski, N. Seifert, A. Steber, M. Muckle, R. Loomis, J. Corby, K. Crabtree, P. Jewell, J. Hollis, F. Lovas, D. Vasquez, J. Nyiramahirwe, N. Sciortino, K. Johnson, M. McCarthy, A. Remijan, and B. Pate, "Detection of E-cyanomethanimine toward Sagittarius B2(N) in the Green Bank Telescope PRIMOS survey", Astrophysical Journal Letters **765** (2013).

[105] J. Cernicharo, Z. Kisiel, B. Tercero, L. Kolesniková, I. Medvedev, A. López, S. Fortman, M. Winnewisser, F. De Lucia, J. Alonso, and J.-C. Guillemin, "A rigorous detection of interstellar CH_3NCO: An important missing species in astrochemical networks", Astronomy and Astrophysics **587** (2016).

[106] L. Kolesniková, J. Alonso, C. Bermúdez, E. Alonso, B. Tercero, J. Cernicharo, and J.-C. Guillemin, "The millimeter wave spectrum of methyl cyanate: A laboratory study and astronomical search in space", Astronomy and Astrophysics **591** (2016).

[107] A. Belloche, R. Garrod, H. Müller, and K. Menten, "Detection of a branched alkyl molecule in the interstellar medium: Iso-propyl cyanide", Science **345**, 1584–1587 (2014).

[108] H. Müller, A. Coutens, A. Walters, J. Grabow, and S. Schlemmer, "Rotational spectroscopy, dipole moment and ^{14}N nuclear hyperfine structure of iso-propyl cyanide", Journal of Molecular Spectroscopy **267**, 100 (2011).

[109] S. Fortman, I. Medvedev, C. Neese, and F. De Lucia, "The complete, temperature-resolved experimental spectrum of ethyl cyanide (CH_3CH_2CN) between 210 and 270 GHz", The Astrophysical Journal **725**, 1682–1687 (2010).

[110] J. Durig and Y. Li, "Microwave spectrum, dipole moment and structure of isopropyl cyanide", Journal of Molecular Structure **21**, 289–297 (1974).

[111] M. LeGuennec, G. Wlodarczak, J. Burie, and J. Demaison, "Rotational spectrum of CH_2DCN and structure of methyl cyanide", Journal of Molecular Spectroscopy **154**, 305–323 (1992).

[112] H. Heise, H. Lutz, and H. Dreizler, "Molecular structure, quadrupole coupling tensor and dipole moment of ethyl cyanide", Zeitschrift für Naturforschung - Section A Journal of Physical Sciences **29**, 1345–1355 (1974).

[113] M. Traetteberg, P. Bakken, and H. Hopf, "Structure and conformation of gaseous butyronitrile", Journal of Molecular Structure **556**, 189–196 (2000).

[114] R. Livingston and C. Rao, "The molecular structure of pivalonitrile by electron diffraction", Journal of the American Chemical Society **81**, 3584–3586 (1959).

[115] J. Casado, L. Nygaard, and G. Sorensen, "Microwave spectra of isotopic benzonitriles. Refined molecular structure of benzonitrile", Journal of Molecular Structure **8**, 211–224 (1971).

[116] F. Allen, O. Kennard, D. Watson, L. Brammer, A. Orpen, and R. Taylor, "Tables of bond lengths determined by X-ray and neutron diffraction. Part 1. Bond lengths in organic compounds", Journal of the Chemical Society, Perkin Transactions 2, S1–S19 (1987).

[117] A. Belloche, R. T. Garrod, H. S. P. Müller, I. Menten K. M. andMedvedev, J. Thomas, and Z. Kisiel, "Re-exploring Molecular Complexity with ALMA (ReMoCA): Interstellar detection of urea", Astronomy and Astrophysics **628**, A10 (2019).

[118] A. Belloche, H. S. P. Müller, R. T. Garrod, and K. M. Menten, "Exploring molecular complexity with ALMA (EMoCA): Deuterated complex organic molecules in Sagittarius B2(N2)", Astronomy and Astrophysics **587**, A91 (2016).

[119] A. Belloche, Private Communication, 2020.

[120] B. Zuckerman, B. Turner, D. Johnson, F. Clark, F. Lovas, N. Fourikis, P. Palmer, M. Morris, A. Lilley, J. Ball, C. Gottlieb, M. Litvak, and H. Penfield, "Detection of interstellar trans-ethyl alcohol", Astrophysical Journal Letters **196**, L99–L102 (1975).

[121] J. Pearson, K. Sastry, E. Herbst, and F. De Lucia, "Gauche ethyl alcohol: Laboratory assignments and interstellar identification", The Astrophysical Journal **480**, 420–431 (1997).

[122] B. E. Turner and A. J. Apponi, "Microwave detection of interstellar vinyl alcohol, CH_2=CHOH", The Astrophysical Journal **561**, L207–L210 (2001).

[123] D. Blackmond, "The origin of biological homochirality.", Cold Spring Harbor Perspectives in Biology **2**, a002147 (2010).

[124] F. Lovas, D. Plusquellic, B. Pate, J. Neill, M. Muckle, and A. Remijan, "Microwave spectrum of 1,2-propanediol", Journal of Molecular Spectroscopy **257**, 82–93 (2009).

[125] J. Hollis, F. Lovas, P. Jewell, and L. Coudert, "Interstellar antifreeze: Ethylene glycol", The Astrophysical Journal **571**, L59–L62 (2002).

[126] S. Vázquez, R. Mosquera, M. Rios, and C. Van Alsenoy, "Ab initio gradient optimized molecular geometry and conformational analysis of 1,2-propanediol at the 4-21G level", Journal of Molecular Structure: THEOCHEM **184**, 323–342 (1989).

[127] W. Caminati, "Conformation and hydrogen bond in 1,2-propanediol", Journal of Molecular Spectroscopy **86**, 193–201 (1981).

[128] T. Lockley, J. Hearn, A. King, and B. Howard, "Detection and analysis of a new conformational isomer of propan-1,2-diol by fourier transform microwave spectroscopy", Journal of Molecular Structure **612**, 199–206 (2002).

[129] J.-B. Bossa, M. Ordu, H. Müller, F. Lewen, and S. Schlemmer, "Laboratory spectroscopy of 1, 2-propanediol at millimeter and submillimeter wavelengths", Astronomy and Astrophysics **570**, A12 (2014).

[130] O. Zakharenko, J.-B. Bossa, F. Lewen, S. Schlemmer, and H. Müller, "Millimeter and submillimeter wave spectroscopy of higher energy conformers of 1,2-propanediol", Journal of Molecular Spectroscopy **333**, 23–26 (2017).

[131] Z. Kisiel and L. Pszczółkowski, "Millimeter-wave rotational spectra of the ^{37}Cl species of 1,1,1-trichloroethane", Journal of Molecular Spectroscopy **181**, 48–55 (1997).

[132] J. M. Hollis, F. J. Lovas, and P. R. Jewell, "Interstellar glycolaldehyde: The first sugar", The Astrophysical Journal **540**, L107–L110 (2000).

[133] Y. Kuan, S. B. Charnley, H. Huang, W. Tseng, and Z. Kisiel, "Interstellar glycine", The Astrophysical Journal **593**, 848–867 (2003).

[134] L. E. Snyder, F. J. Lovas, J. M. Hollis, D. N. Friedel, P. R. Jewell, A. Remijan, V. V. Ilyushin, E. A. Alekseev, and S. F. Dyubko, "A rigorous attempt to verify interstellar glycine", The Astrophysical Journal **619**, 914–930 (2005).

[135] P. A. Jones, M. R. Cunningham, P. D. Godfrey, and D. M. Cragg, "A search for biomolecules in Sagittarius B2 (LMH) with the Australia Telescope Compact Array", Monthly Notices of the Royal Astronomical Society **374**, 579–589 (2007).

[136] M. R. Cunningham, P. A. Jones, P. D. Godfrey, D. M. Cragg, I. Bains, M. G. Burton, P. Calisse, N. H. M. Crighton, S. J. Curran, T. M. Davis, J. T. Dempsey, B. Fulton, M. G. Hidas, T. Hill, L. Kedziora-Chudczer, V. Minier, M. B. Pracy, C. Purcell, J. Shobbrook, and T. Travouillon, "A search for propylene oxide and glycine in Sagittarius B2 (LMH) and Orion", Monthly Notices of the Royal Astronomical Society **376**, 1201–1210 (2007).

[137] P. F. Goldsmith, R. Liseau, T. A. Bell, J. H. Black, J. H. Chen, D. Hollenbach, M. J. Kaufman, D. Li, D. C. Lis, G. Melnick, D. Neufeld, L. Pagani, R. Snell, A. O. Benz, E. Bergin, S. Bruderer, P. Caselli, E. Caux, P. Encrenaz, E. Falgarone, M. Gerin, J. R. Goicoechea, A. Hjalmarson, B. Larsson, J. Le Bourlot, F. Le Petit, M. De Luca, Z. Nagy, E. Roueff, A. Sandqvist, F. Van Der Tak, E. F. Van Dishoeck, C. Vastel, S. Viti, and U. Yildiz, "Herschel measurements of molecular oxygen in Orion", The Astrophysical Journal **737** (2011).

[138] P. Bergman, B. Parise, R. Liseau, B. Larsson, H. Olofsson, K. M. Menten, and R. Güsten, "Detection of interstellar hydrogen peroxide", Astronomy and Astrophysics **531**, L8 (2011).

[139] S. Widicus, B. Drouin, K. Dyl, and G. Blake, "Millimeter wavelength measurements of the rotational spectrum of 2-aminoethanol", Journal of Molecular Spectroscopy **217**, cited By 17, 278–281 (2003).

[140] R. E. Penn and R. F. Curl, "Microwave spectrum of 2-aminoethanol: Structural effects of the hydrogen bond", The Journal of Chemical Physics **55**, 651–658 (1971).

[141] V. Kaushik and R. Woods, "Centrifugal distortion effects in the rotational spectrum of 2-aminoethanol", Zeitschrift für Physikalische Chemie **132**, 117–120 (1982).

[142] D. Loru, I. Peña, J. L. Alonso, and M. Eugenia Sanz, "Intramolecular interactions in the polar headgroup of sphingosine: Serinol", Chemical Communications **52**, 3615–3618 (2016).

[143] D. Zhang, S. Bocklitz, and T. S. Zwier, "Broadband microwave spectroscopy of prototypical amino alcohols and polyamines: Competition between H-bonded cycles and chains", The Journal of Physical Chemistry A **120**, 55–67 (2016).

[144] B. H. Ellingsen, K. M. Marstokk, and H. Møllendal, "Microwave spectrum, conformational equilibrium, intramolecular hydrogen bonding, thermodynamic parameters, dipole moments and centrifugal distortion of 2-amino-1-propanol (alaninol)", Journal of Molecular Structure **48**, 9–23 (1978).

[145] R. Fausto, C. Cacela, and M. L. Duarte, "Vibrational analysis and structural implications of H-bonding in isolated and aggregated 2-amino-1-propanol: A study by MI-IR and raman spectroscopy and molecular orbital calculations", Journal of Molecular Structure **550-551**, 365–388 (2000).

[146] S. Blanco, A. Lesarri, J. C. López, and J. L. Alonso, "The gas-phase structure of alanine", Journal of the American Chemical Society **126**, 11675–11683 (2004).

[147] A. Lesarri, E. J. Cocinero, J. C. López, and J. L. Alonso, "The shape of neutral valine", Angewandte Chemie - International Edition **43**, 605–610 (2004).

[148] E. J. Cocinero, A. Lesarri, J. U. Grabow, J. C. López, and J. L. Alonso, "The shape of leucine in the gas phase", ChemPhysChem **8**, 599–604 (2007).

[149] A. Lesarri, R. Sánchez, E. J. Cocinero, J. C. López, and J. L. Alonso, "Coded amino acids in gas phase: The shape of isoleucine", Journal of the American Chemical Society **127**, 12952–12956 (2005).

[150] K. Altwegg, H. Balsiger, A. Bar-Nun, J. J. Berthelier, A. Bieler, P. Bochsler, C. Briois, U. Calmonte, M. R. Combi, H. Cottin, J. De Keyser, F. Dhooghe, B. Fiethe, S. A. Fuselier, S. Gasc, T. I. Gombosi, K. C. Hansen, M. Haessig, A. Jäckel, E. Kopp, A. Korth, L. Le Roy, U. Mall, B. Marty, O. Mousis, T. Owen, H. Rème, M. Rubin, T. Sémon, C. Y. Tzou, J. H. Waite, and P. Wurz, "Prebiotic chemicals-amino acid and phosphorus in the coma of comet 67P/Churyumov-Gerasimenko", Science Advances **2** (2016).

[151] B. E. Arenas, S. Gruet, A. L. Steber, B. M. Giuliano, and M. Schnell, "Chirped-pulse fourier transform millimeter-wave spectroscopy of ten vibrationally excited states of *i*-propyl cyanide: Exploring the far-infrared region", Physical Chemistry Chemical Physics **19**, 1751–1756 (2017).

[152] S. R. Domingos, C. Pérez, C. Medcraft, P. Pinacho, and M. Schnell, "Flexibility unleashed in acyclic monoterpenes: Conformational space of citronellal revealed by broadband rotational spectroscopy", Physical Chemistry Chemical Physics **18**, 16682–16689 (2016).

[153] H. M. Pickett, R. L. Poynter, E. A. Cohen, M. L. Delitsky, J. C. Pearson, and H. S. Müller, "Submillimeter, millimeter, and microwave spectral line catalog", Journal of Quantitative Spectroscopy and Radiative Transfer **60**, 883–890 (1998).

[154] C. P. Endres, S. Schlemmer, P. Schilke, J. Stutzki, and H. S. Müller, "The cologne database for molecular spectroscopy, CDMS, in the virtual atomic and molecular data centre, VAMDC", Journal of Molecular Spectroscopy **327**, 95–104 (2016).

[155] M.-A. Martin-Drumel, K. L. K. Lee, A. Belloche, O. Zingsheim, S. Thorwirth, H. S. P. Müller, F. Lewen, R. T. Garrod, K. M. Menten, M. C. McCarthy, and S. Schlemmer, "Submillimeter spectroscopy and astronomical searches of vinyl mercaptan, C_2H_3SH", Astronomy and Astrophysics **623**, A167 (2019).

[156] Z. Martins, "The nitrogen heterocycle content of meteorites and their significance for the origin of life", Life **8**, 28 (2018).

[157] W. Irvine, J. Ellder, Å. Hjalmarson, E. Kollberg, O. Rydbeck, G. Sorensen, B. Bak, and H. Svanholt, "Searches for interstellar imidazole and cyanoform", Astronomy and Astrophysics **97**, 192–194 (1981).

[158] M. Schwell, H. Jochims, H. Baumgärtel, and S. Leach, "VUV photophysics and dissociative photoionization of pyrimidine, purine, imidazole and benzimidazole in the 7–18eV photon energy range", Chemical Physics **353**, 145–162 (2008).

[159] V. P. Gupta, P. Tandon, P. Rawat, R. N. Singh, and A. Singh, "Quantum chemical study of a new reaction pathway for the adenine formation in the interstellar space", Astronomy and Astrophysics **528**, A129 (2011).

[160] G. Blackman, R. Brown, F. Burden, and I. Elsum, "Nuclear quadrupole coupling in the microwave spectrum of imidazole", Journal of Molecular Spectroscopy **60**, 63–70 (1976).

[161] J. H. Griffiths, A. Wardley, V. Williams, N. Owen, and J. Sheridan, "Microwave spectra and structures of isothiazole, 1,2,4-oxadiazole and imidazole", Nature **216**, 1301 (1967).

[162] D. Christen, J. Griffiths, and J. Sheridan, "The microwave spectrum of imidazole; complete structure and the electron distribution from nuclear quadrupole coupling tensors and dipole moment orientation", Zeitschrift für Naturforschung A **36**, 1378–1385 (1982).

[163] D. J. Sheehan, C. A. Hitchcock, and C. M. Sibley, "Current and emerging azole antifungal agents", Clinical Microbiology Reviews **12**, 40–79 (1999).

[164] M. Green and T. Long, "Designing imidazole-based ionic liquids and ionic liquid monomers for emerging technologies", Polymer Reviews **49**, 291–314 (2009).

[165] B. J. Harris, "A chirped pulse fourier transform millimeter wave spectrometer for room temperature, gas mixture analysis", PhD thesis (Department of Chemistry, University of Virginia, 2014).

[166] A. Pietropolli Charmet, "In prep.", (2019).

[167] K. Vávra, K. Luková, P. Kania, J. Koucký, and Š. Urban, "Rotational spectra of indole in the lowest vibrational states", Journal of Molecular Spectroscopy **363**, 111175 (2019).

[168] M. Zdanovskaia, B. Esselman, H. Lau, D. Bates, R. Woods, R. McMahon, and Z. Kisiel, "The 103-360 GHz rotational spectrum of benzonitrile, the first interstellar benzene derivative detected by radioastronomy", Journal of Molecular Spectroscopy **351**, 39–48 (2018).

[169] H. Ozeki, R. Miyahara, H. Ihara, S. Todaka, K. Kobayashi, and M. Ohishi, "Millimeter-wave spectroscopy of hydantoin, a possible precursor of glycine", Astronomy and Astrophysics **600**, A44 (2017).

[170] E. R. Alonso, L. Kolesniková, and J. L. Alonso, "Laser ablated hydantoin: A high resolution rotational study", The Journal of Chemical Physics **147**, 124312 (2017).

[171] S. Maret, P. Hily-Blant, J. Pety, S. Bardeau, and E. Reynier, "Weeds: A CLASS extension for the analysis of millimeter and sub-millimeter spectral surveys", Astronomy and Astrophysics **526**, A47 (2011).

[172] P. Gratier, L. Majumdar, M. Ohishi, E. Roueff, J. C. Loison, K. M. Hickson, and V. Wakelam, "A new reference chemical composition for TMC-1", Astrophysical Journal Supplement Series **225**, 25 (2016).

[173] D. P. Zaleski, S. L. Stephens, and N. R. Walker, "A perspective on chemistry in transient plasma from broadband rotational spectroscopy", Physical Chemistry Chemical Physics **16**, 25221–25228 (2014).

[174] W. Sun and J. van Wijngaarden, "Isothiocyanato-containing carbon chains: The laboratory detection of HCCCCNCS and NCCCNCS via rotational spectroscopy", The Journal of Physical Chemistry A **122**, 7659–7665 (2018).

[175] C. Baiano, J. Lupi, N. Tasinato, C. Puzzarini, and V. Barone, "The role of state-of-the-art quantum-chemical calculations in astrochemistry: Formation route and spectroscopy of ethanimine as a paradigmatic case", Molecules **25**, 2873 (2020).

[176] C. A. Gottlieb, "Detection of acetaldehyde in Sagittarius", in Molecules in the galactic environment, edited by M. Gordon and L. Snyder (1973), p. 181.

[177] N. Fourikis, M. Sinclair, B. Robinson, P. Godfrey, and R. Brown, "Microwave emission of the $2_{1,1}$ - $2_{1,2}$ rotational transition in interstellar acetaldehyde", Australian Journal of Physics **27**, 425 (1974).

[178] W. Gilmore, M. Morris, D. Johnson, F. Lovas, B. Zuckerman, B. Turner, and P. Palmer, "Observation of the $6_{1,6}$ - $5_{1,5}$ transitions of acetaldehyde in Sagittarius B2", The Astrophysical Journal **204**, 43–46 (1976).

[179] M. Bell, H. Matthews, and P. Feldman, "Observations of microwave transitions of A-state acetaldehyde in Sgr B2", Astronomy and Astrophysics **127**, 420–422 (1983).

[180] H. Matthews, P. Friberg, and W. Irvine, "The detection of acetaldehyde in cold dust clouds", The Astrophysical Journal **290**, 609–614 (1985).

[181] B. Turner, "A molecular line survey of Sagittarius B2 and Orion-KL from 70 to 115 GHz. ii. Analysis of the data", Astrophysical Journal Supplement Series **76**, 617–686 (1991).

[182] L. Ziurys and D. Mcgonagle, "The spectrum of Orion-KL at 2 millimeters (150-160 GHz)", Astrophysical Journal Supplement Series **89**, 155–187 (1993).

[183] A. Nummelin, J. Dickens, P. Bergman, Å. Hjalmarson, W. Irvine, M. Ikeda, and M. Ohishi, "Abundances of ethylene oxide and acetaldehyde in hot molecular cloud cores", Astronomy and Astrophysics **337**, 275–286 (1998).

[184] D. Williams and T. Hartquist, "The chemistry of star-forming regions", Accounts of Chemical Research **32**, 334–341 (1999).

[185] M. Ikeda, M. Ohishi, A. Nummelin, J. Dickens, P. Bergman, Å. Hjalmarson, and W. Irvine, "Survey observations of c-C_2H_4O and CH_3CHO toward massive star-forming regions", The Astrophysical Journal **560**, 792–805 (2001).

[186] S. Charnley, "Acetaldehyde in star-forming regions", Advances in Space Research **33**, 23–30 (2004).

[187] S. Muller, A. Beelen, M. Guelin, S. Aalto, J. Black, F. Combes, S. Curran, P. Theule, and S. Longmore, "Molecules at z=0.89: A 4-mm-rest-frame absorption-line survey toward PKS 1830-211", Astronomy and Astrophysics **535**, A103 (2011).

[188] L. H. Coudert, L. Margulés, C. Vastel, R. Motiyenko, E. Caux, and J.-C. Guillemin, "Astrophysical detections and databases for the mono deuterated species of acetaldehyde CH_2DCOH and CH_3COD", Astronomy and Astrophysics **624**, A70 (2019).

[189] L. Chun Chia and R. Kilb, "Microwave spectrum and internal barrier of acetaldehyde", The Journal of Chemical Physics **23**, 631 (1956).

[190] R. Kilb, C. Lin, and E. Wilson Jr., "Calculation of energy levels for internal torsion and over-all rotation. ii. CH_3CHO type molecules; acetaldehyde spectra", The Journal of Chemical Physics **26**, 1704–1713 (1957).

[191] P. Turner and A. Cox, "Centrifugal distortion and internal rotation in the microwave spectrum of acetaldehyde", Chemical Physics Letters **42**, 84–88 (1976).

[192] P. Turner, A. Cox, and J. Hardy, "Microwave spectrum of acetaldehyde with asymmetric CH_2D and CHD_2 internal rotors", Journal of the Chemical Society, Faraday Transactions 2: Molecular and Chemical Physics **77**, 1217–1231 (1981).

[193] W. Liang, J. Baker, E. Herbst, R. Booker, and F. De Lucia, "The millimeter-wave spectrum of acetaldehyde in its two lowest torsional states", Journal of Molecular Spectroscopy **120**, 298–310 (1986).

[194] D. Knight, A. Cox, and T. Pedersen, "Internal rotation in nitrosomethane and acetaldehyde: Incremental effect of deuterium substitution on the potential for methyl torsion", Journal of Molecular Structure **189**, 187–201 (1988).

[195] L. Martinache and A. Bauder, "Microwave spectrum of acetaldehyde-1-d_1: Deuterium quadrupole splittings and internal rotation analysis", Chemical Physics Letters **164**, 657–663 (1989).

[196] W. Barclay Jr., M. Anderson, L. Ziurys, I. Kleiner, and J. Hougen, "The laboratory spectrum of acetaldehyde at 1 millimeter (230-325 GHz)", Astrophysical Journal Supplement Series **89**, 221–226 (1993).

[197] I. Kleiner, J. López, S. Blanco, A. McKellar, and N. Moazzen-Ahmadi, "The ground and first torsional states of CD_3CHO", Journal of Molecular Spectroscopy **197**, 275–288 (1999).

[198] A. Cox, K. Hughes, and J. Macdonald, "Torsion-rotation interactions in monodeuterated acetaldehyde", Molecular Physics **101**, 569–574 (2003).

[199] L. Coudert and J. López, "Internal rotation and hyperfine coupling interaction in deuterated acetaldehyde", Journal of Molecular Spectroscopy **239**, 135–145 (2006).

[200] I. Smirnov, E. Alekseev, V. Ilyushin, L. Margulés, R. Motiyenko, and B. Drouin, "Spectroscopy of the ground, first and second excited torsional states of acetaldehyde from 0.05 to 1.6 THz", Journal of Molecular Spectroscopy **295**, 44–50 (2014).

[201] L. Margulés, R. Motiyenko, V. Ilyushin, and J.-C. Guillemin, "Millimeter and submillimeter wave spectra of mono-^{13}C-acetaldehydes", Astronomy and Astrophysics **579** (2015).

[202] D. Zaleski, C. Duan, M. Carvajal, I. Kleiner, and K. Prozument, "The broadband rotational spectrum of fully deuterated acetaldehyde (CD_3CDO) in a CW supersonic expansion", Journal of Molecular Spectroscopy **342**, 17–24 (2017).

[203] P. Solomon, K. Jefferts, A. Penzias, and R. Wilson, "Detection of millimeter emission lines from interstellar methyl cyanide", The Astrophysical Journal **168**, L107 (1971).

[204] M. Gerin, F. Combes, and G. Wlodarczak, "Interstellar detection of deuterated methyl cyanide", Astronomy and Astrophysics **259**, L35 (1992).

[205] H. Ring, H. Edwards, M. Kessler, and W. Gordy, "Microwave spectra: Methyl cyanide and methyl isocyanide", Physical Review **72**, 1262–1263 (1947).

[206] M. Kessler, H. Ring, R. Trambarulo, and W. Gordy, "Microwave spectra and molecular structures of methyl cyanide and methyl isocyanide", Physical Review **79**, 54–56 (1950).

[207] P. Venkateswarlu, J. G. Baker, and W. Gordy, "The millimeter wave spectrum of methyl cyanide and the l-type doubling", Journal of Molecular Spectroscopy **6**, 215–228 (1961).

[208] P. Alston Steiner and W. Gordy, "Precision measurement of dipole moments and other spectral constants of normal and deuterated methyl fluoride and methyl cyanide", Journal of Molecular Spectroscopy **21**, 291–301 (1966).

[209] A. Bauer and S. Maes, "Étude en ondes millimétriques de l'acétonitrile $CH_3C^{14}N$ et $CH_3C^{15}N$: Effets de l'interaction de vibration-rotation et de la perturbation quadripolaire", Journal de Physique **30**, 169 (1969).

[210] A. Bauer, G. Tarrago, and A. Remy, "Analysis of the rotational spectrum of C3v molecules by using factorization and diagonalization of the energy matrix. Application to $CH_3C^{15}N$", Journal of Molecular Spectroscopy **58**, 111–124 (1975).

[211] I. An, W. Rhee, and J. Roberts, "Quadrupole structure in the rotational spectrum of the $\nu_8 = 1$ and 2 and ground vibrational levels of $CH_3C^{14}N$ for the frequency range 17-56 GHz", The Journal of Chemical Physics **86**, 4725–4729 (1987).

[212] F. Sabeh, I. An, W. Rhee, and J. Roberts, "Rotational components of the $\nu_8 = 1$, 2, and 3 and ground vibrational levels of $CH_3C^{15}N$ for the frequency range 17-75 GHz", Journal of Molecular Spectroscopy **125**, 348–357 (1987).

[213] F. Brown, D. Dangoisse, and J. Demaison, "The rotational spectrum of CH_3CN above 1000 GHz", Journal of Molecular Spectroscopy **129**, 483–485 (1988).

[214] H. Tam, I. An, and J. Roberts, "Microwave spectra of the ^{13}C isotopic species of methyl cyanide for the ground and $\nu_8 = 1$, 2 vibrational levels in the frequency range 17-56 GHz", Journal of Molecular Spectroscopy **129**, 202–215 (1988).

[215] J. Pearson and H. Müller, "The submillimeter wave spectrum of isotopic methyl cyanide", The Astrophysical Journal **471**, 1067 (1996).

[216] H. Müller, B. Drouin, and J. Pearson, "Rotational spectra of isotopic species of methyl cyanide, CH_3CN, in their ground vibrational states up to terahertz frequencies", Astronomy and Astrophysics **506**, 1487–1499 (2009).

[217] L. Nguyen, A. Walters, L. Margulès, R. Motiyenko, J.-C. Guillemin, C. Kahane, and C. Ceccarelli, "Extension of the millimeter- and submillimeter-wave spectral databases of deuterated methyl cyanides (CH_2DCN and CHD_2CN)", Astronomy and Astrophysics **553**, A84 (2013).

[218] H. Müller, L. Brown, B. Drouin, J. Pearson, I. Kleiner, R. Sams, K. Sung, M. Ordu, and F. Lewen, "Rotational spectroscopy as a tool to investigate interactions between vibrational polyads in symmetric top molecules: Low-lying states $\nu_8 \leq 2$ of methyl cyanide, CH_3CN", Journal of Molecular Spectroscopy **312**, 22–37 (2015).

[219] H. Müller, B. Drouin, J. Pearson, M. Ordu, N. Wehres, and F. Lewen, "Rotational spectra of isotopic species of methyl cyanide, CH_3CN, in their $\nu_8 = 1$ excited vibrational states", Astronomy and Astrophysics **586** (2016).

[220] H. M. Pickett and T. L. Boyd, "Microwave detection of photolysis products: HCO from acetaldehyde using mercury sensitization", Chemical Physics Letters **58**, 446 (1978).

[221] S. Saito, "Laboratory observations of the $1_{0,1} \leftarrow 0_{0,0}$ transitions for the HCO and DCO free radicals by microwave spectroscopy", Astrophysical Journal Letters **178**, L95 (1972).

[222] L. Snyder, J. Hollis, and B. Ulich, "Radio detection of the interstellar formyl radical", Astrophysical Journal Letters **208**, L91–L94 (1976).

[223] H. Feuchtgruber, F. P. Helmich, E. F. van Dishoeck, and C. M. Wright, "Detection of interstellar CH_3", The Astrophysical Journal **535**, L111 (2000).

[224] J. R. Keeffe, A. J. Kresge, and N. P. Schepp, "Keto-enol equilibrium constants of simple monofunctional aldehydes and ketones in aqueous solution", Journal of the American Chemical Society **112**, 4862–4868 (1990).

[225] J. M. Hollis, P. R. Jewell, F. J. Lovas, A. Remijan, and H. Møllendal, "Green Bank Telescope detection of new interstellar aldehydes: Propenal and propanal", The Astrophysical Journal **610**, L21 (2004).

[226] R. Garrod, S. Widicus Weaver, and E. Herbst, "Complex chemistry in star-forming regions: An expanded gas-grain warm-up chemical model", The Astrophysical Journal **682**, 283–302 (2008).

[227] J. L. Neill, A. L. Steber, M. T. Muckle, D. P. Zaleski, V. Lattanzi, S. Spezzano, M. C. McCarthy, A. J. Remijan, D. N. Friedel, S. L. Widicus Weaver, and B. H. Pate, "Spatial distributions and interstellar reaction processes", The Journal of Physical Chemistry A **115**, 6472–6480 (2011).

[228] R. Rubin, J. Swenson G.W., R. Benson, H. Tigelaar, and W. Flygare, "Microwave detection of interstellar formamide", Astrophysical Journal Letters **169**, L39 (1971).

[229] J. Hollis, F. Lovas, A. Remijan, P. Jewell, V. Ilyushin, and I. Kleiner, "Detection of acetamide CH_3CONH_2: The largest interstellar molecule with a peptide bond", Astrophysical Journal Letters **643**, L25–L28 (2006).

[230] A. J. Remijan, J. Hollis, F. Lovas, W. D. Stork, P. Jewell, and D. Meier, "Detection of interstellar cyanoformaldehyde (CNCHO)", Astrophysical Journal Letters **675**, L85 (2008).

[231] N. Marcelino, J. Cernicharo, B. Tercero, and E. Roueff, "Discovery of fulminic acid, HCNO, in dark clouds", Astrophysical Journal Letters **690**, L27–L30 (2009).

[232] S. Brünken, A. Belloche, S. Martín, L. Verheyen, and K. Menten, "Interstellar HOCN in the galactic center region", Astronomy and Astrophysics **516**, A109 (2010).

[233] A. J. Remijan, L. E. Snyder, B. A. McGuire, H.-L. Kuo, L. W. Looney, D. N. Friedel, G. Y. Golubiatnikov, F. J. Lovas, V. Ilyushin, E. Alekseev, S. Dyubko, B. J. McCall, and J. M. Hollis, "Observational results of a multi-telescope campaign in search of interstellar urea $[(NH_2)_2CO]$", The Astrophysical Journal **783**, 77 (2014).

[234] D. Halfen, V. Ilyushin, and L. Ziurys, "Interstellar detection of methyl isocyanate CH_3NCO in Sgr B2(N): A link from molecular clouds to comets", Astrophysical Journal Letters **812**, L5 (2015).

[235] A. Belloche, A. Meshcheryakov, R. Garrod, V. Ilyushin, E. Alekseev, R. Motiyenko, L. Margulès, H. Müller, and K. Menten, "Rotational spectroscopy, tentative interstellar detection, and chemical modeling of N-methylformamide", Astronomy and Astrophysics **601**, A49 (2017).

[236] N. Marcelino, M. Agúndez, J. Cernicharo, E. Roueff, and M. Tafalla, "Discovery of the elusive radical NCO and confirmation of H_2NCO^+ in space", Astronomy and Astrophysics **612**, L10 (2018).

[237] A. Coutens, N. F. W. Ligterink, J. Loison, V. Wakelam, H. Calcutt, M. N. Drozdovskaya, J. K. Jørgensen, H. S. P. Müller, E. F. van Dishoeck, and S. F. Wampfler, "The ALMA-PILS survey: First detection of nitrous acid (HONO) in the interstellar medium", Astronomy and Astrophysics **623**, L13 (2019).

[238] S. Zeng, D. Quénard, I. Jiménez-Serra, J. Martín-Pintado, V. M. Rivilla, L. Testi, and R. Martín-Doménech, "First detection of the pre-biotic molecule glycolonitrile ($HOCH_2CN$) in the interstellar medium", Monthly Notices of the Royal Astronomical Society: Letters **484**, L43–L48 (2019).

[239] V. M. Rivilla, J. Martín-Pintado, I. Jiménez-Serra, S. Martín, L. F. Rodríguez-Almeida, M. A. Requena-Torres, F. Rico-Villas, S. Zeng, and C. Briones, "Prebiotic precursors of the primordial RNA world in space: Detection of NH_2OH", The Astrophysical Journal **899**, L28 (2020).

[240] M. C. McCarthy, K. L. K. Lee, P. B. Carroll, J. P. Porterfield, P. B. Changala, J. H. Thorpe, and J. F. Stanton, "Exhaustive product analysis of three benzene discharges by microwave spectroscopy", The Journal of Physical Chemistry A **124**, 5170–5181 (2020).

[241] B. Landsberg, A. Merer, and T. Oka, "Infrared spectroscopy of short-lived molecules: Observation of the ν_2 fundamental of HCO by laser electric resonance", Journal of Molecular Spectroscopy **67**, 459–475 (1977).

[242] P. Botschwina, "Unrestricted Hartree-Fock calculation of force constants and vibrational frequencies of the HCO radical", Chemical Physics Letters **29**, 98–101 (1974).

[243] G. A. Blake, K. V. L. N. Sastry, and F. C. De Lucia, "The laboratory millimeter and submillimeter spectrum of HCO", The Journal of Chemical Physics **80**, 95–101 (1984).

[244] H. Ozeki, T. Hirao, S. Saito, and S. Yamamoto, "Laboratory microwave spectroscopy of the cyanomethyl radical, CH_2CN", The Astrophysical Journal **617**, 680–684 (2004).

[245] H. Møllendal, L. Margulés, R. A. Motiyenko, N. W. Larsen, and J.-C. Guillemin, "Rotational spectrum and conformational composition of cyanoacetaldehyde, a compound of potential prebiotic and astrochemical interest", The Journal of Physical Chemistry A **116**, 4047–4056 (2012).

[246] M. C. McCarthy, W. Chen, M. J. Travers, and P. Thaddeus, "Microwave spectra of 11 polyyne carbon chains", Astrophysical Journal Supplement Series **129**, 611–623 (2000).

[247] A. K. Lemmens, D. B. Rap, J. M. M. Thunnissen, B. Willemsen, and A. M. Rijs, "Polycyclic aromatic hydrocarbon formation chemistry in a plasma jet revealed by IR-UV action spectroscopy", Nature Communications **11**, 269 (2020).

Appendix 1: The W-band Spectrum of *iso*-Propyl Cyanide and a Search for its Vibrationally Excited States in the Interstellar Medium

Figure A1.1 shows the atom labelling in *iso*-propyl cyanide required for interpreting Tables A1.1 and A1.2.

Table A1.1 contains the rotational constants for the ^{13}C isotopologues for *iso*-propyl cyanide in the W-band experiment. The coordinates for the carbon atoms determined from the r_s structure analysis of *iso*-propyl cyanide are compared to the theoretical coordinates (at the B3LYP/aug-cc-pVTZ level of theory) in Table A1.2.

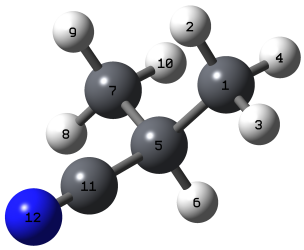

Figure A1.1: Structure of *i*-propyl cyanide showing the labelling of carbon atoms for comparison with the rotational constants and atomic coordinates reported in Tables A1.1 and A1.2.

Table A1.1: Experimentally determined molecular parameters for the ^{13}C isotopologues of *i*-propyl cyanide, following the labelling of Figure A1.1. Values in square brackets were kept fixed to the value of the parent species.

	^{13}C(1) and ^{13}C(7)	^{13}C(5)	^{13}C(11)
A (MHz)	7747.279(28)	7921.780(27)	7939.368(33)
B (MHz)	3927.9450(53)	3956.5392(56)	3939.1212(53)
C (MHz)	2854.3725(40)	2897.6257(31)	2885.7232(30)
D_J (kHz)	0.6061(64)	0.6099(64)	0.5914(64)
D_{JK} (kHz)	11.739(12)	11.497(30)	12.359(37)
D_K (kHz)	[-5.231]	[-5.231]	[-5.231]
d_1 (kHz)	-0.2460(62)	-0.2318(51)	-0.2455(52)
d_2 (kHz)	-0.1914(22)	-0.1759(21)	-0.1929(21)
No. lines	38	32	31
rms (kHz)	41.9	48.3	41.2

Table A1.2: Experimentally determined (following the Kraitchman procedure) and theoretically calculated (at the B3LYP/aug-cc-pVTZ level of theory) atom positions for the four carbon atoms of *i*-propyl cyanide as labelled in Figure A1.1.

Atom number	Element	x_{exp}	x_{theory}	y_{exp}	y_{theory}	z_{exp}	z_{theory}
1	C	-1.123	-1.126	1.272	1.277	0.151	0.154
5	C	-0.463	-0.466	0.000	0.000	-0.402	-0.391
7	C	-1.123	-1.126	-1.272	-1.277	0.151	0.154
11	C	0.967	0.971	0.000	0.000	-0.108	-0.101

Appendix 2: Facilitating Interstellar Searches for the Four Simple Amino Alcohols Alaninol, Valinol, Leucinol, and Isoleucinol

Tables A2.1 to A2.8 contain the experimentally determined rotational constants for the isotopologues of alaninol 1 (g'Gg'), alaninol 2 (gG'g), valinol 1 (g'Gg'G'), valinol 2 (g'Gg'G), leucinol 1 (g'Gg'Tg), isoleucinol 1 (g'Gg'Tt), isoleucinol 2 (g'Gg'G't), and isoleucinol 3 (g'Gg'Tg').

Rotational partition function values, and vibrational partition function values where appropriate, are listed across the standard JPL database temperatures [153] in Tables A2.9 to A2.24. The Q_{rot} values were calculated by the SPCAT programme [63], in which the summation across the rotational energy levels up to the listed J_{max} and K_{max} is performed. When the nuclear quadrupole coupling is considered in the Q_{rot} value calculation, the entry in the table is labelled [$2I$+1=3]. When the nuclear quadrupole coupling is not considered in the Q_{rot} value calculation, the entry in the table is labelled [$2I$+1=1]. The Q_{vib} values were computed by summing the anharmonic energies of the vibrational states up to 500 cm^{-1}, as calculated by the anharmonic frequency calculations.

Table A2.1: The experimental rotational constants for the observed isotopologues of alaninol 1, g'Gg'. Values contained within square brackets were kept fixed to the parent species values.

	^{13}C(1)	^{13}C(2)	^{13}C(3)	^{15}N	^{18}O
A / MHz	7888.420(50)	7935.239(52)	7876.899(49)	7715.121(56)	7944.579(73)
B / MHz	3557.6341(15)	3631.3380(15)	3626.2698(14)	3635.4848(19)	3461.2597(19)
C / MHz	2693.2494(13)	2744.2287(13)	2732.7080(13)	2716.7871(16)	2644.4232(20)
Δ_J / kHz	[0.723447361]	[0.723447361]	[0.723447361]	[0.723447361]	[0.723447361]
Δ_{JK} / kHz	[3.443751915]	[3.443751915]	[3.443751915]	[3.443751915]	[3.443751915]
Δ_K / kHz	[2.024217479]	[2.024217479]	[2.024217479]	[2.024217479]	[2.024217479]
δ_J / kHz	[0.17391486]	[0.17391486]	[0.17391486]	[0.17391486]	[0.17391486]
δ_K / kHz	[2.321861564]	[2.321861564]	[2.321861564]	[2.321861564]	[2.321861564]
χ_{aa} / MHz	-3.723(9)	-3.671(9)	-3.646(8)	-	-3.677(15)
χ_{bb}-χ_{cc} / MHz	-0.0560(224)	-0.1080(284)	-0.1600(236)	-	-0.0720(196)
No. of lines	44	43	44	14	38
σ / kHz	13.8	14.1	13.8	9.4	18.5

Table A2.2: The experimental rotational constants for the observed isotopologues of alaninol 2, gG'g. Values contained within square brackets were kept fixed to the parent species values.

	^{13}C(1)	^{13}C(2)	^{13}C(3)	^{15}N
A / MHz	6348.5973(39)	6442.0197(19)	6421.5158(19)	6309.604(66)
B / MHz	4095.5493(32)	4124.3613(17)	4100.6636(16)	4116.8509(40)
C / MHz	3277.8513(27)	3328.5900(14)	3317.8295(14)	3289.5738(46)
Δ_J / kHz	[1.634351187]	[1.634351187]	[1.634351187]	[1.634351187]
Δ_{JK} / kHz	[4.940081683]	[4.940081683]	[4.940081683]	[4.940081683]
Δ_K / kHz	[-3.700950204]	[-3.700950204]	[-3.700950204]	[-3.700950204]
δ_J / kHz	[0.24993844]	[0.24993844]	[0.24993844]	[0.24993844]
δ_K / kHz	[1.115532359]	[1.115532359]	[1.115532359]	[1.115532359]
χ_{aa} / MHz	-0.6853(2)	-0.705(14)	-0.649(13)	-
χ_{bb}-χ_{cc} / MHz	4.068(72)	4.0384(268)	4.0880(260)	-
No. of lines	21	37	32	5
σ / kHz	20.3	17.4	15.3	3.6

Table A2.3: The experimental rotational constants for the observed isotopologues of valinol 1, g'Gg'G'. Values contained within square brackets were kept fixed to the parent species values.

	^{13}C(1)	^{13}C(2)	^{13}C(3)	^{13}C(4)	^{13}C(5)	^{15}N	^{18}O
A / MHz	4020.1232(14)	4020.4398(18)	4004.2223(11)	3948.5415(15)	3999.9141(14)	3946.0314(33)	4013.470(74)
B / MHz	1692.82142(46)	1700.92434(56)	1691.58057(49)	1686.74869(48)	1672.71042(54)	1698.5943(10)	1629.6483(14)
C / MHz	1279.64920(35)	1283.99785(42)	1277.09091(38)	1268.26992(38)	1265.72637(36)	1274.83000(51)	1242.5404(12)
Δ_J / kHz	[0.108022968]	[0.108022968]	[0.108022968]	[0.108022968]	[0.108022968]	[0.108022968]	[0.108022968]
Δ_{JK} / kHz	[0.182772516]	[0.182772516]	[0.182772516]	[0.182772516]	[0.182772516]	[0.182772516]	[0.182772516]
δ_J / kHz	[0.026376674]	[0.026376674]	[0.026376674]	[0.026376674]	[0.026376674]	[0.026376674]	[0.026376674]
χ_{aa} / MHz	-4.175(10)	-4.200(17)	-4.178(10)	-4.189(15)	-4.172(9)	-	-4.213(31)
χ_{bb}-χ_{cc} / MHz	0.7020(276)	0.668(60)	0.6668(352)	0.696(44)	0.7236(304)	-	0.092(392)
No. of lines	69	55	56	71	58	24	19
σ / kHz	13.7	16.8	12.6	15.6	13.1	14.6	13.1

Table A2.4: The experimental rotational constants for the observed isotopologues of valinol 2, g'Gg'G. Values contained within square brackets were kept fixed to the parent species values.

	^{13}C(1)	^{13}C(2)	^{13}C(3)	^{13}C(4)	^{13}C(5)	^{15}N
A / MHz	4217.25(26)	4230.96(16)	4227.82(18)	4203.53(14)	4165.46(23)	4161.13(46)
B / MHz	1537.6160(10)	1546.15373(94)	1539.5664(10)	1521.8131(10)	1532.9518(10)	1541.7806(52)
C / MHz	1404.8932(10)	1413.57389(91)	1408.5188(10)	1392.5804(10)	1398.6118(10)	1408.0969(39)
Δ_J / kHz	[0.220470222]	[0.220470222]	[0.220470222]	[0.220470222]	[0.220470222]	[0.220470222]
Δ_{JK} / kHz	[0.128885595]	[0.128885595]	[0.128885595]	[0.128885595]	[0.128885595]	[0.128885595]
Δ_K / kHz	[1.039662972]	[1.039662972]	[1.039662972]	[1.039662972]	[1.039662972]	[1.039662972]
δ_J / kHz	[0.043244623]	[0.043244623]	[0.043244623]	[0.043244623]	[0.043244623]	[0.043244623]
δ_K / kHz	[4.82518082]	[4.82518082]	[4.82518082]	[4.82518082]	[4.82518082]	[4.82518082]
χ_{aa} / MHz	[-3.9918]	[-3.9918]	[-3.9918]	[-3.9918]	[-3.9918]	-
χ_{bb}-χ_{cc} / MHz	[-0.6612]	[-0.6612]	[-0.6612]	[-0.6612]	[-0.6612]	-
No. of lines	17	20	13	24	14	7
σ / kHz	13.1	11.4	12.0	12.4	12.0	17.2

Table A2.5: The experimental rotational constants for the observed isotopologues of leucinol 1, g'Gg'Tg. Values contained within square brackets were kept fixed to the parent species values.

	^{13}C(1)	^{13}C(2)	^{13}C(3)	^{13}C(4)	^{13}C(5)	^{13}C(6)	^{15}N
A / MHz	4025.64(40)	4046.97(36)	4032.59(38)	4046.55(44)	4022.16(48)	3984.01(43)	3980.24(49)
B / MHz	898.26547(49)	903.73248(43)	904.24474(46)	899.37101(47)	890.18423(44)	896.39878(41)	900.95139(47)
C / MHz	870.06898(50)	875.96767(42)	875.77149(45)	871.91906(43)	862.41534(44)	868.61992(40)	873.73532(49)
Δ_J / kHz	0.07430(98)	0.06707(84)	0.07240(90)	0.07210(88)	0.06907(87)	0.07393(78)	0.0717(10)
Δ_{JK} / kHz	0.418(14)	[0.467376723]	0.421(21)	0.452(17)	0.524(26)	0.408(11)	0.390(19)
Δ_K / kHz	[1.198405042]	[1.198405042]	[1.198405042]	[1.198405042]	[1.198405042]	[1.198405042]	[1.198405042]
δ_J / kHz	[0.013150605]	[0.013150605]	[0.013150605]	[0.013150605]	[0.013150605]	[0.013150605]	[0.013150605]
δ_K / kHz	[7.582601955]	[7.582601955]	[7.582601955]	[7.582601955]	[7.582601955]	[7.582601955]	[7.582601955]
χ_{aa} / MHz	[-3.8315]	[-3.8315]	[-3.8315]	[-3.8315]	[-3.8315]	[-3.8315]	-
χ_{bb}-χ_{cc} / MHz	[-1.0472]	[-1.0472]	[-1.0472]	[-1.0472]	[-1.0472]	[-1.0472]	-
No. of lines	64	48	60	57	54	57	35
σ / kHz	15.7	10.7	13.5	13.3	13.4	11.3	11.0

Table A2.6: The experimental rotational constants for the observed isotopologues of isoleucinol 1, g'Gg'Tt. Values contained within square brackets were kept fixed to the parent species values.

	^{13}C(1)	^{13}C(2)	^{13}C(3)	^{13}C(4)	^{13}C(5)	^{13}C(6)	^{15}N	^{18}O
A / MHz	3745.439(35)	3756.411(35)	3756.186(34)	3745.884(32)	3755.137(58)	3674.659(34)	3690.030(54)	[3757.59259]
B / MHz	1055.21888(38)	1061.45345(44)	1061.18462(53)	1054.47780(44)	1039.47661(63)	1060.41821(49)	1060.34811(97)	1023.07060(96)
C / MHz	874.74707(33)	879.60403(39)	879.34464(39)	874.51694(34)	864.32850(47)	874.16456(37)	875.01893(65)	853.03472(75)
Δ_J / kHz	[0.02663]	[0.02663]	[0.02663]	[0.02663]	[0.02663]	[0.02663]	[0.02663]	[0.02663]
Δ_{JK} / kHz	[0.3348]	[0.3348]	[0.3348]	[0.3348]	[0.3348]	[0.3348]	[0.3348]	[0.3348]
χ_{aa} / MHz	[-4.2152]	[-4.2152]	[-4.2152]	[-4.2152]	[-4.2152]	[-4.2152]	-	[-4.2152]
χ_{bb}-χ_{cc} / MHz	[0.4968]	[0.4968]	[0.4968]	[0.4968]	[0.4968]	[0.4968]	-	[0.4968]
No. of lines	34	33	32	27	32	33	14	4
σ / kHz	8.7	11.0	12.2	9.2	14.7	10.7	11.6	4.3

Table A2.7: The experimental rotational constants for the observed isotopologues of isoleucinol 2, g'Gg'G't. Values contained within square brackets were kept fixed to the parent species values.

	^{13}C(1)	^{13}C(2)	^{13}C(3)	^{13}C(4)	^{13}C(5)	^{13}C(6)
A / MHz	3153.58(10)	3165.81(10)	3164.531(72)	3155.143(53)	3146.571(91)	3115.826(77)
B / MHz	1097.5552(11)	1102.31684(92)	1101.65514(70)	1097.81391(52)	1083.9272(11)	1097.4694(10)
C / MHz	965.80927(81)	970.32954(76)	970.44690(76)	966.74006(42)	954.15626(77)	962.94059(72)
Δ_J / kHz	[0.08475]	[0.08475]	[0.08475]	[0.08475]	[0.08475]	[0.08475]
Δ_{JK} / kHz	[-0.3651]	[-0.3651]	[-0.3651]	[-0.3651]	[-0.3651]	[-0.3651]
δ_J / kHz	[0.01271]	[0.01271]	[0.01271]	[0.01271]	[0.01271]	[0.01271]
χ_{aa} / MHz	[-4.2156]	[-4.2156]	[-4.2156]	[-4.2156]	[-4.2156]	[-4.2156]
χ_{bb}-χ_{cc} / MHz	[-0.5144]	[-0.5144]	[-0.5144]	[-0.5144]	[-0.5144]	[-0.5144]
No. of lines	8	11	13	14	7	12
σ / kHz	8.7	9.6	11.3	6.4	6.0	7.9

Table A2.8: The experimental rotational constants for the observed isotopologues of isoleucinol 3, g'Gg'Tg'. Values contained within square brackets were kept fixed to the parent species values.

	^{13}C(1)	^{13}C(2)	^{13}C(3)	^{13}C(4)	^{13}C(5)	^{13}C(6)
A / MHz	3059.714(46)	3066.875(42)	3057.472(54)	3060.334(65)	3043.051(47)	3003.892(31)
B / MHz	1204.58462(74)	1212.83793(87)	1210.9503(15)	1201.14812(99)	1193.35906(83)	1210.46269(79)
C / MHz	1003.61816(78)	1010.09609(73)	1009.01817(61)	1002.20154(79)	997.17711(60)	1001.52083(49)
Δ_J / kHz	[0.11429]	[0.11429]	[0.11429]	[0.11429]	[0.11429]	[0.11429]
Δ_{JK} / kHz	[-0.2067]	[-0.2067]	[-0.2067]	[-0.2067]	[-0.2067]	[-0.2067]
δ_J / kHz	[0.02256]	[0.02256]	[0.02256]	[0.02256]	[0.02256]	[0.02256]
χ_{aa} / MHz	[-3.4897]	[-3.4897]	[-3.4897]	[-3.4897]	[-3.4897]	[-3.4897]
χ_{bb}-χ_{cc} / MHz	[0.4780]	[0.4780]	[0.4780]	[0.4780]	[0.4780]	[0.4780]
No. of lines	18	16	16	14	15	14
σ / kHz	11.5	12.1	13.2	10.7	9.9	11.8

Table A2.9: Rotational partition functions (Q_{rot}) for the isotopologues of alaninol 1, g'Gg', where $J_{max} = 220$ and $K_{max} = 40$.

T / K	Q_{rot} ^{13}C(1) [$2I$+1=3]	Q_{rot} ^{13}C(2) [$2I$+1=3]	Q_{rot} ^{13}C(3) [$2I$+1=3]	Q_{rot} ^{15}N [$2I$+1=1]	Q_{rot} ^{18}O [$2I$+1=3]
300	290093.6	283781.0	285406.4	96069.4	140294.9
225	192917.2	188669.5	189815.0	63955.2	115642.5
150	106568.5	104197.5	104862.5	35363.4	81707.9
75	37822.0	36977.3	37218.1	12556.1	36574.6
37.5	13377.2	13078.6	13163.8	4441.0	13606.7
18.75	4734.4	4628.8	4658.9	1571.8	4826.6
9.375	1677.6	1640.3	1650.9	557.0	1710.2
1.5	110.0	107.6	108.3	36.5	112.1

Table A2.10: Rotational (Q_{rot}) and vibrational (Q_{vib}) partition functions for alaninol 2, gG'g, where $J_{max} = 220$ and $K_{max} = 40$.

T / K	Q_{rot} parent [$2I$+1=1]	Q_{rot} parent [$2I$+1=3]	Q_{vib}	Q_{rot} ^{13}C(1) [$2I$+1=3]	Q_{rot} ^{13}C(2) [$2I$+1=3]	Q_{rot} ^{13}C(3) [$2I$+1=3]	Q_{rot} ^{15}N [$2I$+1=1]
300	86814.4	260443.1	4.2	265983.8	261659.2	263141.7	88464.1
225	58300.5	174901.5	3.0	178787.4	175745.7	176770.5	59483.1
150	32518.4	97555.1	1.9	99821.3	98042.4	98631.4	33222.8
75	11597.7	34793.1	1.1	35622.2	34970.3	35184.0	11858.5
37.5	4102.7	12308.0	1.0	12601.4	12370.7	12446.3	4195.0
18.75	1452.2	4356.6	1.0	4460.3	4378.8	4405.5	1484.9
9.375	514.8	1544.3	1.0	1581.0	1552.1	1561.6	526.3
1.5		101.6	1.0	104.0	102.2	102.8	34.6

Table A2.11: Rotational (Q_{rot}) and vibrational (Q_{vib}) partition functions for valinol 1, g'Gg'G', where $J_{max} = 310$ and $K_{max} = 40$.

T / K	Q_{rot} parent [$2I$+1=1]	Q_{rot} parent [$2I$+1=3]	Q_{vib}	Q_{rot} ^{13}C(1) [$2I$+1=3]	Q_{rot} ^{13}C(2) [$2I$+1=3]	Q_{rot} ^{13}C(3) [$2I$+1=3]	Q_{rot} ^{13}C(4) [$2I$+1=3]	Q_{rot} ^{13}C(5) [$2I$+1=3]	Q_{rot} ^{15}N [$2I$+1=1]	Q_{rot} ^{18}O [$2I$+1=3]
300	252432.8	757298.3	10.2	760706.5	757585.8	762542.6	769097.7	770495.6	254852.1	787185.8
225	174088.4	522265.2	7.0	524635.4	522481.6	526017.3	530950.9	531533.2	175945.2	542940.1
150	100345.1	301035.2	3.9	302418.1	301175.4	303307.7	306485.0	306512.5	101567.5	313005.2
75	36815.1	110445.2	1.6	110960.6	110504.1	111325.3	112629.6	112511.5	37327.1	114859.6
37.5	13065.4	39196.2	1.1	39380.2	39218.2	39512.2	39984.8	39933.8	13251.7	40764.5
18.75	4621.7	13865.1	1.0	13930.4	13873.1	13977.1	14144.2	14126.1	4687.7	14419.8
9.375	1635.8	4907.3	1.0	4930.3	4910.1	4946.9	5006.0	4999.6	1659.1	5103.4
1.5		317.7	1.0	319.2	317.9	320.2	324.0	323.6	107.4	330.3

Table A2.12: Rotational partition functions (Q_{rot}) for valinol 2, g'Gg'G, where $J_{max} = 310$ and $K_{max} = 40$.

T / K	Q_{rot} parent [$2I$+1=1]	Q_{rot} parent [$2I$+1=3]	Q_{rot} ^{13}C(1) [$2I$+1=3]	Q_{rot} ^{13}C(2) [$2I$+1=3]	Q_{rot} ^{13}C(3) [$2I$+1=3]	Q_{rot} ^{13}C(4) [$2I$+1=3]	Q_{rot} ^{13}C(5) [$2I$+1=3]	Q_{rot} ^{15}N [$2I$+1=1]
300	249015.5	747046.6	752640.8	747579.4	750680.5	760570.8	758019.6	251165.8
225	171206.0	513617.9	517596.2	514023.9	516176.2	523141.5	521654.5	172858.2
150	98274.2	294822.6	297209.9	295086.7	296338.2	300466.7	299822.8	99359.2
75	35893.5	107680.5	108592.4	107788.9	108252.1	109810.5	109657.5	36343.0
37.5	12727.4	38182.2	38507.9	38221.3	38385.9	38941.4	38892.3	12890.0
18.75	4502.0	13506.1	13621.3	13520.0	13578.1	13774.5	13757.2	4559.6
9.375	1593.5	4780.4	4821.1	4785.3	4805.8	4875.3	4869.2	1613.8
1.5		309.6	312.3	310.0	311.3	315.8	315.4	104.5

Table A2.13: Rotational partition functions (Q_{rot}) for valinol 3, g'Gg'T, where $J_{max} = 310$ and $K_{max} = 40$.

T / K	Q_{rot} parent [$2I$+1=1]	Q_{rot} parent [$2I$+1=3]
300	243028.9	729086.6
225	168520.4	505561.1
150	97900.3	293700.8
75	36253.6	108760.9
37.5	12892.2	38676.7
18.75	4560.8	13682.5
9.375	1614.3	4843.0
1.5		313.8

Table A2.14: Rotational partition functions (Q_{rot}) for valinol 4, gG'gG', where $J_{max} = 310$ and $K_{max} = 40$.

T / K	Q_{rot} parent [$2I$+1=1]	Q_{rot} parent [$2I$+1=3]
300	224996.6	674989.7
225	156543.3	469630.0
150	91391.9	274175.7
75	34056.4	102169.2
37.5	12130.3	36391.0
18.75	4291.5	12874.6
9.375	1519.1	4557.2
1.5		295.5

Table A2.15: Rotational partition functions (Q_{rot}) for leucinol 1, g'Gg'Tg, where $J_{max} = 400$ and $K_{max} = 40$.

T / K	Q_{rot} parent [$2I$+1=1]	Q_{rot} parent [$2I$+1=3]	Q_{rot} ^{13}C(1) [$2I$+1=3]	Q_{rot} ^{13}C(2) [$2I$+1=3]	Q_{rot} ^{13}C(3) [$2I$+1=3]	Q_{rot} ^{13}C(4) [$2I$+1=3]	Q_{rot} ^{13}C(5) [$2I$+1=3]	Q_{rot} ^{13}C(6) [$2I$+1=3]	Q_{rot} ^{15}N [$2I$+1=1]
300	418643.6	1255930.9	1267098.9	1257102.9	1258150.5	1263217.0	1278750.7	1272943.8	422080.7
225	288565.0	865694.9	873649.0	866529.4	867406.3	870728.9	881736.0	8781863	291206.6
150	166217.5	498652.4	503441.4	499149.9	499783.4	501561.4	508140.1	506463.9	167958.0
75	60934.3	182802.8	184643.8	182991.7	183277.2	183873.2	186381.0	185920.3	61662.6
37.5	21618.2	64854.6	65513.6	64922.6	65027.4	65234.7	66130.5	65978.2	21883.0
18.75	7645.3	22935.8	23168.8	22960.0	22997.0	23070.2	23386.8	23333.2	7739.0
9.375	2704.8	8114.3	8196.7	8122.9	8136.0	8161.8	8273.8	8254.9	2737.9
1.5		523.2	528.5	523.8	524.6	526.3	533.4	532.2	176.5

Table A2.16: Rotational partition functions (Q_{rot}) for leucinol 2, g'Gg'Gg', where $J_{max} = 400$ and $K_{max} = 40$.

T / K	Q_{rot} parent [$2I$+1=1]	Q_{rot} parent [$2I$+1=3]
300	390664.9	1171994.6
225	271684.2	815052.7
150	158505.8	475517.5
75	59012.5	177037.4
37.5	21012.1	63036.3
18.75	7432.0	22296.0
9.375	2629.5	7888.5
1.5		509.0

Table A2.17: Rotational partition functions (Q_{rot}) for leucinol 3, gG'gTg', where $J_{max} = 400$ and $K_{max} = 40$.

T / K	Q_{rot} parent [$2I$+1=1]	Q_{rot} parent [$2I$+1=3]
300	404475.5	1213426.5
225	281720.5	845161.4
150	164738.9	494216.5
75	61519.6	184558.9
37.5	21923.0	65769.0
18.75	7754.2	23262.7
9.375	2743.4	8230.3
1.5		530.9

Table A2.18: Rotational partition functions (Q_{rot}) for isoleucinol 1, g'Gg'Tt, where $J_{max} = 400$ and $K_{max} = 40$.

T / K	Q_{rot} parent [$2I$+1=1]	Q_{rot} parent [$2I$+1=3]	Q_{rot} ^{13}C(1) [$2I$+1=3]	Q_{rot} ^{13}C(2) [$2I$+1=3]	Q_{rot} ^{13}C(3) [$2I$+1=3]	Q_{rot} ^{13}C(4) [$2I$+1=3]	Q_{rot} ^{13}C(5) [$2I$+1=3]	Q_{rot} ^{13}C(6) [$2I$+1=3]	Q_{rot} ^{15}N [$2I$+1=1]	Q_{rot} ^{18}O [$2I$+1=3]
300	392586.7	1177760.1	1179320.2	1178979.0	1186611.1	1189720.7	1187149.6	1201983.1	395983.9	1219393.6
225	271767.0	815301.1	816417.7	816178.9	821593.0	824606.0	821960.4	832115.8	274397.5	844135.7
150	157478.9	472436.8	473114.4	472973.8	476219.9	478683.9	476428.3	482219.5	159235.5	489158.2
75	58129.9	174389.6	174653.2	174600.4	175846.7	177078.6	175921.7	178017.9	58882.1	180567.4
37.5	20655.0	61964.9	62059.7	62040.8	62487.5	62951.8	62513.9	63255.3	20930.7	64160.0
18.75	7305.5	21916.5	21950.0	21943.4	22101.3	22265.8	22110.7	22372.8	7403.1	22692.6
9.375	2584.8	7754.3	7766.1	7763.8	7819.6	7877.8	7822.9	7915.6	2619.3	8028.6
1.5		500.2	500.9	500.8	504.4	508.1	504.6	510.5	168.9	517.8

Table A2.19: Rotational partition functions (Q_{rot}) for isoleucinol 2, g'Gg'G't, where $J_{max} = 400$ and $K_{max} = 40$.

T / K	Q_{rot} parent [$2I$+1=1]	Q_{rot} parent [$2I$+1=3]	Q_{rot} ^{13}C(1) [$2I$+1=3]	Q_{rot} ^{13}C(2) [$2I$+1=3]	Q_{rot} ^{13}C(3) [$2I$+1=3]	Q_{rot} ^{13}C(4) [$2I$+1=3]	Q_{rot} ^{13}C(5) [$2I$+1=3]	Q_{rot} ^{13}C(6) [$2I$+1=3]
300	359702.0	1079106.0	1081798.9	1079662.7	1087409.0	1090167.5	1089691.9	1097341.5
225	251665.9	754997.8	757009.1	755395.8	760903.9	763553.9	762492.3	768065.0
150	148165.9	444497.6	445797.0	444739.7	448063.3	450277.2	448990.8	452472.4
75	55855.1	167565.2	168117.8	167660.7	168957.8	170151.1	169303.3	170725.4
37.5	19965.4	59896.1	60101.2	59930.7	60399.6	60870.9	60522.6	61044.3
18.75	7063.6	21190.9	21263.7	21203.2	21369.1	21536.8	21412.6	21597.4
9.375	2499.4	7498.2	7523.9	7502.5	7561.2	7620.5	7576.6	7641.9
1.5		484.1	485.8	484.4	488.2	492.0	489.2	493.4

Table A2.20: Rotational partition functions (Q_{rot}) for isoleucinol 3, g'Gg'Tg', where $J_{max} = 400$ and $K_{max} = 40$.

T / K	Q_{rot} parent [$2I$+1=1]	Q_{rot} parent [$2I$+1=3]	Q_{rot} ^{13}C(1) [$2I$+1=3]	Q_{rot} ^{13}C(2) [$2I$+1=3]	Q_{rot} ^{13}C(3) [$2I$+1=3]	Q_{rot} ^{13}C(4) [$2I$+1=3]	Q_{rot} ^{13}C(5) [$2I$+1=3]	Q_{rot} ^{13}C(6) [$2I$+1=3]
300	381820.0	1145459.9	1147614.9	1147236.4	1153402.4	1158217.9	1152584.8	1168295.0
225	266696.4	800089.1	801668.6	801387.5	805854.9	809723.9	805263.2	816349.1
150	156613.3	469840.0	470833.9	470653.9	473421.3	476146.6	473055.2	479667.6
75	58824.9	176474.6	176882.9	176807.4	177922.9	179187.8	177775.6	180313.8
37.5	21002.0	63006.0	63155.7	63127.9	63534.9	64014.6	63481.1	64393.4
18.75	7430.0	22289.9	22342.9	22333.0	22477.1	22647.4	22458.1	22780.8
9.375	2628.9	7886.8	7905.6	7902.1	7953.0	8013.3	7946.3	8060.4
1.5		509.0	510.2	510.0	513.3	517.1	512.8	520.2

Table A2.21: Rotational partition functions (Q_{rot}) for isoleucinol 4, g'Gg'Gt, where $J_{max} = 400$ and $K_{max} = 40$.

T / K	Q_{rot} parent [$2I$+1=1]	Q_{rot} parent [$2I$+1=3]
300	383498.6	1150495.9
225	845161.4	281720.5
150	494216.5	164738.9
75	184558.9	61519.6
37.5	65769.0	21923.0
18.75	23262.7	7754.2
9.375	8230.3	2743.4
1.5	530.9	

Table A2.22: Rotational partition functions (Q_{rot}) for isoleucinol 5, g'Gg'Gg, where $J_{max} = 400$ and $K_{max} = 40$.

T / K	Q_{rot} parent [$2I$+1=1]	Q_{rot} parent [$2I$+1=3]
300	341068.3	1023204.8
225	241540.8	724622.5
150	145031.4	435094.3
75	56431.6	169294.7
37.5	20448.4	61345.1
18.75	7243.1	21729.3
9.375	2562.8	7688.5
1.5		496.7

Table A2.23: Rotational partition functions (Q_{rot}) for isoleucinol 6, gG'gTt, where $J_{max} = 400$ and $K_{max} = 40$.

T / K	Q_{rot} parent [$2I$+1=1]	Q_{rot} parent [$2I$+1=3]
300	356099.6	1068298.7
225	248913.9	746741.7
150	146335.9	439007.8
75	55051.2	165153.5
37.5	19663.8	58991.3
18.75	6956.5	20869.5
9.375	2461.5	7384.4
1.5		476.8

Table A2.24: Rotational partition functions (Q_{rot}) for isoleucinol 7, gG'gTg', where $J_{max} = 400$ and $K_{max} = 40$.

T / K	Q_{rot} parent [$2I$+1=1]	Q_{rot} parent [$2I$+1=3]
300	332094.1	996282.2
225	232614.8	697844.4
150	137189.0	411567.0
75	51847.6	155542.9
37.5	18549.0	55647.1
18.75	6563.0	19689.0
9.375	2322.4	6967.1
1.5		450.1

Hazards

Hazardous substances according to the Global Harmonised System (GHS) within the European Union:

Chemical	Hazard Statement(s)	Precautionary Statement(s)	GHS Labelling
1,2-propanediol	-	-	-
acetaldehyde	224	201	GHS02
	319	210	GHS07
	335	305+351+338	GHS08
	341	308+313	
	350	403+233	
acetone	225	210	GHS02
	319	305+351+338	GHS07
	336		
acetonitrile	225	210	GHS02
	302+312+332	280	GHS07
	319	301+312+330	
		302+352+312	
		304+340+312	
		305+351+338	
alaninol	314	280	GHS05
		305+351+338	
		310	

Chemical	Hazard Statement(s)	Precautionary Statement(s)	GHS Labelling
ethanol	225	210	GHS02
	319	305+351+338	GHS07
imidazole	302	201	GHS05
	314	260	GHS07
	360D	280	GHS08
		303+361+353	
		305+351+338	
		308+313	
iso-propyl cyanide	225	210	GHS02
	300	261	GHS06
	311	264	
	315	280	
	319	301+310	
	335	305+351+338	
isoleucinol	315	264	GHS07
	319	280	
		302+352+332+313+362+364	
		305+351+338+337+313	
leucinol	315	264	GHS08
	319	280	
		302+352+332+313+362+364	
		305+351+338+337+313	
valinol	315	264	GHS07
	319	280	
		302+352+332+313+362+364	
		305+351+338+337+313	

Figure H1: Global Harmonised System (GHS) codes and symbols.

Acknowledgements

Well, that took a bit longer than I anticipated...

A PhD is a long journey, and mine was one filled with many experiences, opportunities, and people, all of which shaped me and my time as a PhD student. For all of the love, support, and patience: THANK YOU.

I feel very lucky to have had Melanie Schnell as my PhD supervisor. I thank her for giving me the opportunity to work in her group, for giving me the independence and influence to help steer the research direction of the W-band spectrometer, and for supporting me in so many opportunities that came up outside of the lab. Her knowledge and expertise, coupled with her ability to motivate and her empathy and understanding, is inspirational. Thank you pushing me when I needed it, and thank you for listening when it mattered.

To the past and present members of FS-SMP (formerly CoCoMol) - Simon, David, Sabrina, Chris, Jack, Anna, Cristóbal, Sérgio, Amanda, Mariyam, Sébastien, Donatella, Pragya, María, Denis, Daniel, Pablo, Weixing, Diksha, Gayatri, Himanshi, Jason, Wenhao, Freya, and Maureen - thank you for your company, encouragement, and support, for putting up with my singing and terrible (sorry, I mean HILARIOUS) puns, and for eating everything I baked.

I worked more directly under Amanda and Seb. They helped shape my project in the early days, and I learnt many things from them, including how to run an experiment, and, arguably most importantly, what to do when something doesn't go as first planned. Amanda shared many nuggets of information that one only gathers when they have the wealth of experience she has. I am most grateful for the numerous times her interventions saved the experiment/project/day. To Seb, thank you for your calming influence - the group misses your presence. To the astrochemistry sub-group: it has been a pleasure to work with you and see this group grow in number. I remember the days when sub-group meetings consisted of Melanie, Amanda, Seb, and me; we now make up half of the group. Thank you for your contributions and support, and I wish you all luck and success in your endeavours. To the first-draft proof readers - Amanda, Dona, Mariyam, Pablo, and Wenhao - thank you.

The extra special contributions of three people need to be particularly acknowl-

edged. Firstly, to Mariyam - I think I have no words to express how grateful I am that I got to share this journey with you. From the early days of you trying to grab my attention by knocking on the table, to the stresses of trying to organise our numerous trips to the USA (work-related, of course), to the evenings of encouraging each other to keep writing, know our things, and type faster. We have worked, celebrated, suffered, "squabbled", and solved, and I could not have asked for a better work wife. Secondly, to Pragya. For harmonising with me during the office choir sessions, for sharing in no-alcohol and no-sugar challenges, for dreaming about my thesis cave, and for making that dream come true. Having you both in the office made the days shorter, easier, and enjoyable. Thirdly, to Sam, our unofficial office-mate. For the chats, the concerts, the bread, and for being my alcohol consumption facilitator when I needed it.

To the collaborators who brought experiment ideas to Hamburg and who shared their collective years of knowledge - thank you. A special mention to Michela (who I co-authored my first paper with) and Pascal (who I got to share a Scottish journey with; he is as much a friend as he is a colleague). For their support and patience (online, at ISMS, and at BASF), I thank Justin and Matt from BrightSpec.

To my fellow IMPRS-UFAST and PIER PhD students - thank you for the scientific exchanges, the social interactions, and the countless hours of German class.

To Denny. Thank you for reading my first attempt at translating my Abstract into a Zusammenfassung. You have taught me as much about myself as you have about German language, culture, and architecture. Thank you for being one of the good guys.

One of the most memorable experiences of my PhD was my research stay with Prof. Robert W. Field at the Massachusetts Institute of Technology. Bob was in the process of wrapping up the activities of his research group and heading for retirement. Despite this, Bob's passion for science was as strong as I imagine it to have been throughout his scientific career, and it was a privilege to work with him, if only for a few months. I thank him and his group, particularly Tim, for their generous hospitality. To my MIT family - Idaly, Fernanda, Anne, Teo, Thomas, Enzo, Rodrigo, and Nick - thank you for the pitchers at the Muddy Charles, for Mount Washington, for New York, and for Paris. At a critical time, you reminded me about the joys of life outside of the lab.

To Niklas - thank you for the ABBA lyrics, the food, the long walks, the trashy/teary Netflix shows, and, most importantly, the pep talks.

To Stephanie, thank you for always understanding and supporting my indecisiveness, for giving me somewhere to live on my many visits back to the best city in the world, for sharing my love of American television series, for suggesting the best Spotify playlists in existence, for teaching me the correct way to use a tub of butter, and for everything in between. Thank you for being my person.

To those who miss the warm, loving embrace of the Joseph Black Building - Katie, Jenn, Fraser, Ross, Ellie, and Louise - thank you for the reunions, weddings, and Thursday catch-ups. To Robbie - for sharing, from a distance, the ups and downs of doing a PhD. To Chris - for the journeys up and down the A9 and for always being willing to reminisce about the simpler days. And to the inhabitants of the hole - Ollie, Paddy, Janos, and Marcus (and later, Colin) - for helping me start this journey the only way an Edinburgh student knows how and for the quarantine quizzes. Carry on winning.

To Ninang Len - thank you for always having my back.

To the Aquino/Edades/Castañeda/Mamaril/Tamayo family - your love and support has been invaluable. It means the world to me to know that, despite whatever distance may be between us, you are always there for and believe in me.

To Ben Sr., my dad, who never got to see this thesis, thank you for always being proud of me. Finally, and most importantly, I want to thank and dedicate this thesis to my mama, Grace. For your unconditional love, for your wholehearted support, and for your unwavering guidance: thank you. I am who I am because of all that you have taught me - for that, and for so many other countless things, I will be forever grateful. 143 44.

Declaration

I hereby declare that this thesis is my original work, and it has been written by me in its entirety. I have duly acknowledged all the sources of information which have been used in the thesis.

Benjamin E. Arenas

December 2, 2020

Hamburg, Germany